Dissertation
submitted to the
Combined Faculties for the Natural Sciences and for Mathematics
of the
Ruprecht-Karls-Universität Heidelberg
for the degree of
Doctor of Natural Sciences

Put forward by
Oscar Jesús García Montero
born in: *San José, Costa Rica*
Oral examination: *October 17, 2019*

Probing the early-time dynamics of heavy-ion collisions

Referees:

Prof. Dr. Jürgen Berges
Prof. Dr. Bjorn Malte Schäfer

RUPRECHT-KARLS-UNIVERSITÄT HEIDELBERG

DOCTORAL THESIS

Probing the early-time dynamics of heavy-ion collisions

Author:
Oscar Jesus GARCIA MONTERO

Supervisor:
Prof. Dr. Jürgen BERGES

Dissertation
submitted to the
Combined Faculties for the Natural Sciences and for Mathematics
of the
Ruprecht-Karls-Universität Heidelberg

for the degree of
Doctor of Natural Sciences

Abstract

Probing the early-time dynamics of heavy-ion collisions

The objective of this thesis is to contribute to the understanding of the phenomenology of the early stages of Heavy Ion Collision (HIC) experiments. In such settings, it is assumed that two nuclei collide at energies high enough to compress the nucleons into a volume of deconfined quarks and gluons. This *fireball* rapidly thermalizes and expands against the surrounding vacuum. Nevertheless, the question of when and how the fireball thermalizes has not been completely answered, even though wide progress has been done. This work aims to tackle two small pieces of the overarching puzzle. How can we use photons radiated from the medium to probe the initial and pre-equilibrium stages? And how do adding conserved charges, given at initial time of the collision, change the path to thermal equilibrium?

The first question is addressed in three different avenues. We compute the change of the spectrum of photons produced at initial time, by understanding how quarks multiply scatter from a dense hadron, which is taken as a shockwave of gluons. For this, we use the framework of the Color Glass Condensate Effective field Theory. In this work, we present a comparison with proton-proton collision data and predictions for the new run at the Large Hadron Collider (LHC), at center of mass energies of $\sqrt{s} = 13$ TeV.

For the case of collisions with heavy nuclei, a medium of quarks and gluons is created, and photons are radiated throughout the collision. We compute the photon spectrum for the case of the *bottom-up* scenario, which parametrically describes the thermalization of the quark-gluon-plasma. Building on recent developments, we find the non-equilibrium case dominates. We compare it with an early hydrodynamical scenario, where a thermalized quark gluon plasma is assumed to settle at the same initial time as the pre-equilibrium case.

However, the yields cannot be dissected experimentally, and we need an extra observable to distinguish if the photons measured come from earlier or later times. For this, we will use interferometry of photons, in particular Hanbury-Brown-Twiss (HBT) correlations. We compute the associated *HBT radii*, which give information on the spatial extent of the sources, and use them to propose a qualitative method to discriminate between scenarios with and without pre-equilibrium photons.

The second question we ask is motivated by the Chiral Vortical Effect (CVE), and the discovery of the imbalance of $\Lambda/\bar{\Lambda}$ hyperons in STAR at the Relativistic Heavy Ion Collider (RHIC). We aim at understanding the role of angular momentum in the collision, and the road of the gluon medium to thermalization. To kickstart this objective, we use a 2D scalar toy model to explore non-vanishing angular momentum in an overoccupied Quantum Field Theory.

Zusammenfassung

Erforschung der Frühzeitdynamik von Schwerionenkollisionen

Ziel dieser Arbeit ist es zum Verständnis der Phänomenologie früher Stadien von Experimenten von Schwerionenkollisionen (HICs) beizutragen. In solchen Situationen wird angenommen, dass zwei Kerne mit sehr hohen Energien kollidieren, hoch genug, um die Nukleonen zu einem Volumen von freien 'deconfined' Quarks und Gluonen zu komprimieren. Dieser sog. *fireball* thermalisiert schnell und dehnt sich im umliegenden Vakuum aus. Dennoch ist die Frage, wann und wie der fireball thermalisiert, noch nicht vollständig beantwortet, wenngleich bereits großer Fortschritt erzielt wurde. Diese Arbeit zielt darauf ab, zwei kleine Teile dieser übergeordneten Frage zu lösen. Wie können wir Photonen, die vom Medium ausgestrahlt werden, verwenden, um die Anfangs- und Vorgleichgewichtsstufe zu untersuchen? Und wie verändern weitere Erhaltungsgrößen, die zum Anfangszeitpunkt der Kollision gegeben sind, den Weg zum thermischen Gleichgewicht?

Die erste Frage wird auf drei verschiedene Wege adressiert. Wir berechnen das Spektrum der zu Beginn erzeugten Photonen, indem wir verstehen, wie Quarks mehrfach an einem dichten Hadron streuen, das als Gluon-Schockwelle interpretiert wird. Hierfür verwenden wir die effektive Feldtheorie des Color Glass Condensate. In dieser Arbeit präsentieren wir einen Vergleich mit Proton-Proton (p+p) Kollisionsdaten und Vorhersagen für den neuen Run 3 am Large Hadron Collider (LHC) bei Schwerpunktsenergien von $\sqrt{s} = 13\ \mathrm{TeV}$.

Im Fall von Kollisionen mit schweren Kernen wird ein Medium aus Quarks und Gluonen erzeugt, und Photonen werden während der gesamten Kollision emittiert. Wir berechnen das Photonenspektrum für das *bottom-up* Szenario, das die Thermalisierung des Quark-Gluon-Plasmas parametrisch beschreibt. Aufbauend auf den jüngsten Entwicklungen stellen wir fest, dass für dieses Szenario Beiträge aus dem Nichtgleichgewicht tatsächlich dominieren. Wir vergleichen dieses Ergebnis weiter mit einem frühen hydrodynamischen Szenario, in dem ein thermisches Quark-Gluon-Plasma zur Anfangszeit angenommen wird.

Jedoch kann experimentell aus der Gesamtanzahl emittierter Photonen nicht zwischen Photonen aus früheren oder späteren Zeiten unterschieden werden, weshalb eine zusätzliche Observable benötigt wird. Dazu verwenden wir Photoneninterferometrie, insbesondere Hanbury-Brown-Twiss-Korrelationen. Wir berechnen die zugehörigen *HBT-Radien*, die Aufschluss über die räumliche Ausdehnung der Quellen geben, und verwenden sie, um eine qualitative Methode zur Unterscheidung zwischen Szenarien mit und ohne Vorgleichgewichtsphotonen darzustellen.

Die zweite Frage ist motiviert durch den postulierten Chiral-Vortical-Effect (CVE) und die Entdeckung des Ungleichgewichts von $\Lambda/\bar{\Lambda}$-Hyperonen in STAR am Relativistic Heavy Ion Collider (RHIC). Letztendlich wollen wir die Rolle des Drehimpulses in der Thermalisierung des Gluonmediums verstehen. Um dieses Ziel zu erreichen, verwenden wir ein toy model in zwei Dimensionen, um nicht verschwindenden Drehimpuls in einer hochbesetzten skalaren Quantenfeldtheorie zu untersuchen.

Declaration of Authorship

I, Oscar Jesus GARCIA MONTERO, declare that this thesis titled, "Probing the early-time dynamics of heavy-ion collisions" and the work presented in it are my own. I confirm that:

- Where any part of this thesis has previously been submitted for a degree or any other qualification at this University or any other institution, this has been clearly stated.
- Where I have consulted the published work of others, this is always clearly attributed.
- Where I have quoted from the work of others, the source is always given. With the exception of such quotations, this thesis is entirely my own work.
- Parts of this dissertation have been or will be published in the following articles:
  - Benić, S., Fukushima, K., Garcia-Montero, O. and Venugopalan, R. Probing gluon saturation with next-to-leading order photon production at central rapidities in proton-nucleus collisions JHEP 1701 (2017) 115
  - Benić, S., Fukushima, K., Garcia-Montero, O. and Venugopalan, R. Constraining unintegrated gluon distributions from inclusive photon production in proton–proton collisions at the LHC Phys.Lett. B791 (2019) 11-16
  - Garcia-Montero. O. Non-equilibrium photons from the thermalizing Glasma. *In preparation*
  - Berges, J., Garcia-Montero, O., Löher,N., Mazeliauskas, A., and Reygers, K. Probing the evolution of the fireball using higher photon correlations *In preparation*

Signed: _____

Date: _____

Contents

List of Figures

List of Abbreviations

LHC	**L**arge **H**adron **C**ollider
RHIC	**R**elativistic **H**eavy **I**on **C**ollider
HIC	**H**eavy **I**on **C**ollision
QGP	**Q**uark-**G**luon **P**lasma
QFT	**Q**uantum **F**ield **T**heory
QCD	**Q**uantum **C**hromo**d**ynamics
QED	**Q**uantum **E**lectro**d**ynamics
EFT	**E**ffective **F**ield **T**heory
CGC	**C**olor **G**lass **C**ondensate
CYM	**C**lassical **Y**ang-**M**ills
LO	**L**eading **O**rder
NLO	**N**ext-to-**L**eading **O**rder
PDF	**P**arton **D**istribution **F**unction
UGD	**U**nintegrated **G**luon **D**istribution
BMSS	**B**aier, **M**ueller, **S**chiff and **S**on Thermalization Scenario
AMY	**A**rnold, **M**oore and **Y**affe
IVP	**I**nitial **V**alue **P**roblem
CSS	**C**lassical **S**tatistical **S**imulation
HFT	**H**ankel-**F**ourier **T**ransform
DBC	**D**irichlet **B**oundary **C**ondition
VAM	**V**anishing **A**ngular **M**omentum

Introduction

> Light is a thing that cannot be reproduced, but must be represented by something else – by color.
>
> *Paul Cezanne*

The quest to understand how collectivity arises from the interaction of simpler elements is one that spans throughout a vast diversity of fields, from population dynamics, economics and biology [1], down to the quantum level. All around us, individual elements, i.e. particles, molecules, bacteria or planets, self-organize and explode in a plethora of phenomena, where the emergent properties are richer than the sum of the individual ones [2]. One specific avenue of this search is in the area of many-body effects in quantum systems, which prove to be excellent settings to investigate the rise of complexity at the quantum level. In such systems, Quantum Field Theory (QFT) rises as a unifying language, encoding naturally the many-body nature of the Universe. Using QFT we have been able to understand phenomena across vast differences of scales and temperatures, ranging from the early Universe cosmology to experiments of cold quantum gases. In this language we can also formulate questions regarding the emergent properties of fundamental interactions, namely nuclear matter, which can be described microscopically by Quantum Chromodynamics (QCD). In this theory, it is assumed that hadrons are made up of quarks, smaller fermionic species capable of carrying three different charges, traditionally called *colors*. These fermions are coupled via gauge particles called gluons, which are massless, but unlike photons are self-interacting. When thought of as a medium, nuclear matter can exhibit a whole range of exciting phenomena, ranging from normal matter, where QCD matter is confined in nuclei, to exotic superfluid and superconducting phases in the cores of neutron stars [3–5].

To explore the complexity arising from these fundamental interactions, our current main laboratories on Earth are Heavy Ion Collision (HIC) experiments at the Relativistic Heavy Ion Collider (RHIC) and the Large Hadron Collider (LHC). In these experiments, nuclei are smashed against each other after being accelerated close to the speed of light. It is believed that enough energy is deposited in the interaction volume to break down the nucleons, and create a hot, thermal medium of deconfined quarks and gluons [6]. In the literature, such a state of nuclear matter has been extensively called the Quark-Gluon Plasma (QGP). This interpretation has met wide success, as particle yields recovered from the collisions seem to indicate underlying thermal distributions. [7, 8] However, the collision is a violent, completely out-of-equilibrium event. Even if it is expected that the medium thermalizes in a relatively short time of order $\sim 1 \times 10^{-24}$s, still no definite answer to the question of thermalization exists [9]. Therefore, to effectively search for the emergent properties of nuclear matter, one has to keep in mind the main questions to address. Which effects are imprinted by the many-body nature of the initial nuclear state? Which come from the pre-equilibrium stage path the medium takes to

thermalize, and what comes from the thermal medium? Finally, which are the correct observables to answer such questions? This thesis is an exploration on these questions.

Initial stages

At low temperature and density, quarks and gluons are confined inside hadronic states. Furthermore, one of the most striking properties of QCD is that hadronic systems become weakly bound when accelerated to high energies, thanks to the phenomenon of *asymptotic freedom* [10]. In this limit, partons (a collective name for quarks and gluons) which carry the biggest fraction of the longitudinal momentum of the hadron behave like individual, free particles, which allows us to calculate their properties using few-body perturbative physics. Such partons will find it energetically favorable to radiate more partons with smaller momentum fractions. The more energy is pumped into the hadron, the easier it will be for gluons to radiate further, ending up in what is called a cascade, filling up the phase space. The rise of the gluon distributions with energy was shockingly found in the Deep Inelastic Experiments at HERA [11]. In these experiments an electron was used to probe the inner contents of the proton, interact electromagnetically with the quarks via a virtual photon. Alternatively, the photon could fluctuate into a $q\bar{q}$ pair, and probe directly the gluon state in the proton [12]. The process of gluon cascading is slowed down when it becomes equally favorable for them to recombine, that is when the hadron starts to "fill up" with gluons. Then the gluon splitting processes halt and their distribution *saturates*. At this point, the hadron is over-occupied and behaves as a traveling shockwave of coherent gluons [13].

It is a necessary task to isolate the many-body effects intrinsic to hadronic waveforms. Nonetheless, because most probes rising from scatterings off the hadron interact strongly, a probe blind to rescatterings and hadronization is needed. Photons and, as a consequence, dileptons are ideal for this objective. First, we need to clarify that electromagnetic radiation from hadronic collisions comes in three different forms, *prompt*, *direct*, and *decay* photons. The latter are created, as their name suggests, from decay processes of hadrons. These photons exhibit a particular spectrum, and for the case of nucleus-nucleus (A+A) collisions, will dominate the spectra. In this thesis we will neglect these contributions, as they can be sorted out experimentally from known data [14, 15]. The prompt contribution is bremsstrahlung coming from hard scatterings of the incoming probe off the hadron. These probes will be in this case radiated from processes involving (anti) quark lines[1], which after scattering of the initial stage will have different behavior for a saturated state, as opposed to the normal perturbative picture. In Chapter 1 we will use such radiation to help constrain the gluon state at initial time.

Finally, direct photons are those which are emitted from the interacting volume via in-medium scatterings. In the literataure they are classified into the pre-equilibrium and thermal subcategories, but since experimentally discriminating between these yields is near to impossible, we will use these classes only for theoretical considerations. Direct photons are the probes we will choose in Chapters 2 and 3 to explore the route to thermalization.

[1] Additionally, hard quarks and gluons will create jets, which in the process of hadronization will radiate photons. These *fragmentation* or *jet conversion* photons present low transverse energies, and can be dealt with by isolating [16] the main, more energetically photon.

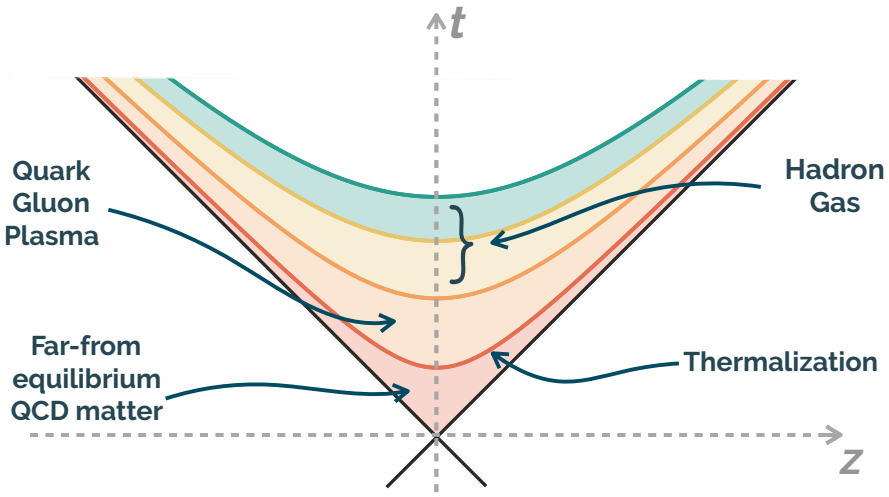

FIGURE 1: Spacetime evolution of a Heavy Ion Collision experiment in the Bjorken picture. As the fireball expands rapidly, the non-equilibrium medium evolves until a thermalized Quark-Gluon-Plasma. The nuclei travel in the light cone, and the collision happens in the origin of this spacetime diagram

The evolution of the fireball

The widely accepted picture of heavy ion collisions is that after some time the medium thermalizes and undergoes rapid expansion [17, 18]. Because of this, the temperature in the hydrodynamically behaving *fireball* will decrease fast until the energy density in the medium is not enough to keep quarks and gluons deconfined (see fig. 1). At this point, there is a change of relevant degrees of freedom, and the QGP becomes a gas of hadronic species, called the Hadron Resonance Gas (HRG) [19]. At this stage, the system continues to expand until the temperature is low enough so that particles stop interacting inelastically and their total yields get fixed. Later on, hadrons will stop having elastic collisions, which sets their spectra. These two processes are normally called the chemical and kinetic freeze-out, respectively [20, 21]. After this last stage, particles stream freely to the detectors. The processes listed here comprise the so called Standard Model of Heavy Ion Collisions.

As it was stated above, a definite answer to the question of which path the system taks to thermalize has not yet been achieved, and it is missing from the Standard Model of HICs[2]. Nevertheless, a wide-spread interest has sparked to understand the route to thermalization, starting from the initial stage. Even when a full simulation that links the initial stage of the collision with the fluid-like stages is not fully set, wide progress has been achieved to understand its time evolution [22–27]. A particular scenario we will focus on in this thesis is the one proposed by Baier, Mueller, Schiff and Son, commonly known as the *bottom-up* scenario [28]. In their seminal paper, it was proposed that after a short and very non-linear stage, in which instabilities highly populate the gluon fields, the nuclear medium undergoes relaxation in three stages. First, elastic collisions broaden the longitudinal spectrum, and even when expanding at the speed of light, particles do not stream freely. Then, inelastic collisions take over and the number of gluons with low transverse momenta rises. Soft particles will exchange energy more effectively, and this

[2] In some works it is even completely omitted from the spacetime diagrams (see fig. 1).

sector will thermalize between the second and third stage. Finally, highly energetic particles will loose their energy to the thermal bath in multiple radiative processes, also called *jet quenching processes*. The striking feature of this scenario is that the path to this relaxation is given parameterically by universal exponents, which arise from a kinetic description, but do not depend on the details of the initial conditions. Moreover, these scaling exponents were confirmed by quantum field theoretical simulations, where it was shown that a dense out-of-equilibrium medium of gauge fields approaches a non-thermal fixed point in along its path to thermalization [26].

It is one of the goals of our work to use phenomenology to try to disentangle the thermal and non-thermal stages from HICs, effectively getting a better understanding of the thermalization of the QGP. For this, just as above, we need an experimental probe that is created throughout the collision and is not sensitive to the medium. Once again it should be emphasized that photons and dileptons are ideal probes to explore the evolution of the fireball, as they can escape the medium virtually unscathed. Furthermore, they are created throughout the collision and should carry out the information of the emission source faithfully to the detectors. Unfortunately, since HIC experiments are the femtoscopic version of long-exposure photography, the photon spectra and total yields will contain all the information together and tangled. This will effectively gloss out the dependence and relevance of the different stages, making it difficult to extract the appropriate spacetime information.

Nevertheless, this can be circumvented by measuring how photon pairs are correlated, as photons close in phase space will experience quantum enhancement. Such measurements, known in the literature as Hanbury-Brown-Twiss (HBT) correlations will be sensitive to the time at which photons are created. In this sense, in Chapter 3 we will be using higher correlations to ask the question of how relevant are photons from pre-equilibrium stage. As a consequence, when compared to experiment we will qualitatively use HBT correlators to ask how relevant these pre-equilibrium scenarios are, to shed a bit more of light to the question of thermalization time.

Conserved quantities

Historically, the expression *Little Bang* has been used as a catchphrase to refer to heavy ion collisions. This was used as an analogy to express the fact that deconfined nuclear matter at high temperatures should be obtained similarly to early cosmological times, before recombination [29, 30]. In reality, this comparison may be deeper, especially when thinking in terms of their dynamics, when the fields are pulled far-from-equilibrium. When those fields allowed to relax, the systems take a parametrically long detour, flowing near a non-thermal fixed point (see fig. 2). The system will cascade, redistributing its conserved charges. The distribution of modes in such a system will relax in a self-similar way,

$$f(t, \boldsymbol{p}) = t^{\alpha} f_S(\boldsymbol{p}\, t^{\beta})$$

where the scaling exponents α and β are universal and therefore do not depend on the initial conditions. It is through these processes that the system effectively looses information of its initial state. After occupations near the characteristic scale fall close to unity, quantum fluctuations become relevant, and the system will further flow to thermal equilibrium [31]. What is striking is that such behavior has been found across scales and temperatures, where the path to thermalization can

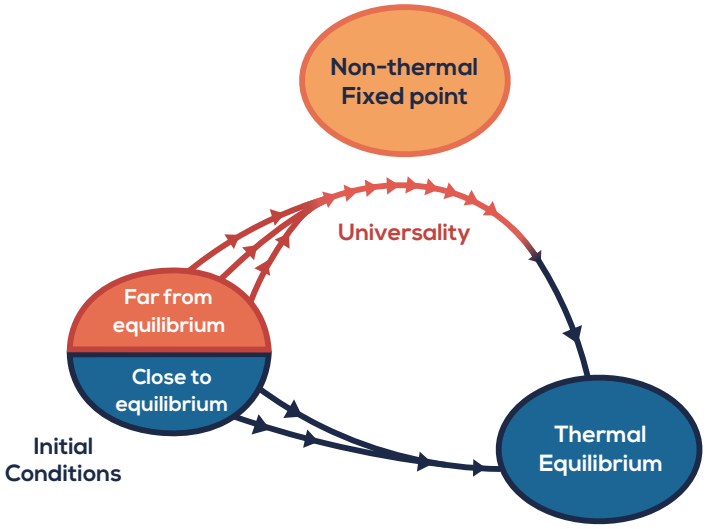

FIGURE 2: When quantum fields are slightly perturbed out-of-equilibrium, they systems falls fast into a new thermal state, thus changing the quantities that describe the system. However, when initialized very far-away from equilibrium, quantum fields relax taking a long detour around a non-thermal fixed point. As quantum fluctuations become relevant, they flow to thermal equilibrium.

be described universally using the same exponents for large classes of models. This is the case, not only for the early Universe cosmology and nuclear matter in HICs, but also in experiments with cold quantum gases[32, 33].

It is commonly thought that for every conserved charge, one can find stationary transport of said charge. It is known [34] that in a HIC, when two nuclei with a non-vanishing impact parameter, say $b \sim 4$ fm, the initial state exhibits extreme values of angular momentum $L_{0,typ} \sim 10^5 \hbar$. This has the consequence that even for centrality classes like $0 - 20\%$ in ALICE and RHIC, we would expect extreme fluctuations of angular momentum. It is natural to expect stationary transport of angular momentum, since it has to be conserved throughout the evolution of the fireball. To be able to eventually address the computation of the thermalization time, it is necessary to know whether the inclusion of states with high angular momentum changes the path to thermalization. In Chapter 4 we have taken a first step into this direction, where we present the first simulation of fields in the over-occupied regime with non-vanishing angular momentum.

Outline of this thesis

The conceptual progression of this work is divided into three fundamental pieces, which can be summarized as *(i)* studies on the initial stage, *(ii)* on the spacetime evolution of the fireball, and *(iii)* on the relevance of conserved quantities on the path to its thermalization.

The first chapter deals exclusively with *(i)*. Here, prompt photons are used as clean probes of saturation for the case of small, asymmetric systems, where the full results are presented up to next-to-leading (NLO) level. This is done in the so-called dilute-dense limit, where one uses a dilute probe, to probe a target in the over-occupied regime. In this limit the traditional power-counting is broken by

the large gluon densities, and for low momentum fraction in the target $x < 0.01$, the NLO $gg \to q\bar{q}\gamma$ channel is expected. This was confirmed numerically in the large N_c limit for forward p+p collisions, where breaking of factorization was also observed. We present a comparison to experimental data at $\sqrt{s} = 7$ TeV, and a prediction of inclusive isolated photons for p+p collisions at a center of mass energy of $\sqrt{s} = 13$ TeV.

In Chapter 2 we will use the BMSS scenario and the results of classical statistical simulations with gauge fields to expand on the parametric estimates from [35]. For this setting, the transverse resolved yield is computed for a simplified two-to-two scattering rate at the leading logarithmic level, where the processes taken into account are quark annihilation $q\bar{q} \to g\gamma$ and mixed Compton scattering $qg \to q\gamma$. Inspired by the results from ref. [36] for the thermal rate, we enhance the non-thermal rate changing the total constant under the log. In a non-equilibrium setting, this change can be enforced by changing the temperature dependence for the characteristic scale. Nonetheless, given that particle measurements do not have time resolution, we need an extra observable to be sensitive to this evolution. Higher correlations are needed to better disentangle the spacetime evolution of the fireball, and in Chapter 2 we have chosen to explore Hanbury-Brown-Twiss interferometry as a tool for this end. From these correlators, one can extract spatial information of the photon source in the shape of the *HBT homogeneity radii*. In this chapter, we will then compute the HBT correlators for two different models. The first model is the same as in Chapter 2, where one finds late thermalization at $\tau_{th} \sim 2$ fm, and subsequently evolves the system as a Bjorken expanding ideal fluid. This system will be the *best case scenario* for pre-equilibrium photons. On the other hand we will take on a more phenomenological approach and present a model which mixes the theoretical considerations of Chapter 2 with a standard hydrodynamical simulation, started at a rather early time $\tau_{th} \sim 2$ fm. We will assume no transverse dynamics at early times, and match the spatial profile to the non-equilbrium stage. This way we have the "best of both worlds" and get photon enhancement from early times, as well as anisotropy in the photon yields, which cannot be satisfied by the BMSS inspired model.

Finally, in Chapter 4 we consider the role of conserved quantities in the path of turbulent thermalization for quantum over-occupied fields. For this we focus on the role of non-vanishing angular momentum expectation values. This question is relevant for HICs, where at off-center collisions, extreme values of angular momentum should be found at initial time. Due to the complexity of such a system for the case of the over-occupied gluonic state of $SU(3)$, a 2D scalar field was chosen as a proxy model to develop the technology needed to tackle more realistic settings in HICs experiments.

Units and variables

Units

Throughout this thesis we will use natural units, which means that both the speed of light and the Boltzmann constant are set to unity, while the Planck constant is set to 2π. We can explicitly write this as

$$c = k_B = \hbar = 1\,.$$

Setting these constants fixes the total number of needed units to one. As a consequence, space and time have the same units, and the mass of a particle is related to its rest energy $E = mc^2 \to m$. The compton wavelength is also related directly by means of $\lambda^{-1} = mc/\hbar \to m$. We can summarize these relationships as follows

$$[\text{Energy}] = [\text{Momentum}] = [\text{Temperature}] = [\text{Length}^{-1}] = [\text{Time}^{-1}] \,.$$

Using the relationships above we can see that, as a consequence, variables associated with angular momentum and entropy will be rendered unitless, $[S] = [L] = 0$. Entropy (or more specifically entropy per unit rapidity $\mathrm{d}S/\mathrm{d}y$) will be used in Chapter 2, and angular momentum is the ancillary concept in Chapter 4.

Additionally, in this thesis QFT will be used extensively. We can set now the units of our fields since setting $\hbar = 1$ makes the action of the respective models dimensionless. This can be used to constrain the fields in a $d+1$ dimensional theory to be

$$[\phi] = [A_\mu] = [\mathcal{A}^a_\mu] = \frac{d-1}{2} \,.$$

We will represent these fields using the following code throughout this work. Scalar fields are given by ϕ, while A_μ and $\mathcal{A}^a_\mu$ represent the photon and color fields, respectively. Fermions will not mentioned as fields but were used to compute quark production in Chapter 1. Such fields will have units of $[\psi] = d/2$.

Regarding the specific units given in this body of work, we will use mostly tera-, giga- and mega-electronvolts, TeV, GeV and MeV, respectively, with

$$\begin{aligned}
1\ \mathrm{GeV}^{-1} &= 0.1973\ \mathrm{fm}\,, \\
1\ \mathrm{GeV}^{-1} &= 6.5822 \cdot 10^{-25}\ \mathrm{s}\,, \\
1\ \mathrm{GeV} &= 1.1605 \cdot 10^{13}\ \mathrm{K}\,, \\
1\ \mathrm{GeV} &= 1.7827 \cdot 10^{-27}\ \mathrm{kg}\,, \\
1\ \mathrm{TeV} &= 10^3\ \mathrm{GeV} = 10^6\ \mathrm{MeV}\,.
\end{aligned}$$

For completeness, we state the conversions between the specified natural units and SI units. Here, instead of meters, m, we associate the distance with fermi units, or femtometers, $\mathrm{fm} = 10^{-15}\mathrm{m}$ which is conventionally used to describe the extremely small distances relevant to heavy ion collision experiments.

Variables

Throughout this work spacetime vectors will be extensively used, where the position vector is $x^\mu = (x^0, x^1, ..., x^d)$ and $p^\mu = (p^0, p^1, ..., p^d)$ is the relativistic momentum. The vector product will be represented by the notations $x^\mu p_\mu$ and $x \cdot p$ interchangeably. If the vector is represented in bold letters it is to be taken as a spatial d dimensional vector, with $\boldsymbol{x} = (x^1, ..., x^d)$. In Chapters 1, 2 and 3 two dimensional transverse vectors $\boldsymbol{k}_\perp = (k^1, k^2)$ will be used. Such vectors represent position and momentum on the plane transverse to the z direction. The specific form (or parametrization) used to express the coordinates will be the most useful for the problem. Chapters 1, 2 and 3 focus on 3+1 dimensional systems, while Chapter 4 focuses on a 2+1 setting. In this system, polar coordinates will be used

extensively, with

$$x^1 = r\,\cos\theta \qquad r^2 = (x^1)^2 + (x^1)^2\,,$$
$$x^2 = r\,\sin\theta \qquad \theta = \arctan(x^2/x^1)\,,$$

as well as $x^0 = t$, where the label t will be used for x^0 in this system to simplify the notation and to make the time evolution more apparent. The momenta variables are complicated in this system and will be explained in Chapter 4. Before we continue, I would like to fix the notation for the following. In Chapter 1 light-cone coordinates are used extensively. It is given by the change in the metric so that $\mathrm{d}s^2 = 2\,\mathrm{d}x^+\mathrm{d}x^- - \mathrm{d}\mathbf{x}_\perp^2$. Explicitly, the four-position vector is given

$$x = (x^+, x^-, \mathbf{x}_\perp) \quad \text{, with} \quad x^\pm = \frac{1}{\sqrt{2}}\left(x^0 \pm x^3\right)\,.$$

These expressions apply also for momenta values.

In Chapter 2 and 3, where boost-invariant systems are assumed, it will be useful to use Bjorken variables, which can be summarized as

$$\tau^2 = (x^0)^2 - (x^3)^2 \qquad x^0 = \tau\,\cosh\eta\,,$$
$$\eta = \frac{1}{2}\log\left(\frac{x^0 + x^3}{x^0 - x^3}\right) \qquad x^3 = \tau\,\sinh\eta\,.$$

Additionally, the Bjorken proper time and rapidity are related to light-cone variables as follows

$$\tau^2 = 2\,x^+\,x^- \qquad x^+ = \frac{\tau}{\sqrt{2}}e^{\eta}\,,$$
$$\eta = \frac{1}{2}\log\left(\frac{x^+}{x^-}\right) \qquad x^- = \frac{\tau}{\sqrt{2}}e^{-\eta}\,.$$

Chapter 1

Probing the initial stage using prompt photons

1.1 Introduction

Quantum Chromodynamics (QCD), which is now accepted as the theory that describes the strong nuclear force, relies on the idea that hadronic species are composite objects made out of fermions called quarks. These fields come in three different charge configurations, or colors, and interact via the non-abelian gauge fields called gluons. At very high energies, the strength of the strong interaction, given by the coupling in QCD, α_s, falls below unity and the systems become loosely bound. This phenomenon is known now as asymptotic freedom [37, 38], and it enabled observables to be computed using the perturbative methods of Quantum Field Theory. This spawned a very succesful research program from which predictions for a high variety of phenomena were computed to great accuracy. Nevertheless, at high energies, the gluon content of the hadron rises faster than the total cross section of the respective hadron. This is solved by noting that at sufficiently high energies, gluon recombination becomes relevant, and the hadron *saturates* at a density of $\sim 1/\alpha_s$. Even in the limit of weak coupling, we arrive at non-perturbative physics. The point at which the rise in the gluon distribution slows downs depends on the scale being probed, which generates an emergent scale Q_s^2 at which saturation is achieved.

Probing saturation in hadron-hadron collisions is a way to understand the many-body facet of QCD, as well as to explore the initial stage of HIC experiments. One then needs observables insensitive to hadronization and in-medium effects. Since photons are blind to color interactions, they can escape the collisions virtually unscathed, which make them clean probes. In this chapter we will explore the possibility of using prompt photons, which are created at the moment of the collision, to explore gluon saturation.

The structure of this chapter is as follows. In the next section we will give an introduction to saturation and how prompt photons can be used to constrain the gluon distributions. In sec. 1.3 a brief description of the Color Glass Condensate Effective field theory is given, as well for an explanation on the dilute-dense limit of the CGC. In section 1.4 the established results for the LO and NLO process are reviewed . The numerical results and predictions for forward p+p collisions is given in sec. 1.4.1. I then proceed to give a summary of the results and the outlook of this program of research. The work presented in this chapter is the result of collaboration with Sanjin Benić, Kenji Fukushima and Raju Venugopalan.

1.2 Small-x physics and and gluon saturation

A hadron is a very complex, non-perturbative object, which can be pictured as a localized state made of gauge and fermion fields. However, the parton picture of hadrons has been quite successful at describing hadronic wavefunctions at higher momentum transfers, where the coupling is weak. In this model, one assumes hadrons to be a simplified quantum state composed of quasireal particles. A couple of *fast* partons carry the biggest portions of the hadron momentum, while being surrounded by a cloud of *slower* partons. These can be sampled via scattering processes, which historically were classified as *hard* and *soft* scatterings. In the former, a highly energetic probe with an off-shell mass, q^2, interacts with the hadron, probing at distances $r_{hard} \sim (q^2)^{-1/2}$ smaller than the size of the hadron, $r_{hard} \ll R_{hadron}$. In such scatterings, the probe interacts with one of the fast partons and knocks out a large part of the momentum $x \sim 1$, where x is the fraction of the total longitudinal momentum the parton carries. For soft scatterings, however, interactions occur through large distances of the order R_{hadron} which means here smaller energies, $q^2 \ll R^{-2}_{hadron}$. The ocurrence of scatterings in this regime is enhanced, which makes the cross-sections non-perturbative. A semihard process is the in-between process. Here, highly virtual probes knocks out only a tiny fraction of the total momentum of the hadron, $x \ll 1$ at a small distances. Since probability of this happening is higher by the enhancement of small parton number, the overall cross-section of these processes is also higher than hard process [39].

A particular application of semihard-process are the Deep Inelastic Scattering (DIS) experiments [13, 40, 41], which consist of a collision of a light probe, i.e. electron, with a hadronic target. Color processes can be sampled via the emission of a virtual photon, which can interact directly with the quarks that compose the hadron. If the electron goes into the collision with a momentum p and scatters of into a final state with p', the transferred momentum is then given by $q = p' - p$, which for a virtual particle will be spacelike, namely $Q^2 \equiv -q^2 > 0$. The variable Q^2 is called virtuality in the literature, and its inverse, $R^2 \sim 1/Q^2$ is the smallest scale that can be probed in the target. If the total hadronic momentum is given by P, the center of mass energy, $s = (p + P)^2$ and the quantity $x = Q^2/(2\,P \cdot q)$[1] characterize further the DIS system.

The DIS experiments served as a clean way to probe the hadronic waveforms, and by doing so, to extract the non-perturbative aspects of the theory. A clear example of the success of this research program is the determination of the parton distribution functions (PDFs), here represented by $x f_i(x, Q^2)$, which were obtained for a given energy and virtuality from the form factors of the proton. In principle, the PDFs are highly non-perturbative and cannot be calculated with standard perturbative techniques. However, given a specific measurement of the PDFs at some scale and energy, $x_0\, f(x_0, Q_0^2)$, one can evolve the distributions by calculating their change via the emission of soft particles. For a fixed energy, or x, the evolution of these equations with virtuality is given in perturbative QCD (pQCD) by the DGLAP equations [43–45]. In the large Q^2limit, the gluon distribution is given by [46]

$$x f_g(x, Q^2) \sim \exp\left\{ 2\sqrt{\frac{N_c}{\pi\beta_2} \ln\left[\frac{\ln(Q^2/\Lambda^2_{QCD})}{\ln(Q_0^2/\Lambda^2_{QCD})}\right] \ln\frac{1}{x}} \right\} \tag{1.1}$$

[1] At lowest order in perturbation theory, x is equivalent to the longitudinal momentum fraction carried by a sampled parton.

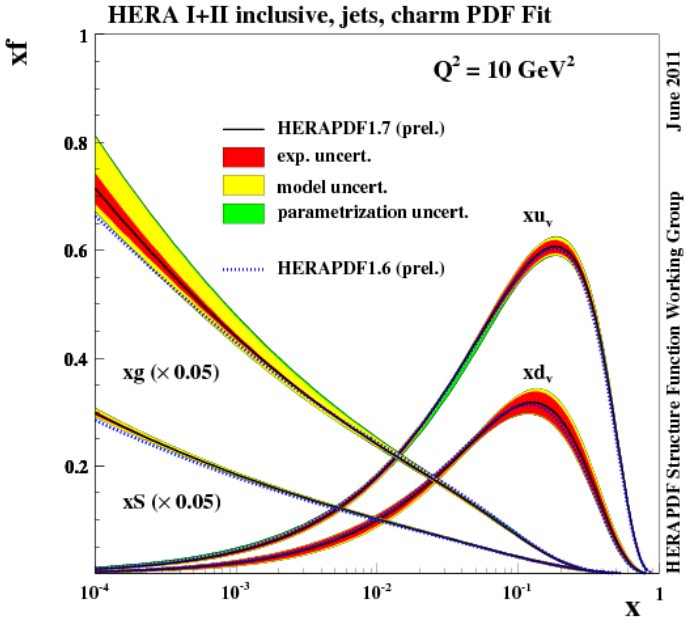

FIGURE 1.1: Parton distribution functions for HERA I+II fits at a virtuality of $Q^2 = 10$ GeV^2. The gluon distribution was found to rise very fast at high energies, as the power law $x^{-\lambda}$, where it was found experimetnally that $\lambda = 0.2 - 0.3$. Figure taken from [42].

where β_2 is the first coefficient of the QCD beta function at one-loop level. Here we can see that for higher virtualities the gluon distribution rises. However, the phase space density is given roughly by the product of eq. (1.1), and the transverse area probed, Q^{-2}. Even when the number of partons resolved increases, it will not increase as faster Q^2, and with increasing virtuality we will see an effective dilution of the gluons in the hadron. On the other hand, for fixed Q^2, the x evolution is governed by the BFKL [47–49] equation, which can be solved at the leading logarithmic level in x to find that the gluon distribution rises fast as the power law $x^{-\lambda}$, with $\lambda = 4N_c\alpha_s \ln 2/\pi$.This result was confirmed by HERA DIS data [50] for fixed values of virtuality. This poses an interesting problem, since such a growth is faster than the overall logarithmic energy dependence predicted by Froissart [51] for the total hadronic cross section[2]. A mechanism to avoid the breaking of this bound was suggested by Gribov, Levin and Ryskin [39], who noted that at high energies, gluon recombination becomes a relevant process. At this point, the rapid increase in the gluon distribution is reduced, and it is said that the hadron *saturates*. These effects are contained simply in the GLR equation [39, 52] in the double leading logarithmic approximation ($\ln x \ln Q^2 \gg 1$),

$$\frac{\partial^2 x f_g(x,Q^2)}{\partial \ln x \, \partial \ln Q^2} = \frac{\alpha_s N_c}{\pi} x f_g(x,Q^2) - \frac{\alpha_s^2 N_c \pi}{2 C_F S_\perp} \frac{1}{Q^2} \left[x f_g(x,Q^2) \right]^2 , \tag{1.2}$$

where the transverse area of the hadron is given by $S_\perp$. The rapid increase given by the first term of the equation is dampened at high densities by the (negative)

[2]Froissart derived this limit using the general argument that S-matrix elements have to be unitary, as well for the short-range limit of strong interactions.

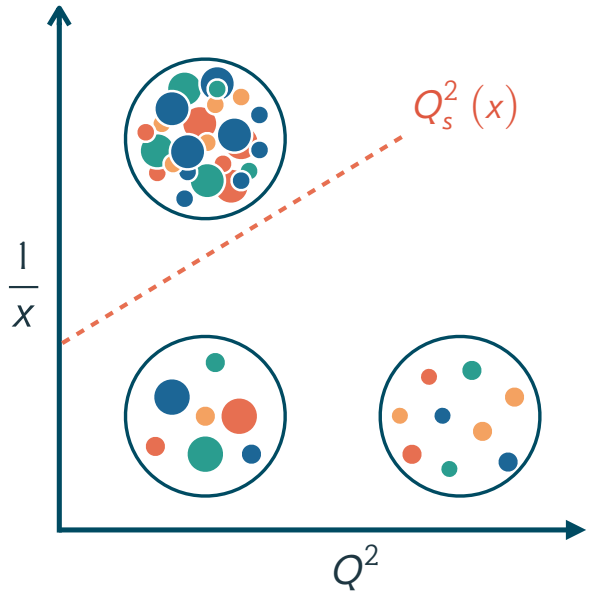

FIGURE 1.2: Simple representation of the partonic phase diagram in a hadron for the Bjorken limit, x fixed, $Q^2 \to \infty$, and the Regge-Gribov limit, x fixed, $Q^2 \to \infty$. Each colored circle represents a parton with an resolvable transverse area $\delta S_\perp \sim Q_s^{-2}$ a momentum fraction $x \sim k^+/P^+$.

quadratic term, fully stopping at the equation's fixed point, where the right-hand-side vanishes. This condition is

$$\frac{1}{S_\perp Q_s^2}\frac{\pi^2}{2C_F} x f_g(x, Q^2) = \frac{1}{\alpha_s} \tag{1.3}$$

where we find the saturation scale, $Q_s^2 \sim x^{-\lambda}$, which composes the boundary in the hadron's phase space at which the rise of the gluon sector stops. At this point, the distribution becomes of order $\sim 1/\alpha_s$, which means that the hadron is now in an over-occupied regime.

It is useful to summarize saturation in a more pictorial way. A highly boosted hadron, which we will here take to be spherical, will effectively look as a disk when looked from the lab frame thanks to Lorentz contraction. This disk contain a collection of partons with a transverse area given by their momenta, $\delta S \sim p_\perp^{-2}$. We can interpret $x f_g(x, Q^2)$ as the number of partons with an area larger than $\delta S \sim Q^{-2}$. If we probe at increasing virtuality, and keep x fixed, the disk gets more dilute, since we are sampling smaller partons which require less phase space. If we instead fix Q^2 and increase the energy, effectively decreasing x, we will start to sample more and more of the same size partons, until the phase space of the hadron is exhausted. At this point, when the partons of a fixed area start overlapping, recombination becomes relevant to keep the total cross-section in check [53].

We need a framework that encodes the effects of saturation in a simple manner to be able to compute phenomenological quantities. For this, we will use the Color Glass Condensate (CGC), which is an Effective Field Theory (EFT) of QCD in the large energy (Regge-Gribov) limit [13]. In this formalism fast and slow partons are separated by an arbitrary cutoff scale Λ_0. The former are taken to be static sources, while the latter are taken to be dynamical degrees of freedom. As a consequence, saturation is recovered as an emergent property. The CGC also presents a

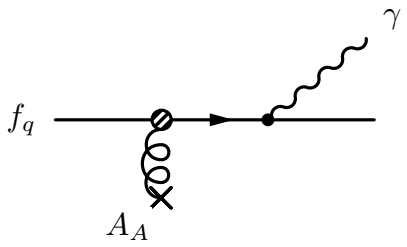

FIGURE 1.3: Leading order (LO) process for the creation of a prompt-photon in the context of dilute-dense collisions, described by the radiation of a photon from a valence quark, which is enabled by multiple scattering of the dense gluon state of the target.

systematic renormalization group-like evolution of its observables with respect to Λ_0, which are encoded on the JIMWLK equations. An outstanding feature of this framework is its ability to give many quantities analytically, and such is the case for the full dynamical gluon field during collision of a *dilute* projectile into a *dense* target. Dilute is a term commonly used to express a hadron in which the characteristic transverse momentum is higher than the saturation scale, $Q_s^2/\boldsymbol{k}_\perp^2 \ll 1$, while dense stands for a hadron in which this ratio is of order one, $Q_s^2/\boldsymbol{k}_\perp^2 \gtrsim 1$, and as a result will present high gluon densities. For the reader it may be useful to recall that partons with higher $p_\perp$ exhibit smaller areas, and probing such partons, one is effectively diluting the projectile.

1.2.1 Probing Cold Nuclear Matter

The case of a dilute-dense system is very interesting in itself, since it gives us the opportunity to analytically compute observables in which one uses a dilute (relatively understood) probe to explore the properties of a saturated nuclear wavefunction. It serves as a way to understand the collective features embedded in this system, but also to use them as benchmarks for dense-dense systems. In the latter, a hot QCD medium is established and to really understand the quantum collective phenomena which arise during its evolution, is indeed imperative to understand the initial stage. Small systems such as proton-proton (p+p) and (proton-nucleus) p+A collisions, will be of interest for this goal, since, outside of rare high-multiplicity events, one would expect nuclear modification to come directly from cold nuclear matter effects.

To be able to achieve such understanding, it is essential to find observables which are not sensitive to rescatterings an in-medium effects. That means that one should find a penetrating probe which decouples from the strongly interacting medium as soon at is radiated. Electroweak probes, and particularly photons, are then the perfect choice for this objective, since their rescattering will be strongly suppressed by powers of the electromagnetic coupling α_e. In fact, even for in-medium rescatterings during nucleus-nucleus collisions photons will escape virtually unscathed, as their mean free-path in a quark-gluon medium is greater than the interaction volume, for which expected length is smaller than $20\ \mathrm{fm}$. These probes are excellent tools to probe both saturation and evolution of the medium created in nuclear collisions.

As stated above, we want to probe the dense target at small-x, which will be achieved by perturbatively producing photons at tree level in the CGC power counting scheme. One can think of four different leading channels to produce prompt photons in this limit, see figs. 1.3 and 1.4. The leading-order contribution is given by the $qg \to q\gamma$ channel (see fig. 1.3), in which a quark from the projectile rescatters off the target, and produces a photon as a consequence. The cross-section for this process has been presented in several works [54–57] where it has been applied for proton-proton (p+p) [58–60] and proton-nucleus (p+A) collisions [61–66]. This process is parametrically of order αf_q, since, even when the quark scattering vertices are suppressed by powers of the coupling g, dense target is an over-occupied state, eq. (1.3), where the whole interaction is ~ 1.

The next three processes are parametrically suppressed by an extra power of α_s. The first process, process I in fig. 1.4, was computed in refs. [67] and is a gluonic radiative correction to the LO case. In the case of a hard quark, $x \sim 1$, this process may be important as a NLO correction of photon-jet correlations. Nevertheless, if the observable one is interested is the inclusive photon cross-section, then the gluon can be absorbed into the renormalization of the quark distribution. In this work we will be focusing in single photon production, which makes process I irrelevant. Process II consists of the splitting of a gluon from the proton into a $q\bar{q}$ pair, which subsequently annihilates into a photon. Alternatively, this gluon can first scatter off the targe before fluctuating into the $q\bar{q}$ pair. This channel was computed in [68], but because of its restricted nature, it is phase-space suppressed and its contribution will be negligible to the total prompt photon cross section. We computed the next-to-leading order (NLO) channel $gg \to q\bar{q}\gamma$ channel in the CGC EFT in ref. [69], process III in fig. 1.4. For photon rapidities that are close to the central rapidity region of the collision, this process dominates over other contributions at this order. It can be visualized as a fluctuation of a gluon from one of the protons into a $q\bar{q}$ dipole,which scatters off the gluon shock wave of the dense target. As in process II, the gluon can first scatter off the target before splitting in to the $q\bar{q}$ pair. In either case, a photon will be radiated from a (anti) quark line.

An important caveat on this expansion is that in the CGC EFT, the straightforward power counting depending on the expansion around α_s is broken for the LO and NLO processes, where the rapid increase on the gluon distribution function makes the parameter $\alpha_s f_g$ the correct expansion parameter for the gluon sector. For the fragmentation region, where the hard photons are emitted off a large-x valence quark, $\alpha_s f_g < f_q$ and the LO contribution will be the dominant channel. Nonetheless, in the small-x region, for softer photons at more central rapidities, where $x < 10^{-2}$ one can find that $\alpha_s f_g < f_q$, and the large gluon density in the proton overcompensates for the α_s suppression in the NLO cross-section arising from the splitting of the gluon into the quark-antiquark pair. As it will be shown explicitely in the next sections, the NLO diagram takes over, dominating the inclusive photon cross section.

As a final comment, we would like to note that the computation of heavy quark pairs $gg \to q\bar{q}$, which by Low's theorem is a limit of our results in the limit of $k_{\gamma\perp} \to 0$, has been computed in this framework. These results were presented with considerable success, to describe heavy quarkonium production in p+p collisions at RHIC and the LHC [70], in p+A collisions at both colliders [71–73] and more recently, high multiplicity p+p and p+A collisions [74]. In the latter case, the framework employed here also gives very good agreement with multiplicity distributions at the LHC [75].

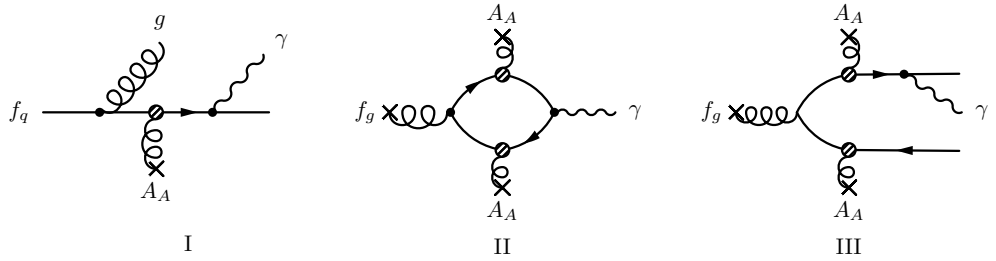

FIGURE 1.4: Prompt photon production in dilute-dense collisions at next-to leading order. Diagram I describes the radiation of a photon and a gluon from a valence quark line. The two rightmost diagrams correspond to a gluon splitting into a $q\bar{q}$ pair, which subsequently undergoes annihilation into a photon (diagram II) or presents photon bremmsstrahlung before or after rescattering off the nuclear shockwave.

1.3 The Color Glass Condensate

In modern particle accelerators, such as RHIC and the LHC, hadronic probes are accelerated to very high energies, and approximately travel along the light cone. One can simplify such systems using the infinite momentum frame (IMF) to good approximation. In this limit, one can define the longitudinal momentum fraction variable, $x = p^+/P^+$[3]. Partons which carry a large x are highly boosted, and thanks to this, their timescales are very time dilated in the laboratory frame. On the other hand, low-x partons exhibit rapid fluctuations and in the saturation scenario, are very highly occupied [13, 76, 77]. A separation of scales can be then introduced at an arbitrary x_0 which effectively splits the system into two sectors. On one hand, the fast partons, with $x \gg x_0$ act as static color sources, while on the other, slow degrees of freedom highly occupied gauge fields. This sharp separation of scales is the main idea the Color Glass Condensate, which is am effective field theory of QCD in the Regge-Gribov limit [78–80], when Q^2 is left fixed and $x \to 0$. On a physical note, the dependence of the resulting theory on the cutoff, x_0, can be then thought in the context of a Wilsonian Renormalization Group (RG) as integrating out the faster degrees of freedom down to the cutoff to find the effective field theory (EFT) that describes the slow fluctuations, which are less boosted and posses faster timescales [76, 77].The interplay between a given static source and the soft sector is given by the classical Yang-Mills equation,

$$[D_\mu, F^{\mu\nu}] = J^\nu \,. \tag{1.4}$$

For a hadron traveling in the positive z-axis in the IMF, its color distribution is fully contracted along the direction of movement, so that the sources can be written as

$$J^{\mu a}(x) = g\,\delta^{\mu +}\,\delta(x^-)\,\rho^a(\boldsymbol{x}_\perp)\,. \tag{1.5}$$

where the picture of a traveling disk, or *pancake*, is commonly used. Since this disk travels along the light cone, it will possess only the one component, J^+, while the others are suppressed by powers of the total hadron momentum, P^+. These sources, while being frozen-out of dynamics, will still have different event-by-event configurations. This can be modeled by taking them to be stochastic objects. In this

[3] We will use the light-cone variables, $x^\pm = \frac{1}{\sqrt{2}}\left(x^0 \pm x^3\right)$, which are first explained in the variables section of the introduction

framework, observables are then taken to be functionals of the sources, and have to be sampled over all configurations, i.e. averaging over the sources. For an arbitrary observable $\mathcal{O}[\rho]$ at a scale x_0, this can be expressed as

$$\langle \mathcal{O} \rangle = \int \mathcal{D}\rho \, W[\rho, x_0] \, \mathcal{O}_{x_0}[\rho], \tag{1.6}$$

where $W[\rho, x_0]$ is a gauge invariant distribution which gives the probability to find a configuration ρ. This functional encodes the dependence of the sources with respect to the change of the cutoff, x_0, and its evolution is given by the Jalilian-Marian, Iancu, McLerran, Weigert, Leonidov and Kovner (JIMWLK) equations [81], which can be simplified to the Balitsky-Kovchegov (BK) equation in the $N_c \to \infty$ limit [53], N_c being the number of colors[4]. For a given configuration of the sources, the solution of eq. (1.4) can be found analytically, and in the Lorenz gauge ($\partial_\mu A^\mu$) it can be expressed in momentum space as follows,

$$\mathcal{A}^{\mu a}(\boldsymbol{k}_\perp) = 2\pi \, g \, \delta^{\mu +} \, \delta(q^-) \, \frac{\rho^a(\boldsymbol{k}_\perp)}{\boldsymbol{k}_\perp^2} \, . \tag{1.7}$$

One can then model the observables obtained with such a field by enforcing correlations of the sources. A particular choice is the so-called McLerran-Venugopalan model (MV), where the nucleus is assumed to be large, and source correlations are taken to be Gaussian and homogeneous in transverse space. All source-source correlations can be then characterized using the following two point source,

$$\langle \rho^a(x^-, \boldsymbol{x}_\perp) \rho^b(y^-, \boldsymbol{y}_\perp) \rangle = \delta^{ab} \mu^2(x^-) \, \delta(\boldsymbol{x}_\perp - \boldsymbol{y}_\perp) \, , \tag{1.8}$$

where it is important to state that $\mu^2(x^-)$ can be interpreted as the color charge density for soft partons. Using the fact that Q_S^2 is a semihard scale, we can relate both quantities via

$$Q_s^2 = 2\pi \, N_c \int \mathrm{d}x^- \mu^2(x^-) \, . \tag{1.9}$$

for the case of the MV model. This model will be relevant in the parametrization of the saturation effects in the photon spectra, which will be shown in the next sections.

1.3.1 Dilute-dense limit

The results summarized in the last section only dealt with one hadronic state, traveling at the speed of light. Nonetheless in collisions at RHIC and LHC, hadronic probes are accelerated towards each other. Following the historical convention, we call the first hadron, traveling along the z-axis the *projectile*, and the second one, moving along the opposite direction, the *target*. This is inherited from the conventions of DIS experiments, however, this distinction is quite useful in the case of asymmetric systems, such as proton-nucleus (p+A) or proton-proton (p+p) collisions at forward rapidities, where one of the hadrons, the projectile, is sampled at relatively large-x, while the target is probed at small-x. The evolution of the full system is still given by the CYM equations, eq. (1.4), now modified by the inclusion of a joint source

[4] The BK equation [82] is a non-linear evolution equation with x for a $q\bar{q}$ pair going through a gluon state which, thanks to the non-linearities, contains saturation effects. In the dilute regime, where the non-linearities are dropped, the BFKL equation is recovered.

$$J^{\mu a}(x) = g\,\delta^{\mu +}\,\delta(x^-)\,\rho_p^a(\boldsymbol{x}_\perp) + g\,\delta^{\mu -}\,\delta(x^+)\,\rho_t^a(\boldsymbol{x}_\perp) \tag{1.10}$$

where ρ_p^a and ρ_t^a stand for the color sources in the projectile and the target, respectively. Solutions can then be found using perturbation theory, where the correct expansion parameter is $g\,\rho$. However, in the regime in which the typical gluon momentum exchange is close to the saturation scale, $Q_s/k_\perp \sim 1$ the sources exhibit high occupations, $\rho \sim 1/g$, and such hadron is said to be *dense*. In this regime, every gluon contribution from the sources is of order $\mathcal{O}(1)$, and has to be included. If both the sources are dense, the expansion on $g\rho_{p,t}$ breaks down, and solutions can be only found numerically.

To be able to get analytical results, at least one of the sources to be dilute, that is $Q_s/k_\perp \ll 1$. The solution can be found analytically to lowest order in both sources, in dilute-dilute limit [83]. We are here interested, however in the dilute-dense regime, where only the lowest order in $\rho_p/\boldsymbol{k}_{1\perp}$ is kept, but all orders of $\rho_t/\boldsymbol{k}_{2\perp}$ are included. For this regime, the solution to eq. (1.4) has been found to be in the Lorenz gauge [84]

$$\begin{aligned} A^\mu(q) = A_p^\mu(q) + \frac{ig}{q^2 + iq^+\epsilon} \int_{\boldsymbol{k}_{1\perp}} \int_{\boldsymbol{x}_\perp} e^{i\boldsymbol{x}_\perp\cdot(\boldsymbol{k}_{2\perp})} \Big\{ C_U^\mu(q,\boldsymbol{k}_{1\perp})[U(\boldsymbol{x}_\perp)-1]^{ba} \\ + C_V^\mu(q)[V(\boldsymbol{x}_\perp)-1]^{ba} \Big\} \frac{\rho_p^a(\boldsymbol{k}_{1\perp})}{\boldsymbol{k}_{1\perp}^2} \quad . \end{aligned} \tag{1.11}$$

The resulting gluon field is the sum of a gluon from the projectile and a modification term to contain all its possible rescatterings off the target. These infinite number of processes can be resummed as in eq. (1.11) to an effective color rotation, given here by the folding of the Wilson lines of the nucelar gluon fields, $U(\boldsymbol{x}_\perp)$ and $V(\boldsymbol{x}_\perp)$[5], with the vector structures C_U and C_V, which are related to the well-known Lipatov vertex [47] via $C_L = C_U + C_V/2$, for a reggeized gluon. The explicit momentum dependence of these structures is not relevant for this chapter. Nevertheless, for the interested reader, they are given in Appendix A. Physically, these structures, and the Lipatov effective vertex, represent an the momentum dependence of the resummed rescattering of a single gluon over a multi-gluon state. The momentum coming from the proton is $\boldsymbol{k}_{1\perp}$, while $\boldsymbol{k}_{2\perp} \equiv \boldsymbol{q}_\perp - \boldsymbol{k}_{1\perp}$ is the momentum transfer from nucleus.

Finally, the Wilson lines U and V account for the modification of the gluon from the proton, product of multiple gluon scatterings. They are both expressed as lines in the adjoint representation of $SU(N)$, and for an arbitrary light-like path are given by

$$\begin{aligned} U(a,b;\boldsymbol{x}_\perp) &= \mathcal{P}_+ \exp\left\{ ig \int_b^a dz^+ A_t^-(z^+,\boldsymbol{x}_\perp)\cdot T \right\}, \\ V(a,b;\boldsymbol{x}_\perp) &= \mathcal{P}_+ \exp\left\{ \frac{ig}{2} \int_b^a dz^+ A_t^-(z^+,\boldsymbol{x}_\perp)\cdot T \right\}, \end{aligned} \tag{1.12}$$

[5]The vector structure C_V is a in fact a gauge artifact, and it is not present in calculations in other gauges [85, 86]. It has been shown to drop out of these ($q\bar{q}$, $q\bar{q}\gamma$) calculations at the level of the amplitude[69, 87]

where $\mathcal{P}_+$ is the light cone time-ordering operator, and T^a are the generators of $SU(N)$ in the adjoint representation. In the fundamental representation, the generators are represented by t^a. The target's gluon field A_t is given by eq. (1.7) after chaging $+ \leftrightarrow -$, since the target is traveling in the negative z direction. We will use the following shorthand notation for the complete Wilson lines $U(\boldsymbol{x}_\perp) \equiv U(\infty, -\infty; \boldsymbol{x}_\perp)$.

In the dilute-dense limit, observables can then be computed in a *semi-perturbative* approach, which in the literature has been often called the hybrid method. For any incoming colored probe, the dense hadron will contribute to all orders of gluon rescattering, giving a contribution which, even in the weak coupling limit, is non-perturbative in nature. This is achieved by the resummation of individual scattering vertices, resulting in the U and V Wilson lines. On the other hand, the dilute hadron will contribute with a single quark or gluon, which for quarks can be directly sampled using the PDFs. For gluons we will use the CGC unintegrated gluon distributions (UGD), which have transverse resolution. However, it is possible to take the collinear limit [6], where the gluon PDF is retrieved, and the projectile becomes fully perturbative. In this chapter the relation to collinearity will only be taken at high-x, where the gluon distributions are matched to the gluon PDF. Finally, as it was stated in the sec. 1.3, physical observables can be computed by averaging the amplitudes in terms of the sources, using namely eq. (1.6). In this chapter the process of averaging is not going to be shown, but the interested reader can find it in refs. [84, 87].

1.4 Prompt photon production

As it was stated before, if one wants to account for all relevant prompt photon productions processes relevant in the dilute-dense approximation, one has to go up to NLO level. First, one has to compute the full cross section for the LO process. For inclusive photon production at NLO in α_S, as noted, there are three different channels which sample the the gluon background state of the target: $qg \to qg\gamma$ [67, 88], $gg \to q^*\bar{q}^* \to \gamma$ [68], and $gg \to q\bar{q}\gamma$ [69]. The collinearly enhanced contributions in the tree-level process $qg \to qg\gamma$ are contained in the LO where the radiative correction is absorbed into the evolution of the quark PDFs. The annihilation channel, $gg \to q^*\bar{q}^* \to \gamma$, is suppressed by the phase space of the virtual dipole and flavor cancellation [68]. In the present chapter, we will consider the region close to mid-rapidity of $0 < Y_p < 2.5$ where the tree-level $gg \to q\bar{q}\gamma$ channel is the dominant contribution. The $qg \to qg\gamma$ channel will be neglected in this discussion. Nonetheless, it is important to have in mind that in the very forward kinematic window for the projectile, this channel is expected play an important role.

We will begin here by summarizing the CGC results for the relevant processes. In this section we will explain our notations and approximations, while the details of the numerical computation will be explained in the next section. The cross-section in the dilute-dense approximation of the LO process $qg \to q(q)\gamma(k_\gamma)$ in the

[6] In this limit the parton is taken to travel perfectly parallel to the hadron, and thus has vanishing $\boldsymbol{k}_\perp$.

dilute-dense collision is given by [54–57]

$$\begin{aligned}\frac{\mathrm{d}\sigma^{\mathrm{LO}}}{\mathrm{d}^2\boldsymbol{k}_{\gamma\perp}\mathrm{d}\eta_\gamma} =& S_\perp \sum_f \frac{\alpha_e q_f^2}{16\pi^2}\int_{\boldsymbol{q}_\perp}\int_{x_{p,\min}}^1 \mathrm{d}x_p\, f_{q,f}^{\mathrm{val}}(x_p,Q^2)\,\tilde{\mathcal{N}}_{t,Y_t}(\boldsymbol{q}_\perp+\boldsymbol{k}_{\gamma\perp}) \\ &\times\frac{1}{q^+l^+}\Bigg\{-4m_f^2\left[\frac{l^{+2}}{(q\cdot k_\gamma)^2}+\frac{q^{+2}}{(l\cdot k_\gamma)^2}+\frac{k_\gamma^{+2}}{(l\cdot k_\gamma)(q\cdot k_\gamma)}\right] \\ &+4\left(l^{+2}+q^{+2}\right)\left[\frac{l\cdot q}{(l\cdot k_\gamma)(q\cdot k_\gamma)}+\frac{1}{q\cdot k_\gamma}-\frac{1}{l\cdot k_\gamma}\right]\Bigg\},\end{aligned} \tag{1.13}$$

where $S_\perp$ is the transverse proton size, and m_f is the quark mass for flavor f. The distributions $f_{q,f}^{\mathrm{val}}(x_p,Q^2)$ are the valence quark distribution function, which are sampled at a scale $Q^2=\max(\boldsymbol{q}_\perp^2,\boldsymbol{k}_{\gamma\perp}^2)$. The gluon shockwave in the dense target is represented by the dipole forward scattering amplitude,

$$\tilde{\mathcal{N}}_{t,Y_t}(\boldsymbol{k}_\perp)=\frac{1}{N_c}\int_{\boldsymbol{x}_\perp}\mathrm{e}^{\mathrm{i}\boldsymbol{k}_\perp\cdot\boldsymbol{x}_\perp}\mathrm{tr}_c\langle\tilde{U}(\boldsymbol{x}_\perp)\tilde{U}^\dagger(0)\rangle_{Y_t}\,. \tag{1.14}$$

In the above, the rapidity of the dense target is $Y_t=\log(1/x_t)$ with $x_t=\sqrt{2/s}\,(q^-+k_\gamma^-)$ and $\tilde{U}(\boldsymbol{x}_\perp)$ is lightlike Wilson line in the fundamental representation. These objects act as color rotation effective vertices on the (anti) quark lines. The light cone momenta of the incoming quark are $l^+=\sqrt{\frac{s}{2}}x_p$ and $l^-=m_f^2/(2l^+)$, those of the final state quark are: $q^+=l^+-k_\gamma^+$ and $q^-=(\boldsymbol{q}_\perp^2+m_f^2)/(2q^+)$. Finally, those of the photon are $k_\gamma^\pm=k_{\gamma\perp}\mathrm{e}^{\pm\eta_\gamma}/\sqrt{2}$. We note that imposing the on-shell condition $q^+>0$ leads to a lower bound on the projectile rapidity, $x_{p,\min}=\sqrt{2}k_\gamma^+/\sqrt{s}$.

The inclusive cross section of the photon production from the $gg\to q(q)+\bar{q}(p)+\gamma(k_\gamma)$ channel was computed in both the Lorenz and light-cone gauges in ref. [69], where the full result was found to explicitely break factorization, containing all twist corrections from the scattering of the target's gluon showckwave. The inclusive photon cross-section is given

$$\begin{aligned}\frac{\mathrm{d}\sigma^\gamma}{\mathrm{d}^2\boldsymbol{k}_{\gamma\perp}\mathrm{d}\eta_{k_\gamma}} =& \frac{\alpha_e\alpha_S^2 q_f^2}{16\pi^4 C_F}\int_0^\infty\frac{\mathrm{d}q^+}{q^+}\frac{\mathrm{d}p^+}{p^+}\int_{\boldsymbol{k}_{1\perp}\boldsymbol{k}_{2\perp}\boldsymbol{q}_\perp\boldsymbol{p}_\perp}(2\pi)^2\delta^{(2)}(\boldsymbol{P}_\perp-\boldsymbol{k}_{1\perp}-\boldsymbol{k}_{2\perp}) \\ &\times\frac{\varphi_p(\boldsymbol{k}_{1\perp})}{\boldsymbol{k}_{1\perp}^2\boldsymbol{k}_{2\perp}^2}\Bigg\{\tau_{g,g}(\boldsymbol{k}_{1\perp};\boldsymbol{k}_{1\perp})\phi_t^{g,g}(\boldsymbol{k}_{2\perp}) \\ &+\int_{\boldsymbol{k}_\perp}2\mathrm{Re}\big[\tau_{g,q\bar{q}}(\boldsymbol{k}_{1\perp};\boldsymbol{k}_\perp,\boldsymbol{k}_{1\perp})\big]\,\phi_t^{q\bar{q},g}(\boldsymbol{k}_\perp,\boldsymbol{k}_{2\perp}-\boldsymbol{k}_\perp;\boldsymbol{k}_{2\perp}) \\ &+\int_{\boldsymbol{k}_\perp\boldsymbol{k}'_\perp}\tau_{q\bar{q},q\bar{q}}(\boldsymbol{k}_\perp,\boldsymbol{k}_{1\perp};\boldsymbol{k}'_\perp,\boldsymbol{k}_{1\perp})\,\phi_t^{q\bar{q},q\bar{q}}(\boldsymbol{k}_\perp,\boldsymbol{k}_{2\perp}-\boldsymbol{k}_\perp;\boldsymbol{k}'_\perp,\boldsymbol{k}_{2\perp}-\boldsymbol{k}'_\perp)\Bigg\}.\end{aligned} \tag{1.15}$$

where $\boldsymbol{P}_\perp=\boldsymbol{q}_\perp+\boldsymbol{p}_\perp+\boldsymbol{k}_{\gamma\perp}$ and the rapidities are $Y_{p,t}=\log(1/x_{p,t})$ with

$$x_p=\sqrt{\frac{2}{s}}\,(q^++p^++k_\gamma^+)\quad\text{and}\quad x_t=\sqrt{\frac{2}{s}}\,(q^-+p^-+k_\gamma^-) \tag{1.16}$$

Here the light-cone momenta of an on-shell particle with 4-momentum p are given by

$$p^\pm=\frac{1}{\sqrt{2}}\sqrt{\boldsymbol{p}_\perp^2+m^2}\;\exp(\pm\eta_p)\,. \tag{1.17}$$

In eq. (1.15), $\varphi_p(\boldsymbol{k}_{1\perp},Y_p)$ is the unintegrated gluon distribution in the proton. And since the full gluon field, eq. (1.11), was found in the dilute-dense expansion

to order $O(\rho_p^1)$, then $\varphi_p(\boldsymbol{k}_{1\perp})$ is given by the two-source correlator

$$\langle \rho_p^a(\boldsymbol{k}_{1\perp})\rho_p^{\dagger b}(\boldsymbol{k}_{1\perp})\rangle = \frac{\delta^{ab}\boldsymbol{k}_{1\perp}^2}{2\pi N_c C_F\, g^2}\,\varphi_p(\boldsymbol{k}_{1\perp}, Y_p)\,, \tag{1.18}$$

For a large nucleus with Gaussian stochastic color sources, this correlator can be directly associated to the color charge density via the relation $\langle \rho_p^a(\boldsymbol{x}_\perp)\rho_p^b(\boldsymbol{y}_\perp)\rangle = \delta^{ab}\delta^2(\boldsymbol{x}_\perp - \boldsymbol{y}_\perp)\mu_p^2$. In the case of the target's unintegrated distribution functions, $\phi_t^{i,}$, the identification of the correlator of color sources can be straightforwardly generalized to correlators of Wilson lines [87, 89, 90]. In conventional pQCD language, these unintegrated momentum distributions resum a sub-class of all twist correlations in the nucleus. Here, a *twist* expansion refers to the expansion of an observable in terms of inverse powers of k/Q, where k is the momentum transfer and is the hard scale of the system [91]. In our case $Q = Q_s$ the saturation scale, while in DIS experiments, the hard scale would be given naturally by virtuality. The correlator of two adjoint Wilson lines can be expressed

$$\begin{aligned}\frac{2N_c\alpha_S}{\boldsymbol{k}_{2\perp}^2}\,\phi_A^{g,g}(\boldsymbol{k}_{2\perp}) \equiv \int_{\boldsymbol{k}_\perp\boldsymbol{k}'_\perp}\int_{\boldsymbol{y}_\perp\boldsymbol{y}'_\perp} & \mathrm{e}^{\mathrm{i}(\boldsymbol{k}_{2\perp}-\boldsymbol{k}_\perp)\cdot\boldsymbol{y}_\perp - \mathrm{i}(\boldsymbol{k}_{2\perp}-\boldsymbol{k}'_\perp)\cdot\boldsymbol{y}'_\perp} \\ & \times \delta^{aa'}\,\mathrm{tr}_c\big\langle t^b U^{ba}(\boldsymbol{k}_\perp) t^{b'} U^{\dagger a'b'}(\boldsymbol{k}'_\perp)\big\rangle\,.\end{aligned} \tag{1.19}$$

where $U(\boldsymbol{k}_\perp)$ represents the Fourier transform of $U(\boldsymbol{x}_\perp)$. Similarly, the three point fundamental-adjoint Wilson line correlator can be expressed as

$$\begin{aligned}&\frac{2N_c\alpha_S}{\boldsymbol{k}_{2\perp}^2}\,\phi_t^{q\bar{q},g}(\boldsymbol{k}_\perp, \boldsymbol{k}_{2\perp}-\boldsymbol{k}_\perp; \boldsymbol{k}_{2\perp}) \\ &\quad\equiv \int_{\boldsymbol{k}'_\perp}\int_{\boldsymbol{y}'_\perp} \mathrm{e}^{-\mathrm{i}(\boldsymbol{k}_{2\perp}-\boldsymbol{k}'_\perp)\cdot\boldsymbol{y}'_\perp}\,\delta^{aa'}\,\mathrm{tr}_c\big\langle \tilde{U}(\boldsymbol{k}_\perp) t^a \tilde{U}^\dagger(\boldsymbol{k}_{2\perp}-\boldsymbol{k}_\perp) t^{b'} U^{\dagger a'b'}(\boldsymbol{k}'_\perp)\big\rangle\,,\end{aligned} \tag{1.20}$$

and likewise for its Hermitean conjugate expression in the cross section. Finally, the four point correlator of fundamental Wilson lines can be expressed as

$$\begin{aligned}&\frac{2N_c\alpha_S}{\boldsymbol{k}_{2\perp}^2}\,\phi_A^{q\bar{q},q\bar{q}}(\boldsymbol{k}_\perp, \boldsymbol{k}_{2\perp}-\boldsymbol{k}_\perp; \boldsymbol{k}'_\perp, \boldsymbol{k}_{2\perp}-\boldsymbol{k}'_\perp) \\ &\qquad\equiv \delta^{aa'}\,\mathrm{tr}_c\big\langle \tilde{U}(\boldsymbol{k}_\perp) t^a \tilde{U}^\dagger(\boldsymbol{k}_{2\perp}-\boldsymbol{k}_\perp)\tilde{U}(\boldsymbol{k}_{2\perp}-\boldsymbol{k}'_\perp) t^{a'} \tilde{U}^\dagger(\boldsymbol{k}'_\perp)\big\rangle\end{aligned} \tag{1.21}$$

In eq. (1.15) the hard factors for this process are also contained, where $\tau_{n,m}$ with $n, m \in \{g, q\bar{q}\}$ represent the Dirac traces, arising from the (anti) quark lines. These traces are given by

$$\tau_{n,m} \equiv \mathrm{tr}\big[(\not{q} + m_f) T_n^\mu (m_f - \not{p})\gamma^0 T'^\dagger_{m,\mu}\gamma^0\big]\,. \tag{1.22}$$

The Dirac matrix products T_n^μ are quite complex and their specific form is unimportant for this discussion. For the interested reader, their explicit forms are specified in the Appendix A.

As it was stated before, the full solution gives an explicit breaking factorization at the level of the photon level. Nonetheless, its numerical evaluation is very expensive, since its phase space is as large as fourteen dimensions in the last term. Given also the size of the trace factors, even a Monte-Carlo integration will need a big amount computation power. We can simplify the equation without restoring factorization in the large N_c limit, where this expression becomes

$$\begin{aligned}\frac{\mathrm{d}\sigma^{\mathrm{NLO}}}{\mathrm{d}^2\boldsymbol{k}_{\gamma\perp}\mathrm{d}\eta_\gamma} =& S_\perp \frac{\alpha_e\alpha_S N_c^2}{64\pi^4(N_c^2-1)}\sum_f q_f^2\int_{\eta_q\eta_p}\int_{\boldsymbol{q}_\perp\boldsymbol{p}_\perp\boldsymbol{k}_{1\perp}\boldsymbol{k}_\perp}\frac{\varphi_p(Y_p,\boldsymbol{k}_{1\perp})}{\boldsymbol{k}_{1\perp}^2}\\ &\times\tilde{\mathcal{N}}_{t,Y_t}(\boldsymbol{k}_\perp)\tilde{\mathcal{N}}_{t,Y_t}(\boldsymbol{P}_\perp-\boldsymbol{k}_{1\perp}-\boldsymbol{k}_\perp)\left[2\tau_{g,g}(\boldsymbol{k}_{1\perp};\boldsymbol{k}_{1\perp})\right.\\ &\left.+4\tau_{g,q\bar{q}}(\boldsymbol{k}_{1\perp};\boldsymbol{k}_\perp,\boldsymbol{k}_{1\perp})+2\tau_{q\bar{q},q\bar{q}}(\boldsymbol{k}_\perp,\boldsymbol{k}_{1\perp};\boldsymbol{k}_\perp,\boldsymbol{k}_{1\perp})\right],\end{aligned} \tag{1.23}$$

The unintegrated gluon distribution in the dilute projectile $\varphi_p(Y_p,\boldsymbol{k}_{1\perp})$ is now defined as

$$\varphi_p(Y_p,\boldsymbol{k}_{1\perp})\equiv S_\perp\,\frac{N_c\,\boldsymbol{k}_{1\perp}^2}{4\alpha_S}\mathcal{N}_{p,Y_p}(\boldsymbol{k}_{1\perp})\,, \tag{1.24}$$

since in the large N_c the color charge density can be identified to the dipole amplitude, $\mathcal{N}_{p,Y_p}(\boldsymbol{k}_\perp)$, thanks to the replacement of the Balitsky-JIMWLK hierarchy with the BK equation. The proectile dipole amplitude is expressed in terms of the adjoint lightlike Wilson line $U(\boldsymbol{x}_\perp)$ as

$$\mathcal{N}_{p,Y_p}(\boldsymbol{k}_\perp)=\frac{1}{N_c}\int_{\boldsymbol{x}_\perp}\mathrm{e}^{\mathrm{i}\boldsymbol{k}_\perp\cdot\boldsymbol{x}_\perp}\mathrm{tr}_c\langle U(\boldsymbol{x}_\perp)U^\dagger(0)\rangle_{Y_p}\,. \tag{1.25}$$

The product of fundamental dipoles in eq. (1.23), to $O(1/N_c^2)$ in a largeN_c expansion, represents general multi-gluon correlators describing the dense target; these too can be represented formally as UGDs [87].

If $k_{\gamma\perp}$ is much larger than the typical momenta exchanged from the dense target, namely $k_\perp$ and $|\boldsymbol{P}_\perp-\boldsymbol{k}_{1\perp}-\boldsymbol{k}_\perp|$, eq. (1.23) simplifies to a $k_\perp$-factorized expression,

$$\begin{aligned}\frac{\mathrm{d}\sigma^{\mathrm{NLO}}_{k_\perp\text{-fact}}}{\mathrm{d}^2\boldsymbol{k}_{\gamma\perp}\mathrm{d}\eta_\gamma} =& S_\perp\sum_f\frac{\alpha_e\alpha_S N_c^2 q_f^2}{64\pi^4(N_c^2-1)}\int_{\eta_q\eta_p}\int_{\boldsymbol{q}_\perp\boldsymbol{p}_\perp\boldsymbol{k}_{1\perp}}\frac{\varphi_p(Y_p,\boldsymbol{k}_{1\perp})}{\boldsymbol{k}_{1\perp}^2}\\ &\times\mathcal{N}_{t,Y_t}(\boldsymbol{P}_\perp-\boldsymbol{k}_{1\perp})\left[2\tau_{g,g}(\boldsymbol{k}_{1\perp})+\tau_{q,q}(\boldsymbol{k}_{1\perp})\right.\\ &\left.+\tau_{\bar{q},\bar{q}}(\boldsymbol{k}_{1\perp})+2\tau_{g,q}(\boldsymbol{k}_{1\perp})+2\tau_{g,\bar{q}}(\boldsymbol{k}_{1\perp})\right],\end{aligned} \tag{1.26}$$

where $\tau_{n,m}$ takes the same form as in eq. (1.22) for $n,m\in\{g,q,\bar{q}\}$ with the additional Dirac structures T_q^μ and $T_{\bar{q}}^\mu$ also specified Appendix A. In this limit, the higher twist contributions in the projectile and the target gluon distributions are small corrections and the $k_\perp$-factorized formula (1.26) smoothly turns into the leading twist, or dilute-dilute, approximation of eq. (1.23).

It is crucial to note that we employ only the valence quark distribution in eq. (1.13) and not the sea quark distribution. When valence quarks radiate gluons, the collinear gluon emissions are enhanced and generate a gluon distribution. If the photon is emitted off a sea quark leg emitted from a collinear gluon, after integration over the phase space of the spectators, will give a contribution that formally will have the structure of our LO result. However, this result is entirely contained in our NLO expression and can be obtained by taking the appropriate collinear limits thereof. Hence including sea quarks in the LO computation would amount to double counting their contribution. We therefore perform the flavor summation in eq. (1.13) only over the valence u and d quarks, while the flavor summation in eq. (1.23) and (1.26) runs over u, d, s, c and b quarks.

1.4.1 Isolated photons in proton-proton collisions

Our computation was performed within the dilute-dense approximation in the CGC EFT [84, 87], where one computes pair production (and subsequent photon emission) by solving the Dirac equation in the classical background field generated in the scattering process to lowest order in $\rho_p/k_{p\perp}^2$ and to all orders in $\rho_t/k_{t\perp}^2$. Here ρ_p (ρ_t) are the color charge densities in the projectile (target) proton, and $k_{p\perp}$ ($k_{t\perp}$) are the associated transverse momenta. This approximation is strictly valid in the forward rapidity region where the momentum fraction x_t of the parton from the target proton is much smaller than x_p, the momentum fraction of the parton from the projectile proton. Note that for these assumptions to be a priori robust, even the projectile parton should have $x_p \leq 0.01$. In our computations, we will cover kinematic regimes that will fall outside this preferred kinematic regime; the systematic uncertainties of the computation increase in that case due to the increased contributions of other channels and/or higher order effects.

In this work, we will extend the application of the dilute-dense CGC EFT to single inclusive photon production in p+p collisions at the LHC energies. The photon data available thus far is from ATLAS and CMS [92–96] where $k_{\gamma\perp} > 20$ GeV, with the exception of one data point extending below 20 GeV. While these values of the photon $k_{\gamma\perp}$ are too hard to be directly sensitive to small x dynamics in the proton wavefunction, it is anticipated that ALICE will measure lower-$k_{\gamma\perp}$ photons. Especially promising are the forward LHC upgrades [97], such as the LHCf [98] and the proposed ALICE FoCal [99] upgrades.

As a reasonable estimate of the kinematic reach of the CGC EFT, we will impose the condition that the average x in the target proton is $x < 0.01$; for LHC energies, this corresponds approximately to $k_{\gamma\perp} \lesssim 20$ GeV at mid-rapidities. The CGC-based formulas, as explicitly laid out in the following, have a systematic $k_\perp$-factorized (or dilute-dilute) limit, wherein the cross–section is factorized into the product of unintegrated gluon distributions (UGDs) in each of the protons. Deviations from this $k_\perp$ limit increase with increasing values of either $\rho_p/k_\perp^2$ or $\rho_t/k_\perp^2$, with maximal contributions coming from $k_\perp \sim Q_s$, where Q_s is the saturation scale in the projectile or target at a given x. Thus in the CGC framework one can extract information on the UGD distributions by comparing the computed inclusive photon distributions to data as well as quantify saturation effects by looking for systematic deviations from the $k_\perp$ factorized formalism along the lines predicted in the CGC EFT.

Prompt photon production includes both the direct photon component described by the above formulae as well as the contribution from fragmentation photons that we do not compute here. Experimentally, the two contributions can be separated by imposing an isolation cut along lines similar to that proposed in [100]; while this minimizes the fragmentation contribution, it does not eliminate it completely and this uncertainty is part of the quoted experimental systematic errors. We will adopt here the same isolation cut as used in the experiments to compare our results to the data. The above formulas must be convoluted with

$$\theta\left(\sqrt{(\eta_\gamma - \eta)^2 + (\phi_\gamma - \phi)^2} - R\right), \tag{1.27}$$

where $\theta(x)$ is the step function, η, ϕ are respectively the rapidity and the azimuthal angle of either[7] q or $\bar{q}$, while η_γ and ϕ_γ denote the rapidity and the azimuthal angle of the photon. The CMS and the ATLAS experiments use $R = 0.4$, estimating the

[7] Hence, for the $gg \to q\bar{q}\gamma$ channel one needs to insert two step functions.

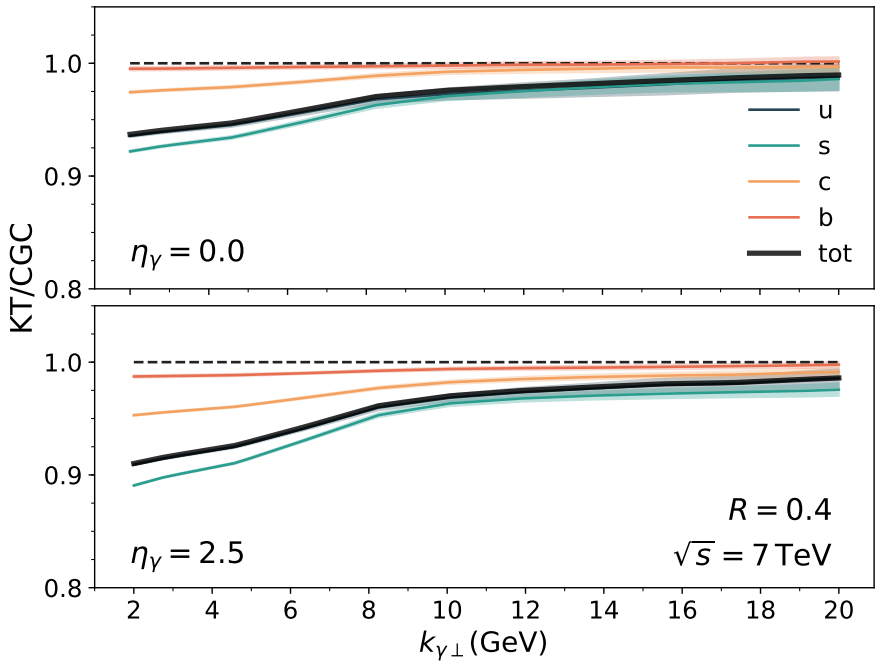

FIGURE 1.5: Ratios of the $k_\perp$-factorized results to the full CGC results as a function of $k_{\gamma\perp}$ at $\sqrt{s} = 7$ TeV with the isolation cut $R = 0.4$. The upper panel is for the photon rapidity $\eta_\gamma = 0$ and the lower for $\eta_\gamma = 2.5$. The band represents the error estimate from performing multidimensional integrals using the VEGAS Monte Carlo integration routine.

remaining fragmentation component to 10% of the total cross section [101, 102]. We use $R = 0.4$ throughout this work.

We will now present some of the numerical details in our computation of eqs. (1.13), (1.23) and (1.26). For the valence quark distribution, we use the CTEQ6M set [103]. The small-x evolution of the dipole distributions is obtained from the running coupling Balitsky-Kovchegov (rcBK) [82, 104], which is a good approximation [105] to the general expression for the dipole forward scattering amplitude given by the Balitsky-JIMWLK hierarchy [104, 106–109]. In solving the rcBK equation numerically, the initial condition for the dipole amplitude at $x_0 = 0.01$ is given by the McLerran-Venugopalan (MV) model with anomalous dimension $\gamma = 1$, the saturation momentum at the initial x_0 of $Q_0^2 = 0.2$ GeV^2, and the IR cutoff for the running couping $\Lambda_{\rm IR} = 0.241$ GeV–see [110] for details of the rcBK initial conditions. With the initial condition fixed, the rcBK equation is solved to determine the dipole amplitude for $x < x_0$. For $x > x_0$, we use the extrapolation suggested in Ref. [70] wherein the UGD can be matched to the CTEQ6M gluon distribution. The matching procedure fixes the proton radius R_p, to $R_p = 0.48$ fm, or equivalently $S_\perp = \pi R_p^2 = 7.24$ mb. Note that this value of R_p is quite close to that extracted from saturation model fits to exclusive DIS data [111]. In our computations, we will take quark masses to be typically $m_u = m_d = 0.005$ GeV, $m_s = 0.095$ GeV, $m_c = 1.3$ GeV and $m_b = 4.5$ GeV. We will discuss later the effects of varying the parameters on model to data comparisons.

Evaluating the full CGC formula for the single inclusive photon cross-section as a function of photon transverse momenta $k_{\gamma\perp}$ and rapidity η_γ in eq. (1.23) involves

performing 10-dimensional integrations while the simpler $k_\perp$-factorized approximation in eq. (1.26) involves 8-dimensional integrations. Such multidimensional integrations are most efficiently performed by employing the VEGAS Monte Carlo (MC) algorithm. For the $k_\perp$-factorized integral, 10^8 points were used to sample the approximate distribution of the integrand, until convergence with a significance of $\chi = 0.3$ was obtained. For the CGC calculations, we used the same algorithm but sampled the integrand with 10^9 points. As a numerical check of our computation, we confirmed that in the small $k_{\gamma\perp}$ limit the NLO result reproduces the soft photon theorem–see Eqs. (B.7)-(B.11) in Ref. [69].

At low to moderate $k_{\gamma\perp}$, the full-CGC computation of the inclusive photon cross section based on (1.23) breaks $k_\perp$-factorization. This is also the case for inclusive quark production, as shown previously [89]. Our results for $k_\perp$-factorization breaking are shown in Fig. 1.5, where we plot the ratio of the full CGC inclusive photon cross-section to the $k_\perp$-factorized cross-section at $\sqrt{s} = 7$ TeV and $R = 0.4$. The results are plotted for central and forward photon rapidities, for individual flavor contributions, and for the net sum over flavors. The breaking of $k_\perp$-factorization is greater for forward rapidities and for decreasing quark mass, with negligible breaking of $k_\perp$-factorization observed for the heaviest flavor. Quantitatively, the breaking is maximally $\sim 10\%$ breaking at the lowest $k_{\gamma\perp}$, approaching unity for $k_{\gamma\perp} \gtrsim 20$ GeV. As suggested by the discussion in [90], when $k_{\gamma\perp}$ is small, the quark-antiquark pair are more likely to both scatter off the gluon shockwave in the target; the $k_\perp$-factorized configuration, where multiple scattering of both the quark and antiquark does not occur, is therefore suppressed. As also suggested by Fig. 1.5, the reverse is true at large $k_{\gamma\perp}$.

Next, to illustrate the importance of the NLO ($gg \to q\bar{q}\gamma$) channel quantitatively relative to the LO ($qg \to q\gamma$) channel, we plot in Fig. 4.5 the NLO / (NLO+LO) fraction as a function of $k_{\gamma\perp}$. The left panel shows the collision energy dependence of the ratio for $\sqrt{s} = 0.2$, 2.76, 7 and 13 TeV with $\eta_\gamma = 1.0$. We observe that the NLO fraction of the inclusive photon cross-section at the highest RHIC energy of $\sqrt{s} = 0.2$ TeV is quite small, $\sim 10\%$. This is because, for the relevant $k_{\gamma\perp}$, quite large values of x are probed in the proton where the gluon distribution does not dominate over that of valence quark distributions. However, already at $\sqrt{s} = 2.76$ TeV, the NLO contribution is more than 60% even for the largest values of $k_{\gamma\perp}$ shown, and increasing the center-of-mass energy to $\sqrt{s} = 7$ TeV and 13 TeV enhances the NLO contribution to more than $\sim 90\%$. These results confirm that at LHC energies gluons dominate the proton wavefunction, even for photons with $k_{\gamma\perp} = 20$ GeV. The right panel shows the ratio for photon rapidities of $\eta_\gamma = 0$, 1.5, 2.5 at a fixed $\sqrt{s} = 7$ TeV. The NLO contribution dominates completely at central rapidities and supplies 50% of the cross-section even at $\eta_\gamma = 2.5$ and $k_{\gamma\perp} = 20$ GeV.

A significant source of theoretical uncertainty in our computations are the contributions from the large $k_{\gamma\perp}$ region. Starting from $k_{\gamma\perp} \sim 10$ GeV, the small-x logs compete with transverse momentum logs $\log(k_\perp^2/\Lambda^2_{\rm QCD})$ associated with DGLAP evolution[8] where a matching between the two formalisms becomes necessary. We will therefore show our results for $k_{\gamma\perp} \leq 20$ GeV where the average value of x_t is $\langle x_t \rangle \leq 0.01$, as demonstrated on Fig. 1.7. For a systematic approach to this matching [113] it will be necessary to include higher order corrections to our framework. In addition to higher order contributions in QCD evolution and in the matrix elements, there are uncertainties in the extraction of the transverse area $S_\perp$. Though

[8] According to a recent estimate [112], small-x effects in DIS become important for $\log 1/x \geq 1.2 \log Q^2/\Lambda^2_{\rm QCD}$. This estimate is process dependent and may be different in the case of inclusive photon production.

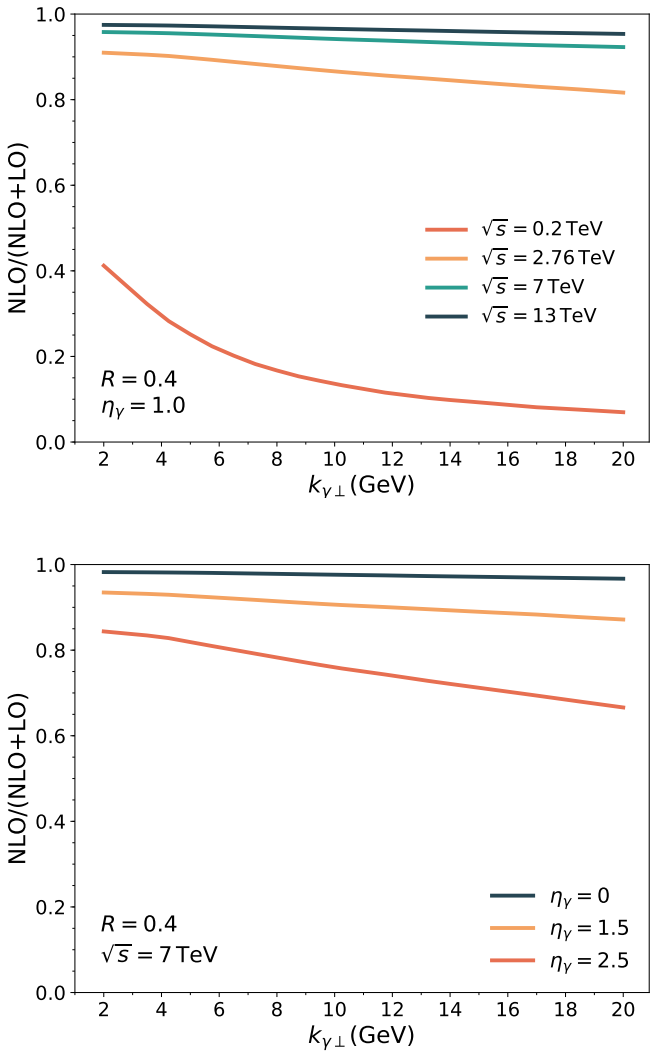

FIGURE 1.6: Fraction of the inclusive photon cross section from the NLO $gg \to q\bar{q}\gamma$ channel relative to the total NLO+LO contribution, as a function of $k_{\gamma\perp}$. Here, and in subsequent plots, the NLO computation was performed employing the $k_\perp$-factorized formula eq. (1.26). The left panel shows the collision energy dependence at $\sqrt{s} = 0.2, 2.76, 7, 13$ TeV for $\eta_\gamma = 1.0$. The right panel shows the photon rapidity dependence at $\eta_\gamma = 0, 1.5, 2.5$ for $\sqrt{s} = 7$ TeV. In both cases, $R = 0.4$.

$S_\perp$ is constrained from the matching to parton distributions at large x, there can easily be 50% uncertainties in the overall cross-section that are absorbed by the extraction of the K-factor from comparison of the computed cross-sections to data. Until we can quantify the sources contributing to this K-factor separately, we should understand these sources of uncertainty as being "bundled" together in the value extracted.

We should note further that there are other sources of uncertainty. We previously mentioned the $1/N_c^2$ corrections in using the BK truncation of the JIMWLK hierarchy. In practice, these are significantly smaller, specially so in the regime where $k_\perp$-factorization is applicable. Another source of systematic uncertainty are the values of the quark masses. Varying the quark masses in the ranges $m_{u,d} = 0.003 - 0.007$ GeV, $m_s = 0.095 - 0.15$ GeV, $m_c = 1.3 - 1.5$ GeV and $m_b = 4.2 - 4.5$

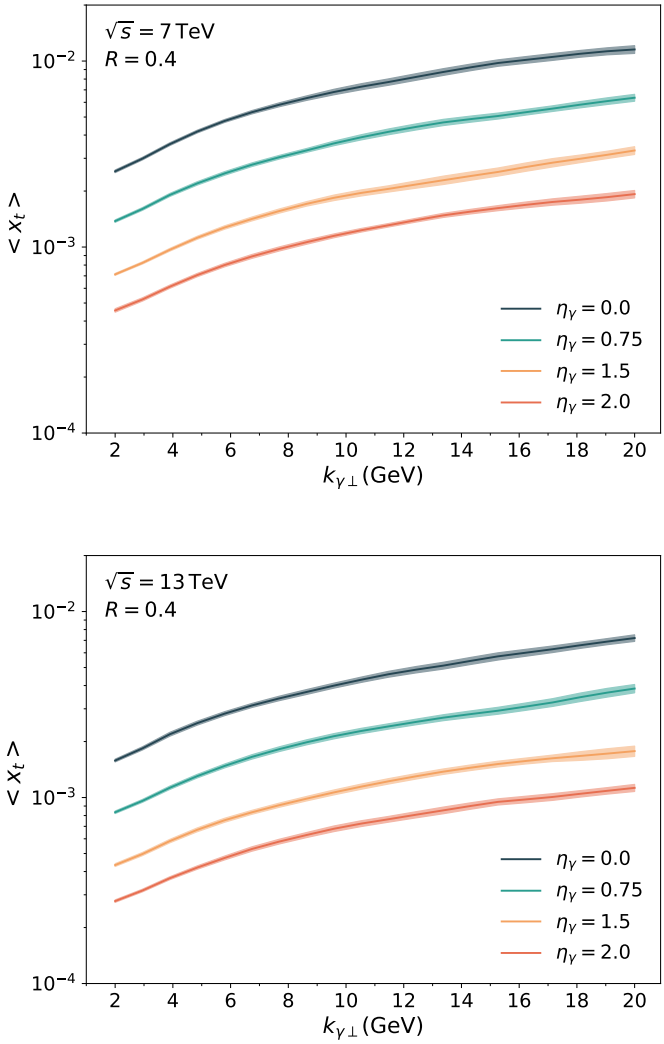

FIGURE 1.7: Left (right) panel shows $\langle x_t \rangle$, the average value of x_t, in the target proton as a function of $k_{\gamma\perp}$ at $\sqrt{s} = 7$ TeV (13 TeV). The different curves correspond to $\eta_\gamma = 0.0, 0.75, 1.5$ and 2.0. In both cases, $R = 0.4$.

GeV, we observed that the cross section for $10\,\text{GeV} < k_{\gamma\perp} < 50\,\text{GeV}$ varies by $5-10\%$ for the light u, d, and s quarks, while the heavier c and b quarks have small variations of order $0-5\%$. There is an overall degree of uncertainty in performing the Monte Carlo integrals, which is quantified by the error estimate of the VEGAS algorithm. This error estimate for the $k_\perp$-factorized inclusive cross-section is the range of $0-5\%$ for all flavors. Based on these sources of uncertainty, we have included a systematic error band of 15% in comparisons to data.

In Fig. 1.8 (Fig. 1.9), we show the numerical results for the inclusive photon cross section based on Eqs. (1.13) and (1.23) at 7 TeV (13 TeV) integrating over several η_γ ranges up to $|\eta_{k_\gamma}| < 2.5$. In particular, we are covering the mid-rapidity region that can be measured by the LHC experiments. The particular rapidity ranges shown are those where ATLAS and CMS data exist presently at higher values of $k_{\gamma\perp}$. These data sets are for the CMS p+p data at 2.76 TeV [92] and at 7 TeV [94] for values $k_{\gamma\perp} \geq 20$ GeV. The ATLAS p+p data set is given for 7 TeV, where one data point exists below $k_{\gamma\perp} = 20$ GeV. We have chosen the central value of this lowest lying ATLAS

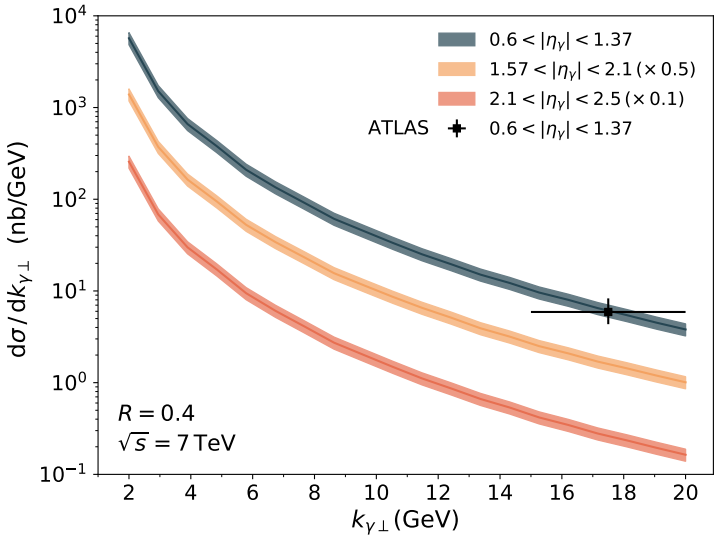

FIGURE 1.8: Numerical results for the p+p photon data at $\sqrt{s} = 7$ TeV across several rapidity bins. The central lines are obtained by multiplying our numerical results with a K-factor of $K = 2.4$. The data point is from the ATLAS experiment [95].

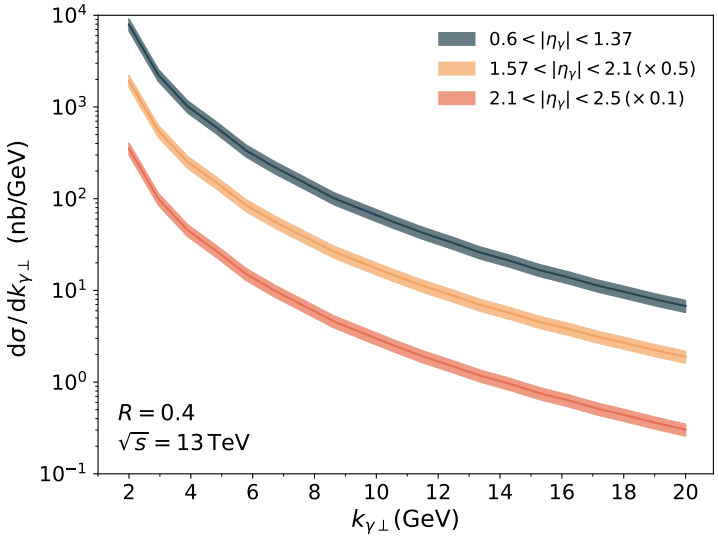

FIGURE 1.9: Predictions for the inclusive photon production at $\sqrt{s} = 13$ TeV across several rapidity bins. The central lines have the same K-factor as Fig. 1.8.

point in order to normalize our results and found that the required K-factor is $K = 2.4$. Interestingly, this is very close to the K-factor of 2.5 extracted in computations of D-meson production in this dilute-dense CGC framework [74]. We have not shown a comparison to data above $k_{\gamma\perp} = 20$ GeV because the contribution of logs in $k_\perp$ begin to dominate significantly over logs in x around these values of $k_{\gamma\perp}$; the systematic treatment of these is beyond the scope of the present computation.

1.5 Conclusions

This chapter summarizes the results of an on-going research program which seeks to constrain the gluon unintegrated functions of the proton and nuclei using photon observables. The results from ref. [69] comprise the conclusion of the analytical calculation of the photon inclusive cross-section at the NLO level using the hybrid framework of the CGC EFT. Apart from single photon production, these results can be used to compute the cold nuclear matter modification of many observables, such as photon-jet or photon-$q\bar{q}$ (called *onium* in the literature) correlations. In the future, such measurements will help further constraint the gluon unintegrated functions of the proton and the nucleus. These results exhibit the correct limits at the $k_\perp$-factorization and collinear limits, which then can pose as systematic continuation of the known results for higher momenta.

The results presented in the last section are an important first step towards constraining the proton UGDs at small-x from inclusive photon production at the LHC. We have quantified for the first time the dominant contributions to inclusive photon production at LO and NLO. We found that the contribution of the NLO channel is significantly larger than the LO at central rapidities at the LHC. This is because at LHC energies the results are sensitive to small-x values in the proton that have high gluon occupancy. We showed further that coherent rescattering contributions in the CGC that break $k_\perp$-factorization are at most about 10% in the low $k_{\gamma\perp}$ region and negligible beyond $k_{\gamma\perp} \simeq 20$ GeV. We have provided several numerical results for the inclusive isolated photon cross section that can be tested at the LHC.

Future investigations will extend the analysis presented here to make predictions for p+A collisions and high multiplicity p+p and p+A collisions, and examine as well their sensitivity to available HERA dipole model fits [114]. Prior studies have only considered LO contributions to inclusive photon production. Another important avenue where progress is required is in the computation of higher order effects which formally are NNLO in this approach but are essential to quantify running coupling corrections and for matching to results from collinear factorization computations [102, 115] at high $k_{\gamma\perp}$.

Chapter 2

Non-equilibrium photons from thermalizing Glasma

Direct photons are ideal probes to test the space-time evolution of hot nuclear matter. They are radiated throughout all the collision and, due to a lack of final-state interactions, can escape the medium virtually unscathed. As a consequence, these probes may be the only observable sensitive to the different stages of the rapidly expanding fireball. In small systems, such as $p+p$ or $p+A$ collisions, direct photons produced are mostly prompt photons, whose invariant yield can be calculated perturbatively [116–118] or using hybrid approaches [16, 69] to account for nuclear modification factors. However, in collisions of large nuclear systems, direct photons in the small transverse momentum range exhibit exponential enhancement, commonly explained by thermally equilibrated, hydrodynamical models.

In addition to those findings, the transverse plane anisotropy of the photon multiplicities was studied [119], finding non-vanishing flow coefficients [120, 121]. This anisotropy is thought to arise from the space-time evolution of the underlying medium. To compute such quantities, hydrodynamical quark-gluon-plasma (QGP) and transport models have been compared to the available data. Unfortunately, the simultaneous reproduction of the yields and the photon flow coefficients, v_n, has been out of reach [122–124] up to today. This challenging situation has been named the *direct photon puzzle* in the literature [125].

Nevertheless, in those calculations the pre-equilibrium physics of the medium is not accounted for, which leads to the introduction of several uncertainties including the initial conditions for the hydrodynamical evolution. Pre-equilibrium sourced photons are also omitted, and while it is the traditional idea that an early-times photon source is suppressed by volume, new results seem to suggest that, in fact, such a source may contribute on the same order of magnitude as the thermal stages [126–128]. In a novel estimate, [35], thermal and Glasma total photon yields were parametrically found using the *bottom-up* thermalization scenario by Baier, Mueller, Schiff and Son (BMSS) [28]. They were found to be comparable to thermal total yields. For this, a phenomenological matching was performed to account for the energy scale Q_S in the system as well as for the thermalization time, τ_{th} and temperature, T_{th}. While a full phenomenological simulation that links the initial stage of the collision with the onset of hydrodynamics is still out of reach, broad progress has been achieved to understand its dynamics. The initial stage of the collision is classical and highly non-linear in the gluon fields and after a parametrically short time, the evolution leads to instabilities, which overpopulate the gluon fields [13, 26, 129]. Using classical statistical simulations, it was shown that an over-occupied Glasma approaches a non-thermal fixed point [130, 131], and by doing so loses its memory of the details about the initial conditions. In this simulations, it was found that the system goes through a universal scaling regime, which

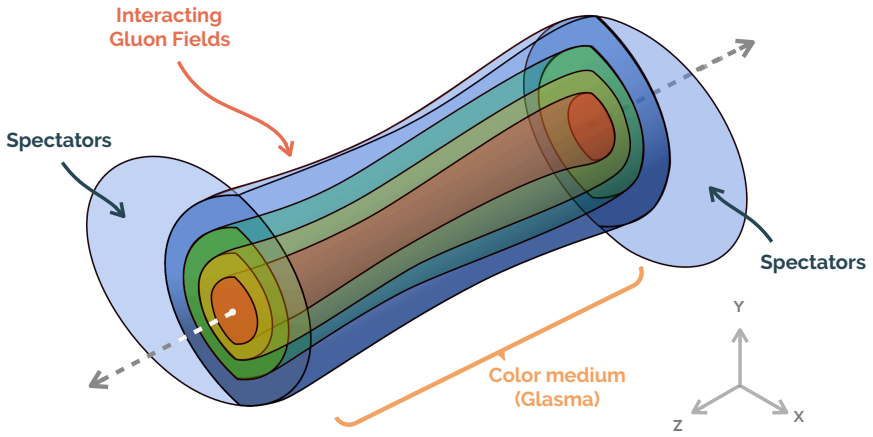

FIGURE 2.1: When hadronic species collide at very high energies, in RHIC and LHC, a medium of interacting gluon fields is created, which is called Glasma in the literature. In the figure, simplified diagramatic rendition of the Bjorken expansion of the Glasma.

means that the gluon distribution function behaves as

$$f_g(\tau;\, p_\perp, p_z) = \frac{1}{\alpha_s}\, \tau^\alpha\, f_S(p_\perp\, \tau^\beta, p_z\, \tau^\gamma), \tag{2.1}$$

where f_S is a time independent function, whose shape is given by non-perturbative physics of the theory. The exponents $\alpha = -2/3$, $\beta = 0$ and $\gamma = -1/3$ thus confirm the parametrical descriptions of the BMSS scenario [132], thus identifying its approach to thermalization as the correct description of the expanding Glasma.

In this paper, we use the $2 \leftrightarrow 2$ kinetic photon rate to calculate the $p_\perp$ resolved spectra following the assumptions for the estimates of ref. [35]. This is done in the context of the *bottom-up* thermalization scenario. The rate is further simplified using a small-angle approximation. For this calculation, the momentum dependent non-thermal distribution of quarks is needed, which is sampled via the hard $g \to q\bar{q}$ approximation. This means that $f_q \sim \alpha_s f_g$, where f_g is taken to be the non-equilibrium scaling solution from eq. (2.1). The non-equilibrium rates are enhanced using a bremsbremstrahlung ansatz analogous to the complete leading order (LO) thermal rate [133]. The different contributions from the Glasma, as well as the later thermal stage, will be compared, to establish their relative dominance in this model. Finally, will fix the model's parameters phenomenologically to present a qualitative comparison with data.

This work is organized as follows. In section 2.2 the reader can find a small account of the kinetic framework used, as well as the low-$p_\perp$ enhancement ansatz used for the non-equilibrium case. In section 2.1 we summarize the BMSS thermalization scenario and present the $2 \leftrightarrow 2$ leading log (LL) results for the Glasma in this context. In sec. 2.3, we will review the parameter fixing of Ref. [35] and apply it to the $p_\perp$ resolved spectra. The main body of the results achieved in this work is given in sec. 4.5. Here, a comparison of the different contributions to direct photons will be presented for both the LL and the LO case. Furthermore, we will also compare photon production in the BMSS scenario with its early thermalization counterpart. Finally, a qualitative comparison to ALICE and PHENIX data will be presented. This section is my own original work, but it stems from and intersects with work done with Jürgen Berges, Klaus Reygers, Nicole Löher and Aleksas Mazeliauskas,

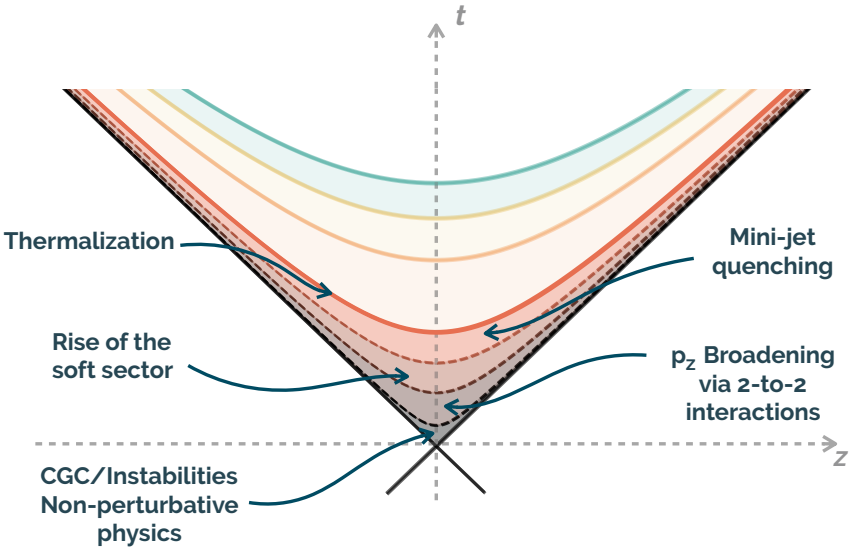

FIGURE 2.2: Space-time diagram of the *bottom-up* thermalization scenario. The darkest dotted line represent the initial time $Q_s\,\tau_0 \sim 1$. The following ones represent the boundaries between the three different stages.

presented in next Chapter.

2.1 The *bottom-up* thermalization scenario

The main assumption of the *bottom-up* scenario, and also this work, is that gluonic saturation physics takes place for energies at LHC and RHIC[1]. This means that at the moment of impact, the colliding nuclei are two Lorentz contracted, highly dense, coherent gluonic states. In the bottom-up scheme, this initial state creates a non-thermal colored medium undergoes three stages in its path for thermalization, which can be parametrically separated as

$$\begin{aligned}
&\text{(i)}\ \ 1 \ll Q_s\,\tau \ll \alpha_s^{-3/2} \\
&\text{(ii)}\ \ \alpha_s^{-3/2} \ll Q_s\,\tau \ll \alpha_s^{-5/2} \\
&\text{(iii)}\ \ \alpha_s^{-5/2} \ll Q_s\,\tau \ll \alpha_s^{-13/5}
\end{aligned}$$

In the beginning of the collision, at $\tau < Q_s^{-1}$ the physics of the glue is highly non-perturbative, and the states can be characterized by very non-linear macroscopic fields. During this stage, instabilities highly populate modes with $p_\perp \lesssim Q_s$ [134]. After these modes have been occupied, the system is completely dominated by hard modes, for which $p_\perp \sim Q_s$. These modes are approximately conserved, but due to Bjorken expansion their number density is diluted as $n_h \sim Q_s^3/(Q_s\,\tau)$. During this stage, gluons interact via $2 \leftrightarrow 2$ hard scatterings, with a very small momentum exchange. This produces a broadening, or melting, of the distribution of longitudinal momentum $p_z \sim Q_s\,(Q_s\,\tau)^{-1/3}$. The produced effect is a decrease of the typical occupation number as $f_g \sim \alpha_s^{-1}\,(Q_s\,\tau)^{-2/3}$.

The second stage starts when the typical occupation f_g falls below unity. This happens parametrically at $Q_s\,\tau \sim \alpha_s^{-3/2}$. During this stage, the number of soft gluons rise rapidly via collinear splitting. Nonetheless, hard gluons still dominate

[1] For a brief introduction to saturation see Chapter 1

the total number, with their number densities given by

$$n_h \sim \frac{Q_s^3}{Q_s\,\tau} \quad \text{and} \quad n_s \sim \frac{\alpha_s^{1/4}\,Q_S^3}{(Q_S\,\tau)^{1/2}}\,. \tag{2.2}$$

In this stage, soft gluons possess a typical momentum of $p_{soft} \sim \alpha^{1/2}\,Q_s$. It can be seen that $n_{soft}/p_{soft} \gg n_{hard}/p_{hard} \sim n_{hard}/Q_s$. This makes the Debye integral peaked strongly around the soft sector, from which m_D can be found to be $m_D^2 \sim \alpha_s\,n_{soft}/p_{soft} \sim \alpha_s^{3/4}\,Q_s^2\,(Q_s\,\tau)^{-1/2}$. The typical longitudinal momentum of hard gluon stops decreasing in (ii) and converges to $p_z \sim \alpha_s\,Q_s$, which means that the anisotropy of the system saturates at finite value.

The thermalization stage (iii) starts around the time $Q_s\,\tau \sim \alpha^{-5/2}$, where n_h and n_s become comparable, while $p_{soft} \ll p_{hard}$. This signals that soft modes are now dominant both in number densities and in the screening mass. Soft gluons thermalize very fast via $2 \leftrightarrow 2$ soft scatterings, and act as a thermal bath to which the hard sector looses energy via mini-jet quenching [135]. Since hard gluons act as a source of energy to the bath, the temperature rises with $T = c_T\,\alpha_s^3\,Q_s^2\,\tau$, to finally achieve full thermalization of the medium at

$$\tau_{th} \sim c_{eq}\,\alpha^{-13/5} Q_s^{-1} \quad \text{and} \quad T_{th} \sim c_T\,c_{eq}\,\alpha^{2/5} Q_s\,. \tag{2.3}$$

Using this model to estimate the evolution of the Glasma, we can use these results to calculate the photon spectra produced on the road to thermalization.

In the following, we use the Bjorken variables $\tau = \sqrt{t^2 - z^2}$, $\eta = \arctan(z/t)$ and $y = \operatorname{artanh}(p_z/E)$. For the transverse plane, we employ a polar parametrization, $p_x = p_\perp \cos\phi$ and $p_y = p_\perp \sin\phi$ in terms of the transverse momentum $p_\perp$, longitudinal momentum p_z and azimuthal angle ϕ. The photon multiplicities will be obtained by integrating the eq. (2.7) over the four-volume of the evolution for each stage, using $\mathrm{d}^4X = \tau \mathrm{d}\tau \mathrm{d}\eta d^2x_\perp$ and $\mathrm{d}^3p/E = \mathrm{d}y \mathrm{d}^2p_\perp$.

2.2 Approximate kinetic description

Following Ref. [35], the photon rate for a thermalizing colored medium will be calculated using a kinetic description. The emission rate of an on-shell photon with three-momentum $\boldsymbol{p} = (p_x, p_y, p_z)$ at a space-time point $X = (t, x, y, z)$ from two-to-two scatterings is given generally by [136, 137]

$$\begin{aligned} E\frac{\mathrm{d}N}{\mathrm{d}^4X\mathrm{d}^3p} = \frac{1}{2\,(2\,\pi)^{12}} \int \frac{\mathrm{d}^3\,p_3}{2E_3}\frac{\mathrm{d}^3\,p_2}{2E_2}\frac{\mathrm{d}^3\,p_1}{2E_1}\,|\mathcal{M}|^2 \\ \times\ (2\,\pi)^4\,\delta^4(P_1 + P_2 - P_3 - P) \\ \times\ f_1(p_1)\,f_2(p_2)\,[1 \pm f_3(p_3)]\ , \end{aligned} \tag{2.4}$$

with $P_i = (E_i, \boldsymbol{p}_i)$, $i = 1, 2, 3$. The total squared amplitude $|\mathcal{M}|^2$ is understood as summed over spins, colors and flavors of all in and outgoing particles. For massless quarks, the annihilation of a quark-antiquark pair into a photon and a gluon yields the squared amplitude

$$|\mathcal{M}_{\mathrm{anni}}|^2 = \frac{160}{9}\,16\pi^2\,\alpha\,\alpha_s\,\frac{u^2 + \bar{t}^2}{u\,\bar{t}}, \tag{2.5}$$

with the strong interaction coupling α_s and the electromagnetic coupling α. The squared amplitude for mixed Compton scattering, where a gluon kicks a (anti)quark

producing a photon is

$$|\mathcal{M}_{\rm Comp}|^2 = \frac{320}{9}\, 16\pi^2\, \alpha\, \alpha_s\, \frac{u^2+s^2}{-u\, s}. \tag{2.6}$$

These are given in terms of the Mandelstam variables $s = (p_1+p_2)^2$, $\bar{t} = (p_1-p)^2$, and $u = (p_3-p_1)^2$.

To estimate the scattering rates, we will consider these two processes. Furthermore, the production of photons may be simplified using the small-angle approximation [138, 139]. In this case, one finds the rate

$$E\frac{{\rm d}N}{{\rm d}^4X{\rm d}^3p} = \frac{40}{9\pi^2}\, \alpha\, \alpha_S\, \mathcal{L}\, f_q(\mathbf{p})\, I_g\,, \tag{2.7}$$

where f_q is the quark distribution. The $I_{g,q}$ integrals are given by

$$I_{g,q} = \int \frac{{\rm d}^3p}{(2\pi)^3}\frac{1}{p} f_{g,q}(\boldsymbol{p})\,. \tag{2.8}$$

The Coulomb logarithm $\mathcal{L}$ in (2.7) serves as a regulator and quantifies the ratio between the infrared and hard scales of the system,

$$\mathcal{L} = \log\left(\frac{\Lambda_{UV}}{\Lambda_{IR}}\right)\,. \tag{2.9}$$

In a thermal medium, the hard scale Λ_{UV} is given by the temperature T, while the infrared scale for the kinetic description is defined by the screening mass, $m_D \sim gT$, with $\alpha_s \equiv g^2/(4\pi)$. More generally, the Debye screening mass squared of the medium is estimated by $m_D^2 = 4g^2(N_c I_g + N_f I_q)$.

The rate (2.7) still neglects the resummation of multiple interactions with the medium that would contribute at leading order in α and α_s [140]. In thermal equilibrium the naive rate (2.7) differs from the full leading-order result by about a factor of two in the relevant photon momentum range. For simplicity, and to also effectively take this into account, we adopt the prescription of Refs. [35, 136] to replace the Coulomb logarithm in (2.9) by

$$\mathcal{L} \longrightarrow 2\log\left(1+2.912/g^2\right) \tag{2.10}$$

to match the leading log (LL) thermal result. This will be employed for all the small-angle estimates shown in this work.

2.2.1 Bremsstrahlung Ansatz

The small angle approximation gives the correct limit for thermal radiation at the LL level, once the coulomb logarithm has been identified as in eq. (2.10). Nonetheless, it has been shown in ref. [36] that in a thermal medium, near-collinear bremsstrahlung dominates the rates for photon energies of $p \lesssim 2T$, while at intermediate photon momenta, $2T \lesssim p \lesssim 10T$, the $2 \leftrightarrow 2$ contribution is comparable to the near-collinear ones. One would expect this simple result to be the case in the non-equilibrium setting of the Glasma, with one general caveat. In the Glasma, the characteristic momentum scale is given by Q_s, making the near-collinear contributions during the early stages dominant at $p \lesssim 2Q_s$ which for RHIC and LHC

energies covers most of the kinematic window at which excess has been observed ($0.5 - 3\,\mathrm{GeV}$).

Following this argument, the bremmstrahlung contribution has to be included, and we will do so by changing the total constant under the log in eq. (2.7) where the temperature has to be substituted for the characteristic scale of the Glasma. Following the result from [36] the leading order (LO) thermal rate can be expressed as

$$E\frac{d\,N}{d^4\,X\,d^3\,p} = A(p)\,\nu\left(\frac{E}{T}\right) \tag{2.11}$$

where

$$A(p) = 2\alpha d_F\left[\sum_c q_c^2\right]\, m_D^2\, f_{q,eq}\left(\frac{E}{T}\right) \tag{2.12}$$

with the thermal screening mass $m_D^2 = C_F\, g_s^2\, T^2/4$ and the Casimir operators $d_F = 3$ and $C_F = 4/3$ for $SU(3)$ [141] . The function ν represents the constant under the log, and can be represented by different functions for both the LL and LO cases,

$$\begin{aligned} LL &: \nu\left(\frac{E}{T}\right) \to \nu_{LL}\left(\frac{E}{T}\right) \to \mathcal{L} \\ LO &: \nu\left(\frac{E}{T}\right) \to \nu_{LL}\left(\frac{E}{T}\right) + C_{bremss}\left(\frac{E}{T}\right) + C_{anni}\left(\frac{E}{T}\right). \end{aligned}$$

The explicit forms of C_{bremss} and C_{anni} can be found in ref. [140]. In the non-equilibrium case, one can expand the former results by using the same LO function, while changing the temperature dependence for the appropriate characteristic scale of the system, Q_s. Using this change, we can write down the function as follows

$$\begin{aligned} LL &: \nu\left(\frac{E}{Q_s}\right) \to \nu_{LL}\left(\frac{E}{Q_s}\right) \to \mathcal{L} \\ LO &: \nu\left(\frac{E}{Q_s}\right) \to \nu_{LL}\left(\frac{E}{Q_s}\right) + C_{bremss}\left(\frac{E}{Q_s}\right) + C_{anni}\left(\frac{E}{Q_s}\right) \end{aligned}$$

In what follows, both the $2 \leftrightarrow 2$ and the LO ansatz results will be presented to allow an appropriate comparison with the estimates presented by Berges et al, as well as to show a better case scenario for photons coming from the BMSS scenario. For this, the non-equilibrium rates of Stages (i) and (ii) will be computed via eq. (2.7) but would receive near-collinear enhancements thanks to the substitution from above In the case of the third stage, the rate is already given by the LL thermal rate, which means it can be just upgraded to the LO thermal rate, as it is parametrized in ref. [36], for the appropriate space-time dependence of the temperature.

2.2.2 Thermal Photons

For photon production from a thermal medium, we may further simplify the computations by using thermal Boltzmann distributions for quarks and gluons at high energies in (2.7). This leads to

$$E\,\frac{\mathrm{d}N^{\mathrm{th}}}{\mathrm{d}^4X\mathrm{d}^3p} = C\frac{5}{9}\frac{\alpha\alpha_S}{2\pi^2}T^2e^{-E/T}\,. \tag{2.13}$$

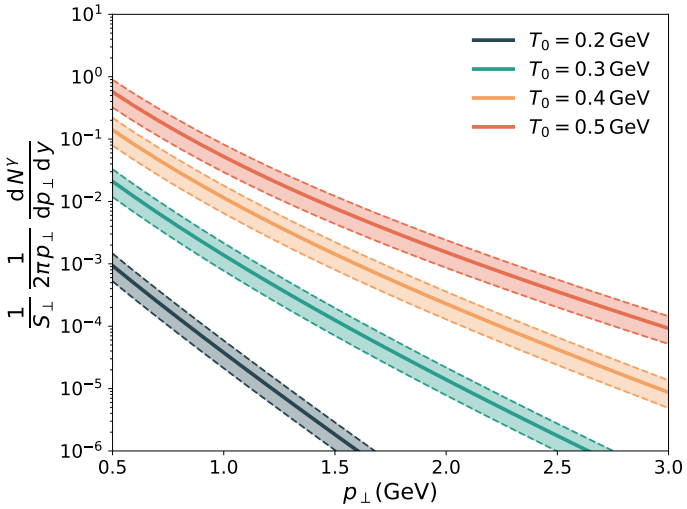

FIGURE 2.3: Thermal multiplicities for different thermalization temperature, T_{th}, in terms of $p_\perp$. In all the curves, the thermalization time has been fixed to $\tau_{th} = 2\,\mathrm{fm}$, while the error bands correspond to 50% variation over the thermalization time τ_{th}.

From this expression the photon multiplicity is obtained by integrating (2.13) over the four-volume of the evolution,

$$\frac{\mathrm{d}N^{\mathrm{th}}}{\mathrm{d}y\mathrm{d}^2p_\perp} = C\frac{5}{9}\frac{\alpha\alpha_S}{2\pi^2}\int \mathrm{d}\tau\,\mathrm{d}\eta\,\mathrm{d}^2x_\perp\,\tau\,T^2\,e^{-p_\perp\cosh(\eta-y)/T}\,. \tag{2.14}$$

Here, we made the equation explicitly Lorentz invariant by $E \to p^\mu u_\mu = p_\perp\cosh(\eta - y)$ with the comoving four-velocity $u_\mu = (\cosh\eta, 0, 0\sinh\eta)$.

The integration itself depends on the spacetime temperature profile. This can be derived from simplified hydrodynamical models or from direct simulation. The simplest scenario would be the evolution for a system invariant under η, $x_\perp$ and ϕ transformations. From basic symmetry arguments, one can get the evolution of the energy density,

$$\epsilon = \epsilon_{\mathrm{th}}\left[\frac{\tau_{\mathrm{th}}}{\tau}\right]^{4/3}\,. \tag{2.15}$$

Using that $\epsilon \sim T^4$, one gets the τ-dependent temperature profile of the expansion,

$$T(\tau) = T_{\mathrm{th}}\left[\frac{\tau_{\mathrm{th}}}{\tau}\right]^{1/3}\,, \tag{2.16}$$

where T_{th} is the thermalization temperature, and τ_{th} is the proper time at which it thermalizes. In the bottom-up thermalization scenario [28], their parameteric dependence is given by

$$\begin{aligned} T_{\mathrm{th}} &\sim c_T c_{\mathrm{eq}}\,\alpha_s^{2/5}\,Q_s\,, \\ \tau_{\mathrm{th}} &\sim c_{\mathrm{eq}}\,\alpha_s^{-13/5}\,Q_s^{-1}\,. \end{aligned} \tag{2.17}$$

Here, c_{eq} is a coefficient of order unity, which arises from the uncertainty from the parametric dependence of the thermalization time, τ_{th}. The other coefficient, c_T, is a constant needed to finish to constraint the thermalisation temperature in the BMSS scheme [28, 142]. These coefficients are constrained in sec. **??** using the method in

ref. [35]. For the thermal epoch, the system will evolve from the thermalization time, until the critical time, τ_c, which signals the arrival to the critical temperature. At this point, the deconfined quark-gluon-plasma phase transitions via a crossover to the hadronic phase. For this work we will take $T_c = 0.154\,\mathrm{GeV}$ [143, 144], while τ_c can be from the temperature profile as follows

$$\tau_c = \tau_{th}\left(\frac{T_{th}}{T_c}\right) \tag{2.18}$$

To start, we want to derive the photon multiplicity for the thermal case. For this, as it was noted before, we integrate emission function, eq.2.13 , over the 4-volume. This gives

$$\frac{\mathrm{d}N_\gamma}{\mathrm{d}^2p_\perp \mathrm{d}y} = S_\perp\,\tilde{C}\,\frac{5}{9}\,\frac{\alpha\,\alpha_S}{2\pi^2}\int_{\tau_{th}}^{\tau_c}\mathrm{d}\tau\,\tau\int_{-\infty}^{\infty}\mathrm{d}\eta\,\tau\,T^2(\tau) \times e^{-p_\perp\cosh[\eta-y]/T(\tau)}\,. \tag{2.19}$$

Here,the temperature profile is assumed to be homogeneous in the transverse plane, which yields the $\boldsymbol{x}_\perp$ integration trivial. The integration can be continued by the rapidity dependent part of the integrand. Using

$$2\,K_0(z) = \int_{-\infty}^{\infty}\mathrm{d}\eta\,e^{-z\cosh\eta}\,, \tag{2.20}$$

where $K_n(x)$ stands for the modified Bessel function of order n. After this integration, we find

$$\frac{1}{S_\perp}\frac{\mathrm{d}N_\gamma}{\mathrm{d}^2p_\perp\mathrm{d}y} = \frac{5}{9}\,\frac{\alpha\,\alpha_S}{\pi^2}\int_{\tau_{th}}^{\tau_c}\mathrm{d}\tau\,\tau\,T^2(\tau)K_0(p_\perp/T(\tau))\,. \tag{2.21}$$

By transforming the integration from proper time to inverse temperature, $\beta = 1/T$, one can get the integral

$$\begin{aligned}\frac{1}{S_\perp}\frac{\mathrm{d}N_\gamma}{\mathrm{d}^2p_\perp\mathrm{d}y} &= \frac{5}{3}\,\frac{\alpha\,\alpha_S}{\pi^2}\,\tau_{th}^2\,T_{th}^6\int_{\beta_{th}}^{\beta_c}\mathrm{d}\beta\,\beta^3\,K_0(\beta\,p_\perp)\\ &\equiv \frac{5}{3}\,\frac{\alpha\,\alpha_S}{\pi^2}\,\tau_{th}^2\,T_{th}^6\,B_{th}(p_\perp)\,.\end{aligned} \tag{2.22}$$

The function $B_{th}(p_\perp)$ can be found by analytical integration, to get

$$B_{th}(p_\perp) = \beta_{th}^4\left[\frac{K_1(\beta_{th}p_\perp)}{\beta_{th}p_\perp} + 2\frac{K_2(\beta_{th}p_\perp)}{(\beta_{th}p_\perp)^2}\right] - \beta_c^4\left[\frac{K_1(\beta_c p_\perp)}{\beta_c p_\perp} + 2\frac{K_2(\beta_c p_\perp)}{(\beta_c p_\perp)^2}\right].$$

It is important to note that this function is reliable when $p_\perp > T$, since the emission function we used had the assumption of $E >> T$. Finally, one can find the total yield by integrating over the transverse momentum

$$\begin{aligned}\frac{1}{S_\perp}\frac{\mathrm{d}N_\gamma}{\mathrm{d}y} &= \frac{10}{3}\,\frac{\alpha\,\alpha_S}{\pi}\,\tau_{th}^2\,T_{th}^6\int_0^{\infty}\mathrm{d}p_\perp\,p_\perp B_{th}(p_\perp))\\ &\equiv \frac{5}{3}\,\frac{\alpha\,\alpha_S}{\pi}\,\tau_{th}^2\,T_{th}^4\left(\frac{T_{th}^2}{T_c^2}-1\right)\,.\end{aligned} \tag{2.23}$$

where we find the same yield than in ref. [35] Here, as in the previous estimates, we have integrated from $p_\perp = 0$ instead of $p_\perp = T$, where the formula is valid.

Here we quantify the error to be of order $K_2(1)$, which will give a relative error of $\mathcal{O}(1)$.

2.2.3 Glasma, Stage I

In the first stage of the evolution of the Glasma, quarks are taken to inherit their properties from the gauge sector via hard gluon splitting. This means that $f_q \sim \alpha_s\, f_g$, where f_g is the gluon distribution found in classical statistical simulations. A small caveat has to be noted here regarding the quantum statistics of this function. This approximation is only valid while $\alpha_s\, f_g \ll 1$ which will be the case for realistic parameters The distribution exhibits self-similarity, and during the scaling regime, dynamics is given by a time-independent function f_S, from which one gets the gluon distribution via the relation

$$f_g(\tau;\, p_\perp, p_z) = \frac{1}{\alpha_S}(Q\tau)^{-2/3}\, f_S(p_\perp, p_z\,(Q\tau)^{1/3}) \tag{2.24}$$

This scaling solution, f_S, was found in numerical studies for Bjorken expanding lattices [130, 132, 145], and it is given by the form

$$f_S(p_\perp, p_z) = f_0 \frac{Q}{p_\perp}\, \exp\left[-\frac{1}{2}\frac{p_z^2}{\sigma_0^2}\right]\, W_r[p_\perp - Q_s]\,, \tag{2.25}$$

which was fitted from the results of ref. [132], where we define $W_r[p_\perp - Q_s]$ as the function that guarantees the suppression of the distribution function around $p_\perp = Q_s$, as observed by simulations in [130]. The parametrization taken from the fits for $W_r[p_\perp - Q_s]$ is as follows,

$$W_r[p_\perp, Q_s] = \theta(Q_s - p_\perp) + \theta(p_\perp - Q_s)\, e^{-\frac{1}{2}(\frac{p_\perp - Q_s}{r\, Q_s})^2} \tag{2.26}$$

where r is a free parameter of $\mathcal{O}(1)$ that allows the correct suppression at higher momenta. During this stage, the gluon occupancy is dominated by hard gluons, which are approximately conserved, up to the expansion dilution factor τ^{-1}. This behaviour determines the time dependence of I_g, which can also be found by simply using the scaling properties in eq. (3.49). An overall normalization constant, κ_g, is used as a proportionality constant. This constant was found in ref. [35] to be given $\kappa_g = c/(2\,N_c)$ where $c = 1.1$ is the gluon liberation coefficient [146]. Having this together, we can write the gluon integral as

$$I_g(\tau) = \frac{Q_s^2}{4\,\pi^2 \alpha_s}\frac{\kappa_g}{(Q_s\,\tau)} \tag{2.27}$$

Using the aforementioned ingredients, the rate for the first stage now looks like

$$E\frac{\mathrm{d}N}{\mathrm{d}^4\, x \mathrm{d}^3\, p} = \frac{10}{9\pi^4}\,\alpha\,\mathcal{L}\,\kappa_g\,\frac{Q_s^2}{(Q_s\,\tau)} f_q(\mathbf{p}) \tag{2.28}$$

For the computation of the photon multiplicity of the first stage, we assume that the photon momentum p is on shell, which means $p_0 = p_\perp \cosh(y-\eta)$, as well as $p_z = p_\perp \sinh(y-\eta)$ in the Bjorken parametrization. To get the yield of the first stage

one starts with the space-time integration of the rate in eq. (2.28),

$$\frac{1}{S_\perp}\frac{\mathrm{d}N_\gamma}{\mathrm{d}^2p_\perp \mathrm{d}y} = \frac{40}{9\pi^2}\frac{\alpha_e\,\kappa_g}{4\pi^2}\,Q_s^2\int_{\tau_0}^{\tau_1}\mathrm{d}\tau\,\tau\int_{-\infty}^{\infty}\mathrm{d}\eta \times \frac{1}{Q_s\,\tau}\,f_q(\tau,p_\perp,p_z). \tag{2.29}$$

Here, the spatial extent of the fireball is taken to be a Bjorken expanding cylinder, where the transverse area is parametrised by $S_\perp$, which can be taken then from the Glauber model. By taking $p_z/p_\perp = \sinh(y-\eta) \equiv v$, and defining the dimensionless time $\tilde{\tau} \equiv Q_s\,\tau$ one can find

$$\frac{1}{S_\perp}\frac{\mathrm{d}N_\gamma}{\mathrm{d}^2p_\perp \mathrm{d}y} = \frac{40}{9\pi^2}\frac{\alpha_e\,\kappa_g}{4\pi^2}\,f_0\,\frac{Q_s}{p_\perp}\,\mathcal{I}_{2/3}(p_\perp)W_r[p_\perp,Q_s] \tag{2.30}$$

where the unitless function $\mathcal{I}_a(p_\perp)$ can be defined, and is given by

$$\mathcal{I}_a(p_\perp) = \int_{\tilde{\tau}_0}^{\tilde{\tau}_1}\frac{\mathrm{d}\tilde{\tau}}{\tilde{\tau}^{-a}}\int_{-\infty}^{\infty}\frac{\mathrm{d}v}{\sqrt{1+v^2}}e^{-\frac{1}{2}\left(\frac{p_\perp v}{\sigma(\tilde{\tau})}\right)^2}. \tag{2.31}$$

The v integral can be performed to find the expression

$$\int_{-\infty}^{\infty}\frac{\mathrm{d}v}{\sqrt{1+v^2}}e^{-\frac{1}{2}\left(\frac{p_\perp v}{\sigma(\tilde{\tau})}\right)^2} = e^{\frac{1}{4}\left(\frac{p_\perp}{\sigma(\tilde{\tau})}\right)^2}K_0\left(\frac{p^2}{4\,\sigma^2(\tilde{\tau})}\right). \tag{2.32}$$

The $\mathcal{I}$ function can be then fully integrated to find the invariant yield,

$$\frac{1}{S_\perp}\frac{\mathrm{d}N_\gamma}{\mathrm{d}^2p_\perp \mathrm{d}y} = \frac{10}{3\pi^4}\frac{\alpha_e\,\kappa_g}{\sqrt{2\pi}}\,f_0\,\frac{\sigma_0}{Q_s}\,W_r[p_\perp,Q_s]\,\frac{Q_s^2}{p_\perp^2} \times G^{2,2}_{2,3}\left(\frac{p_\perp^2}{2\,\sigma^2(\tau)}\,\middle|\,\begin{matrix}1\,,\,1\\ 1/2,\,1/2,\,0\end{matrix}\right)\Bigg|_{\tau_0}^{\tau_1}. \tag{2.33}$$

Here G stands for the Meijer-G function (see Ref. [147]). By keeping $p_\perp$ fixed and expanding up to leading order in $\sigma_0/p_\perp$ and substituting $Q_s\,\tau_0 = 1$ and $Q_s\,\tau_1 = \alpha_s^{-3/2}$, one can obtain the simplified and more meaningful expression for the photon $p_\perp$ resolved multiplicity. This gives equation (2.34), namely

$$\frac{1}{S_\perp}\frac{\mathrm{d}N_\gamma}{\mathrm{d}^2p_\perp \mathrm{d}y} = \sqrt{\frac{\pi}{2}}\frac{20}{9\pi^4}\alpha_e\,\kappa_g\,f_0\,\frac{\sigma_0}{Q_s}\,\log\left(\frac{\tau_1}{\tau_0}\right) \times \frac{Q_s^2}{p_\perp^2}\,W_r[p_\perp - Q_s]\,, \tag{2.34}$$

using the limit of $\sigma_0/Q_s \to 0$. The initial and final times are then substituted for $\tau_0 = c_0\,Q_s^{-1}$ and $\tau_1 = c_1\,\alpha_s^{-3/2}\,Q_s^{-1}$, where c_0 and c_1 are unknown proportionality constants of order $\mathcal{O}(1)$. As it was stated before, a precise description of the Glasma will include such coefficients, but it is out of the scope of this work. In this model, these coefficients will be set to unity. This is in fact, supported by slow, logarithmic dependence of the coefficient ratio c_1/c_0 in eq.(2.34). The final form of the invariant yield, which is the main analytical result of this chapter, is then given by

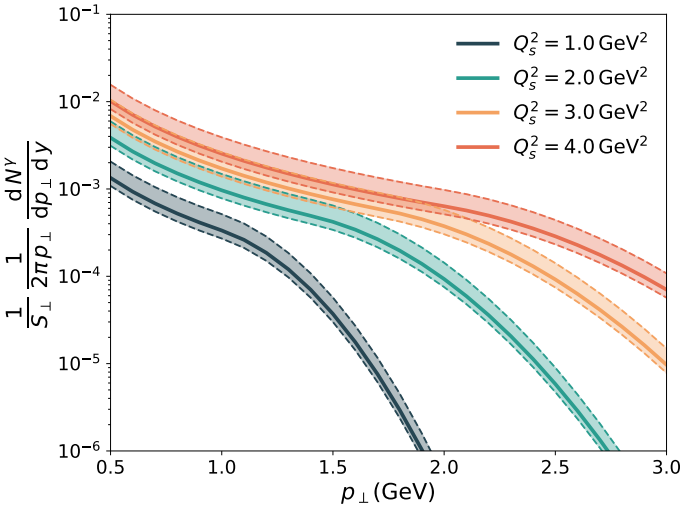

FIGURE 2.4: Photon invariant yield from the first stage of the Glasma for different values of Q_s^2. The error bands correspond to a factor of 2 variations of the anisotropy parameter,σ_0.

$$\frac{1}{S_\perp}\frac{\mathrm{d}N_\gamma}{\mathrm{d}^2p_\perp\mathrm{d}y} = \sqrt{\frac{\pi}{2}}\frac{20}{9\pi^4}\alpha_e\,\kappa_g\,f_0\,\frac{\sigma_0}{Q_s}\,\log\left(\alpha_s^{-3/2}\right) \times \frac{Q_s^2}{p_\perp^2}\,W_r[p_\perp - Q_s]\,, \tag{2.35}$$

This expansion is safe as long as one is interested in the $p_\perp > \sigma_0$ portion of the spectrum. Experimentally, this is the case, as we will be interested in the kinematic window $p_\perp \geq 1\mathrm{GeV}$, and given that in RHIC and LHC, the characteristic saturation scales are thought to be $Q_s \gtrsim 1\mathrm{GeV}$ for heavy ions, we can see that the interesting momenta for this setup are indeed satisfy this condition, for $\sigma_0 \lesssim 0.1\,Q_s$. Nonetheless, below that threshold, the approximation fails, and using such an expression would give an artificially diverging total rate.This means that to find the yield per unit rapidity, $\mathrm{d}N_\gamma/\mathrm{d}y$, the full result, eq. (2.33), has to be integrated. This gives the function

$$\frac{1}{S_\perp}\frac{\mathrm{d}N_\gamma}{\mathrm{d}y}\bigg|_{p_\perp<Q_s} = \frac{10}{3\pi^3}\frac{\alpha_e\,\kappa_g}{\sqrt{2\pi}}\,f_0\,\sigma_0\,Q_s \times G^{2,3}_{3,4}\left(\frac{p_\perp^2}{2\,\sigma^2(\tau_1)}\,\middle|\,\begin{matrix}1,1,1\\ \frac{1}{2},\frac{1}{2},0,0\end{matrix}\right)\Bigg|_{\tau_0}^{\tau_1} \tag{2.36}$$

Once again, we can expand this expression to find (2.37) at LO in terms of the normalized anisotropy parameter, σ_0/Q_s,

$$\frac{1}{S_\perp}\frac{\mathrm{d}N_\gamma}{\mathrm{d}y}\bigg|_{p_\perp<Q_s} = \sqrt{\frac{\pi}{2}}\frac{20}{9\,\pi^3}\alpha_e\,\kappa_g\,f_0\,\sigma_0\,Q_s \times \log(\alpha_s^{-3/2})\log\left(\frac{Q_s^2}{\sigma_0^2}\right)\,, \tag{2.37}$$

which is identical to the result in ref. [35] after performing matching the normalisation of the distribution function , f_0 in terms of the anisotropy parameter, σ_0/Q_s,

$$f_0 \frac{\sigma_0}{Q_s} = \sqrt{\frac{2}{\pi}} \kappa_q \left[\log\left(\frac{Q_s^2}{\sigma_0^2} \right) \right]^{-1} , \tag{2.38}$$

We will use this matching from now on this work. The rest of the yield can be found by integrating eq. (2.34) above the saturation scale Q_s, which gives the result

$$\begin{aligned} \frac{1}{S_\perp} \frac{\mathrm{d}N_\gamma}{\mathrm{d}y}\bigg|_{p_\perp < Q_s} =& \sqrt{\frac{\pi}{2}} \frac{40}{9\,\pi^3} \alpha_e\, \kappa_g\, \kappa_q\, Q_s^2\, \chi_r \\ & \times \log(\alpha_s^{-3/2}) \left[\log\left(\frac{Q_s^2}{\sigma_0^2} \right) \right]^{-1} \end{aligned} \tag{2.39}$$

where $\chi_r$quantifies the number of UV ($p_\perp > Q_s$) photons, and it is regulated by the parameter r. It can be also found analytically to be

$$\chi_r = \frac{1}{2} e^{-\frac{1}{2r^2}} \left(\pi \mathrm{erfi}\left(\frac{1}{\sqrt{2}r} \right) - \mathrm{Ei}\left(\frac{1}{2r^2} \right) \right) . \tag{2.40}$$

In the strict limit of full anisotropy, this contribution vanishes. For the set of parameters used in this work it will contribute to around 5% of the total yield from the Glasma. From these results it can be seen that the total yield of photons of the first stage of the Glasma is basically insensitive to the fit parameters used in eq. (2.25).

2.2.4 Glasma, Stage 2

After a time $\tau \sim Q_s^{-1}\, \alpha_s^{-3/2}$, the typical gluon occupation drops below unity, and the rate should be revised. At this point, hard gluons still dominate the total number density, but soft modes take over the behaviour of the Debye mass. This change affects the time dependence of the I_g integral, which behaves as $I_g \sim \alpha_s^{-1}\, m_D^2$ [28]. This leads to the expression

$$I_g(\tau) = \frac{\kappa_g\, \alpha_s^{-1/4}}{4\,\pi^2 \sqrt{c_1}} \frac{Q_s^2}{(Q_s\,\tau)^{1/2}} \tag{2.41}$$

where the overall normalization of I_g has been modified to match the expression of stage (i) at $\tau \sim Q_s^{-1}\, \alpha_s^{-3/2}$.The fermionic sector is always dominated by hard quarks, which can still be described by $f_q = \alpha_s\, f_g$, with f_g as in eqs. (3.49) and (2.25). With those changes, the full rate for stage (ii) now is given by

$$E \frac{\mathrm{d}N}{\mathrm{d}^4 x \mathrm{d}^3 p} = \frac{10}{9\pi^4}\, \alpha \alpha_s^{3/4}\, \mathcal{L}\, \frac{\kappa_g}{\sqrt{c_1}} \frac{Q_s^2}{(Q_s\,\tau)^{1/2}} f_q(\mathbf{p}) \tag{2.42}$$

The photon multiplicity for this stage can be found by again integrating over the full space-time volume and expanding to leading order in the anisotropy parameter, to get

$$\begin{aligned} \frac{1}{S_\perp} \frac{\mathrm{d}N_\gamma^{(ii)}}{\mathrm{d}^2 p_\perp \mathrm{d}y} =& \sqrt{2\,\pi} \frac{20}{9\pi^4} \alpha_e\, \kappa_g\, f_0\, \frac{\sigma_0}{Q_s} \frac{Q_s^2}{p_\perp^2} \\ & \times W_r[p_\perp - Q_s] \left(\sqrt{\frac{c_2}{c_1}} \alpha_s^{-1/2} - 1 \right) \end{aligned} \tag{2.43}$$

For the second stage of the Glasma, the integration proceeds in the same fashion. We start now with the rate at stage II,

$$\frac{1}{S_\perp}\frac{\mathrm{d}N_\gamma}{\mathrm{d}^2p_\perp \mathrm{d}y} = \frac{40}{9\pi^2}\frac{\alpha_e\,\kappa_g}{4\pi^2}\,Q_s^2\int_{\tau_1}^{\tau_2}\mathrm{d}\tau\,\tau\int_{-\infty}^{\infty}\mathrm{d}\eta \times \frac{1}{(Q_s\,\tau)^{1/2}}\,f_q(\tau,p_\perp,p_z) \tag{2.44}$$

By making the same substitutions as before, one can find the general expression

$$\frac{1}{S_\perp}\frac{\mathrm{d}N_\gamma}{\mathrm{d}^2p_\perp \mathrm{d}y} = \frac{40}{9\pi^2}\frac{\alpha_e\,\kappa_g}{4\pi^2}\,f_0\,\frac{Q_s}{p_\perp}\,\mathcal{I}_{1/2}(p_\perp)W_r[p_\perp,Q_s] \tag{2.45}$$

where integrating $\mathcal{I}_{1/2}(p_\perp)$ as above, one can find the total result for the invariant yield of the second stage of BMSS scenario,

$$\frac{1}{S_\perp}\frac{\mathrm{d}N_\gamma}{\mathrm{d}^2p_\perp \mathrm{d}y} = \frac{10}{3\pi^4}\frac{\alpha_e\,\kappa_g}{2^{5/4}\sqrt{\pi}}\,f_0\,\frac{\sigma_0}{Q_s}\,W_r[p_\perp-Q_s]\,\frac{Q_s^2}{p_\perp^2} \times G^{2,2}_{2,3}\left(\frac{p_\perp^2}{2\sigma^2(\tau)}\middle|\begin{matrix}1,\frac{7}{4}\\ \frac{5}{4},\frac{5}{4},0\end{matrix}\right)\Bigg|_{\tau_1}^{\tau_2} \tag{2.46}$$

To find a simplified version of the rate for the kinematic window of interest, we expand in terms of $\sigma_0/p_\perp$ and substitute $\tilde{\tau}_1 = \alpha_s^{3/2}$ and $\tilde{\tau}_2 = \alpha_s^{5/2}$ find eq. (2.43), namely

$$\frac{1}{S_\perp}\frac{\mathrm{d}N_\gamma}{\mathrm{d}^2p_\perp \mathrm{d}y} = \sqrt{2\,\pi}\frac{20}{9\pi^4}\alpha_e\,\kappa_g\,f_0\,\frac{\sigma_0}{Q_s}\,\frac{Q_s^2}{p_\perp^2} \times W_r[p_\perp-Q_s]\,\left(\alpha_s^{-1/2}-1\right) \tag{2.47}$$

Just as with stage (i), this yield is divergent at low-$p_\perp$ and to be able to find the total yield, one has to integrate eq. (2.46). We find the expression

$$\frac{1}{S_\perp\,Q_S^2}\frac{\mathrm{d}N_\gamma}{\mathrm{d}y}\bigg|_{p_\perp<Q_s} = \frac{20}{3\pi^3}\frac{\alpha_e\,\kappa_g}{2^{3/4}\sqrt{\pi}}\,f_0\,\left(\frac{\sigma_0}{Q_s}\right)^{5/2} \times G^{2,3}_{3,4}\left(\frac{1}{2\,\sigma^2(\tau)}\middle|\begin{matrix}1,\frac{7}{4},\frac{7}{4}\\ \frac{5}{2},\frac{5}{2},0,\frac{3}{4}\end{matrix}\right)\Bigg|_{\tau_1}^{\tau_2}. \tag{2.48}$$

Fro which, once again, we can confirm the parametrical results from [35] by expanding in terms of σ_0/Q_s, as in eq. (2.49)

In the weak coupling limit, the system stays in (ii) a parametrically long time, which naturally leads to a higher yield than the stage (i). Here, as in the first stage, the dependence on the c_2/c_1 ratio is also slow and, since we expect these coefficients to be of order $\mathcal{O}(1)$, it will be taken to be unity.

The known result for the total yield can be found by again expanding in σ_0/Q_s up to lowest order. Applying the matching from eq. (2.38) we get

$$\frac{1}{S_\perp\,Q_S^2}\frac{\mathrm{d}N_\gamma}{\mathrm{d}y}\bigg|_{p_\perp<Q_s} = \sqrt{\frac{\pi}{2}}\frac{40}{9\,\pi^3}\alpha_e\,\mathcal{L}\,\kappa_g\,\kappa_q\,\left(\alpha_s^{-1/2}-1\right) \tag{2.49}$$

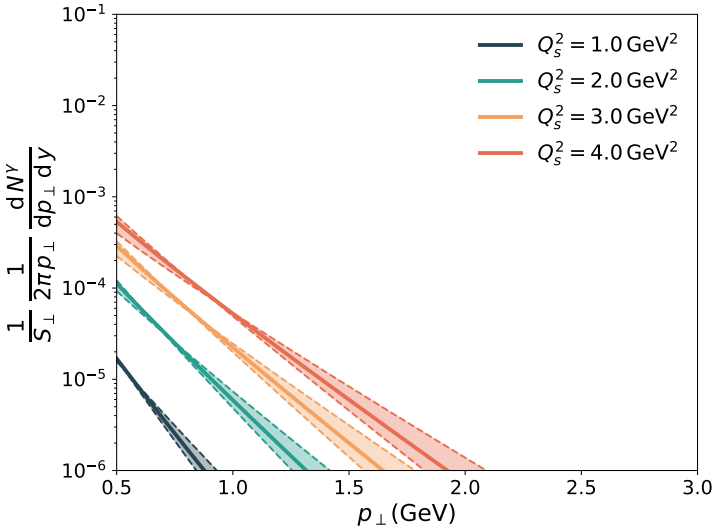

FIGURE 2.5: Photon invariant yield from the first stage of the Glasma for different values of Q_s^2. The error bands correspond to a factor of 2 variations of the anisotropy parameter,σ_0.

This result is identical to the one found the previous estimate [35]. The yield for photons with $p_\perp > Q_s$ can be found by integrating eq. (2.43),

$$\frac{1}{S_\perp Q_S^2}\frac{\mathrm{d}N_\gamma}{\mathrm{d}y}\bigg|_{p_\perp > Q_s} = \sqrt{\frac{\pi}{2}}\frac{80}{9\pi^3}\alpha_e\,\mathcal{L}\,\kappa_g\,f_0\,\frac{\sigma_0}{Q_s}\chi_r\,\left(\alpha_s^{-1/2}-1\right) \tag{2.50}$$

where χ_r was defined in eq. (2.40). Once again, it can be observed that the total yield exhibits independence to the fit parameters, just as in stage (i).

2.2.5 Glasma, Stage 3

During this stage, soft gluons take over the number density. The beginning of this stage is at time parametrically larger than the relaxation time, $\tau_2 > \tau_{\mathrm{rel}}$, which means that soft gluons modes have thermalized already. Therefore, the distribution can be calculated using the rapidity integrated thermal rate (see sec. 2.2.2), which can be further integrated in time to find the invariant yield,

$$\frac{1}{S_\perp}\frac{\mathrm{d}N_\gamma}{\mathrm{d}^2p_\perp\mathrm{d}y} = \frac{5}{9}\frac{\alpha\,\alpha_S}{\pi^2}\,\mathcal{L}\int_{\tau_2}^{\tau_{th}}\mathrm{d}\tau\,\tau\,T^2(\tau)K_0(p_\perp/T(\tau))\,. \tag{2.51}$$

In this stage, the temperature of the soft gluon bath increases linearly in time, and can be parametrized as

$$T = c_T\,\alpha_s^3\,Q_s^2\,\tau \tag{2.52}$$

Substituting the time parameter τ in the thermal rate integral, we get

$$\frac{1}{S_\perp}\frac{\mathrm{d}N_\gamma}{\mathrm{d}^2p_\perp\mathrm{d}y} = \frac{5}{9}\frac{\alpha\,\alpha_S^{-5}}{\pi^2 c_T^2}\frac{\mathcal{L}}{Q^4}\int_{T_2}^{T_{th}}\mathrm{d}T\,T^3\,K_0(p_\perp/T)\,. \tag{2.53}$$

Once again it is important to notice that the parametrisation used in this equation works only for values of the transverse momentum such that $p_\perp \gtrsim T$. However, for the kinematic window of interest, $p_\perp \geq 1\,\mathrm{GeV}$, it is also parametrically satisfied that $p_\perp > T_{th}$, which means that the rate can be approximated using the

	Centrality	N_p	$S_\perp\,(\mathrm{fm}^2)$	$Q_s^2\,(\mathrm{GeV}^2)$	$c_{eq}\,c_T^{3/4}$
PHENIX 200GeV	0-5%	353.0 ± 10.0	143.3 ± 2.7	2.00 ± 0.04	0.306 ± 0.005
	0-20%	277.5 ± 6.5	122.1 ± 1.9	1.67 ± 0.02	0.318 ± 0.006
	20-40%	135.5 ± 7.0	75.7 ± 2.6	1.12 ± 0.04	0.343 ± 0.008
ALICE 2.76 TeV	0-5%	383.5 ± 1.9	155.8 ± 0.5	3.60 ± 0.01	0.278 ± 0.004
	0-20%	307.2 ± 2.6	135.6 ± 0.7	2.90 ± 0.02	0.289 ± 0.004
	20-40%	160.3 ± 2.7	87.1 ± 1.0	1.81 ± 0.02	0.321 ± 0.006

TABLE 2.1: Relevant parameter fixing for diverse centrality classes in RHIC and LHC . For details on the fixing process see text and ref. [35]

asymptotic form

$$K_0(x) \sim \sqrt{\frac{\pi}{2\,x}}\,e^{-x} \quad \text{for} \quad x \gg 1\,. \tag{2.54}$$

Throughout this stage the temperature rises, which makes the assumption safer, since $T < T_{th} < p_\perp$. In the next section we will show that for the photon kinematic window and for realistic parameters this is always the case. Using this approximation, the integral for the photon invariant yield in the third stage can be found to be

$$\begin{aligned}\frac{1}{S_\perp}\frac{\mathrm{d}N_\gamma}{\mathrm{d}^2p_\perp \mathrm{d}y} =& \sqrt{\frac{\pi}{2}}\frac{5}{9}\frac{\alpha\,\alpha_S^{-5}}{\pi^2 c_T^2}\frac{p_\perp^4}{Q^4}\frac{32}{945}\,\mathcal{L}\left(\sqrt{\pi}\mathrm{erf}\left(\sqrt{\frac{p_\perp}{T}}\right)\right. \\ &\left. + \sqrt{\frac{T}{p_\perp}}e^{-\frac{p}{T}}\left(1 - \frac{1}{2}\frac{T}{p_\perp} + \frac{3}{4}\frac{T^2}{p_\perp^2} - \frac{15}{8}\frac{T^3}{p_\perp^3} + \frac{105}{16}\frac{T^4}{p_\perp^4}\right)\right)\Bigg|_{T_2}^{T_{th}}\end{aligned} \tag{2.55}$$

2.3 Parametrical fixing and comparison

This model depends strongly in a collection of parameters which describe the non-equilibrium dynamics of the BMSS scenario. To partially alleviate the arbitrariness of picking these parameters, one can use a phenomenological matching to pin down some of these parameters. The first coefficient to fix is the semi-hard scale, Q_s, from which all the BMSS dynamics is dependent. Itcan be found in terms of the energy and N_{part} using IP-Glasma model [148–151]. The IP-Glasma model combines the IP-Sat model [111, 152] with the Glauber model dependence on the geometry of the system [153]. Since only the mixed quantity $\langle S_\perp\,Q_s^2\rangle \equiv \int d^2\boldsymbol{x}_\perp Q_s(\boldsymbol{x}_\perp, \sqrt{s})$ can be calculated in terms of N_{part}, we will approximate the transverse average $Q_s(x, N_{part})$ by using

$$Q_s(x, N_{part}) = \frac{\langle S_\perp\,Q_s^2\rangle}{\langle S_\perp\rangle} \tag{2.56}$$

where $\langle S_\perp\rangle$ is calculated using the Glauber model. We have adjusted the overall normalization to a reference $Q_s^2 = 2\,\mathrm{GeV}$ for the highest centrality class, $0-5\%$, with $N_{part} = 353$. This can be done because we lack a first-principles determination of the hard scale in the Glasma, which makes it possible to vary the definition while keeping in mind it should be a *semihard* scale.

The next step is to relate the coefficients c_{eq} and c_T, used in secs. 2.1 and 2.2.2 to measured quantities. For this the entropy per unit rapidity of QGP was matched the entropy of produced charged hadrons.For an ideally expanding fluid, entropy

is conserved, and one can perform the matching at thermalization time and temperature. The calculation is given in ref. [35], and results in the expression

$$c_{eq}\, c_T^{3/4} = \left[\frac{45}{148\pi^2} k_{S/N} \alpha^{7/5} \frac{N_{part}}{Q_s^2\, S_\perp} \frac{2}{N_{part}} \frac{\mathrm{d}N_{ch}}{\mathrm{d}y}\right]^{1/4} . \tag{2.57}$$

Here, the experimental input is the multiplicity of charged hadrons per unit rapidity, $\mathrm{d}N_{ch}/\mathrm{d}y$, in terms of N_{part}, given in ref. [154–156]. The parameter $k_{S/N}$, is the proportionality constant that links total entropy of the hadronic phase with the measured multiplicity of charged hadrons. We will adopt the value $k_{S/N} = 7.2$ which has been extracted from particle spectra and particle interferometry [157, 158]. We have adopted a running coupling parametrisation given by

$$\alpha_s(Q_s) = \frac{12\pi}{(33 - 2N_f) \log\left(\frac{Q_s^2}{\Lambda_{QCD}^2}\right)} \tag{2.58}$$

where we take $\Lambda_{QCD} = 0.2\,\mathrm{GeV}$, and the number of in-medium quarks is taken to be $N_f = 3$. Using this data we get the phenomenologically interesting parameters listed in table 2.1, where Q_s, $S_\perp$, and $c_{eq}\, c_T^{3/4}$ are given for different centrality classes, that is N_{part}, for RHIC and LHC energies. The quantities c_{eq} and c_T can only be fixed together, as specified in eq. (2.57). However, the thermalization temperature coefficient was found in ref. [142] up to logarithmic accuracy to be $c_T = 0.18$, and will vary it over an overall factor of 2.

An important caveat is that, using the expressions for τ_{th} and T_{th}, as well for the temperature evolution in a Bjorken expansion, one can find also a phenomenological matching for τ_c, which is given by

$$\tau_c = \frac{45}{74\pi^2} k_{S/N} \frac{1}{S_\perp} \frac{\mathrm{d}N_{ch}}{\mathrm{d}\eta} \frac{1}{T_c} . \tag{2.59}$$

This renders τ_c insensitive to Q_s and α_s, while dependent uniquely on the number of participants in the collisions, N_{part}. Because, for $N_{part} \lesssim 150$ we find that $\tau_c \lesssim \tau_{eq}$ we will only take on account events which lie inside the $0 - 20\%$ centrality range.

2.4 Results

To be able to properly perform comparisons of the model, all the sources for direct photons have to be accounted for. That is, apart from the BMSS and QGP radiation, one should include also thermally produced photons from a hadronic gas (HG) after the hadronization of the QGP phase. Photons produced by hard scattering and annihilation of the participating partons, referred normally as *prompt photons* have to be also included. The total direct invariant yield is then given by

$$\frac{\mathrm{d}N}{\mathrm{d}^2p_\perp \mathrm{d}y} = T_{AA} \frac{\mathrm{d}\sigma^{pp}}{\mathrm{d}^2p_\perp \mathrm{d}y} + K^\gamma \left[\frac{\mathrm{d}N^{gl}}{\mathrm{d}^2p_\perp \mathrm{d}y} + \frac{\mathrm{d}N^{th}}{\mathrm{d}^2p_\perp \mathrm{d}y}\right] . \tag{2.60}$$

where the hadronic the σ^{pp} label stands for prompt photon (pQCD) cross section [159], which will be scaled by a centrality dependent factor, T_{AA}, with $A = \mathrm{Au}, \mathrm{Pb}$. This can be calculated directly from the Glauber model. For the extension of the scaled pQCD to lower $p_\perp$ values, which is needed to sum this contribution to the

in-medium spectra, we have used the following functional form,

$$\frac{\mathrm{d}\sigma^{pp}}{\mathrm{d}^2 p_\perp \mathrm{d}y} = A_{pp}\left(1+\frac{p_\perp^2}{P_0}\right)^{-n} \tag{2.61}$$

which was used by PHENIX to fit the $p+p$ results in [160]. In eq. (2.60), hadronic bremsstrahlung of photons is included as a thermal contribution, and summed over the QGP rate. In this work we included meson and baryonic rates, the $\pi\,\pi$ bremsstrahlung rate, as well as reactions of the $\pi\,\rho\,\omega$ meson system. [161–163]. This is calculated naively for a Bjorken expanding system by switching from the QGP to the HG rate at a freezout temperature of $154\,\mathrm{MeV}$. A mild variation of this parameter did not affect the result.

To account for the Glasma radiation, we have used $\sigma_0/Q_s = 0.15$ where a variation of 50% has been included as error bands. It can be seen parametrically from eqs. (2.34) and (2.43) that the dependence on this parameter is parametrically slow. The suppression parameter is chosen to be $r = 0.35$ for a better fit to data. It is always important to note that even when both r and σ_0 are parameters physically motivated by ab-initio calculations, the particular value is picked as free parameter with soft constraints. This is indeed a source of systematic error in the model, but solving this issue with better simulations is outside of the scope of this work. Besides the gluon fitting parameters, other sources of uncertainty come from the thermalization time and temperature. These quantities vary with the constants c_T and c_{eq}. As mentioned before, the product $c_{eq}\,c_T^{3/4}$ has been fixed together using eq. (2.57), which still leaves freedom to vary c_T around the value calculated in ref. [142]. This will have an effect on the thermal invariant yield per transverse area since it is given parametrically by $\tau_{th}^2\,T_{th}^2$ parametrically, which means that after fixing it still depends polynomially on $c_T^{-10/3}$. For changes of a factor of 2 in c_T, that still amounts for an extra $\mathcal{O}(1)$ coefficient when one takes on account the changes in the temperature. The Glasma stages (i) and (ii) are also mildly sensitive to the coefficients c_0, c_1 and c_2, which can result in the rates picking up also extra order $\mathcal{O}(1)$ factors. Nevertheless, such fine tuning of the transition times is not the scope of this discussion.

We have also included the fitting prefactors K^γ to account for the total uncertainties of the parameters which may amount for overall normalization discrepancies, such as the initial volume and its evolution, as well as uncertainties in the spatial dependence of initial energy density and subsequent translation to the thermalization temperature and time. It can be seen in eqs. (2.34), (2.43), as well as for the thermal rate, eq. (2.23), that these rates could in principle be sensitive to the inclusion of fluctuations of the spatial profile of Q_s. This factor is found to be $K^\gamma = 2.8$. The result of this fitting can be seen in fig. 2.7, where we get fair agreement, particularly for ALICE data.

In the previous estimates [35], the difference between the thermal and Glasma total yields was found to be of order $\mathcal{O}(1)$ In this work we confirm analytically these results (see sec.2.2) from the fit, regardless of the choosing of parameters, once the matching of the constants has been enforced. Nonetheless, in the $p_\perp$ differential result, a dominant structure was found for Glasma photons. We want to make an emphasis on the fact that this structure is a signal from the thermalization process. Although its particular shape is model dependent as it strongly depends on the quark distribution, a more refined calculation from kinetic theory would give a reshuffling, or stretching of this yields, giving a more exponential look, while keeping the same order of magnitude around Q_s, since the small angle approximation is

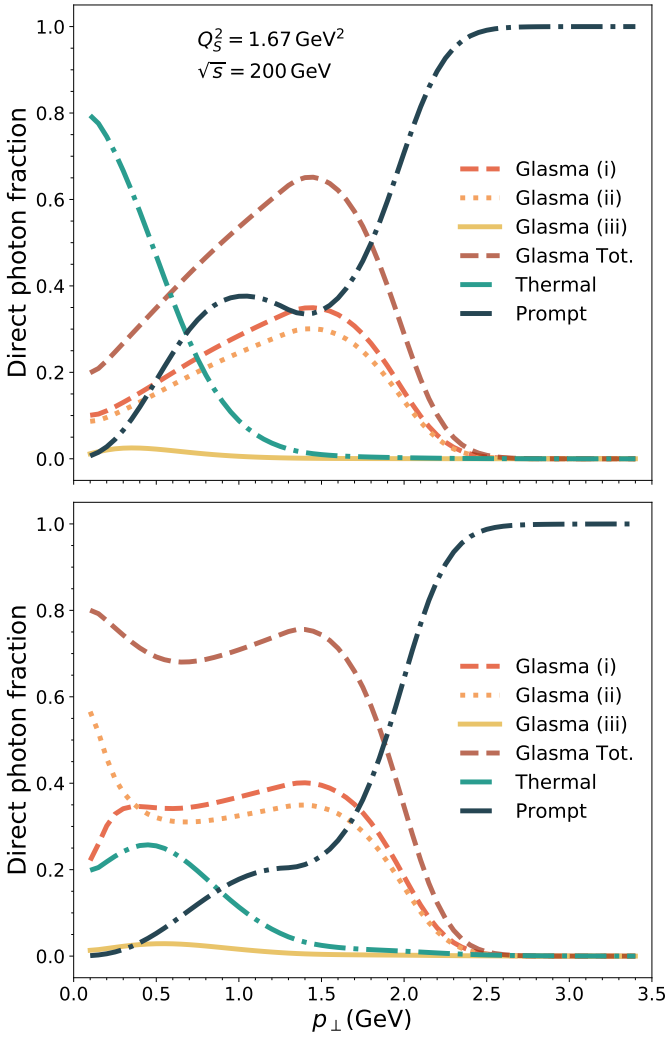

FIGURE 2.6: Fraction for each contribution to the total direct photon multiplicity at RHIC energy, $\sqrt{s} = 200\,\mathrm{GeV}$, for $0 - 20\%$ centrality class, and a saturation scale of $Q_s^2 = 1.67\,\mathrm{GeV}^2$.*Up*: LL fractions for the Glasma and QGP multiplicities. *Down*: Glasma and QGP multiplicities taken from their LO rates.

a good approximation for the hard scatterings of the $2 \leftrightarrow 2$ processes in the Glasma.

For the LL results, this structure is dominant at higher energies, and it is peaked at $p_\perp \sim Q_s$, while the thermal case strongly dominates at small energies, as can be seen in fig. 2.6. However, once enhanced to the LO rate this is not the case, as Glasma photons completely dominate over the thermal rates. In a realistic simulation, this may become less apparent, as the radial flow from the hydrodynamical expansion will blue-shift the thermal spectrum [164], changing its slope, as well as enhancing the number of photons in this kinematic window.

Apart from a clear-cut comparison between the stages of the evolution of the fireball, the LO version of fig 2.6 allows us also to see the BMSS scenario in action, specifically from the curves for the first and second stages of the Glasma. The direct photon fraction for the first stage exhibits, in the very low-$p_\perp$ limit, a dip compared to its second stage counterpart. This comes directly from the screening mass time-dependence given in eq. (2.41). We can see that the rise of soft gluons impacts the system such that it enhances the production of low-$p_\perp$ photons. In a

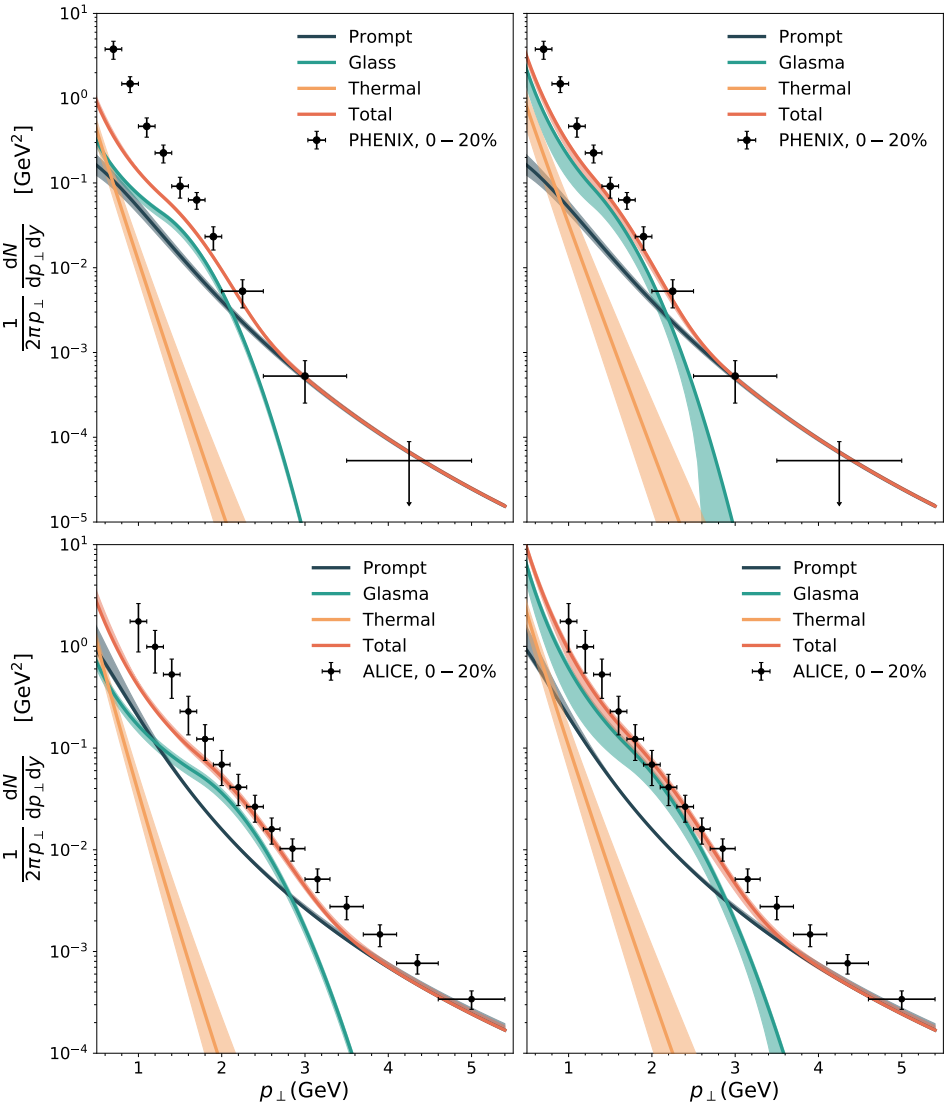

FIGURE 2.7: Comparison of the model BMSS+thermal to experimental data from RHIC [160] and LHC [165]. *Upper left and right*: Comparison of the model with the yield from the $2 \leftrightarrow 2$ and collinearly enhanced rates, respectively, at $\sqrt{s} = 200\,\mathrm{GeV}$, and $Q_s^2 = 1.67\,\mathrm{GeV}^2$. *Lower left and right*: Comparison of the model with the yield from the $2 \leftrightarrow 2$ and collinearly enhanced rates, respectively, at $\sqrt{s} = 2.76\,\mathrm{TeV}$, and $Q_s^2 = 2.89\,\mathrm{GeV}^2$.

violently evolving Glasma, the overoccupied gluons enhance the number of scatterings, which gives the conditions for photon production.

As it can be seen in fig. 2.7 and was stated above, in this model the direct photon contribution is dominated by the Glasma, while the thermal contribution is relevant only in the deeper infrared part of the kinematic window $p_\perp \lesssim Q_s$. This happens because of the BMSS estimate of τ_{th} and T_{th}, which gives a late and quite *colder* thermalization, both in RHIC. One has to remember that in more refined calculations, this may change softly, since the BMSS scenario poses as a upper bound for the thermalization time. Nonetheless, the calculation here serves as a proof of concept, showing that photons are extremely relevant and may serve a as extra source which may help solve the *photon puzzle*. This has to be contrasted, of course, with current phenomenological ideas, regarding the extra photons to come from

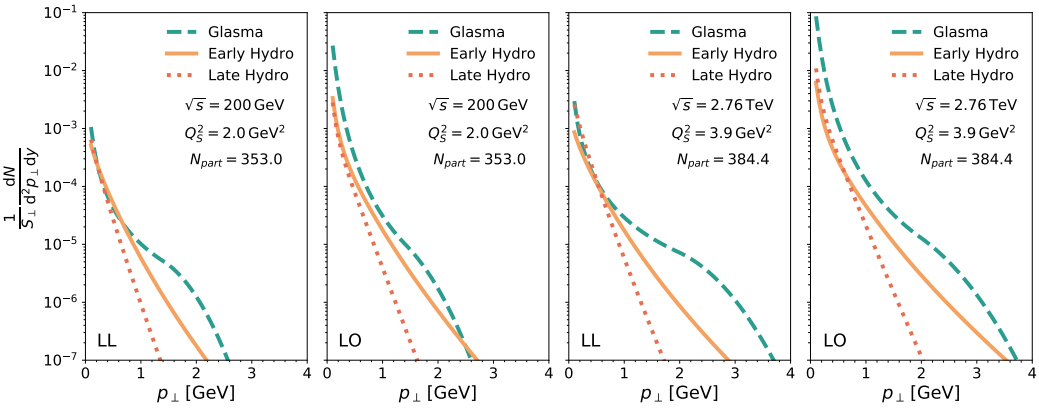

FIGURE 2.8: Comparison of BMSS scenario with early thermalization at $0-5\%$ centrality class for RHIC and LHC energies. *Leftmost*: small angle approximation (LL) comparison at $sqrts = 200\,\text{GeV}$.*Center left*: LO results at RHIC. The infrared enhancement from section 2.2.1 makes the BMSS scenario dominant. *Center right*: LL invariant yields at $sqrts = 2.76\,\text{TeV}$. *Right*: LO results at RHIC. The infrared enhancement from section 2.2.1 makes the BMSS scenario completely dominant in the kinetic window of interest.

later times [124]. A comparison as such stresses the need for higher correlation functions, especially those which are more sensitive to the space time evolution. Photon correlations, i.e. Hanbury-Brown-Twiss correlations [166–168], may be able to help us discriminate between the two different scenarios.

Aside from the comparisons with the invariant yield from fig.2.7, we want to compare also to the total number of photons, in a way which total normalization drops off. For this, we will use the total yield per unit rapidity, taken as a sum of all momenta, with an infrared cutoff of p_0. This quantity in the language of this work is given by

$$\frac{\mathrm{d}N_{p_0}}{\mathrm{d}y} \equiv 2\,\pi \int_{p_0}^{\infty} \mathrm{d}\,p_\perp\,p_\perp \frac{\mathrm{d}N_\gamma}{\mathrm{d}^2p_\perp \mathrm{d}y} \tag{2.62}$$

and will be normalized by its minimum bias counterpart. For this observable at PHENIX (see fig. 2.9) we observe excellent agreement with the data except for deviations from this trend at $p_0 = 1.2\text{GeV}$. Furthermore, we checked numerically that for the LO case this observable is completely independent of the choosing r, within reasonable ranges given softly by constrain of the data from [160, 165].

2.4.1 Comparison to Early Hydro

For the phenomenologically matched system the *bottom-up* scenario gives a thermalization time and temperature in the order of $\tau_{th} \sim 2\,\text{fm}$ amd $T_{th} \sim 0.2\,\text{GeV}$. This contrasts with how normally hydrodynamical simulations are initialized, with initial times down to $\tau_i \sim 0.4 - 0.6\,\text{fm}$ and average initial temperatures as high as $\langle T \rangle_i \sim 0.4 - 0.6\text{GeV}$. In this section we will compare the Glasma spectrum with a system in which thermalization occurs at $Q_s\,\tau_0 \sim 1$. For this comparison, we will call *Early thermalization* the integrated QGP rate from τ_0 until τ_{th}, for a Bjorken expanding fireball. For the results of this section, the hadronic bremsstrahlung is not taken on account, since for this discussion one is mostly interested in what happens before the system arrives to the freeze-out temperature.

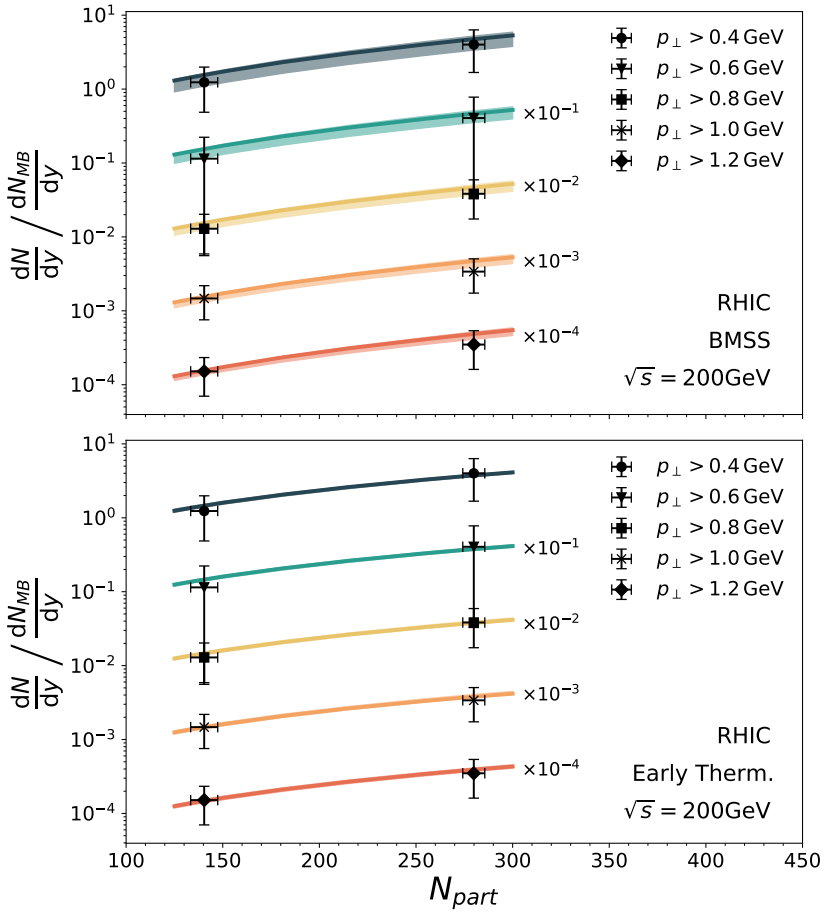

FIGURE 2.9: Comparison of the total yield of the Prompt+BMSS+Late Thermal (*up*) and Prompt+Early+Late Thermal (*down*) scenarios to experimental data in terms of N_{part} [160]. Here, the total yield is normalized by its minimum bias value ($N_{part} = 106 \pm 5.0$).

In fig. 2.8 the reader can see a comparison of the early thermalization scenario with its Glasma counterpart. As a reference, we also give a curve for the late contribution from the thermal QGP. It is immediately apparent that in all results, the structure at $p_\perp \sim Q_s$ dominates, and it is higher than the early hydro contribution. We don't expect the slope of the latter contribution to change significantly with a full-fledged simulation, since the initial conditions normally assigned require the pressure gradients to build up to start the expansion, which will result in the eventual blueshift of the spectrum.

In the case of the LL results, the three contributions deliver similar results for the total photon yield, eq. (2.62), as they have similar dependences at the infrared level. This is, however, not the case for the collinearly enhanced result (LO) in which, even though the early hydro and Glasma contributions are still of the same order, the Glasma dominates. This case is particularly strong for higher energies, in which the results of this work seem to suggest that thermalizing matter is more relevant for the production of photons. In a higher energy system like Pb-Pb at $\sqrt{s} = 2,76\,\text{TeV}$ in ALICE, hard gluons are generally speaking, harder. Apart from increasing the overall order of the radiation, this means that all the system will be shifted towards higher energies, which allows for the near-collinear radiation to be greatly enhanced for the Glasma.

On a final note, it is commonly argued [164, 169] that the hydro expansion has to be initialized early on for the pressure gradients to build up, which will cause the blueshift expected from radial flow, as well to account for the transverse anisotropy coefficients, v_n. However, this assumption lays on top of a specific election of initial conditions for the evolution, starting from an initial energy density, without any pre-equilibrium evolution. For a better understanding, a study of the fluctuations of the non-thermal evolution transverse pressure has to be done to start shedding light into this matter. Furthermore, a comprehensive matching of the resulting effective kinetic theory would give the correct initial conditions for hydro evolution, which, conceivably, would start from non-zero transverse velocities. Thus, the assumption that a late thermalization scenario can't account for the anisotropy coefficients has to be checked via real-time lattice simulations, as it may not be correct.

2.5 Conclusions

In this work, we derived the photon invariant yield from the Glasma using the *bottom-up* thermalization framework. My results expand on the parametric estimates for the total photon yields from ref. [35] by obtaining analytically a transverse momentum resolution for the leading log spectra. In this scenario, a sizeable contribution coming from early times was found, which dominates the total direct photon spectra for $p_\perp \sim Q_s$ and realistic parameters at LHC and RHIC energies. The LL results fail, however, to properly describe the low $p_\perp$ window of the measured spectra. The aforementioned results where improved by using the complete LO thermal rates, as well as introducing a bremsstrahlung modification ansatz for the non-equilibrium rates. With this ansatz, the non-thermal contribution becomes mostly dominant and a fair comparison to data can be found up to the overall normalization. To account for this uncertainty an order $\mathcal{O}(1)$ parameter is introduced.

Apart from the overall normalization, this model is very sensitive to the specific shape of the quark distribution. This uncertainty is just an extension of weak coupling methods to assess collective QCD at RHIC and LHC energies. Nonetheless, this simple model serves as a proof of concept to challenge the idea that pre-equilibrium photon production is suppressed. Nonetheless, as was stated in the text, it was found that the total number of photons is affected only by the assumption of scaling in the quark distribution and not by the fit parameters σ_0 and r, and thus both remain free -yet physically motivated- parameters. This issue may be solved by more thorough calculations, in the context of classical statistical simulations or kinetic theory [22, 170, 171]. Even if weak coupling assumption has to be kept, this model can be improved by directly fitting the quark distributions from such more involved calculations.

As it was stated before, the inclusion of anisotropies is beyond the scope of this work, as we have taken all the distributions to be isotropic and homogeneous in the transverse plane. This approximation, while useful for building this model, relies only on the assumption that flow is suppressed at early times, and its accuracy is not clear in the extreme non-equilibrium setting of the early stages of a Heavy Ion collision. The inclusion of such anisotropies can in principle be added to a simplified model like this one, and lies within the scope of future investigations.

Even though the BMSS scenario poses as an estimate for the upper limit of the thermalization time, we would like to argue that this work presents theoretical evidence that pre-equilibrium photons may be essential to fully understand the photon spectra recovered from heavy ion collisions. These results, as well as other

previous works [126, 128, 172, 173], seem to suggest that the *direct photon puzzle* may be solvable by the thorough and spatially resolved calculation of non-thermally sourced photons.

Chapter 3

Probing space-time evolution using higher correlations

In the last chapter, a proof of concept calculation of non-equilibrium photons was presented, which shows that photons from the pre-equilibrium stage show a sizeable contribution, comparable to thermal radiation. Nonetheless, with the current experimental photon invariant yield it is very hard to discriminate between different scenario and models. To be able to untangle the space-time evolution of the yield, we need extra observable sensitive to size of the source of the photons. Interferometry, called in this context *femtoscopy*, of the particles produced is needed as a sensitive tool to address this problem. We will use the Hanbury-Brown-Twiss (HBT) correlations, which are the only known way how to directly extract space-time information from the particles measured in HICs experiments. HBT correlations were originally created to measure the radii of stars using the interference of the incoming photons. Additionally, HBT correlations have been used extensively across physics, from cold atom experiments [174, 175], to being used to succesfully describe the sources of pion production at the freezout surface [168, 176, 177] in HICs experiments. I would like to stress here once again the importance of photon correlations. While pion femtoscopy has been a succesful research program, pions are mostly produced at freeze-out, and therefore the resulting size measurement will indicate only the size of the freeze-out surface. Photons, on the other hand, are virtually insensitive to rescatterings and in-medium effects in the fireball, which makes the photon HBT sensitive to the whole evolution. This comes with a caveat, as in collision experiments we cannot access a time-dependent description of the photon signal, as photon yields and correlators can be measured as only final states in the detector [178, 179]. Nevertheless, every contribution to a HBT correlation is weighed by its yield. Therefore, relevance to the total spectrum can be used to compare to the final extracted HBT radii. This means that the photon radii can be used to contrast different models and scenarios where t . These measurement can then be used to give us additional understanding, and even help discriminate models in the long run.

The work presented in this chapter was done in collaboration with Jürgen Berges, Klaus Reygers, Nicole Löher and Aleksas Mazeliauskas, where a manuscript is currently in preparation. The structure of this chapter goes as follows. In the next section I will sketch a derivation of the HBT for photons following a quantum field theoretical notation and language. I will proceed to present results for a two scenarios, the homogenous BMSS model presented in the last chapter, as well for a Glasma-Hydro hybrid model. The latter is mixture between the BMSS and early hydro cases of sec. 4.5 which stands for a "best of both worlds" scheme from which, in the absence of a pre-equilibrium evolution of anisotropies, we can get both a pre-equilibrium enhancement and the pressure gradients needed to account for

anisotropies.

3.1 Hanbury-Brown-Twiss Correlations

Quantum statistical effects were used to understand the spacetime distribution of particle sources in the context of astrophysics [180, 181]. Hanbury-Brown and Twiss proposed a modified Michelson interferometer that had as a goal to use electromagnetic radiation to give an independent measurement the radii of stars. The principle that governs HBT interferometry is base on interference from quantum statistics. Picture a photon source extending over some region of space-time with a radius R. To simplify the argument, we assume spherical symmetry for this source. Given a simultaneous measurement of two photons with position and momentum x_1, p_1 and x_2, p_2, repectively, we know that if we define, their position and momentum space separation are $\delta x^2 = (x_1 - x_2)^2$ and $\delta p^2 = (p_1 - p_2)^2$, respectively. When the photon pair is far away from each other in phase space, it will behave as classical particles, with Maxwell-Boltzmann statistics [182]. This happens when

$$\delta x\, \delta p \gg 2\pi\hbar\,, \tag{3.1}$$

Here, $\hbar$ is kept explicit to make the quantum nature of the phenomenon apparent. Quantum mechanical effects start to be important when the two particles are close together in phase space. This means that for a phase space separation that satisfies

$$\delta x\, \delta p \lesssim 2\pi\hbar\,. \tag{3.2}$$

quantum statistics will take over, and the Bose enhancement [1] of photon correlations can be observed, thus deviating from classicality. Since in the source is limited by a spatial extent, the maximum separation one can obtain is $\delta x = 2R$, which means that if we chose to keep the two photons close in momentum space, namely smaller than $\tilde{q} = \pi\hbar/R$, we would be able to extract the radius from such a measurement. In the context of HIC experiments, we are interested in finding the spatial extension of the photon source in the fireball. For this, we will be using the two-particle distribution function,

$$E_{\boldsymbol{p}_1} E_{\boldsymbol{p}_2} \frac{\mathrm{d}N}{\mathrm{d}^3 p_1 \mathrm{d}^3 p_2} = E_{\boldsymbol{p}_1}\, E_{\boldsymbol{p}_2} \sum_{\lambda_1,\lambda_2} \langle a^\dagger_{\boldsymbol{p}_1,\lambda_1} a^\dagger_{\boldsymbol{p}_2,\lambda_2} a_{\boldsymbol{p}_2,\lambda_2} a_{\boldsymbol{p}_1,\lambda_1} \rangle\,. \tag{3.3}$$

which can be expressed in terms of asymptotic states, i.e. creation and annihilation operators of a gauge field. Here, $\boldsymbol{p}_n$ and λ_n are, respectively, the spatial momenta of the detected photons and polarization mode of the nth photon. The reader will notice that this is just the density operator for a general two-photon state. Additionally, in a field theoretical language, this can be computed generally from a four-point correlator of gauge fields in momentum space, for equal in- and outgoing momenta. Following the argument on the onset of quantum statistics give above, one can then normalize eq. (3.9) with the single photon distributions and define the HBT correlator,

[1] In the case of fermion interferometry, fermions are pushed together in phase space, and will become anticorrelated.

$$C(\boldsymbol{p}_1, \boldsymbol{p}_2) = \frac{E_{\boldsymbol{p}_1} E_{\boldsymbol{p}_2} \dfrac{\mathrm{d}N}{\mathrm{d}^3 p_1 \mathrm{d}^3 p_2}}{E_{\boldsymbol{p}_1} \dfrac{\mathrm{d}N}{\mathrm{d}^3 p_1} E_{\boldsymbol{p}_2} \dfrac{\mathrm{d}N}{\mathrm{d}^3 p_2}} \,. \tag{3.4}$$

This will be the observable we will be focusing on, since deviation from unity for this quantity signals quantum correlation effects, from which we will be extracting the spatial information. The denominator of eq. (3.4), which is the product of the invariant yield of both photons, can be expressed with asymptotic states as follows,

$$E_{\boldsymbol{p}} \frac{\mathrm{d}N}{\mathrm{d}^3 p} = E_{\boldsymbol{p}} \sum_{\lambda} \langle a^{\dagger}_{\boldsymbol{p},\lambda} a_{\boldsymbol{p},\lambda} \rangle \,. \tag{3.5}$$

We can further simplify eq. (3.4) by noting that one can split any full four-point function into connected and disconnected parts, and noting that for a dilute gas of particles, the photon-photon interaction vertex is very small. One can apply the *factorisation approximation*, and neglect the connected part,

$$\langle a^{\dagger}_{\boldsymbol{p}_1,\lambda_1} a^{\dagger}_{\boldsymbol{p}_2,\lambda_2} a_{\boldsymbol{p}_2,\lambda_2} a_{\boldsymbol{p}_1,\lambda_1} \rangle \sim 0 \,. \tag{3.6}$$

This approximation works since photon fields during a HIC are not highly occupied in-medium, and since the electromagnetic coupling is weak, higher correlations will be small compared to the two-point function thanks to the power counting. In other words, perturbation theory works on the photon sector, and that suppresses the creation of an effective photon-photon in-medium interactions. In this case, Wick's theorem is applicable and four-point (and higher) correlations can be constructed from two-point field correlation functions. In terms of the expectation value in Eq. 3.9, Wick's theorem states that

$$\begin{aligned} \langle a^{\dagger}_{\boldsymbol{p}_1,\lambda_1} a^{\dagger}_{\boldsymbol{p}_2,\lambda_2} a_{\boldsymbol{p}_2,\lambda_2} a_{\boldsymbol{p}_1,\lambda_1} \rangle \simeq & \langle a^{\dagger}_{\boldsymbol{p}_1,\lambda_1} a_{\boldsymbol{p}_1,\lambda_1} \rangle \langle a^{\dagger}_{\boldsymbol{p}_2,\lambda_2} a_{\boldsymbol{p}_2,\lambda_2} \rangle \\ & + \langle a^{\dagger}_{\boldsymbol{p}_1,\lambda_1} a_{\boldsymbol{p}_2,\lambda_2} \rangle \langle a^{\dagger}_{\boldsymbol{p}_2,\lambda_2} a_{\boldsymbol{p}_1,\lambda_1} \rangle \end{aligned} \tag{3.7}$$

where the correlator of two creation-annihilation operators can be related to the general density matrix element via the relationship

$$\rho\left(\boldsymbol{p}_1, \lambda_1, \boldsymbol{p}_2, \lambda_2\right) = \sqrt{E_{\boldsymbol{p}_1} E_{\boldsymbol{p}_2}} \, \langle a^{\dagger}_{\boldsymbol{p}_1,\lambda_1} a_{\boldsymbol{p}_2,\lambda_2} \rangle \,, \tag{3.8}$$

The off-diagonal element, which quantifies overlap of two photon states with momentum $\boldsymbol{p}_2$ an $\boldsymbol{p}_1$ vanishes exactly in the vacuum. However, in a medium this is not forbidden, and one can find in this contribution the truly interesting non-trivial behaviour for the $C(\boldsymbol{p}_1, \boldsymbol{p}_2)$ function. The two-photon correlation function can be expressed in terms of density matrix elements as follows

$$\begin{aligned} E_{\boldsymbol{p}_1} E_{\boldsymbol{p}_2} \frac{\mathrm{d}N}{\mathrm{d}^3 p_1 \mathrm{d}^3 p_2} = & \sum_{\lambda_1} \rho\left(\boldsymbol{p}_1, \lambda_1, \boldsymbol{p}_1, \lambda_1\right) \sum_{\lambda_2} \rho\left(\boldsymbol{p}_2, \lambda_2, \boldsymbol{p}_2, \lambda_2\right) \\ & + \sum_{\lambda_1, \lambda_2} \rho\left(\boldsymbol{p}_1, \lambda_1, \boldsymbol{p}_2, \lambda_2\right) \rho\left(\boldsymbol{p}_2, \lambda_2, \boldsymbol{p}_1, \lambda_1\right) \,. \end{aligned} \tag{3.9}$$

where, as expected, the diagonal elements constitute the one-particle distributions (3.5). We can get more insight on the density matrix elements by taking on account

the specifics of Quantum Electrodynamics (QED). For the Lorentz gauge ($\partial \cdot A = 0$), a free massless spin-1 field under the action of an external source follows the equation of motion

$$\partial^2 A_\mu(x) = J_\mu(x)\,. \tag{3.10}$$

where the evolution of the photon field is driven by the introduction of the chaotic classical source $J_\mu(x)$, which satisfies thanks to charge conservation, satisfies the appropriate Ward identity, $p_\mu\, J^\mu(\boldsymbol{p}) = 0$ in momentum space. A chaotic current is a superposition of an ensemble of elementary functions, or wave packages, emitting photons with random phases. It is known that for the presence of such a source, a photon field is generated in a coherent state,

$$|J\rangle = e^{-\bar{n}/2} \exp\left[\int \frac{\mathrm{d}^3 p}{(2\pi)^3}\frac{1}{2\,E_p}\sum_\lambda J_\mu(\boldsymbol{p})\,\varepsilon^\mu(\boldsymbol{p},\lambda)\,a^\dagger_{\boldsymbol{p},\lambda}\right]|0\rangle \tag{3.11}$$

where $e^{-\bar{n}/2} = \int \frac{\mathrm{d}p}{(2\pi)^3}\frac{1}{2\,E_p} J^*_\mu(\boldsymbol{p}) J^\mu(\boldsymbol{p})$ serves as the normalization of the state. The reader can refer to ref. [166] for a more involved discussion of these states. For this case, it was was proven by [167, 168] that these states exhibit the property that

$$a_{\boldsymbol{p},\lambda}|J\rangle = \mathrm{i}\, J_\mu(\boldsymbol{p})\,\varepsilon^\mu(\boldsymbol{p},\lambda)\,|J\rangle \tag{3.12}$$

from which the density matrix elements can be directly computed. Here, $\varepsilon^\mu(\boldsymbol{p},\lambda)$ stand for real and spacelike polarisation vectors[2]. From such considerations, it can be seen that a general density matrix element can be expressed in terms of the momentum space current, via eq. (3.12),

$$\begin{aligned}\rho(\boldsymbol{p}_1,\lambda_1,\boldsymbol{p}_2,\lambda_2) &= \sqrt{E_{\boldsymbol{p}_1}\,E_{\boldsymbol{p}_2}}\,\varepsilon^\mu(\boldsymbol{p}_1,\lambda_1)\,\varepsilon^\nu(\boldsymbol{p}_2,\lambda_2)\,\left\langle J^\dagger_\mu(\boldsymbol{p}_1) J_\nu(\boldsymbol{p}_2)\right\rangle \\ &\equiv \varepsilon^\mu(\boldsymbol{p}_1,\lambda_1)\,\varepsilon^\nu(\boldsymbol{p}_2,\lambda_2)\,S_{\mu\nu}(\boldsymbol{p}_1,\boldsymbol{p}_2)\end{aligned} \tag{3.14}$$

where we can finally see that the density matrix is directly related to the current-current correlator. Here, the expectation value symbol, $\langle\cdots\rangle$ stands for a trace over the coherent states, $|J\rangle$. We have also defined here the tensor structure,

$$\begin{aligned}\tilde{S}_{\mu\nu}(\boldsymbol{p}_1,\boldsymbol{p}_2) &= \sqrt{E_{\boldsymbol{p}_1}\,E_{\boldsymbol{p}_2}}\int \mathrm{d}^4x_1\,\mathrm{d}^4x_2\,e^{\mathrm{i}x_1\cdot p_1}\,e^{-\mathrm{i}x_2\cdot p_2}\,\langle J_\mu(x_1)\,J_\nu(x_2)\rangle \\ &= \int \mathrm{d}^4x\,e^{\mathrm{i}x\cdot q}\,S_{\mu\nu}(x,\boldsymbol{K})\end{aligned} \tag{3.15}$$

by rotating the spatial variables in the Fourier transform in to the average an relative position, that

$$\begin{aligned} x_1,\,x_2 \quad &\to x = (x_1+x_2)/2,\;\; y = x_1 - x_2 \\ p_1,\,p_2 \quad &\to K = (p_1+p_2)/2,\;\; q = p_1 - p_2\end{aligned} \tag{3.16}$$

[2]The polarisation vectors describe the transverse modes of the photon, $p_\mu\,\varepsilon^\mu(\boldsymbol{p},\lambda) = 0$ andthey are spacelike $\varepsilon_\mu(\boldsymbol{p},\lambda)\varepsilon^\mu(\boldsymbol{p},\lambda') = g_{\lambda\lambda'}$. One can use them to construct a polarization tensor,

$$\sum_\lambda \varepsilon^\mu(\boldsymbol{p},\lambda)\varepsilon^\nu(\boldsymbol{p},\lambda) = -g^{\mu\nu} - \frac{k^\mu k^\nu}{(k\cdot n)^2} + \frac{k^\mu n^\nu + n^\mu k^\nu}{k\cdot n}\,, \tag{3.13}$$

for an arbitrary timelike unitary vector n ($n^2 = 1$).

which will give us now two different transforms in terms of the relative and average momenta of the pair, $\tilde{S}_{\mu\nu}(\boldsymbol{p}_1, \boldsymbol{p}_2) = \tilde{S}_{\mu\nu}(\boldsymbol{q}, \boldsymbol{K})$. In eq. 3.15 we defined $S_{\mu\nu}(x, \boldsymbol{K})$ as the tensorial Wigner density of the source currents,

$$S_{\mu\nu}(x, \boldsymbol{K}) = \sqrt{E_{\boldsymbol{p}_1} E_{\boldsymbol{p}_2}} \int \mathrm{d}^4 y \, e^{\mathrm{i}y\cdot K} \left\langle J^\dagger_\mu \left(x + y/2\right) J_\nu \left(x - y/2\right) \right\rangle . \tag{3.17}$$

The vectorial nature of the currents, which make up for the spin physics expected from gauge fields is encoded on its tensor structure. This expression is useful from a field theoretical vantage, where the structure of the source currents is known. Nontheless, for a system in which photons are radiated chaotically, and only rates can be calculated, one has to average out spin effects. The first step to do this is to sum over polarizations, for which we can obtain a clear simplified expression for 1PD, by using eqs. (**??**) and (3.13)

$$E_{\boldsymbol{p}} \frac{\mathrm{d}N}{\mathrm{d}^3 p} = \sum_\lambda \rho(\boldsymbol{p}, \lambda, \boldsymbol{p}, \lambda) = S^\mu_\mu(0, \boldsymbol{p}) . \tag{3.18}$$

Following the same process and identities, the 2PD can be found, and it is given by eq. (3.9)after the sum of polarizations,

$$E_{\boldsymbol{p}_1} E_{\boldsymbol{p}_2} \frac{\mathrm{d}N}{\mathrm{d}^3 p_1 \mathrm{d}^3 p_2} = \left[S^\mu_\mu(0, \boldsymbol{p}_1) S^\nu_\nu(0, \boldsymbol{p}_2) + S^{\mu\nu}(\boldsymbol{q}, \boldsymbol{K}) S^*_{\nu\mu}(\boldsymbol{q}, \boldsymbol{K}) \right] . \tag{3.19}$$

Using eqs. (3.18) and (3.19), the HBT correlator is now simply given by

$$C(\boldsymbol{p}_1, \boldsymbol{p}_2) = 1 + \frac{S^{\mu\nu}(\boldsymbol{q}, \boldsymbol{K}) S^*_{\nu\mu}(\boldsymbol{q}, \boldsymbol{K})}{S^\mu_\mu(0, \boldsymbol{p}_1) S^\nu_\nu(0, \boldsymbol{p}_2)} \tag{3.20}$$

On the other hand, spin effects have to be averaged at the level of the currents, which will lead to the reduction of the tensor Wigner density into its scalar counterpart, which can be associated with the so-called *emission function*, used for example in the Cooper-Frye [183, 184] formula. One can use charge conservation, and the fact that measured photons are on-shell, to decompose the currents into a scalar part, $J(\boldsymbol{p})$, which modulates the vector structure, which is restricted to be composed of polarization vectors, namely

$$J_\mu(\boldsymbol{p}) = J(\boldsymbol{p}) \left[\varepsilon^\mu(\boldsymbol{p}, 1) \cos\psi + \varepsilon^\mu(\boldsymbol{p}, 2) \sin\psi \right] . \tag{3.21}$$

where ψ corresponds to a rotation angle that describes the relative alignment of the current to each polarization. Taking the average of the phase angle one can find the relation between the tensor and scalar Fourier transformed Wigner densities,

$$S_{\mu\nu}(x, \boldsymbol{K}) = \frac{1}{2} S(x, \boldsymbol{K}) \sum_\lambda \varepsilon^\mu(\boldsymbol{p}_1, \lambda) \varepsilon^\nu(\boldsymbol{p}_2, \lambda) . \tag{3.22}$$

The scalar transformer wigner function can be calculated from the amplitude of the current,

$$S(x, \boldsymbol{K}) = \sqrt{E_{\boldsymbol{p}_1} E_{\boldsymbol{p}_2}} \int \mathrm{d}^4 y \, e^{\mathrm{i}y\cdot K} \left\langle J^\dagger \left(x + y/2\right) J \left(x - y/2\right) \right\rangle . \tag{3.23}$$

One can apply then this result to eq. (3.20), which gives the fully spin-averaged HBT correlator.

$$C(\boldsymbol{p}_1, \boldsymbol{p}_2) = 1 + \frac{1}{2} \frac{\left|\tilde{S}(\boldsymbol{q}, \boldsymbol{K})\right|^2}{\tilde{S}(0, \boldsymbol{p}_1)\tilde{S}(0, \boldsymbol{p}_2)} \,. \tag{3.24}$$

The reader can see that this modifies the scalar HBT-correlator only by a relative factor o f $1/2$, which works as a degeneracy factor. In what follows, both $S(\boldsymbol{q}, \boldsymbol{K})$ and $S(0, \boldsymbol{p})$ will be calculated by associating the Wigner function with kinetic rates , that is

$$\tilde{S}(x, \boldsymbol{K}) \leftrightarrow E_K \frac{\mathrm{d}N}{\mathrm{d}^4x \mathrm{d}^3K} \,. \tag{3.25}$$

The rates used in this chapter can be found in Chapter 2 for the prequilibrium case, and in Appendix C for the thermal rates of the QGP and the hadron resonance gas.

3.2 Variables and Approximations

We would like to give a few definitions of variables that will be used. As it was stated above, p_n is the nth photon four-momentum, and for the case here presented, photons will always be taken to be on-shell. In this case, we can define the nth photon's energy and rapidity, E_n and y_n, respectively. The exchange between this coordinates will be used extensively throughout this text. Therefore, it is very important to always remember the relations

$$\begin{aligned} E_n &= p_{n\perp} \cosh y_n \\ p_n^3 &= p_{n\perp} \sinh y_n \,. \end{aligned} \tag{3.26}$$

which is the momentum parametrization in terms of transverse momentum and particle rapidity. The average and relative momentum variables, q and K where defined also above, and here we would like to expand on their meaning. Without loss of generality, one can express both as

$$\begin{aligned} K &= (K^0, K_\perp, 0, K^3) \\ q &= (q^0, q_o, q_s, q_l). \end{aligned} \tag{3.27}$$

Here, we have rotated the transverse plane to align it to the total momentum of the pair. When measuring a real pairs have arbitrary average direction. For this, the photon-photon system is rotated back, and in the case of central collisions, the angle contributions is averaged out. In the case of azimuthally anisotropic systems, it is useful to keep the angular dependence, as it can be used to estimate the eccentricity of the system [185]. It is very useful to think about q in terms of projection components, where we define the *longitudinal*, *outwards*, and *side* directions. These projections are given by

$$\begin{aligned} q_o &= (\boldsymbol{q}_\perp \cdot \boldsymbol{K}_\perp)/K_\perp = q_\perp \cos\varphi \\ q_s &= |\boldsymbol{q}_\perp - (\boldsymbol{q}_\perp \cdot \boldsymbol{K}_\perp)\boldsymbol{K}_\perp/K_\perp| = q_\perp \sin\varphi \\ q_l &= q^3 \,, \end{aligned} \tag{3.28}$$

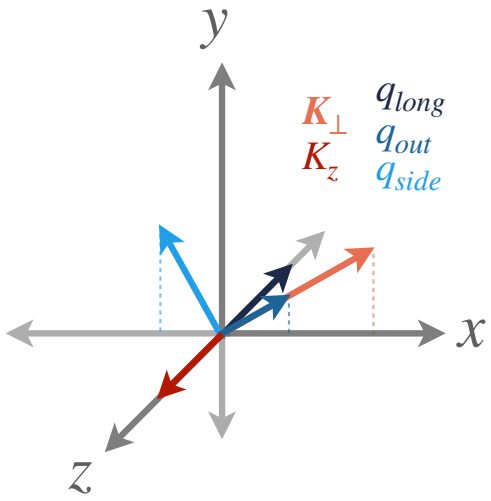

FIGURE 3.1: Diagrammatic representation . In this studies, we will be focusing on the case for which $K_z \sim 0$

where φ stands for the angle between the relative and total transverse momenta. As it was said in the introduction, the main goal of HBT interferometry is to find the spatial extents of the sources using the relative momenta as a guide. Therefore, if the source emits a pair of photons, these projected coordinates are normally used to understand the respective axes of the source, from the particle pair frame of reference (see fig.3.1).

Since both photons are on-shell, both the pair and relative momenta will be necessarily off-shell. Nonetheless, because photons are massless, we can find an orthogonality relationship, which gives the constraint

$$\boldsymbol{q} \cdot \boldsymbol{K} = 0 \quad \Rightarrow \quad q^0 = \frac{\boldsymbol{q} \cdot \boldsymbol{K}}{K^0} \tag{3.29}$$

We would like to emphasize that this relationship is exact for any two identical on-shell particles, regardless of their mass or spin.

In the case of pion-pion interferometry, two approximations are taken to further simplify the computation of the HBT correlator. In the literature they are commonly referred as the *on-shell* and *smoothness* approximations. We will expand first on the former. For this approximation, the pair momenta itself is taken to be on-shell, $K^0 \approx E_K = |\boldsymbol{K}|$. In pion interferometry, this can be used to good approximation, since expanding

$$\begin{aligned} K^0 &= \frac{1}{2}\left[\sqrt{(\boldsymbol{K}+\boldsymbol{q}/2)^2} + \sqrt{(\boldsymbol{K}-\boldsymbol{q}/2)^2}\right] \\ &\approx E_K \left[1 + \frac{\boldsymbol{q}^2}{8E_K^2}\left(1 - \cos\theta_{qK}\right) + \mathcal{O}\left(\frac{\boldsymbol{q}^4}{E_K^4}\right)\right] . \end{aligned} \tag{3.30}$$

Because of large masses of hadrons, and even pions, the second term (and higher orders) are suppressed by E_K for all average momenta. In general, in such calculations, all corrections coming from this expansion are suppressed by either this ratio, or are controlled by the group velocity $\boldsymbol{\beta} = \boldsymbol{K}/K^0$ [182]. However, photons are massless, and this expansion will break at $|\boldsymbol{q}| \sim |\boldsymbol{K}|$. Then, any computation of the HBT correlator using the on-shell approximation can be trusted for

$|\boldsymbol{q}|/(2|\boldsymbol{K}|) \ll 1$. Unfortunately, in experimentally realizable settings at the LHC, the direct photon signal is contaminated by photons from decays, which form the vast majority of the signal. This leaves direct photons with a deficiency in statistics. As a consequence, photon pairs cannot be correlated for infinitesimal $|\boldsymbol{q}|$, with reasonable confidence. This means that in general $|\boldsymbol{q}|$ and $|\boldsymbol{K}|$ will be on the same order of magnitude.

Even in this case, for a single gaussian source, this poses no problem. The correlator will be perfectly gaussian for such a source, and the radii can be directly extracted by fitting the curves [186] , or by found by computing the curvature of the correlator at $\boldsymbol{q} = 0$, (see next section). But in reality, we will be having photons from different sources (stages of the fireball) which will present different scales. Thus, the condition $|\boldsymbol{q}|/(2|\boldsymbol{K}|) \ll 1$ cannot be met for all the kinematic regime. Furthermore, the Wigner function in eqs. (3.23) and (3.17) is generally given for any combination of momenta. The function can be evaluated off-shell [182, 185], and therefore to avoid unexpected from uncontrolled terms found in the expansion in eq. (3.30), we choose to avoid it .

The other approximation normally used in the literature is called the *smoothness approximation*, which consists in neglecting the $\boldsymbol{q}$ dependence in the denominator of eq. (3.24), via $S(0, \boldsymbol{p}_{1,2}) \to S(0, \boldsymbol{K})$. The correlator is given in this limit

$$C(\boldsymbol{q}, \boldsymbol{K}) = 1 + \frac{1}{2}\left|\frac{\tilde{S}(\boldsymbol{q}, \boldsymbol{K})}{\tilde{S}(0, \boldsymbol{K})}\right|^2 \equiv 1 + \frac{1}{2}\left\langle e^{iq\cdot x}\right\rangle , \tag{3.31}$$

for which we will introduce the averaging notation used commonly in the literature [185].

$$\langle f(x)\rangle = \frac{\int \mathrm{d}^4x f(x)\, S(x,K)}{\int \mathrm{d}^4x S(x,K)}^{\prime} ,. \tag{3.32}$$

The smoothness approximation is accurate if the curvature logarithm of the one particle distribution is small [187], which is not true for photons at small momentum (see figs. 2.7 and 2.8). In reference [185] it was found that the convergence of the smoothness approximated to the full correlator is restricted for values of $|\boldsymbol{q}| < 2\,\boldsymbol{K}$. The reader will notice that this is the same scale the signals the breakdown of the on-shell approximation. We will be using this approximation for the case of 1D slices for $q_{o,s}$, where the other directions of q are set to zero. In this case, the $q_{o,s}$ direction will look gaussian, and the explored $K_\perp$ values will be larger than the inverse half width of the correlator.

3.3 Homogeneity Radii

As it was said in the introduction of this chapter, one of the most interesting parts of the HBT correlator is its half width. This is related to the critical relative momentum at which the photons will present quantum enhancement. For a d dimensional source, these half-width are in fact a $(d+1)\times(d+1)$ tensor, but we will see in this section that such tensor in fact has only $d(d+1)/2$ independent components, thanks to the orthogonality condition, eq. (3.29). For an arbitrary source, $S(x, \boldsymbol{K})$,

one can expand its Fourier transform, $S(\boldsymbol{q}, \boldsymbol{K})$ in terms of $q \cdot x \ll 1$ as follows,

$$S(\boldsymbol{q}, K) = \int d^4x \, S(x, \boldsymbol{K}) \left[1 + \mathrm{i} q \cdot x - \frac{1}{2}(q \cdot x)^2\right] + \mathcal{O}((q \cdot x)^3) \tag{3.33}$$

Plugging this into the HBT correlator, and expanding on the denominator we get the expression

$$C(\boldsymbol{q}, \boldsymbol{K}) \approx 1 + \frac{1}{2}\left[1 - q_\mu \, q_\nu \left(\langle x^\mu x^\nu \rangle - \langle x^\mu \rangle \langle x^\nu \rangle\right)\right] . \tag{3.34}$$

We can use this expression to give the radii of homogeneity,

$$R^{\mu\nu} = \langle x^\mu x^\nu \rangle - \langle x^\mu \rangle \langle x^\nu \rangle . \tag{3.35}$$

As long as the relative momenta is lower than its inverse, we will be able to observe quantum enhancement. Notice that this expansion is the same as for a Gaussian function, making$R^{\mu\nu}$ directly related to the half widths of the correlator. Assuming gaussianity, we can get a general form for an arbitrary source around the origin in $\boldsymbol{q}$ space

$$C(\boldsymbol{q}, \boldsymbol{K}) = 1 + \frac{1}{2} \exp\left[-q_\mu \, \tilde{R}^{\mu\nu} \, q_\nu\right] , \tag{3.36}$$

where this approximation is valid only for small relative momenta, or for a Gaussian source. For sources with small non-gaussianities this approximation will also work the perturbations around C rise at high $\boldsymbol{q}$ values [188]. The half-width tensor is a function of the pair momentum, $\tilde{R}^{\mu\nu} = \tilde{R}^{\mu\nu}(\boldsymbol{K})$, but we will not use the explicit dependence on the radii to clean the notation. Using the orthogonality relationship $\boldsymbol{q} \cdot \boldsymbol{K} = 0$, we can reduce this expression to

$$C(\boldsymbol{q}, \boldsymbol{K}) = 1 + \frac{1}{2} \exp\left[-q_i \, R^{ij} \, q_j\right] , \tag{3.37}$$

by redefining $R^{ij} \equiv \beta^i \, \beta^j \, R^{00} + 2 \, \beta^i \, R^{0j} + R^{ij}$. Because of symmetry, $R^{ij} = R^{ji}$, we only get 6 independent components. In this work we will use the l, o, s introduced above, which means that we can parametrise the half-width tensor as

$$R_{ij}(\boldsymbol{K}) = \begin{bmatrix} R_o^2 & R_{os}^2 & R_{ol}^2 \\ R_{os}^2 & R_s^2 & R_{sl}^2 \\ R_{ol}^2 & R_{sl}^2 & R_l^2 \end{bmatrix} . \tag{3.38}$$

In this work we will only focus in the diagonal of this matrix. While it has been shown that for longitudinally expanding sources the R_{os} term is relevant [189], it is also true that numerically calculating such cross-terms is more computationally complex. In future work we will like to work on this terms. In the following sections we will focus mostly on the longitudinal directions.

3.3.1 RMS Variances

It is a standard method to extract variances from a gaussian distribution by calculating the curvature at the origin. We can do this in our case by using the standard cartesian parametrization, eq. (3.37), and assuming the validity of the gaussian

approximation. From this, we get that the radii of homogeneity are given by [190]

$$\begin{aligned} R_{ij}^2 &\equiv \langle(\bar{x}_i - \beta_i\bar{t})(\bar{x}_j - \beta_j\bar{t})\rangle \\ &= \left.\frac{\partial^2 C(\boldsymbol{q},\boldsymbol{K})}{\partial q_i \partial q_j}\right|_{\boldsymbol{q}=0}, \end{aligned} \tag{3.39}$$

with $\bar{x}_\mu \equiv x_\mu - \langle x_\mu\rangle$. It has been as well shown that this method is unstable for photon correlators in the on-shell approximation, where the outward radius, R_o, is not uniquely defined [185]. We will not be using that approximation, for which the widths will not present this problem. Nevertheless, one may argue that this method may give a biased answer, as it takes an weighted average of the curvatures at $\boldsymbol{q} = 0$. This may be problematic for the sum of several sources (see fig. 3.2), where such result may fail to describe the actual correlation length, at which it decays to unity.

3.3.2 Gaussian Fits

To avoid the possible biases described above, one may chose to perform a fit over the full correlator, assuming gaussianity [186]. For azimuthally symmetric systems [191], the following general expression is assumed for gaussian sources,

$$C(\boldsymbol{q},\boldsymbol{K}) = 1 + \Lambda(\boldsymbol{K})\exp\left[-q_s^2R_s^2 - q_o^2R_o^2 - q_l^2R_l^2 - q_sq_oR_{so}^2\right] \tag{3.40}$$

where all the homogeneity radii, R_i with $i = l, o, s, os$, are taken to be functions of $\boldsymbol{K}$, but their dependence is suppressed for simplicity of notation. In this work we will only fit for 1D slices in the o, s, l will be performed.

This method is highly dependent on the range of values at which it is performed. For a gaussian correlator, this will be trivially equal, but for one with non-gaussianities may yield very different answers depending on the chosen values. For such cases, fits had been made using very small cutoffs [185]. In such cases, it does not qualitatively affect the half-width measurement. Nonetheless, in our case, this becomes a complex problem since Gaussian fits seem to be blind to the addition of several stages, and will tend to favor the contribution with the biggest radius, if the fitting is performed for small q_i parameters. Alternatively, one could extend such ranges, but this makes the fitting process unstable.

3.3.3 Characteristic scale

We will present another way of computing a measure of the homogeneity radii, which is stable for correlators with strong non-gaussianities [192].. For this we will use the moments[3] of the true correlator $C(\boldsymbol{q},\boldsymbol{K}) - 1$ in relative momentum space,

$$\langle\langle q_iq_j\rangle\rangle = \int \mathrm{d}^3q q_i\, q_j\, g(\boldsymbol{q};\boldsymbol{K}) \equiv \frac{1}{2}(R^{-1})_{ij} \tag{3.41}$$

where R^{-1} is the inverse matrix of eq. (3.38). We have defined the distribution function

$$g(\boldsymbol{q};\boldsymbol{K}) \equiv \frac{C(\boldsymbol{q},\boldsymbol{K}) - 1}{\int \mathrm{d}^3q\, [C(\boldsymbol{q},\boldsymbol{K}) - 1]} \tag{3.42}$$

[3]Notice that we use the notation $\langle\langle\cdots\rangle\rangle$ for the averaging with respect to the correlator. We will keep the $\langle\cdots\rangle$ notation for averages with respect to the emission function.

to ensure correct normalization. Because of the symmetry properties of the correlator, we can safely assume the one-point functions vanish.

For simplicity, and because we will not be exploring the off-diagonals, we will keep the notation one-dimensional. That means that the homogeneity radii are going to be given by

$$R_i^2 = \frac{1}{2}\langle\langle q_i^2\rangle\rangle^{-1}, \quad \text{with} \quad i \in \{l, o, s\} \tag{3.43}$$

It is important to clarify that this method requires the correlator to be highly localized around $\boldsymbol{q} = 0$, to give sensible results for the characteristic scale. In other words, the correlator may need to decay faster than a power-law. We can use also this method to quantify the deviations from gaussianity we can compute the *normalized excess kurtosis* (NEK) ,

$$\Delta_i = \frac{\langle\langle q_i^4\rangle\rangle}{3\langle\langle q_i^2\rangle\rangle^2} - 1 \tag{3.44}$$

which, as expected, vanishes in the gaussian limit.

In theoretical calculations of HBT correlations, going to higher values of q_i requires only better numerical precision. However, it may pose as a problem for experiment, where high relative momentum values will suffer from statistics. As pairs for a given q bin must be found in experiment, pairs from higher bins will be less probable to encounter. For now we will focus on this method as a cross-check to extract theoretical information of the correlations.

3.4 HBT for the homogeneous BMSS model

We want to apply the technology introduced in the last sections into a model, to understand the effects of spacetime evolution in the correlators. For this, a simple, semi-analytical option is at hand in the BMSS inspired model from last chapter. In this model, the saturated state of gluons relaxes and thermalizes in three stages, and it features a high dominance of pre-equilibrium photons. We can compare how pre-equilibrium affects the HBT correlator[4] by comparing it with the early thermalization scenario, also presented in last chapter. This comparison is a clear-cut showcase of the stark difference between media in- and out- of equilibrium, particularly because both cases start at the same space-time volume, but photons will be produced with different rates. This will yield very different HBT curves as a consequence. We will show that for such a model, the contrast between the two cases is in fact quite high, and so, this model exhibits the best case scenario for the pre-equilibrium HBT case.

This model is taken to be homogenous in the transverse plane, for which the dependence of $q_\perp$ factorizes out of the integral in eq. (3.15). This means explicitly that

$$S(\boldsymbol{q}, \boldsymbol{K}) = S_\parallel(\boldsymbol{q}, \boldsymbol{K})\, S_\perp(\boldsymbol{q}_\perp) \tag{3.45}$$

The transverse part of the Fourier transform, $S_\perp(\boldsymbol{q}_\perp)$, can be computed analytically by regularising the transverse area integral into an ellipse with semi axes a

[4]The on-shell one photon distribution, or yield, is given by $S(0, K)$ and can be found in figs. 2.7 and 2.8.

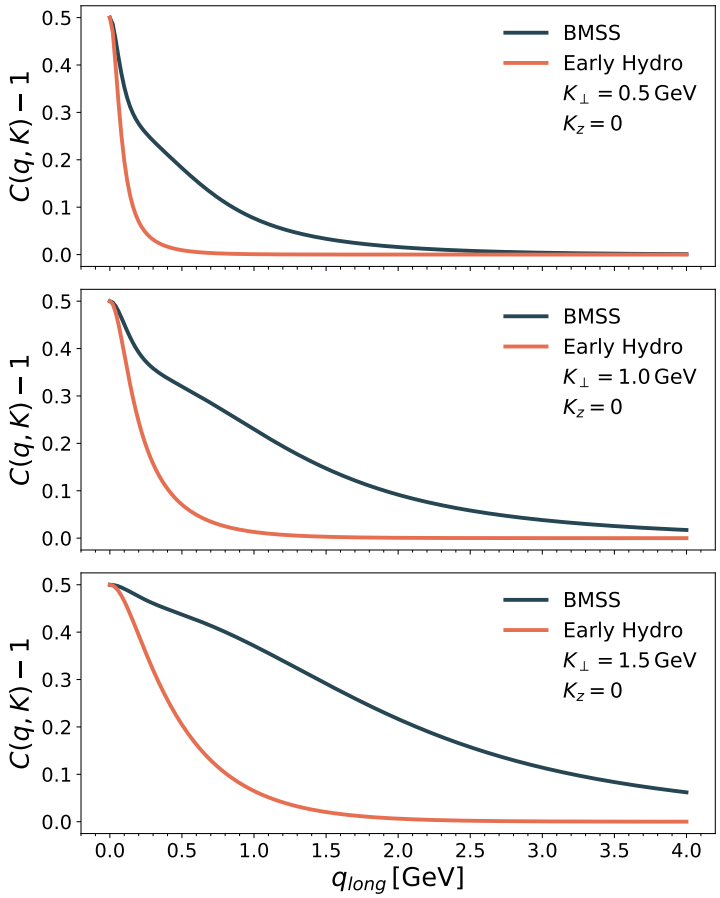

FIGURE 3.2: The HBT correlator for a Bjorken expanding (transversally homogeneous) volume for $q_{long} = q_{out} = 0$. Here it is given at mid-rapidity $K_z \sim 0$ and $K_\perp = 0.5, 1.0, 1.5\,\mathrm{GeV}$. A stark contrast can be seen between curves for the early thermalization and BMSS scenarios, increasing with $K_\perp$.

and b, namely

$$S_\perp(q_\perp) = \int \mathrm{d}^2\boldsymbol{x}_\perp e^{\mathrm{i}(\boldsymbol{q}_\perp\cdot\boldsymbol{x}_\perp)} = 2\pi\, ab\, \frac{J_1(\tilde{q_\perp} R_\perp)}{\tilde{q_\perp}}\,. \tag{3.46}$$

where J_n stands for the nth Bessel function of the first kind, and $\tilde{q_\perp} = \sqrt{(q_o a)^2 + (q_s b)^2}$ .This is a very trivial dependence of q_o and q_s, where basically their radii are given by the free parameters a and b. Nonetheless, this calculation is in its own right a benchmark for the initial conditions. Since radial expansion only make the effective radii larger, one would expect the transverse HBT measure to have the transverse area recovered from the Glauber modeling as a lower bound. On the other hand, the longitudinal section of this transform is given by

$$S_\parallel(\boldsymbol{q}, \boldsymbol{K}) = \int \mathrm{d}\tau\, \tau\, \mathrm{d}\eta\, e^{\tau\, q\cdot u} S(\tau, \eta; \boldsymbol{K}) \tag{3.47}$$

where $u = (\cosh\eta, 0, 0, \sinh\eta)$ is the proper velocity of the Bjorken expanding system. The longitudinal portion, $S_\parallel(\boldsymbol{q}, \boldsymbol{K})$, is a very involved set of integrals, and

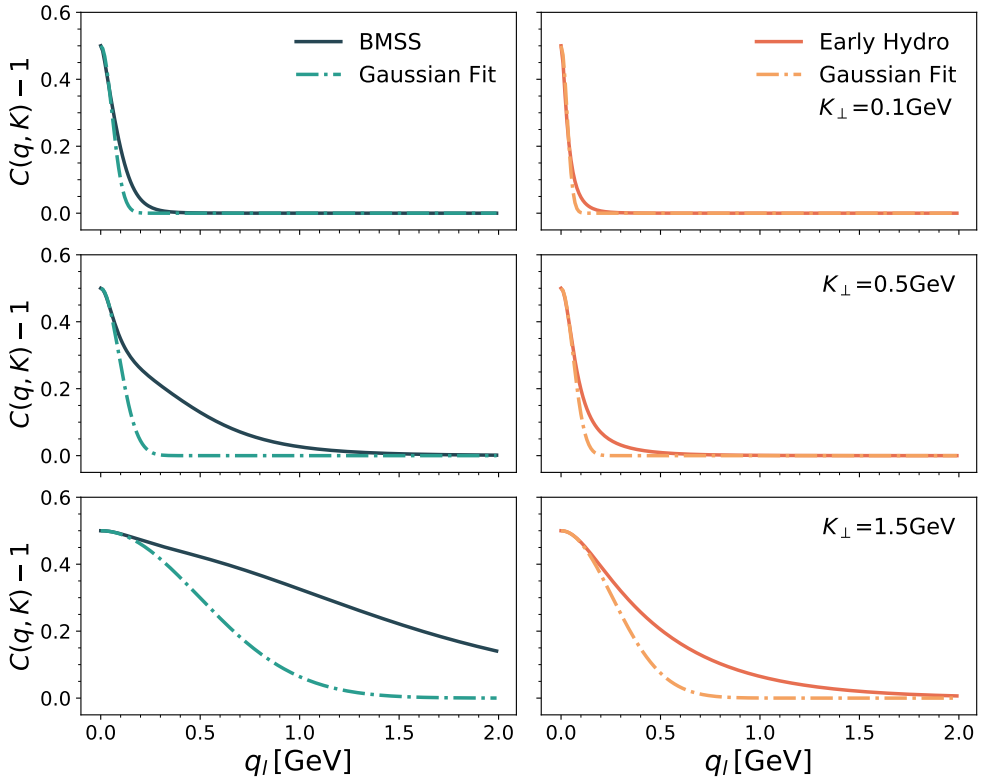

FIGURE 3.3: Gaussian fits for the q_l HBT correlator with $q_s = q_{out} = 0$ at mid-rapidity, $K_z \sim 0$, and $K_\perp = 0.5, 1.0, 1.5\,\text{GeV}$. To keep the curve-fitting under control, we have to restrict it to a maximum range of $q_l = 0 - 0.2$ GeV.

unfortunately can't be computed analytically even for the small-angle simplified rates. We will compute it numerically using the pre-equilibrium rates mentioned in the last chapter, as well as the thermal rates that can be found on Appendix C, switching between them appropriately for each epoch the evolution of the fireball. In other words, when we talk about the correlator $C(\boldsymbol{q}, \boldsymbol{K})$ we refer to the normalized version given in eq. (3.24), from which the functions $S^i_{\parallel}(\boldsymbol{q}, \boldsymbol{K})$ and added and squared.

The full HBT correlator was computed for along the longitudinal direction, q_l, $q_o = q_s = 1$ for midrapidity pairs, $K_z = 0$. We will focus on ALICE energies, $\sqrt{s} = 2.76$ TeV for the parameters fixed in table 2.1. Curves for different values of $K_\perp$ can be found in fig. 3.2. It can be seen in that for low values of the pair momentum, the two scenarios are quite close. However, for moderated and high $K_\perp$, this changes, and the correlator exhibits a characteristic structure, or shoulder for the pre-equilibrium case. Such bump rises from the fact that pre-equilbrium photons dominate the yield completely at harder momenta, and they are created earlier times. The resulting correlation length of C is sensitive to this, and will be shifted to smaller, values, yielding a curve with a longer decay.

We extracted the longitudinal radius. R_l for different values of the pair transverse momentum, $K_\perp = 0.1 - 1.5$ GeV. Although there is physics to learn in the radii above this value, it this region seems to be experimentally unachievable. Also, by restricting ourselves to such values, we restrict the contributions from prompt photons, which at this values of $K_\perp$ are negligible (see fig. 2.7). We extracted the radii using the three methods given above: RMS variance, Gaussian fitting and

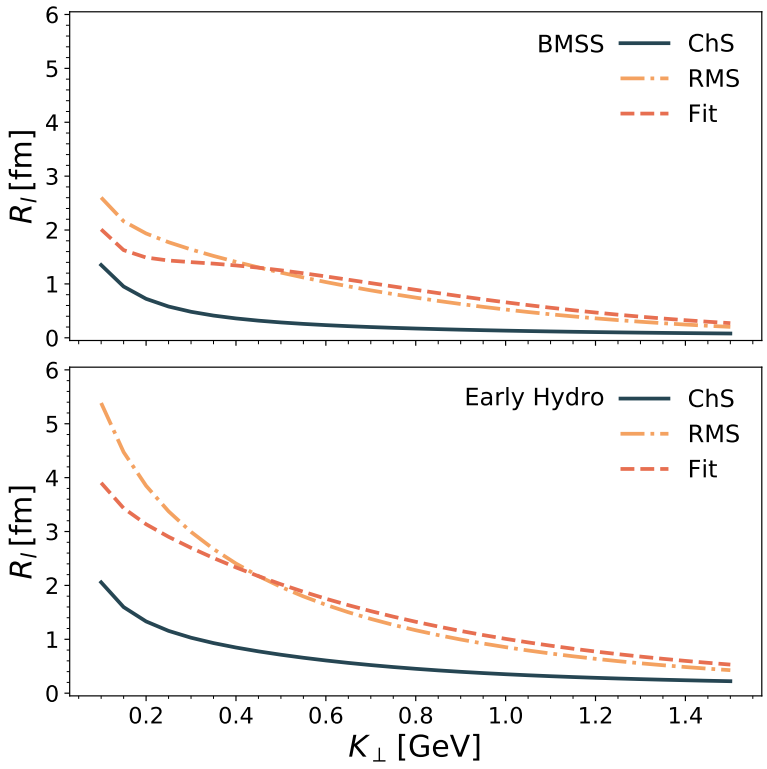

FIGURE 3.4: HBT longitudinal radii extracted from the Gaussian fitting (Fit), RMS variance and characteristic (ChS) methods. We get comparatively large radii for both. This is mainly due to non-gaussianities.

the method of characteristic scale (ChS). The results can be found in fig. 3.4. For the RMS variance method used eq. (3.39), where the derivative was taken numerically over a 1D slice. Gaussian fitting was performed using the prescription of ref. [185], where we have restricted the fitting to small values of relative momentum $q_l < 0.1$ GeV. This results in a good fit for the peak at $q_l = 0$, but misses the secondary structure. The fit fails the features of the correlator even at large values of $K_\perp$, where the contribution of the pre-equilbrium epoch should dominate and overtake with its own gaussian behaviour. The RMS variance radii and the values extracted from fitting seem to be compatible with each other. Finally, we have computed the radii using the characteristic scale method, where we have computed the correlator for very large values, $q_l = 10$ GeV, to be able to calculate its second moment. For this, better precision is needed to compute the rapidly oscillating integrals.

As it was stated in last section, the RMS and fitting methods exhibits bias, and we can see in fig. 3.4, they miss the features of the secondary structure. However, it also seems that non-gaussianities contaminate the signal of the ChS method, muddling the distinction between the two scenarios. Nevertheless, because we know that the correlator exhibits very stark differences between the two scenarios, we would like to compare the sensibility of these three methods. For this, we have taken the ratios of the radii from each scenario, $R_{l,BMSS}/R_{l,EH}$ (see fig. 3.5). One can observe that the ChS method is the one that captures best the differences seen in fig. 3.2.

We would like to add that for these two cases, radii may not be a good tool

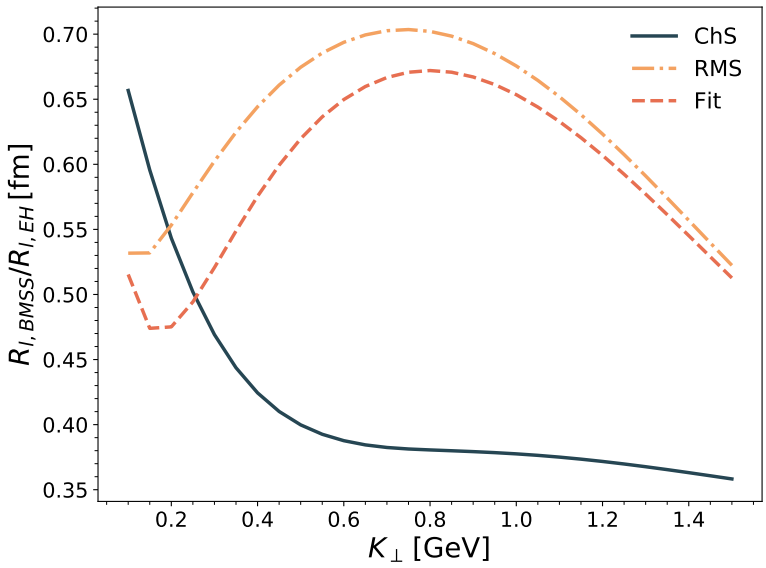

FIGURE 3.5: HBT longitudinal radii extracted from the BMSS inspired model in comparison to the early thermalization one.

to perform a comprehensive comparison. This because the longitudinal radii extracted from the fitting and the RMS variance methods are not so sensitive to the pre-equilibrium epoch (see fig. 3.5), for which future experimental data may not be precise enough to disentangle. On the other hand, statistics in the experiment may render characteristic scale method unusable. Given the results above, it must be noted that the correlator itself is the most powerful tool to discriminate between the early thermalization and the BMSS scenarios, where for moderate transverse pair momentum, $K_\perp \approx 0.5$ GeV the difference may already be measurable.

3.5 HBT for a Hybrid model

In the last section, a comparison of the longitudinal HBT correlation and radii was performed for early and late (BMSS) thermalization scenarios. However, the model introduced does not take into account the spatial distribution of the energy deposition, or transverse expansion. If one wants to extract information about the transverse sizes of the fireball, one needs to include the information about spatial inhomogeneities. To do this, we present here a *hybrid model*, which takes the spatial resolution from standard hydrodynamical calculation while including a pre-equilibrium stage. This pre-equilibrium stage is taken to be the first stage of the glasma, where the rates are enhanced the most. We assume Bjorken expansion during this stage, which makes it transversally static. The transition between non-thermal and hydrodynamical stages is then enforced by matching the energy density at (thermal) initial time, τ_{hydro}. The spatial distribution is given by matching the characteristic scale at the beginning of the collision to the temperature profile at , $Q_s^2(\boldsymbol{x}_\perp) = Q_s^2[T(\boldsymbol{x}_\perp)]$. In some sense, this is similar conceptually similar to the IP-Glasma model where at some arbitrary time, τ_{hydro}, the evolution in switched to a hydrodynamical simulation, by giving in an energy density. In our case, this time is given by the end of the first stage of the *bottom-up* thermalization scenario, $\tau_{hydro} \equiv Q_0^2\,\alpha_s^{-3/2}$. For the case of LHC energies at ALICE, this means

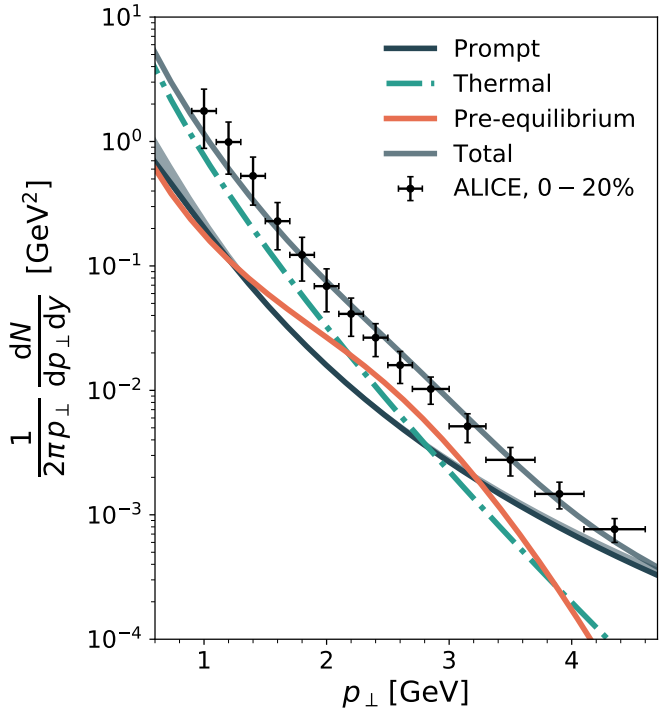

FIGURE 3.6: Comparison of the photon invariant yield for the hybrid model against ALICE experimental data for $0-20\%$ centrality class.

$\tau_{hydro} \approx 0.6$ fm. We will use this value to switch between the pre-equilibrium and thermal stages.

Nevertheless, this is not the best case scenario for the pre-equilibrium emission of photons. As it was shown in Chapter 2, the second stage of the bottom-up scenario, $\alpha_s^{-3/2} < \tau\, Q_0 < \alpha_s^{-5/2}$, (fig. 2.6) produces more infrared photons thanks to the rise of the soft gluon sector. The end time of this stage is $\tau \approx 2$ fm. Evolving up to the end of the second stage and then instantaneously thermalizing would have an effect in the creation of pressure gradients, where anisotropies would not build up as fast as needed. Such a late initial time initial will prove to be lacking not the production of transverse anisotropies to describe the data, [193], but also enough blue shifting of the photon yields, which comes from the radial expansion. There is, however, a big caveat for this statement. As it was previously stated in Chapter 2 it is commonly assumed that during the early -pre-equilibrium- times, pressure gradients do not grow as fast as in later times. Therefore, transverse anisotropies, which may be captured by our HBT observable, will not be sensitive to them. This assumption needs to be revisited in order to understand whereas the initial conditions of hydrodynamical simulations are consistent with the understanding of the pre-equilibrium stages. If that should be the case, then photon HBT will also be the go-to observable to better distinguish between predictions. In the current absence of a good phenomenologically available calculation that captures these early times, we have chosen to keep avoid some *ad hoc* solution and keep for now this assumption by assuming Bjorken expansion in the $Q(x_\perp)$ profile, while keeping static, with no evolution of the velocities. In the following we will state the details of the computation.

3.5.1 Pre-equilibrium stage

In the previous sections, we have include thermal rates for the hydrodynamic evolution of the quark gluon plasma. However, the results above found the pre-equilibrium contribution for photons to be non-negligible. In these estimates, the "bottom-up" thermalization scenario (or BMSS) [28] of the Glasma has been used as a framework. The results rely mostly on the first stage on the Glasma, where gluons are highly occupied, and the system goes near a non-thermal fixed point.

We wish to investigate this stage and its contribution to photon multiplicities and HBT correlators. To include the early-time contribution we use a phenomenological model, using the rate given in ref. [35] for the first stage of the Glasma evolution, and switching to the hydrodynamical evolution later. We then match the energy densities from the pre-equilibrium stage to the Glauber initial conditions used for hydro.

For the rate, we will use the enhanced kinetic rate given in sec. 2.2.1

$$E\frac{\mathrm{d}N}{\mathrm{d}^4\,x\mathrm{d}^3\,p} = \frac{10}{9\pi^4}\,\alpha\,\mathcal{L}_{LO}\,Q_S^2\,\kappa_g\,\left(\frac{\tau_0}{\tau}\right)\,f_q(\tau,\mathbf{p}) \tag{3.48}$$

notice that in this case we have substituted $Q\,\tau$ for τ/τ_0. This initial time is going is then set to be the phenomenologically fixed $\langle Q_s^2\rangle^{-1/2}$ from sec. 2.3 (specific values can be found in Table 2.1). As we are upgrading the early-time energy density to be transverse-space dependent, and so the saturation scale, we use the average to enforce scale-setting, not only at the level of initial time, but also for the coupling α_s. Once again the quark distribution, f_q, is taken from hard splitting of gluons in-medium, namely $f_q \sim \alpha_S\,f_g$, which in turn is extracted from classical statistical simulations [130], and is given by a scaling solution,

$$f_g(\tau;\,p_\perp,p_z) = \frac{1}{\alpha_S}\left(\frac{\tau}{\tau_0}\right)^{-2/3}\,f_S\left(p_\perp,p_z\,\left(\frac{\tau}{\tau_0}\right)^{1/3}\right) \tag{3.49}$$

where τ_0 is The scaling function is parametrized as in sec. 2.2. In this section we have, however, enforced the Pauli blocking by setting a top on the occupation, given by the thermally equilibrated limit, $f_q < 1/2$. This because the function as given in of the wide range of Q_s values that will be sampled, which shakes the assumption at higher values of $Q_s(\boldsymbol{x}_\perp)$.

The spatial profile of the scale $Q_S(\boldsymbol{x}_\perp)$ is given by the matching of the energy density in the pre-equilibrium and hydro stages at the moment of instant thermalization,

$$\epsilon_{neq}(\boldsymbol{x}_\perp)|_{\tau_{hydro}} = \epsilon_{eq}(\boldsymbol{x}_\perp))|_{\tau_{hydro}}\,. \tag{3.50}$$

In the pre-equilibrium stage, most of the energy density resides in the gluonic sector. Using the gluon pre-equilibrium and QGP energy densities one can obtain the spatial profile

$$Q_s(\boldsymbol{x}_\perp) = T(\boldsymbol{x}_\perp)\left[\sqrt{\frac{2}{\pi}}\frac{37\pi^2(2\pi)^2\alpha_S}{30(1+\sqrt{2\pi}\,r\,+2\,r^2))}\frac{\tau_{hydro}}{\tau_0 f_0\,s}\right]^{1/4} \tag{3.51}$$

where τ_0 is taken to be the spatially averaged saturation scale, $\langle Q_S\rangle^{-1}$, and can be determined parametrically using the method described in sec. 2.3 (see table 2.1).

The parameter space of this model can be further narrowed by demanding that

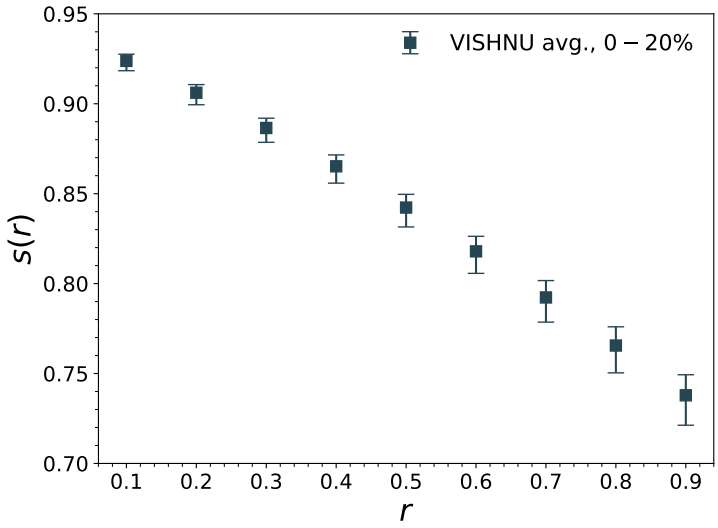

FIGURE 3.7: The anisotropy parameter $s = \sigma_0/Q_s$, here fixed in terms of the average saturation scale (see table 2.1), and the suppression parameter r.

the resulting $Q_s(\boldsymbol{x}_\perp)$ is properly normalized, so that $\langle Q_s^2 \rangle$ coincides to the homogeneous case[5], which was found in sec. 2.3. This results in fixing the anisotropy parameter, s for a given r, which remains a free parameter, up to comparison with data. The reader may notice that the values for the anisotropy parameter here used are considerably higher than in the homogeneous BMSS case. This change is in fact physical, and comes from the choice to instantaneously thermalize the Glasma to a hotter QGP relative to the energy density of the early thermalization in sec. 4.5. Not only this extra energy has to be accounted in the gluon distribution, but also in the hybrid model, the system does not have stages (ii) and (iii) which undergo further relaxation, . We choose then to fix s since the resulting yields have a more trivial dependence to it than to r.

3.5.2 Thermal evolution

Thermal photons were calculated from both the QGP and HRG epochs of the evolution of the fireball. The rates used for the QGP emission were the complete LO rates [140], while the hadronic bremmstrahlung comes from both $\pi\pi$ scattering and in-medium thermal ρ emission. These rates need a temperature and velocity profile as input, whose space-time evolution was performed for a relativistic 2+1D fluid using the publicly available IEBE-VISHNU package [194, 195]. We used the default model parameters, which have been tuned to fit experimental data, to simulate the hydrodynamical evolution of QGP and hadron resonance gas of 200 Pb-Pb collision events at the centre of mass energy $\sqrt{s_{\rm NN}} = 2.76\,$TeV in a centrality class of 0-20%. The initial conditions at matching time, t_{hydro}, are set in the two-component MC-Glauber model [196]. The evolution of the hydrodynamical quantities was performed for a fixed shear viscosity over entropy ratio $\eta/s = 0.08$ at the decoupling density, $e = 0.1\,\text{GeV/fm}^3$. The events that are used to compute photon observables, namely the T and $\boldsymbol{v}_\perp$ profiles, were then recorded on a coarse grid, with a lattice spacing of $dx = dy = 0.4$fm and $d\tau = 0.2\,$fm ($x_{\rm max} = y_{\rm max} = 25.2\,$fm). Variations of

[5]The errors are given here by taking on account fluctuations of this quantity, that is $\left(\langle Q_s^4 \rangle\right)^{1/2}$

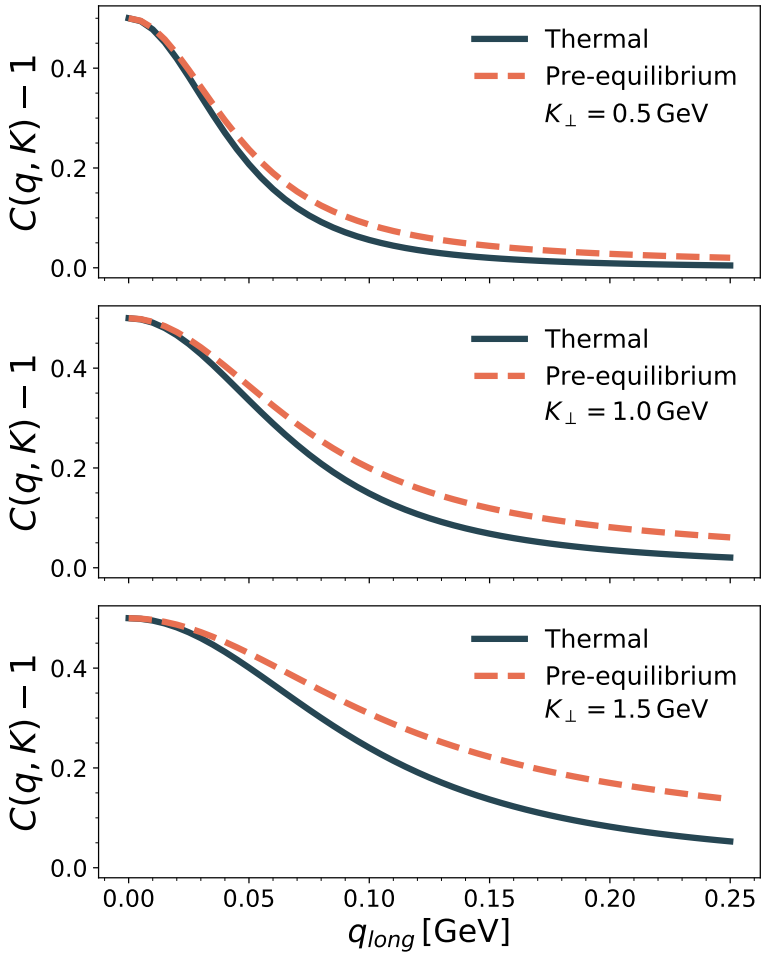

FIGURE 3.8: HBT correlation function in theq_l, $q_o = q_s$ direction for different values of $K_\perp$.

the final time $\tau_{\max}$ depended on the initial conditions, but at least 100 independent events were recorded with $\tau_{\max} \geq 15.8\,\text{fm}$.

3.5.3 Results

The full HBT correlator was computed for midrapidity pairs, $K_z = 0$, along the three diagonals, which means it is given by q_l with $q_o = q_l = 0$, q_o with $q_s = q_l = 0$ and q_s with $q_o = q_s = 0$. We will again focus on ALICE energies, $\sqrt{s} = 2.76$ TeV where the average saturation scale is given in table 2.1. We will be comparing two cases, the thermal evolution alone, and the scenario of a pre-equilibrium stage followed by thermal evolution. The latter will call the *full* evolution.

As expected, the longitudinal curves are the most sensitive to the inclusion of the pre-equilibrium stage. The reader can find in fig. 3.8 the comparison of the full case with the thermal evolution for different values of $K_\perp$. We once again extracted the longitudinal radii using the three methods include above, where as it can be seen in fig. 3.10, we get very different values for the ChS method, while the fitting for $q_{max} = 0.1$ GeV and RMS variance method give very similar results. From these radii we can learn that even when not dominating at small momenta, the pre-equilibrium photons will be able to reduce the effective homogeneity radius in the longitudinal direction.

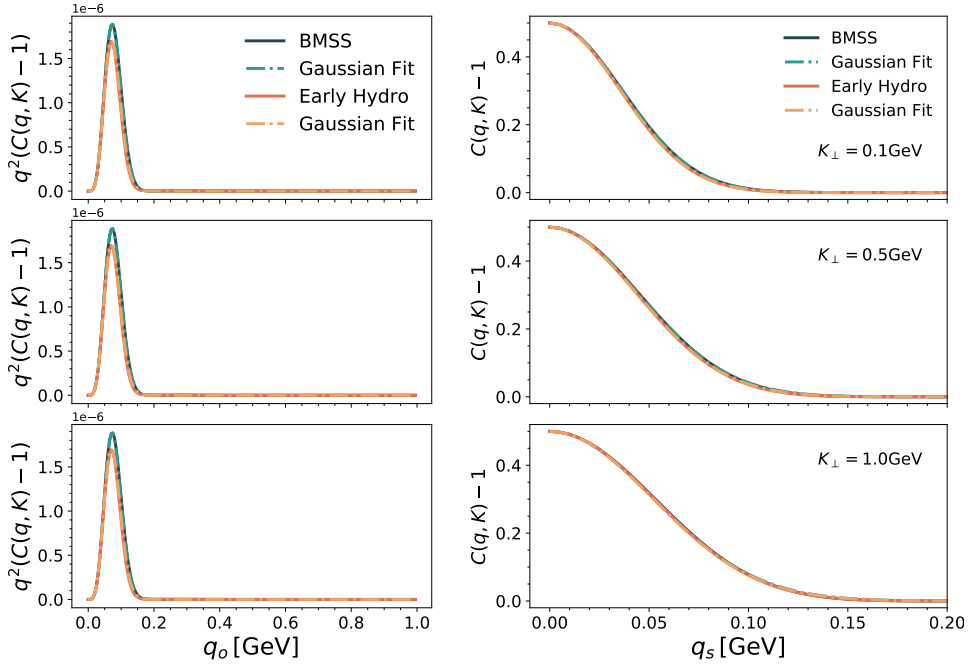

FIGURE 3.9: Gaussian fits for the q_o and q_s HBT correlator at mid-rapidity, $K_z \sim 0$, and $K_\perp = 0.1, 0.5, 1.0\,\text{GeV}$. Gaussian fitting gives excellent results for these directions.

The sideward and outward direction correlator were also computed for this model. We performed gaussian fits, which were quite robust to the change of the fitting range, q_{max}. In fig. 3.9, we use $q_{max} = 0.5$ GeV, for which the fits work effectively at describing the half-length of the correlators. From this method, as well as the RMS and ChS methods, we computed R_o and R_s (see fig. 3.10). For these two directions, it was found that the three methods were roughly equivalent, and we have picked the traditional fitting method to present our findings. We computed also the change induced in $R_{o,s}$ by the inclusion of the pre-equilibrium stage, and have found it to be in the $10-20\%$ for the outward direction, and $0-10\%$ for the sideward direction. This gives an interesting case for experimental data. If pre-equilibrium photons are relevant at the yield level, and the assumption that the pre-equilibrium stage does not create enough pressure gradients is correct, thermal models will be able to reproduce the $R_{o,s}$ but may fail to reproduce R_l.

We also computed the NEKs, eq. (3.44), for the three diagonals. A clear hierarchy is found, where q_l breaks gaussianity the most, followed by q_o and q_s. We find that the sidewards direction is to good approximation gaussian (see fig. 3.12). The non-gaussianities, as was explained above and in ref. [185] arise from the longitudinal expansion of the fireball. In the case of massless particles these effects will be considerable more important than for i.e. pions. Additionally volume emission will further enhance these effects, opposed to Cooper-Fry surface emission. The aforementioned non-gaussianities are quite intuitive to understand in the case of the q_l direction, since the boosting from longitudinal expansion is biggest for the q_l variable. However, the easiest way to see how the outward direction gets contributions from the expansion is eq. (3.39) for the computation of the RMS variances. From this formula we see that for the outward direction, R_o gets a non zero contribution from contributions from $\beta_o t = tK_\perp/K^0$, while the sideward direction, by the definition, will not. This means that the outward homogeneity radius not only

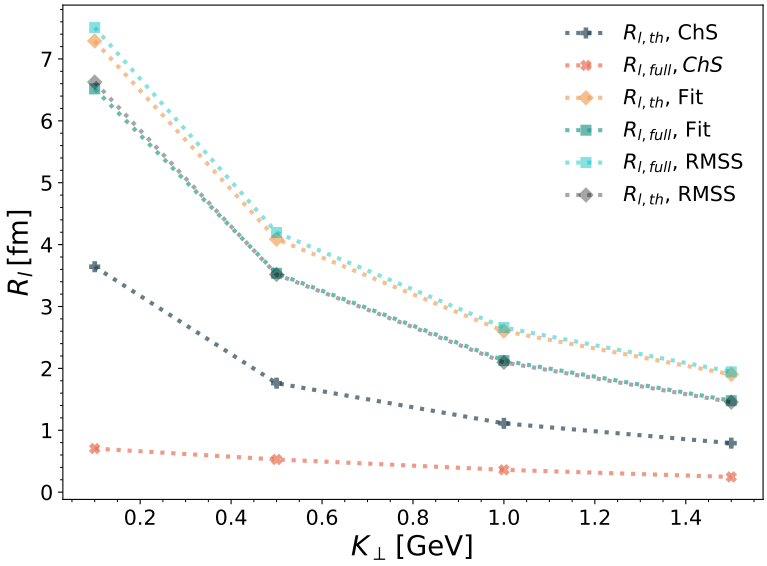

FIGURE 3.10: HBT longitudinal radii extracted from the hybrid model for the thermal and full cases. The radii we computed with the three methods described in sec. 3.3.

depends on the spatial size of the source, but also on the lifetime of emissions [182]. While Δ_i gives a very nice comparison and measurement of the non-gaussianities, it is unusable in an experimental setting, since, as it was discussed in last section, higher q bins suffer from statistics.

3.6 Conclusions

In this Chapter, we presented a brief derivation of the HBT correlator for a spin-1 particle. We have also presented the technology commonly used in particle interferometry, which include the variables and approximation commonly used in the area. In previous work [185], photon HBT correlators and radii were presented, making emphasis in the transverse ranges as a way to measure the eccentricities of non-central collisions. In the work presented here we have focused, in contrast, on these observables as a source of information of the pre-equilibrium stages, as well as a tool to discriminate between different models.

To showcase this line of thought, we have computed the HBT photon correlators for two different scenarios. First, we have the transversely homogeneous, full *bottom-up* scenario, which presents a rather late thermalization time, in contrast to the thermalization time normally imposed as initial condition in standard hydrodynamical simulations. We have then contrasted the *bottom-up* scenario with its early thermalization counterpart. We find stark differences at the longitudinal HBT correlator level, where the early thermalization gives significative larger correlation lengths. We have computed the homogeneity radii using three different methods, for which the RMSS variance, and gaussian fitting procedures roughly agree. These two methods, however, are blind to the mixing of signals with differing correlation lengths and fail to reproduce the properties of the correlator product of the non-equilibrium epoch. On the other hand, the characteristic scale method is particularly sensitive to non-gaussianities, and it seems to give a better answer for the case of the BMSS scenario.

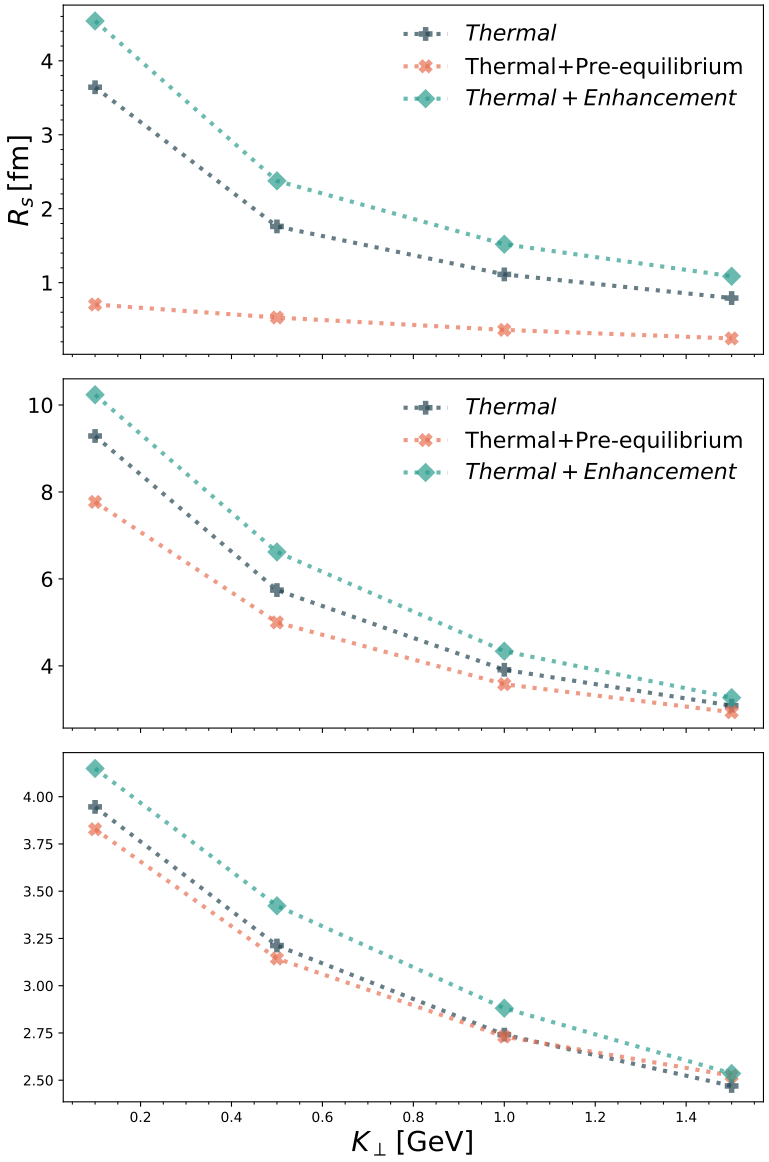

FIGURE 3.11: HBT $R_{o,s}$ radii extracted from the hybrid model for the thermal and full cases. Below, we can observe the deviation from the thermal, caused by the inclusion of pre-equilibrium.

There is one caveat about this model we have to emphasize. The one-photon distributions meet fair agreement with data (see fig. 2.7) after fitting the overall normalization constant, which encodes volume uncertainties. For this section this correction is not needed, since only direct photons at low $\boldsymbol{k}_\perp$ contribute to and the prefactor drops out. Additionally, it was said in Chapter 2 that errors come into this model in a variety of ways. Nevertheless, this is an exploratory work on the incidence of pre-equilibrium in the HBT correlators. In the future more quantitative studies can be achieved by computing the theoretical error bands for the two models.

In the second model probed, we have used pre-equilibrium to enhance a hydrodynamical computation, which is known to reproduce the invariant yield up to overall normalization. This idea came originally as a way to solve the *photon puzzle*, which is the inability to explain with current models both the yields of the photons

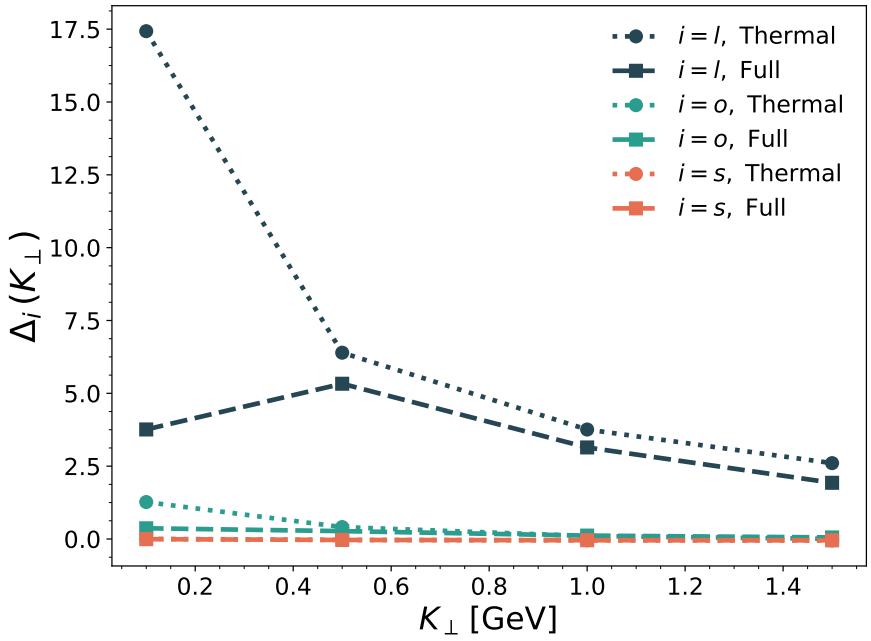

FIGURE 3.12: Normalized excess Kurtosis for the q_i direction, with $i = l, o, s$. It can be seen that the longitudinal case differs from gaussianity the most, followed by the outwards direction. Finally, the sidewards direction is basically gaussian.

and their anisotropy. For this, we added the pre-equilibrium photons, which would enhance the total yields, given that they are expected to be of the same order the thermal contributions [35]. In contrast, this extra source is not expected to enhance the anisotropy coefficients, since it is for this model assumed to be static in the transverse plane, as the space-time anisotropies are not yet fully understood. For this model, we get fair agreement with data at the level of yields, (see fig. 3.6).

We have computed the HBT correlators in the diagonal directions, q_i for $q_j = q_k = 0$ for $j, k \neq i$. For this we have observed non-gaussianities in the l and o directions, while the s correlator was approximated fairly well by a gaussian source. We computed the normalized excess kurtosis to quantify these effects, confirming the decreasing non-gaussianity in the l, o, s direction. From these correlators we extracted R_l, R_o, and R_s using the same methods as for the BMSS model. The longitudinal radius exhibits the biggest difference between the thermal and the *full* evolution, while the pre-equilibrium epoch causes small incidence in the o and s radii, for which we see changes of $10 - 20\%$ and $0 - 10\%$, respectively. From these results and the ones for the BMSS model we conclude that these changes in the radii can be used to test the BMSS scenario. If the thermal model can predict the $R_{o,s}$ radii, but fails to do so for the longitudinal direction, it will be a strong indication, this scenario, strong pre-equilibrium, no early radial expansion,. may be achieved.

Chapter 4

Turbulent Thermalization of Rotating Quantum fields

4.1 Introduction

In a Heavy Ion collision experiment, two nuclei fly into each other roughly at the speed of light, finally colliding at some given impact parameter. This collision occurs at very high center of mass energies, which translates to high longitudinal momenta. If the nuclei collide off-center, at an impact parameter b, then the initial orbital angular momentum, L_0, will present very high values. This quantity is given for a specific configuration by

$$L_0 \sim \frac{1}{2} A \sqrt{s_{NN}}\, b\,, \tag{4.1}$$

with A the nuclear mass number and $\sqrt{s_{NN}}$ the center of mass energy per nucleon. For the case of Au-Au collisions at RHIC, where the energy is $\sqrt{s_{NN}} = 200$ GeV, the total orbital angular momentum of a event with $b \sim 5$ fm is $L_0 \sim 5 \times 10^5$. For LHC events, this number is between one and two orders of magnitude, depending on the selected $\sqrt{s_{NN}}$, for the different runs. It was also found in ref [34] that, as it would be expected, the angular momentum deposited in the interaction zone peaks at some given impact parameter, b^*, and then decreases rapidly. For the case of Au-Au collisions, to $b^* \sim 3$ fm which corresponds to events found at high centrality classes. Furthermore, it was found that, for this case, the angular momentum deposited in the fireball accounts for 30% of the total orbital angular momentum L_0.

The deposited angular momentum is then conserved throughout of the evolution of the fireball by virtue of Noether's theorem [197]. Since the initial state is very far away from equilibrium, it is reasonable to think that the degrees of freedom associated to angular momentum need a mechanism to relax to their equilibrium values. Since it is commonly assumed that every conserved quantity presents an associated charge transport cascade, one would then expect to see an *angular momentum cascade*, where the system, having an initially restricted set of L states, flows towards. Such a cascade would create a dynamical re-distribution of degrees of freedom.

This can be understood on a very intuitive way, using the famous ice-skater analogy. One starts with a state which presents L fluctuations -vortices- of the size $r_v \sim \langle p \rangle^{-1} \equiv Q^{-1}$, with an arbitrary characteristic scale Q. This system will relax to redistribute energy, where $\langle p \rangle$ will go to higher values, meaning the effective vortice size will be reduced. Because of conservation, the system will flow also to modes with higher angular momentum.

$$f(t, l, p) = t^{\alpha} f_S(t^{\beta}\, l, t^{\beta}\, p) \tag{4.2}$$

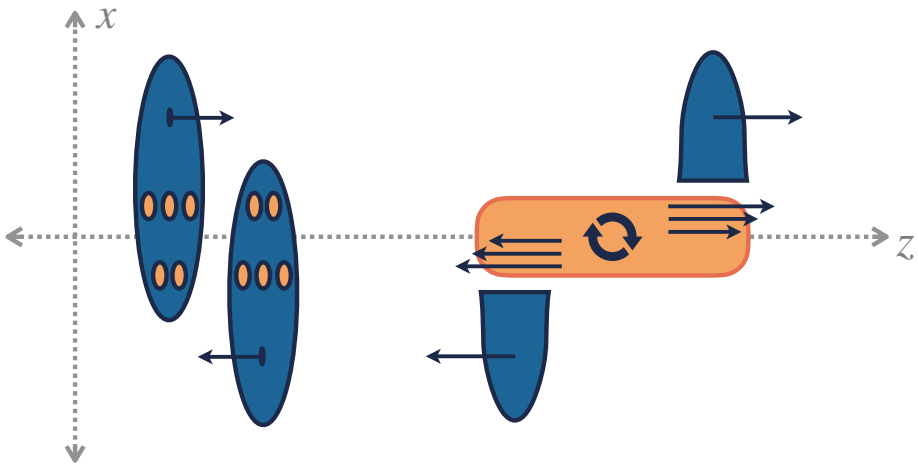

FIGURE 4.1: Before the collision, w

It is sensible to ask the question of whether the route to thermalization [31]that such system would take would be in the same universality class as the systems explored previously, where initial conditions present exactly vanishing L [131]. The reasoning behind this comes from the simple fact of the conservation of angular momentum, where a system which initially has non-vanishing L will not be able to flow into a non-rotating one.

Apart from investigating the role of angular momentum in the evolution of the system, exploring the role of angular momentum and its fluctuations is promising since vorticity has been shown to couple to chiral degrees of freedom. This phenomenon has been called the Chiral Vortical Effect (CVE) [198–200] in the literature. Instabilities and turbulence arising from angular momentum transport from highly occupied quantum fields in nuclear matter may lead to the appearance of anomalous currents. Non-vanishing angular momentum manifests to be important at this point because it guarantees an imbalance of the currents created, which may result in observable effects[201], such as the imbalance of hyperons [202]. Such non-equilibrium effects should be investigated in the future.

As seen above, the early stages of a HIC are rich in novel and interesting physics, which can shed light into the way we think about quantum collectivity in the setting of high energy nuclear matter. This is why it is in my interest to set as a long term goal to achieve the full 3D classical statistical simulation of a $SU(N)$ simulation for a finite system and initial conditions with non-vanishing angular momentum in a Bjorken expanding setting. This is, nonetheless, a daunting task to take on right away, starting with the fact that Dirichlet bounded problems in NEQFT are a relatively unexplored area. To start to create such a body of research, and settle the technology needed for the main goaI, I proposed a 2D $\lambda\phi^4$ scalar theory as a toy model to better understand the role of angular momentum and its fluctuations in the process of relaxation, scaling and further on, thermalization. This model consists of a scalar field, $\phi(t, r, \theta)$, bounded to a disk, which requires Dirichlet boundary conditions, $\phi(t, R, \theta) = 0$ to enforce continuity of the field values between the *inside* and *outside* of the area of interest. The transition to polar coordinates facilitates then the expression of the field values in terms of angular momentum numbers. We selected initial conditions which guarantee the initialization with non-vanishing total angular momentum.

On another note, a system like this simple toy model in fact also relevant for the

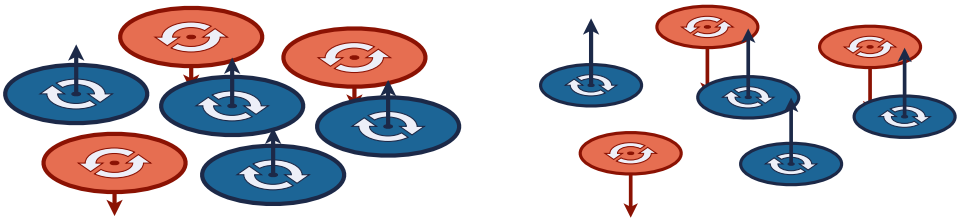

FIGURE 4.2: Simplified representation of an angular momentum cascade. As the characteristic momentum flows to the UV, triggering a reduction of the characteristic correlation lengths, angular momentum is forced to flow to higher values.

case of analog quantum simulators, where the scaling exponents of non-relativistic scalar theories have been already observed in experiments [32, 203]. For the model presented here, a 2D system may be realized with an optical trap, the boundaries may be approximated by our Dirichlet fixed boundaries .

In this chapter we present the first non-equilibrium quantum field theoretical simulation of a system non-vanishing total angular momentum. The research presented in this chapter was done in collaboration with Jürgen Berges and Peter Kaposvari, and it is a first exploration towards better understanding the role of conserved charge transport in quantum non-equilibrium settings. This chapter is divided as follows, in sec. 4.2 we review non-equilbrium QFT, where we will briefly derive the classical statistical framework as well as the classicality condition. In sec. 4.3 we introduce the scalar toy model. We present the solution for a free scalar field , as well as the observable and initial conditions relevant for this setting. In sec. 4.4 we summarize the numerical scheme used, novel in classical statistical setting. We then present our results in section 4.5, where new scaling exponents will be presented. Finally we end the chapter with a summary and outlook.

4.2 Out-of-equilibrium Quantum Field Theory

Quantum field theory in vacuum or thermal settings is different in one fundamental way from its non-equilibrium counterpart, time invariance is assumed. For time evolution to be manifest, one has to reformulate QFT as an initial value problem (IVP). This was achieved by Schwinger and Keldysh in the sixties in the so called *in-in* formalism [204, 205]. In it, unitary evolution is encoded in a close-time contour $\mathcal{C}$, which can be divided into a *forward* and a *backward* branch, $\mathcal{C}^+$ and $\mathcal{C}^-$, respectively. The former runs from the initial time t_0 up to $t \to \infty$, and the latter takes the inverse path. While in scattering theory one projects the evolution into in- and outgoing asymptotic states, in this formalism the state is known instead for a single time slice t_0. In that case, the evolution of the state is given by its Hamiltonian, which gives the unitary operator $U(t, t0)$. One can project the observable along the time axis in the Heisenberg picture using

$$\langle \mathcal{O}(t) \rangle = Tr \left\{ \rho_0 \, U(t_0, t) \, \mathcal{O} \, U(t, t_0) \right\} \tag{4.3}$$

Such evolution can be read as evolving the state up to a time t, to then project it back to t_0, to be able to take the trace with respect to the initial energy density. For the following, we would like to redefine the partition function $Z[\rho] = \langle 1 \rangle = 1$ as a path integral. This is useful, since we can then introduce a source J so that $Z[\rho] \to Z[J;\rho]$, which allows to compute the n-point correlations functions using

$$\langle \mathcal{T}_{\mathcal{C}} \phi_{a_1}(x_n) \cdots \phi_{a_n}(x_n) \rangle = \left. \frac{\delta^n Z[J;\rho]}{\mathrm{i}\delta J_{a_1}(x_1) \cdots \mathrm{i}\delta J_{a_n}(x_n)} \right|_{J=0} \tag{4.4}$$

where the contour operator $\mathcal{T}_{\mathcal{C}}$ orders the operators from right to left in increasing order of appearance of time in the Schwinger-Keldysh contour. In this work we will be considering a relativistic real scalar theory for a single field in two spatial dimensions. For completeness we will derive in this section the non-equilibrium functions and classical statistical limit for the case of a general $O(N)$ theory [33, 206], but for the simulation results, $N = 1$. The indices $a, b \in 1, \cdots, N$ represent the components of the theory, and they respect the Einstein sum convention. The classical action is given by

$$S[\phi] = \int_{x,\mathcal{C}} \left[\frac{1}{2} \partial_\mu \phi_a(x) \partial^\mu \phi_a(x) - \frac{m^2}{2} \phi_a(x) \phi_a(x) - \frac{\lambda}{4!N} \left(\phi_a(x) \phi_a(x) \right)^2 \right] . \tag{4.5}$$

Here we use the notation $\int_{x,\mathcal{C}} = \int_{\mathcal{C}} \int_{\boldsymbol{x}}$, where $\mathcal{C}$ stands for the closed-time-path from fig. 4.3. From this action one can get the classical equations of motion (EOM) which are given in a coordinate free form by

$$\left[\partial^2 + m^2 + \frac{\lambda}{6N} \left(\phi_b(x) \phi_b(x) \right) \right] \phi_a(x) = 0 \, . \tag{4.6}$$

We can quantize the theory by enforcing equal time commutation relations between the field operator [1], $\hat{\phi}_a(x)$ and its conjugate momentum, $\hat{\Pi}_a(x) \equiv \partial_{x^0} \phi_a(x)$,

$$[\hat{\phi}_a(x), \hat{\Pi}_b(y)] \Big|_{x^0 = y^0} = \mathrm{i} \delta_{ab} \delta(\boldsymbol{x} - \boldsymbol{y}) \, . \tag{4.7}$$

Given these considerations, we can put up the partition function for this theory as a path integral. The derivation of the partition function is cumbersome and will not be presented here. In it one divides the evolution in infinitesimal time-slices, and project the evolution into coherent states $|\phi\rangle$ which are eigenstates of the field operators in the Heisenberg picture. This means explicitly $\hat{\phi}_a(x)|\phi\rangle = \phi_a(x)|\phi\rangle$.This is how the forward+backward time integration appears in the action. For a real $O(N)$ theory, the partition function can be expressed as

$$Z[J;\rho] = \int \mathcal{D}\phi_0^+ \mathcal{D}\phi_0^+ \langle \phi_0^+ | \rho_0 | \phi_0^- \rangle \int_{\phi_0^-}^{\phi_0^+} \mathcal{D}'\phi e^{\mathrm{i}S[\phi] + \mathrm{i}\int_{x,c} J_a(x)\, \phi_a(x)} \tag{4.8}$$

where as mentioned above we have included a one-point source, $J_a(x)$. In textbooks of non-equilibrium QFT another source is normally introduced via the inclusion of $\phi_a(x) R_{ab}(x,y) \phi_b(y)$ term. This is useful for the derivation of the two particle irreducible effective action (2PI), as well as it can be used to absorb the initial density matrix for the case of initial Gaussian states. However, in this work we will not

[1] For non-equilibrium settings, the instant form is the most straightforward [207]. However, quantization can be done using the front form (along the light-cone, like in Hamiltonian QCD [208, 209]) or along proper time surfaces.

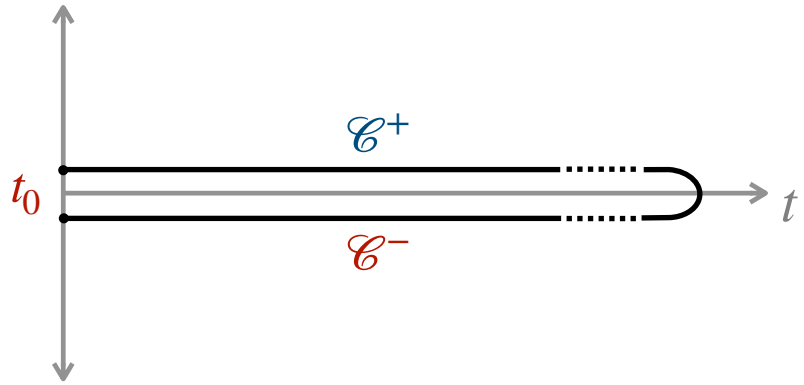

FIGURE 4.3: The closed-time path, also called Schwinger-Keldysh countour.

be using that technique. Therefore we will not introduce this extra term.

In a quantum theory, all the information is encoded in the correlation functions. By obtaining all relevant correlations, one effectively solves the theory. Since we are going to take the classical statistical limit of QFT, we are interested particularly in the one- and two-point functions,

$$\begin{aligned} \Phi_a(x) &= \langle \phi_a(x) \rangle \\ G_{ab}(x,y) &= \langle \mathcal{T}_{\mathcal{C}} \phi_a(x) \phi_b(x) \rangle - \Phi_a(x) \Phi_a(y) \\ &= \langle \mathcal{T}_{\mathcal{C}} \phi_a(x) \phi_b(x) \rangle_c \end{aligned} \tag{4.9}$$

which are here expressed as connected Green functions. It is not only conceptually, but also computationally useful to redefine the two-point correlator, also called the *connected propagator*, in terms of the commutator and anticommutator correlation functions,

$$G_{ab}(x,y) = F_{ab}(x,y) - \mathrm{i}\,\mathrm{sgn}_{\mathcal{C}}(x^0 - y^0)\rho_{ab}(x,y) \tag{4.10}$$

where $\mathrm{sgn}_{\mathcal{C}}(x^0 - y^0)$ stands for the contour sign function, which is defined to be $+1$ if $x^0 > y^0$ along the contour, -1 if $x^0 < y^0$. This means, i.e. that if $x^0 \in \mathcal{C}^+$ is in the and $y^0 \in \mathcal{C}^-$ branch, then $\mathrm{sgn}_{\mathcal{C}}(x^0 - y^0) = -1$. The real and imaginary parts of the connected propagator are given by

$$\begin{aligned} F_{ab}(x,y) &\equiv \langle \{\phi_a(x), \phi_b(x)\} \rangle_c \\ \rho_{ab}(x,y) &\equiv \langle [\phi_a(x), \phi_b(x)] \rangle \end{aligned} \tag{4.11}$$

where in the literature $F_ab(x,y)$ and $\rho_ab(x,y)$ are commonly called the *statistical* and *spectral* functions. The former is associated to the average occupancy of the energy modes, while the latters contains information of the dispersion relation, as well as the *availability* of said modes.

4.2.1 Classical Statistical limit

When a quantum field theory lives in a state in which most of the energy density is condensed in the one-point function, or when fluctuations are highly occupied, it can be mapped into a classical statistical theory [210, 211]. Then the dynamics are dominated by the classical equation of motion, while fluctuations around this can be sampled from an ensemble of initial conditions. This method constitutes a

simplification which can serve to tackle problems where high momentum fluctuations are not yet relevant, in setting such as inflationary cosmology and preheating [31, 212, 213], in the area of quantum simulation [214, 215] and in the area of this work, HICs [134, 216, 217]. The latter has been particularly useful to probe the pre-equilibrium dynamics in an ab-initio way, which is unfortunately not available for techniques such as the 2PI formalism [218].

We will sketch in this section a brief derivation of the classical statistical formalism. For this we start by splitting the action into the forward and backward branches of the closed-time path,

$$S[\phi] = \int_{x,\mathcal{C}} \mathcal{L}[\phi] = \int_x \left(\mathcal{L}[\phi^-] - \mathcal{L}[\phi^+]\right) \tag{4.12}$$

where we have used that where $\int_x = \int_{t_0}^{\infty} \int_{\boldsymbol{x}_\perp}$

we will Wigner rotate our contour field variables

$$\begin{aligned} \bar{\phi} &= \frac{1}{2}\left(\phi^+ + \phi^-\right) \\ \tilde{\phi} &= \phi^+ - \phi^- \end{aligned} \tag{4.13}$$

It is important to note that the one-point function cannot depend on the branch of the contour, $\Phi_a^+(x) = \Phi_a^-(x) \equiv \Phi_a(x)$ [33]. This gives as a consequence a condition for the rotated fields, $\langle \bar{\phi}_a(x) \rangle = \Phi_a(x)$ and $\langle \tilde{\phi}_a(x) \rangle = 0$. For this reason, in the literature $\bar{\phi}$ and $\tilde{\phi}$ are called the classical and quantum fields, respectively. Which means that for the source term we get

$$\begin{aligned} \int_{x,\mathcal{C}} J_a(x)\phi_a(x) &= \int_x \left(J_a^+(x)\phi_a^+(x) - J_a^-(x)\phi_a^-(x)\right) \\ &\equiv \int_x \left(\tilde{J}_a(x)\bar{\phi}_a(x) - \bar{J}_a(x)\tilde{\phi}_a(x)\right) \end{aligned} \tag{4.14}$$

where we get the rotated sources using the same transformation than for the fields, eq. (4.13). The partition function is now given by

$$\begin{aligned} Z[\bar{J},\tilde{J};\rho] = \int \mathcal{D}\bar{\phi}_0\, \mathcal{D}\tilde{\phi}_0\, \langle \bar{\phi}_0 + \frac{1}{2}\tilde{\phi}_0 | \rho_0 | \bar{\phi}_0 - \frac{1}{2}\tilde{\phi}_0 \rangle \\ \times \int_{\bar{\phi}_0,\tilde{\phi}_0} \mathcal{D}'\bar{\phi}\mathcal{D}'\tilde{\phi} e^{\mathrm{i}S[\bar{\phi},PQ] + \mathrm{i}\int_{x,c} \bar{\phi}_a(x)\,\tilde{J}_a(x) + \tilde{\phi}_a(x)\,\bar{J}_a(x)} \end{aligned} \tag{4.15}$$

The connected two-point functions for the quantum and classical field can be found by taking functional derivatives of the connected generating functional, $W[J] = -\mathrm{i}\log Z[J]$,

$$\begin{aligned} F_{a,b}(x,y) &= \langle \bar{\phi}_a(x)\bar{\phi}_b(y)\rangle_c = \frac{\mathrm{i}\delta^2 W[J;\rho]}{\mathrm{i}\delta\tilde{J}_a(x)\mathrm{i}\delta\tilde{J}_b(y)} \\ G^R_{a,b}(x,y = \langle \bar{\phi}_a(x)\tilde{\phi}_b(y)\rangle_c &= \frac{\mathrm{i}\delta^2 W[J;\rho]}{\mathrm{i}\delta\tilde{J}_a(x)\mathrm{i}\delta\bar{J}_b(y)} \\ G^A_{a,b}(x,y) &= \langle \tilde{\phi}_a(x)\bar{\phi}_b(y)\rangle_c = \frac{\mathrm{i}\delta^2 W[J;\rho]}{\mathrm{i}\delta\bar{J}_a(x)\mathrm{i}\delta J_{a_n}(x_n)} \end{aligned} \tag{4.16}$$

where the $\langle \tilde{\phi}\tilde{\phi} \rangle$ propagator vanishes exactly. The retarded, G^R, and advanced G^A, propagators can be related to the spectral function by using $\rho = G^R - G^A$. The

action in terms of the classical and qunatum fields is given by

$$S[\bar{\phi},\tilde{\phi}] = \int_x \Big[\partial_\mu \bar{\phi}_a(x)\partial^\mu \tilde{\phi}_a(x) - m^2 \bar{\phi}_a(x)\tilde{\phi}_a(x) - \frac{\lambda}{6N}\bar{\phi}_a(x)\bar{\phi}_a(x)\bar{\phi}_b(x)\tilde{\phi}_b(x) - \frac{\lambda}{24N}\tilde{\phi}_a(x)\tilde{\phi}_a(x)\tilde{\phi}_b(x)\bar{\phi}_b(x)\Big]. \tag{4.17}$$

One can perform an integration by parts on the first term, which gives a boundary term, $\int_x \partial x^0[\Pi_a(x)\phi_a(x)] = \int \mathrm{d}^d x \Pi_a(t_0,\boldsymbol{x})\phi_a(t_0,\boldsymbol{x})$. we can now group terms in eq. (4.17), and we get

$$S[\bar{\phi},\tilde{\phi}] = S_{cl}[\bar{\phi},\tilde{\phi}] + I_q[\bar{\phi},\tilde{\phi}] - \int \mathrm{d}^d x \Pi_a(t_0,\boldsymbol{x})\phi_a(t_0,\boldsymbol{x}) \tag{4.18}$$

where he have defined a classical action, $S_{cl}[\bar{\phi},\tilde{\phi}]$, an interaction term, $I_q[\bar{\phi},\tilde{\phi}]$ and the aforementioned boundary term. These effective pieces are given explicitly by

$$\begin{aligned} S_{cl}[\bar{\phi},\tilde{\phi}] &= \int_x \tilde{\phi}_a(x)\Big[-(\partial^2+m^2)\bar{\phi}_a(x) - \frac{\lambda}{6N}\bar{\phi}_a(x)\bar{\phi}_a(x)\bar{\phi}_b(x)\tilde{\phi}_b(x)\Big] \\ I_q[\bar{\phi},\tilde{\phi}] &= -\frac{\lambda}{24N}\int_x \tilde{\phi}_a(x)\tilde{\phi}_a(x)\tilde{\phi}_b(x)\bar{\phi}_b(x) \end{aligned} \tag{4.19}$$

We can get rid of the boundary term by observing that the projected density matrix can be defined as the functional Fourier transform of a Wigner function, depending on the initial classical field and its canonical momentum,

$$\langle \bar{\phi}_0 + \frac{1}{2}\tilde{\phi}_0 | \rho_0 | \bar{\phi}_0 - \frac{1}{2}\tilde{\phi}_0 \rangle \equiv \int \mathcal{D}\Pi_0 W[\phi_0,\Pi_0]\, e^{\mathrm{i}\int \mathrm{d}^d x \Pi_a(t_0,\boldsymbol{x})\phi_a(t_0,\boldsymbol{x})} \tag{4.20}$$

Furthermore, one can approximate this full action by neglecting the interaction term, $I_q[\bar{\phi},\tilde{\phi}]$. This is the classical statistical approximation. We now put all together, after realizing that we can integrate with respect to the quantum field, since the action is linear on $\tilde{\phi}$ after neglecting I_q. This integration yields

$$Z[\tilde{J};\rho] = \int \mathcal{D}\bar{\phi}_0\, \mathcal{D}\Pi_0\, W[\phi_0,\Pi_0]\, \delta[\phi-\phi_{cl}]\,. \tag{4.21}$$

This means that after integration, we have a system for which dynamics is given by the classical equations of motion. Nevertheless, as it was said at the beginning of this section, fluctuations around this dynamics have to be sampled, using the Wigner function, $W[\phi_0,\Pi_0]$. This means that for a general observable, the expectation value is given by

$$\langle \mathcal{O}[\phi,\pi]\rangle|_{cs} = \int \mathcal{D}\phi_0 \mathcal{D}\Pi_0\, W[\phi_0,\Pi_0]\mathcal{O}[\phi[\phi_0,\pi_0],\Pi[\phi_0,\Pi_0]]\,, \tag{4.22}$$

where the classical statistical average is done by sampling the evolved observable over all realizations. Additionally, there is an argument that can be made about this approximation. In eq. (4.17) we can see that we find two effective vertices, $\bar{\phi}^3\tilde{\phi}$ and $\bar{\phi}\tilde{\phi}^3$, called the calssical and quantum vertex, respectively. By throwing away the quantum vertex, we are drastically reducing the number of advanced and retarded propagator in the diagrams pertaining the approximated theory. This translates

to a reduced importance spectral. It is reasonable to translate this into the simple relation

$$F^2(x,y) \gg \rho^2(x,y) \tag{4.23}$$

where the squaring comes from the shape of the self energy at two-loops [216] in the 2PI, from which one can recover the classical statistical approximation. In terms of the occupation number, one finds that

$$\left[f(t,\boldsymbol{p}) + \frac{1}{2}\right]^2 \gg 1 \tag{4.24}$$

where the distribution of modes must be significantly higher than the *quantum one-half* bound, $f(t,\boldsymbol{p}) \gg 1/2$. In the next section, this function will be defined with respect to the evolving fields.

4.3 Bounded rotating scalar fields

As it was stated in the section above, scalar theories in the over-occupied regime play an important role in i.e. cosmological settings, where they have been thoroughly investigated. These systems relied, however, in periodic boundary conditions, needed to enforced translational invariance. The length of the lattice, L is not taken to be physical, and instead, the studies conducted were only trusted as the infrared *arctifacts* vanish. Nonetheless, we will see that when total angular momentum is taken to be non-vanishing, such considerations are not valid anymore [200]. If one wants to unambiguously include a total angular momentum, an axis of rotation has to be introduced, which breaks explicitly translational symmetry. Once translational invariance is broken, the free solution for such setting does not allow for periodic boundaries, since the solutions decay with radia distance. Because of this we chose to bind our system inside a finite disk, at which the field set to vanish, namely

$$\phi(t,R,\theta) = 0\,. \tag{4.25}$$

This Dirichlet boundary condition (DBC) is not realistic in the setting of heavy ion collisions, as it imposes a barrier, and thus forbids the expansion of the interacting field against the vacuum. Nonetheless, the main point in the discussions of this study, and so this chapter, is to understand the role of angular momentum and finite size in the path to thermalization. With the former we would like to explore the transport of "angular momentum charge" through the scales of the system. With the latter, to understand the creation of a physical mass gap, since the finite radius of our setting effectively quantizes the momenta states in the system, and creating a ground state with non-zero radial momentum. Because of the geometry of the system, and to facilitate the definition of angular momentum states, we will use polar coordinates to compute the classical equations of motion, which are given by

$$\left(\partial_t^2 - \partial_r^2 - \frac{1}{r}\partial_r - \frac{1}{r^2}\partial_\theta^2 + m^2\right)\phi(t,r,\theta) = -\frac{\lambda}{6N}\phi^3(t,r,\theta)\,,. \tag{4.26}$$

Because of angular momentum conservation, imposing it at initial time is enough. For this, we need to devise a constrain over the fields to be able to enforce it. Next section will use the field definition to come up with such a condition.

4.3.1 Angular momentum

Angular momentum conservation is given in a general field theory by Noether's theorem, where the current triggered by an inifinitesimal transformation of the Lorentz group

$$(\mathcal{J}^{\mu})^{\rho\sigma} = x^{\rho}\, T^{\mu\sigma} - x^{\sigma}\, T^{\mu\rho} \tag{4.27}$$

This current is conserved via the equation $\partial_{\mu}\ (\mathcal{J}^{\mu})^{\rho\sigma} = 0$. This quantity contains d conserved charges, namely $Q^{0j} = \left(\mathcal{J}^{0}\right)^{0j}$, associated to boosts, and $d(d-1)/2$ charges $Q^{ij} = \left(\mathcal{J}^{0}\right)^{ij}$, associated to angular momentum. For the case of our two dimensional system, we get two boosts, and one angular momentum,

$$\mathcal{L} = \frac{1}{2}\,\varepsilon_{ij}\, Q^{ij} \tag{4.28}$$

which for the case of a $O(N)$ theory in Minkowski spacetime is given by the expression

$$\begin{aligned} \mathcal{L} &= -\int \mathrm{d}^2x\, \Pi_a(x)\ [x\partial_y - y\partial_x]\, \phi_a(x) \\ &= -\int \mathrm{d}^2x\, \Pi_a(x)\, \partial_\theta \phi_a(x) \end{aligned} \tag{4.29}$$

This is the condition we need to enforce non-vanishing total angular momentum momentum (NVL). From this expression we can see that at initializing with plane wave mode functions will fail to give $\mathcal{L} \neq 0$. This means that by construction, these initial conditions [131, 219] will not only have $\langle \mathcal{L} \rangle = 0$, but also that each realization will present exactly vanishing angular momentum. We need to find an initial solution for the fields for which this is not the case.

4.3.2 Mode decomposition of free $O(N)$ theories on a Disk

To solve a scalar $O(N)$ theory inside a bounded area, one has to solve the Klein-Gordon equation, and enforce continuity conditions for the field at the boundary of the system. For a disk of radius R, and expressed in polar coordinates, this translates into the system.

$$\begin{aligned} \left(\partial_t^2 - \partial_r^2 - \frac{1}{r}\partial_r - \frac{1}{r^2}\partial_\theta^2 + m^2\right)\phi(t,r,\theta) = 0\,, \\ \phi(t,R,\theta) = 0\,. \end{aligned} \tag{4.30}$$

Because we have a linear equation for the free theory, we can diagonalize the field, and express it as a sum of harmonic oscillators.

$$\phi(t,r,\theta) = \sum_{\boldsymbol{p}} \left[a_{\boldsymbol{p}}\varphi_{\boldsymbol{p}}(t,r,\theta) + a^{\dagger}_{\boldsymbol{p}}\varphi^{*}_{\boldsymbol{p}}(t,r,\theta)\right] \tag{4.31}$$

where we define the momentum index for a general two dimensional space. We will replace it in the next sections with a 2D array of quantum numbers (l,n), as we will see that both the radial and the angular directions get effectively quantized because of the DBC. We will apply for the mode functions the cseparation of variables ansatz. Because of the form of the derivatives, we will assume plane wave shape for the t and θ directions, namely

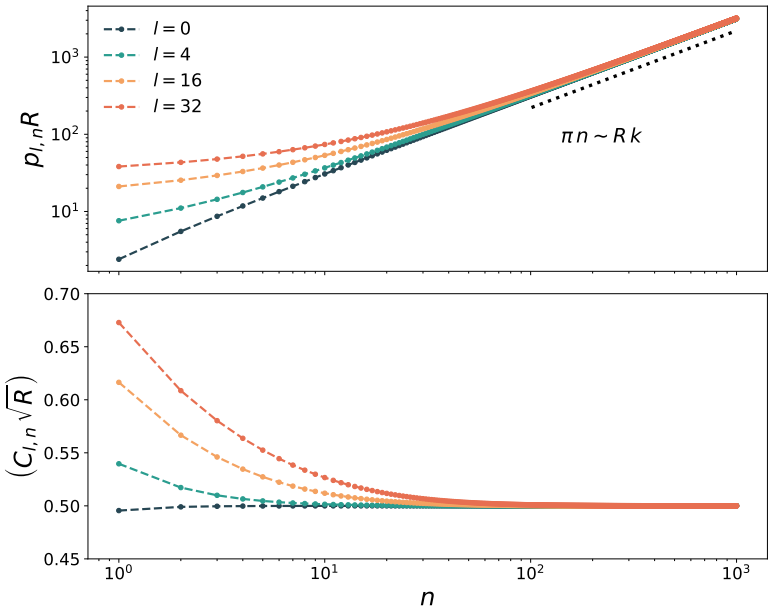

FIGURE 4.4: *Up: Down:*

$$\varphi_{\boldsymbol{p}}(t,r,\theta) = C_{\boldsymbol{p}}\, e^{-\mathrm{i}(\omega t - l\theta)}\rho(pr)\,. \tag{4.32}$$

where $C_{\boldsymbol{p}}$ corresponds to the normalization of the modefunctions. The angular direction is compact, which means that l will be quantized, so that l can only take integer values. We can use this ansatz to get the equation for the radial portion of the mode function,

$$\left[r^2\partial_r^2 - r\partial_r - (p^2\, r^2 - l^2)\right]\rho(r) = 0\,, \tag{4.33}$$

This is the Bessel equation [220], for which the solution is given by the lth Bessel function of the first order, $\rho(r) = J_l(px)$, in which the radial momentum is $p^2 + m^2 = \omega^2$. Then the full solution for the free mode functions is

$$\varphi_{\boldsymbol{p}}(t,r,\theta) = C_{\boldsymbol{p}}\, e^{-\mathrm{i}(\omega_{\boldsymbol{p}} t - l\theta)} J_l(pr)\,. \tag{4.34}$$

The boundary condition can be then found by enforcing $\phi(t,R,\theta) = 0$ on these mode functions. This effectively quantizes the radial momentum functions, where the physical modes are given by

$$p \to p_{ln} = \frac{u_{l,n}}{R}, \quad \text{with} \quad J_l(u_{l,n}) = 0\,. \tag{4.35}$$

where $u_{l,n}$ stands for the nth zero of the lth Bessel function. Because the lowest zero is positive and non vanishing, we have a system with no zero point mode. This means that introducing a physical maximum radius creates a mass gap (see fig. 4.7) [199]. As a consequence, the non-vanishing macroscopic field initial, $\Phi_0(t)$, condition is not physically realizable in this setting, which was to be expected from the geometry of the system itself.

We will now change to the l, n notation, with $\omega \to \omega_{l,n}$, $\varphi_{\boldsymbol{p}} \to \varphi_{l,n}$ and $C_{\boldsymbol{p}} \to C_{l,n}$.The latter, which corresponds to the normalization of the modefunctions, which is enforced by

$$\int \mathrm{d}^2x\, \varphi^*_{l,n}(x)\varphi_{l',n'}(x) = \frac{1}{2\omega_{l,n}}\delta_{l,l'}\delta_{n,n'}\,, \tag{4.36}$$

from which we can find,

$$C_{l,n} = \frac{1}{\sqrt{2\pi\omega}R|J'_l\left(p_{l,n}R\right)|} \tag{4.37}$$

With this solution the condition (4.29) is satisfied easily, and the total angular momentum is given by

$$\mathcal{L} = \sum_{l,n} l\, f_{l,n}(t)\,. \tag{4.38}$$

From this, we can see that if the distribution function is asymmetric, the total angular momentum will not vanish.

4.3.3 Observables and initial conditions

The most relevant observable we will compute is the distribution function, which in our case will give us information of the occupation of angular momentum modes, as well as the distribution of energy modes. To calculate it, we make an instantaneous projection against the free eigenmodes of the cylinder. That means that the process involves using

$$a_{l,n}|_t \equiv a[\phi_{l,n}(t), \pi_{l,n}(t)] \tag{4.39}$$

where $\phi_{l,n}(t)$ and $\pi_{l,n}(t)$ are the Fourier-Hankel transformed fields. This transformation is the one natural in our setting, because of the geometry of the disk., It takes a function from the coordinates r, θ to the l, n quantum numbers, and it is given by

$$f_{l,n} = \int \mathrm{d}r\, r \int \mathrm{d}\theta\, e^{-\mathrm{i}\, l\, \theta}\, J_l(p\, r)\, f(r,\theta) \tag{4.40}$$

$$f(r,\theta) = \frac{1}{\pi R^2}\sum_{l=-\infty}^{\infty}\sum_{n=1}^{\infty}\frac{1}{(J_{l+1}(u_{ln}))^2}e^{\mathrm{i}\, l\, \theta}\, J_l(p\, r)\, f(r,\theta)\,. \tag{4.41}$$

where the normalization, $(J_{l+1}(u_{ln}))^{-2}$, is necessary to guarantee that the Hankel-Fourier Transform (HFT) has a properly normalized inverse transform, However, this also gives the correct limit of the integral in the $R \to \infty$, limit. With this in mind, we can use expression 4.39 to calculate the mode distribution function

$$\langle a^\dagger_{ln} a_{ln}\rangle|_t = \left(f_{ln}(t) + \frac{1}{2}\right) \tag{4.42}$$

where the average is taken with respect to the classical statistical ensamble, which we will sample for two sets of initial conditions. We have the angular momentum depending initial conditions (LICs), where we highly occupy all the transverse modes for a particular angular momentum mode with $l = l_0$, namely

$$f_{0,ln} = \frac{n_0}{\lambda}\,\delta_{ll_0}\,\Theta(Q - p_{ln})\,. \tag{4.43}$$

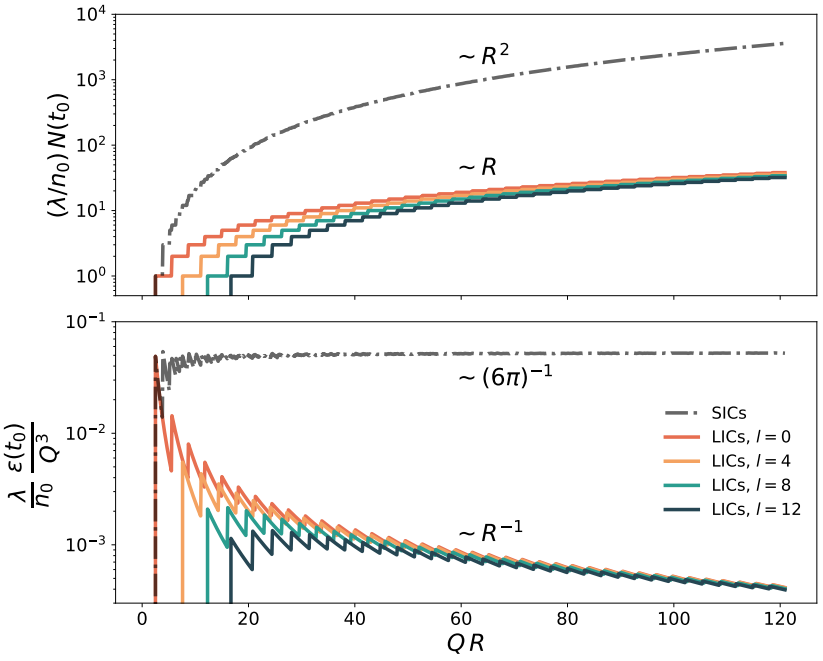

FIGURE 4.5: *Up:* Initial total number $N(t_0) = \sum_{l,m} f_{l,m}(t_0)$ in terms of the radius of the system. The angular momentum specific initial conditions (LICs) exhibit linear rise with the total R, while the standard initial conditions (SICs) rise quadratically on $N(t_0)$. *Down:* Initial energy density $\epsilon(t_0) = (\pi R^2)^{-1} \sum_{l,m} \omega_{l,m} f_{l,m}(t_0)$, in terms of the total radius. In the $R- > 0$ limit, the SICs saturate to the continuum limit result.

This initial condition can be contrasted by the *standard* initial conditions (SICs), in which all modes are highly occupied to some scale Q,

$$f_{0,ln} = \frac{n_0}{\lambda}\,\Theta(Q - p_{ln})\,. \tag{4.44}$$

It is important to note that our initial conditions are a construct of the finite size. In fig **??**fig:frac one can see the total initial occupancy and energy density for the LICs and SICs. As the radius increases, the SIC's occupation grows with the area, while the LICs do linearly with the radius. This has the consequence that in the $R \to \infty$ limit, our initial conditions will give a negligible amount of energy to the system. Nevertheless, in systems where angular momentum is relevant we will also have finite size effects, making this set if initial conditions important to study. In this work, we will only focus on the LICs, but in the future we would like to conduct a comprehensive comparison with the SICs. These are the angular momentum initial conditions (LICs). This ICs have a definite initial value for the $\mathcal{L}$, and one interesting point is that for a LIC at $l = 0$ we will have the only system in this work with exactly vanishing angular momentum. Finally, as it was said before, the homogeneous macroscopic field is not achievable in this setting, so we will not be testing it.

Before we jump to the discussion, we would like to explain the numerical discretization .

4.4 Lattice Discretization

For the numerical simulation we employ a uniform polar grid, meaning that the radial and the angular lattice spacing, Δr and $\Delta\theta$ are held constant. The lattice has N_r annuli plus the node at $r = 0$. Each annulus consists subsequently of N_θ lattice points. This results in a lattice spacing of $\Delta r = \frac{R}{N_r}$ and $\Delta\theta = \frac{2\pi}{N_\theta}$, where R is the radius of the disk. Solving the equation of motion requires the calculation of the time derivatives (achieved with the Runge–Kutta-4 method [221]) and the Laplacian on the uniform polar lattice:

$$\Delta = \partial_r^2 + \frac{1}{r}\partial_r + \frac{1}{r^2}\partial_\theta^2. \tag{4.45}$$

The radial derivatives are determined with the help of the finite-difference method. This means that in our polar grid (see figure 4.6), we can define the radial derivative as

$$\partial_r f(r,\theta) = \frac{1}{2\,\Delta r}\left(f_{n_r+1,n_\theta} - f_{n_r-1,n_\theta}\right), \tag{4.46}$$

and the second derivative as

$$\partial_r^2 f(r,\theta) = \frac{1}{(\Delta r)^2}\left(f_{n_r+1,n_\theta} - 2f_{n_r,n_\theta} + f_{n_r-1,n_\theta}\right), \tag{4.47}$$

where $f_{n_r,n_\theta} = f(r = \frac{n_r}{N_r}R, \theta = 2\pi\frac{n_\theta}{N_\theta})$ with $n_r \in \{1,...,N_r\}$, $n_\theta \in \{1,...,N_\theta\}$ two indices. We use a different method at the origin, considering it is a singular point of the Laplacian in polar coordinates. We switch to Cartesian coordinates and want to use the usual formula for the Laplacian in two dimensions:

$$\begin{aligned}\Delta f(0,0) = &\frac{1}{(\Delta x)^2}(f_{n_x+1,n_y} - 2f_{n_x,n_y} + f_{n_x-1,n_y}) \\ &+ \frac{1}{(\Delta y)^2}(f_{n_x,n_y+1} - 2f_{n_x,n_y} + f_{n_x,n_y-1}).\end{aligned} \tag{4.48}$$

We can choose our Cartesian coordinate system in $N_\theta/4$ different ways, always rotated by $\Delta\theta$ with respect to the previous system. In all of these systems, we calculate the Laplacian and average them out to get the final expression at the origin:

$$\Delta f(0,0) = \frac{4}{N_\theta(\Delta r)^2}\left(\sum_{n_\theta=0}^{N_\theta-1} f_{n_r=1,n_\theta} - N_\theta f_{n_r=0}\right). \tag{4.49}$$

The angular derivatives are carried out, by using spectral derivatives. This is feasible because of the periodic boundary condition of the angle. Spectral derivation yields more accurate results than finite-difference method, but requires more computational time.

For a function f defined on the discrete lattice of $\theta_n = \frac{2\pi n}{N_\theta}$, with $n \in \{0,1,...N_\theta - 1\}$, one can get the momentum modes $f(l)$, with $l \in \{-\frac{N_\theta}{2},...,\frac{N_\theta}{2}-1\}$, by discrete Fourier transforming:

$$f(l) = \sum_{n=0}^{N_\theta-1} f(\theta_n)\cdot e^{i\frac{2\pi}{N_\theta}ln}. \tag{4.50}$$

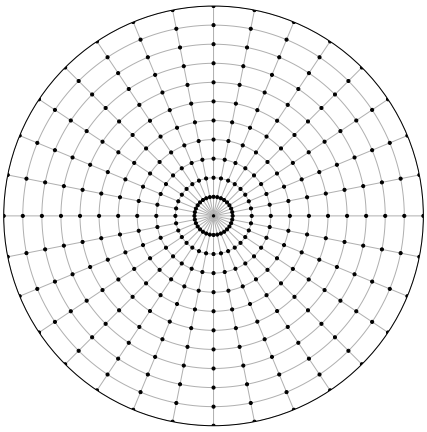

FIGURE 4.6: Pictorial representation of the discretization scheme used in this work.

Then, knowing the field in momentum space we can rewrite the second angular derivative in the following manner:

$$\begin{aligned}\partial_\theta^2 f(\theta_n) &= \sum_{l=-\frac{N_\theta}{2}}^{\frac{N_\theta}{2}-1} f(l)\,\partial_\theta^2 e^{-i\frac{2\pi}{N_\theta}ln} \\ &= -\sum_{l=-\frac{N_\theta}{2}}^{\frac{N_\theta}{2}-1} f(l)\,l^2 e^{-il\theta_n}.\end{aligned} \tag{4.51}$$

This means, that the second angular derivative of the field is just the discrete Fourier transform of $l^2\,f(l)$.

4.5 Results

We performed simulations for a single massless scalar in the polar grid, where we restricted us to the two initial conditions from the last section. We fix the number of points in the radial and angular dimensions to $N_\theta = N_r = 256$, where changes in the UV cutoff where performed, and no change was observed. We will present here simulations for a radius of $R = 64/Q$, for which the exponents of the angular momentum cascade proved to be insensitive. The radius dependence will become of importance As it is the case for the radius, every quantity in this section will be given in units of Q, the initial characteristic scale. For all the simulations presented here the coupling was chosen to be $\lambda/Q = 10^{-4}$.

If one wants to extract the full information of the distribution function, say angular and transverse momentum degrees of freedom, then the system appears to be sensitive to statistics. In studies conducted before [31, 131] the distribution is binned (folded) on some particular variable like the full direction or the azimuthal angle. This binning cures the dependence on statistics, making convergence faster. Nevertheless, if we want to extract scaling exponents for the full distribution, larger sample sets are needed. For the results at hand, we took ensambles of $N = 64$ realizations.

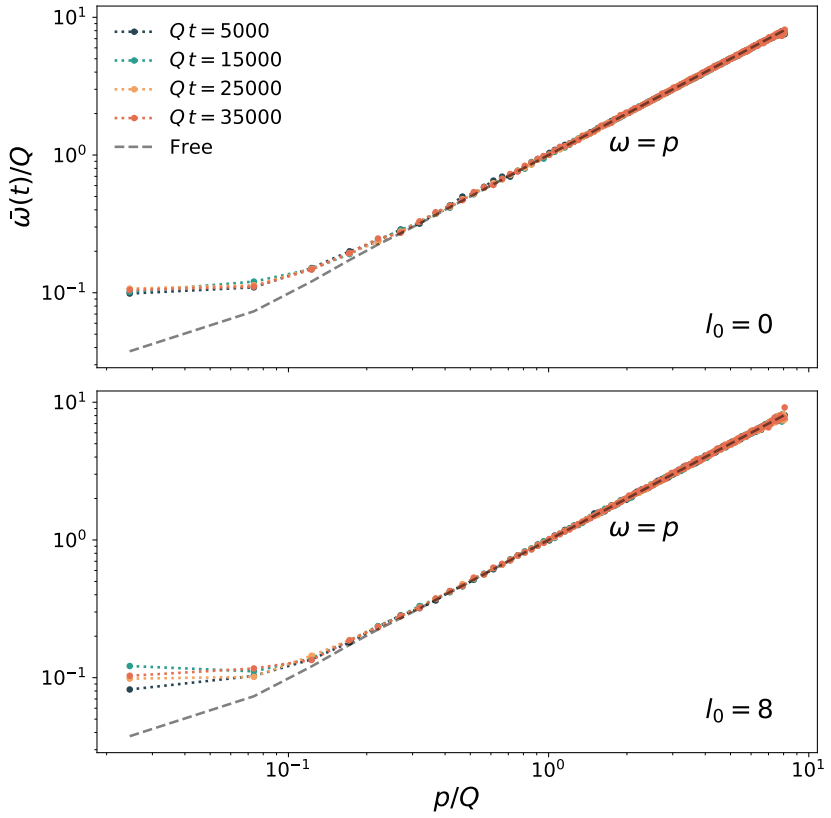

FIGURE 4.7: Generation of mass in the case of LICs, for $l_0 = 8$ and $l_0 = 8$. The dynamical mass gap is in both cases computed by fitting the curve with $w = \sqrt{m_{dyn}^2 + p^2}$, where $m_{dyn} = 0.082\,Q$. The dashed line corresponds to the free case, where a a geometrical mass gap $m_G = 0.02\,Q$ can be observed.

Nevertheless if we want to visualize our data effectively, binning will be necessary. We will present the angular momentum binned distributions, which is computed by averaging over on the transverse modes,

$$\tilde{f}_l(t) = \frac{1}{n_{max}} \sum_n f_{l,n}(t)\,. \tag{4.52}$$

We will also project the distribution along the physical p_{ln} modes, in what we will call p-binning. Nonetheless, the physical transverse momentum states are not equally spaced in momentum space. For this we created histograms of the modes, which makes the p-binning computationally more involved, where the spacing of the bins will not be smaller than the UV cutoff. The p-binned distribution function $\bar{f}(t,p)$ can be directly compared to the p dependent distribution, $f(t,|\boldsymbol{p}|)$, from ref. [131].

4.5.1 Generation of dynamical mass

In previous studies over relativistic scalar theories, the creation dynamical creation of a mass gap has been consistently observed. In our system, however, the creation of such mass gap has to dominate the dispersion over the *geometrical mass gap*, $m_G \sim 1/R$. To confirm the creation of such effect, we computed the dispersion

relation of the system, $w^{dyn}_{l,n}(t)$,

$$w^{dyn}_{l,n}(t) = \sqrt{\frac{K_{l,n}(t)}{F_{l,n}(t)}} \,. \tag{4.53}$$

with the correlation functions

$$\begin{aligned} F_{l,n}(t) &\equiv \langle \phi_{l,n}(t)\phi_{l,n}(t)\rangle_{cs} \,, \\ K_{l,n}(t) &\equiv \langle \Pi_{l,n}(t)\Pi_{l,n}(t)\rangle_{cs} \,. \end{aligned} \tag{4.54}$$

The resulting dispersion relation is a function of both quantum numbers, but it can be binned in p, to give a better sense of the scale at which mass is generated. The resulting dispersion, $\bar{\omega}(t,p)$ can be fitted the resulting curve with $\omega = \sqrt{m^2_{dyn} + p^2}$, where m_{dyn} gives the generated mass. In figure 4.7 we compare $\bar{\omega}(t,p)$ to the free case, obtained by binning $\omega_{l,n} = p_{l,n}$, where $p_{l,n}$ are the momentum eigenstates of the disk. We find a mass gap of $m_{dyn} = 0.082Q$, consistent for different initial angular momenta. It can be seen that the m_{dyn} dominates over the geometrical mass,$m_G = 0.02\,Q$. In previous works, this mass gap signals the separation of the relativistic and non-relativistic regime. Nevertheless, in this work, we will not focus on the inverse cascade regime [33, 131], since the finite size restricts strongly the momenta available to the system. In other words, in our current simulations we do not have enough modes to probe the scaling regime. We will the focus on more UV physics, where the system will redistribute its energy.

4.5.2 Scaling Exponents

We compute the exponents following the method of ref. [170], which depends in uses the moments of the distribution function to define an instantaneous set of exponents at an arbitrary time t. Given the scaling ansatz for our distribution,

$$f(t,l,p) = t^{\alpha} f_S(t^{\beta}\, l, t^{\beta}\, p) \,. \tag{4.55}$$

One can define the n,mth moment of the distribution as follows

$$g_{b,c} = \frac{1}{2R} \sum_{l,m} |l|^b \, p^c_{l,m} f_{l,m}(t) \,, \tag{4.56}$$

where one can use them to get an algebraic equation,

$$\frac{\mathrm{d}\, g_{a,b}(t)}{\mathrm{d}\log t} = \alpha(t) + b\,\beta(t) + c\,\gamma(t) \,. \tag{4.57}$$

To solve for this equation, one needs to pick a set of of three different moments,

$$\begin{aligned} \begin{pmatrix} g'_{a_1,b_1}(t) \\ g'_{a_2,b_2}(t) \\ g'_{a_3,b_3}(t) \end{pmatrix} &= \begin{pmatrix} 1 & a_1 & b_1 \\ 1 & a_2 & b_2 \\ 1 & a_3 & b_3 \end{pmatrix} \begin{pmatrix} \alpha \\ \beta \\ \gamma \end{pmatrix} \\ &\equiv A \begin{pmatrix} \alpha \\ \beta \\ \gamma \end{pmatrix} \,. \end{aligned} \tag{4.58}$$

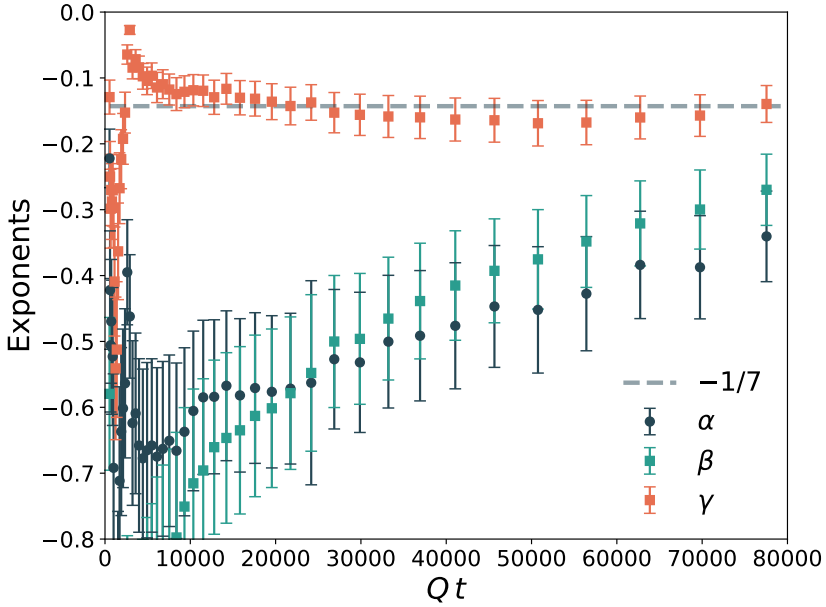

FIGURE 4.8: Exponents

We compute the exponents by solving for moments with $n, m = 1, ..., 4$, for all contributions with $\det A \neq 0$ and we average over them. One can find the variance of the average to quantify the error.

The processes observed in these simulations are of two kinds, an angular momentum cascade, which pushes l to higher values, and a energy cascade, pushing energy modes to higher values. For each of these processes, there is an associated conservation law. In the case of angular momentum,

$$\mathcal{L} = \sum_{l,n} l\, f_{l,n}(t)\,. \tag{4.59}$$

Plugging in the scaling ansatz, eq.(4.55), one can get a constrain on the exponents $\alpha = \beta$. On the other hand, if energy is conserved on a regime of the distribution,

$$\epsilon = \frac{1}{2R} \sum_{l,n} p_{l,n}\, w_{l,n}\, f_{l,n}(t)\,, \tag{4.60}$$

since for a relativistic scalar $\omega(p) = t^{-\beta z}\omega(pt^{\beta})$, then one can see that for a two-dimensional, discreet system one gets, $\alpha = 2\gamma$. The p binned function, however, gets an extra power of γ in the binning process, behaving like the expected continuum function[2]. We therefore obtain two different gammas, where $\bar{\alpha} = 3\alpha/2$. For the relativistic energy cascade the following exponents were found [33, 131] for a perturbative kinetic kernel with scaling function, $f(t,p) = t^{\alpha} f_S(pt^{\gamma})$,

$$\alpha = -\frac{d+1}{2m-1}, \quad \gamma = \frac{-1}{2m-1} \tag{4.61}$$

where m stands for the respective power of the self-interaction in the scalar Lagrangian. In our case, ϕ^4, so $m = 4$. This means that we get for a 2 dimensional

[2] In the large R limit, the integral becomes $\langle p_n \rangle = \frac{1}{2R} \sum_{i=bins} p^n\, f(t,p) \to \int \mathrm{d}p\, p^n\, \bar{f}(t,p)$

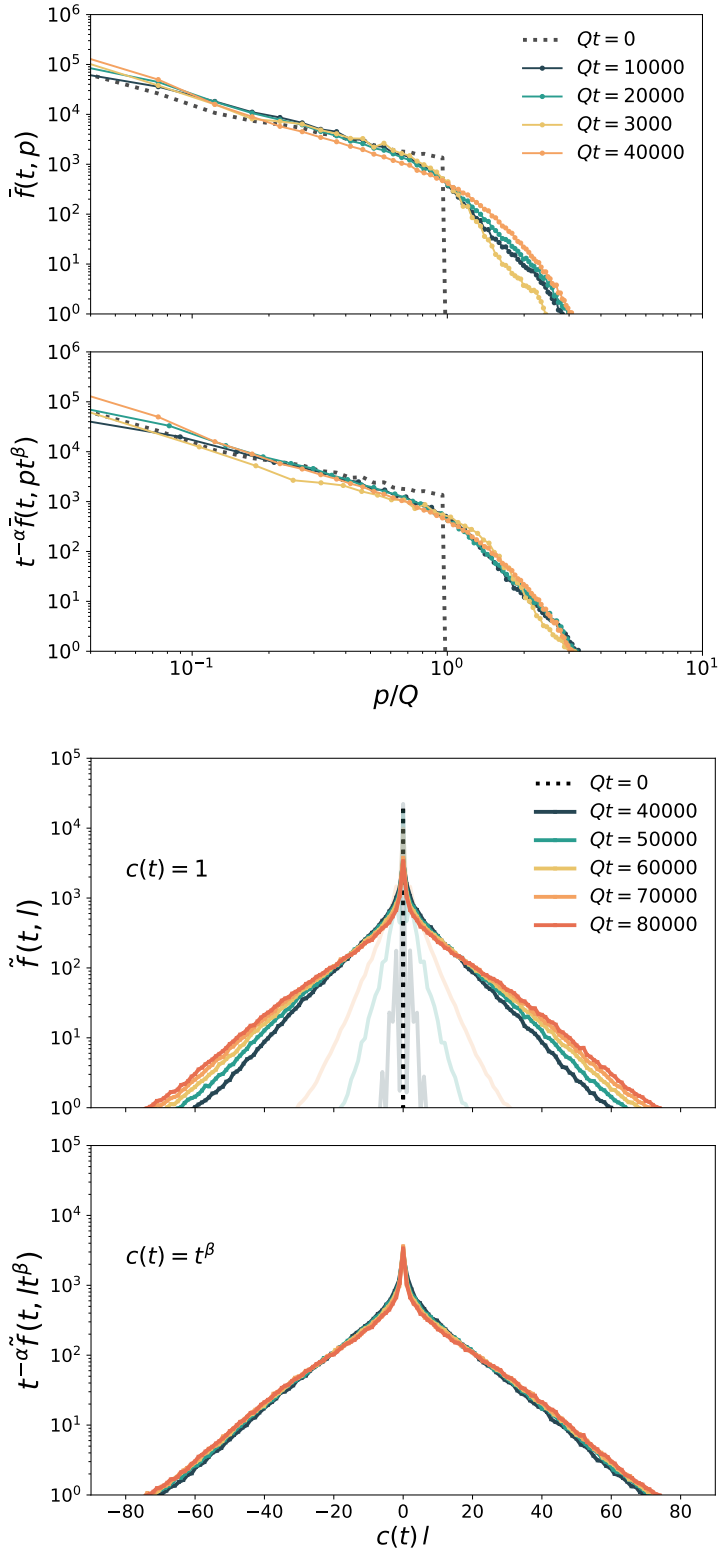

FIGURE 4.9: Scaling of the p and l-binned, *up* and *down*, respectively, distribution $\tilde{f}(t,p)$ for vanishing initial angular momentum, using $\gamma = -1/7$ and $\alpha = \beta = -2/7$.

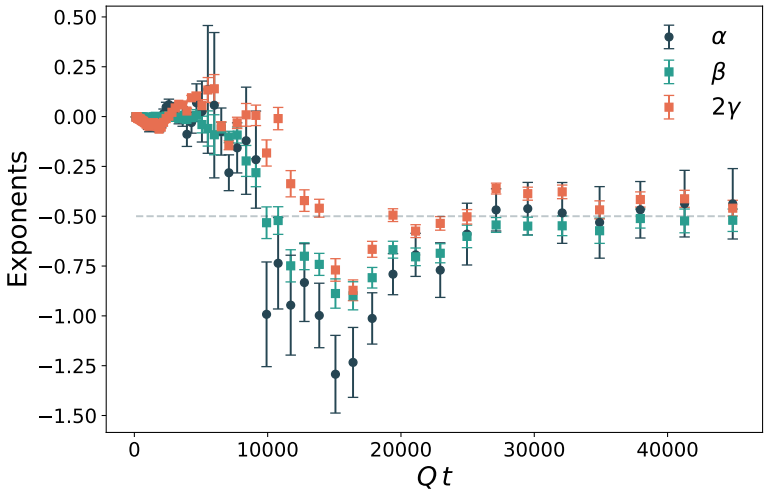

FIGURE 4.10: Scaling exponents for the non-vanishing angular momentum case, where $\alpha = \beta = 2\gamma \approx 0.5$. These exponents are quite robust agains changing the position of the initial peak.

system, $\alpha = -3/7$, and $\gamma = -1/7$. We can confirm this exponent for the case vanishing angular momentum, $l_0 = 0$. For this case, it is observed that γ evolves in time to rapidly converge close to the value of $-1/7$ (see fig. 4.8). Notice also that, up to errorbars, α and γ are the same. This is a consequence of angular momentum conservation. Moreover, we can observe how the global conservation of $\mathcal{L}$ is a stronger constraint that the energy conservation. Naturally, this will be also a feature of the non-vanishing systems. Under these considerations the system seems to be continuously relaxing towards the simultaneous conservation of L and ϵ.

In fig. 4.9 we can see the time evolution of the distribution function. It is clear to see that in transverse momentum, the system is redistributing its energy to higher p values. Nevertheless, using the skater analogy, this cascade is expected to trigger the shift to higher angular momenta, which can also be seen in fig. 4.9. Particles in this system will start to rotate (counter)-clockwise in equal amounts, which will create highly occupied fluctuations in $\mathcal{L}$, even if the total value is conserved. This shift is a consequence of the system trying to relax into the thermal equilibrium state [200],

$$f_{l,n} = \left[\exp\left(\frac{\omega_{l,n}}{T} - l\,\Omega\right) - 1\right]^{-1} \tag{4.62}$$

where Ω is the total global rotation of the system, and signals the total angular momentum after thermalization. Because of angular momentum conservation, for $l_0 = 0$ one would get $\Omega = 0$.

The role of angular momentum

We performed simulations for non-vanishing angular momentum by placing the over-occupied peak at $l_0 = 4$ and $l_0 = 8$. The results found don't depend on the position of the peak. For this system we found $\alpha = \beta = 2\gamma \approx 0.5$. It is particularly interesting to observe here the behavior of γ, in contrast for the $\mathcal{L} = 0$ case. In this case, this exponent diverges from the prediction from kinetic theory, being completely incompatible to this value for the statistical error bars. Nevertheless, the statistical uncertainties for β and α are still quite high, and more simulations

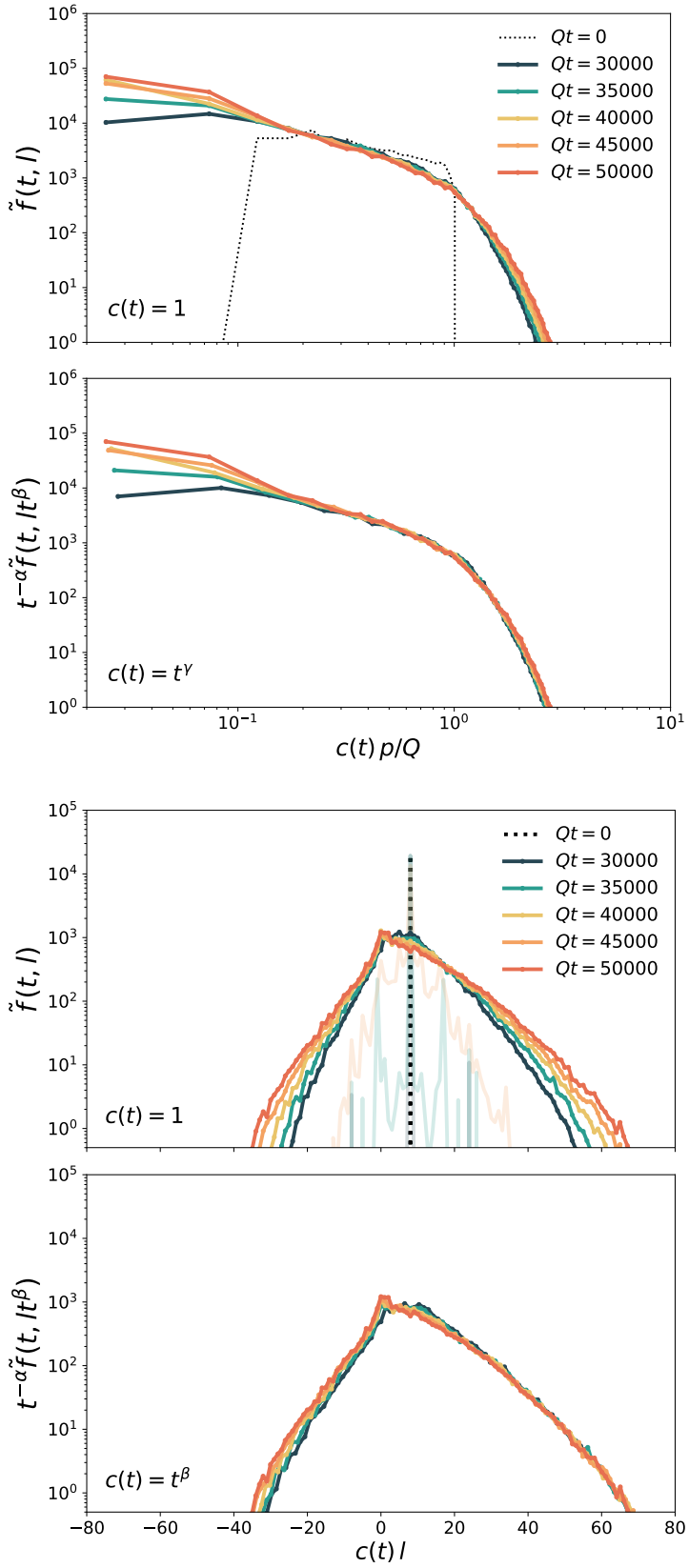

FIGURE 4.11: Scaling of the p and l-binned, *up* and *down*, respectively, distribution $\tilde{f}(t, p)$ for vanishing initial angular momentum, using $\gamma = -1/7$ and $\alpha = \beta = -2/7$.

are needed to better understand these exponents. We observe that for these initial conditions both the energy and angular momentum conservation cascades are achieved quite rapidly. We can observe that the relations between the exponents are satisfied in fig. 4.10.

Just as in in the case with vanishing angular momentum, in fig. 4.11 we can see the time evolution of the distribution function. Once again, it is the same mechanism, there is a shift of energy momenta to higher values, which triggers the shift of to higher angular momenta. In this case, particles are accelerated, but there is a clear imbalance in the direction of rotation. An interesting caveat, is that the system is not a shift of last section's to non-vanishing l. Instead, at late times, it presents its maximum occupancy around $l = 0$, but with different tails for negative and positive angular momentum (see the l-binned function in fig. 4.11). Just as in the case for Ω in thermal equilibrium, this means that modes moving along the global rotation will feel enhanced. However, the $l = 0$ mode will be blind to this effect.

4.6 Conclusions

In this chapter we presented the first simulation of a classical statistical system for a total non-vanishing angular momentum, as well as the first dynamical simulation of a Dirichlet bound system. Although exactly vanishing boundaries are not realizable in real life, systems for which exhibit physical boundaries and finite size effects may benefit from these studies, such as trapped cold atoms and the expanding fireball in HICs experiments. An angular momentum cascade was found regardless of the initial angular momentum, the characteristic angular momentum is pushed to higher values. We interpret that this cascade seems to be triggered by an energy cascade. In the case of vanishing angular momentum, we recover the perturbative results.

It was also found that for non-vanishing angular momenta, we cannot recover the standard two-dimensional results, found in ref. [131]. These novel exponents seem to be universal, as they are insensitive to the position of the initial angular momentum peak. However, whether we have here a new universality class or not, needs to be investigated further.

This is currently work in progress, and in our next goal is to extend these studies to have a comprehensive dependence on the system size, R. This will allow us to access more infrared modes, for which presumably we would get back the inverse cascade of ref. [131]. Since infrared modes do not contribute largely to the total angular momentum, one can speculate that the exponents for an inverse cascade will not change. Furthermore, there are still many features of this system to be explored before going to more complex settings, such as full $O(N)$ or full gauge $SU(N)$. In future work, we want to focus on the standard initial conditions. We would like to compute also the angular momentum operator, for which fluctuations may be explored.

Summary and Outlook

As a unit, the work presented in this summarizes our interest in the question of complexity arising from quantum degrees of freedom. We have engaged especifically in the thermalization of quantum fields, especially nuclear matter, in the area of Heavy Ion Collision experiments. For this endeavor, a wide array of techniques have been applied, including from semi-perturbative QCD, kinetic theory, hydrodynamical modeling as well as non-equilibrium QFT in the classical statistical limits. This thesis is then a collection of studies which comprise the efforts to understand the initial and early stages of the creation of a gluon medium, prior to the thermalization of the QGP.

In Chapter 1 we introduced the Color Glass Condensate framework, which is an effective field theory of QCD at high energies. In this theory, one enforces a separation of scales and from this retrieves the features of gluon saturation as an emergent property. Both saturation and the CGC are concepts of vital importance for the rest of the thesis, especially Chapters 2 and 3. Using the CGC EFT [13], we computed the NLO cross-section for the $gg \to q\bar{q}\gamma$ channel in the dilute-dense limit, when the projectile partons exhibit low densities, $\rho_p/\boldsymbol{k}_{1\perp}^2 \ll 1$, while the target is probed at high occupancies, $\rho_t/\boldsymbol{k}_{2\perp}^2 \approx 1$. This channel, the collinearly enhanced gluon-photon bremsstrahlung process, $qg \to qg\gamma$, and the annihilation channel, $gg \to q^*\bar{q}^* \to \gamma$ comprise all the contributions at the NLO. Nonetheless, for inclusive photon production at high energies or small rapidities, where small-x, is probed, our process dominates the cross-section.

Furthermore, because of the rapid increase of the gluon distributions when probing low-x gluons, the traditional power counting is broken[68, 69], making necessary to compare not only powers of α_s, but also include the distributions themselves into the weighing of the processes. The reader can see in fig. 1.1, that already around $x \sim 10^{-2}$ the gluon distribution is higher than their valence quark counterpart, with $xf_q(x,Q^2) \lesssim xf_g(x,Q^2)$ [42]. This compensates parametrically any process which happens after a gluon from the target splits into $q\bar{q}$ pair, finally shifting the order of contributions. In this work we showed this numerically, where at high energies and small rapidities, the NLO $gg \to q\bar{q}\gamma$ process takes over the cross-section. We use the one data point inside our range of validity to fix the normalization with an overall parameter which arises from the uncertainty of the volume fixing, as well as the logarithmic corrections. This paramater was used to make our prediction on isolated photon at p+p collision for $\sqrt{s} = 13$ TeV. In future investigations we will use this fixing to compute the observables for p+A collision in RHIC and ALICE.

In Chapter 2, we propose a simple model, inspired in the *bottom-up* thermalization scenario [28] and the parametric estimate of ref. [35]. This assumes gluon saturation happens for heavy nuclei at RHIC and LHC. The collision of two saturated nuclei creates a highly occupied colored medium of deconfined gluons , commonly called Glasma in the literature. As the medium expands against the vacuum, the dilution of the gluon density is mitigated by the effect of the gluon scatterings.

Later on, low-energetic gluons take over, and thermalize fast. This low-energetic sector serves as a bath for the rest of the system, which then thermalizes at a time $Q_s\,\tau_{th} \approx \alpha_s(s)^{-13/5}$. Furthermore, the behaviour described by the bottom-up scenario was confirmed by classical statistical simulations [132, 145, 170]. Using the results of the BMSS scenario for the evolution of the gluon unintegrated distribution, we compute the photon invariant and total yields using a kinetic theoretical approach for the two-to-two LO processes, where the full computation has been simplified by using the small angle approximation. For this, quarks are taken to be created in-medium via hard gluon splitting, $f_q = \alpha_s f_g$, where they directly inherit the scaling properties from their parent gluon .

The different contributions of the scenario were compared. It was found that, while the thermal and non-thermal total photon yield are of the same order [35], the spectrum is completely dominated by the enhanced pre-equilibrium contribution. Furthermore, we performed a one-to-one comparison of thermal and non-thermal scenarios where in the *early thermalization* scenario we initialize the hydrodynamical phase at the initial bottom-up time, $Q_s\,\tau_0 \approx 1$. The pre-equilibrium stages give still a higher contribution, but for realistic realizations, the spectra is not distinguishable by experiment. Finally, we find good agreement with data, when compared to ALICE and PHENIX photon spectra and total yields. This agreement holds up to a normalization constant, which bundles the uncertainty from the volume and from the cut-off in the small angle approximation.

Because of the homogeneity and late thermalization in this model, it fails to explain the photon flow coefficients. Nevertheless, this does not mean, by any accounts, that angular anisotropies may not be reproducible by an enhanced version of our model. In future investigations, we would like to introduce spacetime anisotropies in the spectrum. In future investigations, we would like to look into the evolution of the fluctuations around the scaling solutions. From such results, a phenomenologically reachable parametrisation may be found to account for the expansion during the early stages.

In Chapter 3, we have explored photon Hanbury-Brown-Twiss interferometry in HIC experiments as a tool to probe the space-time evolution of the fireball. As it was said above, it is difficult, if not impossible, for an experiment to distinguish between the thermal and non-thermal contributions using one-photon distribution (or invariant yield). However, photons are produced at all times during the expansion of the fireball. One can then extract information directly by investigating how are they correlated to each other. In Chapter 3 we have introduced the HBT correlator, as well as the approximations and variables commonly used in the literature. We have also introduced the concept of the homogeneity radii, which will be used as a means to discriminate models and to extract information of the spatial and temporal size of the photon sources.

Using this framework, we have performed a comparison for the model introduced in Chapter 2, inspired by the *bottom-up* scenario, as well as its early thermalization counterpart. We observed a big contrast between these two cases, where the longitudinal correlator for pre-equilibrium photons decays in a significant slower pace. This translates to a smaller measurable homogeneity radius, which was computed using three different methods. It was observed that non-gaussianities, which contain information from the expansion of the fireball decrease the effective correlation lengths computed using the second moment of the correlator. The other two methods had very similar results, but being based in the assumption that the correlators are Gaussian, they fail to account the mixing of signals in the model. We

postulate then that if the BMSS scenario is the correct description of the early expanding fireball, we would be able to observe big deviations from the longitudinal correlator.

From this model we get, however, no understanding of the transverse plane. To account for spatial distributions and anisotropies, we propose a hybrid model that enhances a hydrodynamical simulation with a pre-equilibrium stage. The latter will be identical to the first stage of the BMSS scenario, which we match using the energy density at thermalization time, $\tau_{th} = 0.6$ fm. This extra source is expected to affect the yields, but not the anisotropy parameters. We computed the HBT correlators in the diagonal directions, q_i and $q_j = q_k = 0$, with $j, k \neq i$, where we observe that the longitudinal one is the most non-gaussian, followed by the outward direction, and last we see an almost Gaussian sideward correlator. We observe small changes in the s, o directions coming from the pre-equilibrium source, while the l-direction exhibits more change. This translates to the homogeneity radii where we extracted R_l, R_o, and R_s. In the longitudinal radius we can observe the biggest difference between the thermal and the *full* evolution, while the other two directions present corrections smaller than 15%. Based on this, we propose that if thermal model can predict the $R_{o,s}$ radii, but not R_l, this is strong evidence that a longer pre-equilibrium stage is realized in experiment.

It is the opinion of the author that the true power of photon HBT lies in their stark sensitivity to the evolution of the fireball. We can take advantage of this property to use the correlators and the radii, to further discriminate ideas of the evolution of the fireball. Furthermore, in the future, HBT may prove to be useful to understand experimentally the onset of hydrodynamics.

At initial time, a HIC with non-vanishing impact parameter will exhibit an incredible amount of angular momentum. This has been explored for thermal settings [34, 200], where it has been suggested that anomalous currents will rise, from the coupling of chiral charge with the angular momentum [222]. Nevertheless, the relevance of introducing this extra conserved quantity in non-equilibrium simulation has never been addressed. In Chapter 4 we have introduced a toy model which mimics two features not represented before in classical statistical simulations, non-vanishing angular momentum and a physical, finite volume. For this we bind a scalar field theory inside a two-dimensional disk, setting the field to vanish outside of this area. The field was initialized in a highly occupied state, for specific single angular momentum states, $l = l_0$. During the evolution of the system, an angular momentum cascade is observed for all values of initial l_0, where occupation is pushed forward, to faster rotating modes.

For vanishing angular momentum, we recover the perturbative results for a relativistic energy cascade. However, for the non-vanishing angular momentum case, we were not able to do so. Interestingly, the exponents computed for the latter case, $\alpha = \beta = 2\gamma \approx 0.5$, are insensitive to the change of the position of the initial peak. To be able to elucidate whether the inclusion of angular momentum consists a new class of universality, we will have to conduct a comprehensive study over the system. Two main avenues are needed, a deeper study on the radial dependence on dynamics, and a comparison with what we called in Chapter 4, the standard initial conditions. These SICs are interesting, since they give a vanishing expectation value for$\mathcal{L}$, but event-by-event they present non-vanishing values. These future studies will allow us to better understand the role of rotation quantum fluids in the path to thermalization.

Foreword

Heavy ion collision experiments are at the intersection of many areas in physics. While the main obejective of this research program may be to explore the possibility of obtaining a deconfined medium of quarks and gluons, the techniques and underlying mechanisms can be translated to a plethora of other systems. It is the case, for example, of non-equilibrium quantum field theory, which as it has extensively been repeated in this work, unifies in one language the phenomena occurring across a vast expanse of scales and temperatures. This is just the beginning. With the recent convergence of quantum computation and nuclear physics, [223] heavy-ion collision experiments pose as an exciting path to explore collectivity and complexity, not only by itself, but also by walking the road of interdisciplinarity.

Acknowledgements

First of all, I want to thank my supervisor, Jürgen Berges for having me in his working group. I have learned many things from him, in the scientific realm, but also outside of it. I want to thank him for being understanding and encouraging both in my worst and best times. Working with him is always inspiring, and I by doing it I have also learned a lot about myself. I thank you for that.I would like to thank Raju Venugopalan for triggering me to take on the road to phenomenology. He has been a great mentor, and I always enjoy our discussions (which are always at 14:15 pm).

I would like to thank everyone that read this work: Aleksas, Kirill, Torsten, Robert and Felipe.

Of course, I thank my parents, who have always been unconditionally there for me. They have been exceptional parents to me, and I hope always to show them how much I love them. Without their support, their help, their mere presence, this work would have not been possible. And my sister, who has been always proud of me, but not, by a long shot, as much as I am of her.

To my office mates across space and time: Asier, Valentin, Ignacio, and Michael. My interactions with you guys ranged from the infuriating to hilarious, going through the realm of the painly bizarre. I would specially like to thank Torsten, who has had the nightmarish task of sharing an office with me. I thank also Robert, for constantly *broing* out. I thank Alexander Lehman for his extreme take on this last bit. I will say our office life could be a sitcom, I stand by it. To all other group members, friends of the which were great, Naoto, Jan, Aleksandr, Alexander, Alexander and Alexander. I thank Eduardo Grossi, for our general talks, both accompanied by either a coffee or a beer (I think exclusively). Many thanks to Aleksas Mazeliauskas for being insanely motivating or an absolute pain in my back, depending on what was needed.

To Santiago Casas, who is the most obnoxiously funny person to ever roam the Earth. A lot of great stories I have from Heidelberg are thanks to that, I have to confess. Mary Baeb, always there to listen to my emotional knots. To Fabio, the Bro, who was always up for a beer, or a coffee, or just talking. May you never forget your ID ever again in the future. To my friends from Chile, who welcomed me in their group when I didn't know anyone else in this city: Mauricio, Fabian, Gustavo, Marcelo, Miguel and Alda (the chilombian). You have made me laugh beyond repair, and I thank you for that. To my friend and flatmate Fabian, the blonde latino. He was always interested in the ideas contained in this work. Always asked me about the little drawings in my papers -that includes equations-, and enquired about them. To my friend Ana Marta, who was my support towards the end, as I hope I have been for her, d as well as company in despair. My close friends in Costa Rica, Oscar, Melissa, Paula, and Raquel. Although the distances are long, you are always in my heart, and you were my second anchor for the times I was back home, but I felt like a tourist in my own land.

To Felipe Momo, I could write paragraphs on you, mate. I am going to summarize it by saying that you are a real friend to me. Between the parties, freak-outs and discussions on physics, which sometimes were not mutually exclusive in time, as well as the visits to Köln and your visits here I have great stories to tell. As I said, I a true friend in you, I hope to have demonstrated that it goes both ways.

To Heike, who was my support during most of this process and even across the distance. This is my achievement as much as yours.

I would like to thank multiple cafés around Heidelberg that had me at some point writing this thesis, some paper, or just being there working on some project. I would like to thank particularly Rada Café and of course my friend Rafael, for always being interested in my work, even when I may have strayed in my explanations. On that note, I would like to thank Coffee, Mate and Tea once again for all their help and joy throughout these years.

To anyone else I may have forgotten, I apologize.

Finally, I would like to thank HGS-HIRe for their financial support throughout these years. Particularly the administrative staff, who was always extremely helpful and diligent. I would especially like to thank also Manuela Wirschke and Tina Kuka, who have been always kind to me, even when I made mistakes and need my hide to be rescued. This work is part of and supported by the DFG Collaborative Research Centre "SFB 1225 (ISOQUANT)".

Appendix A

Dirac traces

In the calculation of the NLO a grand total of fourteen non-vanishing diagrams need to be summed over to get the total amplitude, which can be then squared and integrated over to give the inclusive photon cross-section. These diagrams have the property that they can be classified into four different classes. Class A in fig. A.1 refers to a gluon first scattering of the target's shockwave to then split into a $q\bar{q}$ pair, which afterwards emits a photon. In Class C the gluon fluctuates into the pair, which interacts with the dense state, while emitting, before or after a single photon. Class B represents the same process, but restricted to only the (anti) quark scattering off the target. The last diagram in fig. A.1 (Class D) arises from the gauge choice and it is not present in the case of light cone gauge. Physically it represents the probability of the pair scattering off the shockwave exactly at the phase space point at which it is created.

Diagrams of Class A and D have to be summed over, and yield the cancellation of the gauge artifact C_V. The hard factor resulting of the multiple scattering of the projectile gluon off the target is given then by

$$T_g^\mu(\boldsymbol{k}_{1\perp}) \equiv \sum_{\beta=1}^{2} R_\beta^\mu(\boldsymbol{k}_{1\perp})\,, \tag{A.1}$$

where $R_\beta^\mu(\boldsymbol{k}_{1\perp})$ stand for the the Dirac structures of each individual diagram. For the case of the rescattering of a gluon, $\beta = 1, 2$, the hard factors are given explicitly by

$$\begin{aligned} R_1^\mu(\boldsymbol{k}_{1\perp}) &\equiv -\gamma^\mu \frac{\not{q} + \not{k}_\gamma + m}{(q+k_\gamma)^2 - m^2} \frac{\not{C}_L(P, \boldsymbol{k}_{1\perp})}{P^2}\,, \\ R_2^\mu(\boldsymbol{k}_{1\perp}) &\equiv \frac{\not{C}_L(P, \boldsymbol{k}_{1\perp})}{P^2} \frac{\not{p} + \not{k}_\gamma - m}{(p+k_\gamma)^2 - m^2} \gamma^\mu\,. \end{aligned} \tag{A.2}$$

The vector structure C_L is the well-known Lipatov vertex, and represents an effective rescattering of a reggeized gluon off an incoming single gluon. It is given in momentum space by

$$\begin{aligned} C_L^+(q, \boldsymbol{k}_{1\perp}) &= q^+ - \frac{\boldsymbol{k}_{1\perp}^2}{q^- + \mathrm{i}\epsilon}\,, \\ C_L^-(q, \boldsymbol{k}_{1\perp}) &= \frac{(\boldsymbol{q}_\perp - \boldsymbol{k}_{1\perp})^2}{q^+} - q^-\,, \\ C_{L\perp}(q, \boldsymbol{k}_{1\perp}) &= \boldsymbol{q}_\perp - 2\boldsymbol{k}_{1\perp}\,. \end{aligned} \tag{A.3}$$

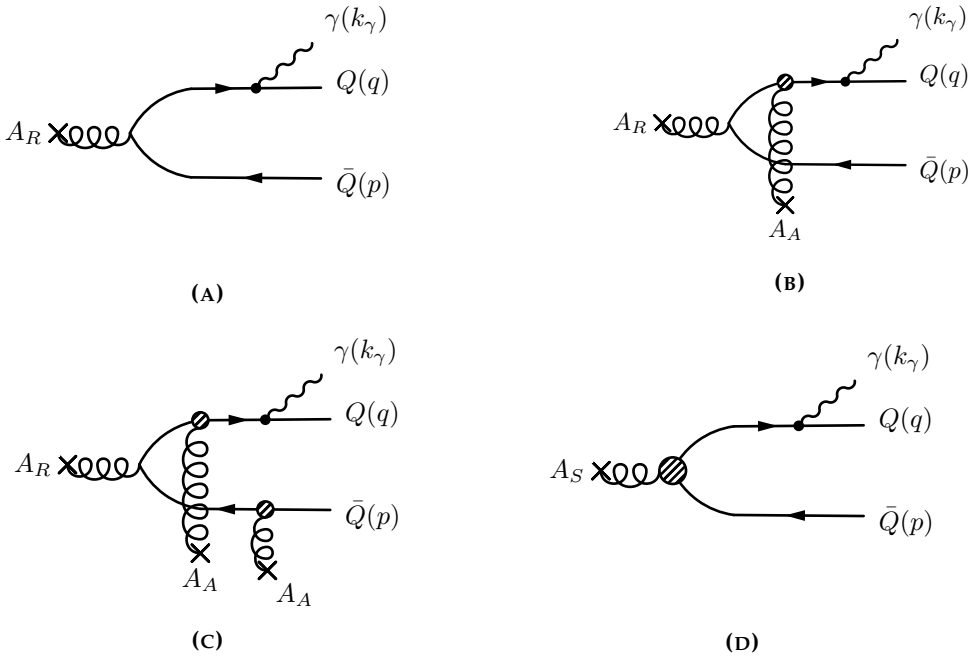

FIGURE A.1: The four sub-classes contributing to the full NLO contribution in the CGC power counting. In these diagrams, A_R corresponds to the regular field, for which $q\bar{q}$ splitting happens explicitly outside of the target, while A_S the remaining term, in which the splitting happens exactly at the moment of scattering. The gluon scattering effective vertex, given here by the small blob, contains all twist corrections to the rescatetering. Diagrams taken from ref. [69]

As it was stated in sec. 1.3, the Lipatov vertex is related to the quantities C_U and C_V via the relation $C_L = C_U + C_V/2$, where these vectors are expressed as

$$\begin{aligned} C_U^+(q,\boldsymbol{k}_\perp) &\equiv -\frac{\boldsymbol{l}_\perp^2}{q^- + i\epsilon}, & C_V^+(q) &\equiv 2q^+, \\ C_U^-(q,\boldsymbol{k}_\perp) &\equiv -\frac{\boldsymbol{k}_{2\perp}^2 - \boldsymbol{q}_\perp^2}{q^+}, & C_V^-(q) &\equiv 2\frac{\boldsymbol{q}_\perp^2}{q^+} - 2q^-, \\ \mathbf{C}_{U\perp}(q,\boldsymbol{k}_\perp) &\equiv -2\boldsymbol{k}_\perp, & \mathbf{C}_{V\perp}(q) &\equiv 2\boldsymbol{q}_\perp \ . \end{aligned} \tag{A.4}$$

The diagrams of Class B bring up six additional hard factors, which are encoded in the Dirac traces T_q and $T_{\bar{q}}$. The former encodes all diagrams for the single scattering of the quark off the target, while the latter comprises the same process for the antiquark line,

$$T_q^\mu(\boldsymbol{k}_{1\perp}) \equiv \sum_{\beta=3}^{5} R_\beta^\mu(\boldsymbol{k}_{1\perp})\,, \qquad T_{\bar{q}}^\mu(\boldsymbol{k}_{1\perp}) \equiv \sum_{\beta=6}^{8} R_\beta^\mu(\boldsymbol{k}_{1\perp})\,. \tag{A.5}$$

Note that these are the same structures that come about in the $\boldsymbol{k}_\perp$-factorized result (1.26), and in the collinear limit, comprise the hard factors of the pQCD calculation. The structures T_q and $T_{\bar{q}}$ can be expressed in terms of the individual,

which are

$$
\begin{aligned}
R_3^\mu(\boldsymbol{k}_{1\perp}) &\equiv \gamma^\mu \frac{\not{q} + \not{k}_\gamma + m}{(q+k_\gamma)^2 - m^2}\gamma^+ \frac{\not{k}_{1\perp} - \not{p}_\perp + m}{2(q^+ + k_\gamma^+)p^- + M^2(\boldsymbol{k}_{1\perp} - \boldsymbol{p}_\perp)}\gamma^- \,, \\
R_4^\mu(\boldsymbol{k}_{1\perp}) &\equiv -\gamma^+ \frac{\not{q} + \not{k}_{1\perp} - \not{P}_\perp + m}{2q^+(p^- + k_\gamma^-) + M^2(\boldsymbol{k}_{1\perp} - \boldsymbol{p}_\perp - \boldsymbol{k}_{\gamma\perp})} \\
&\quad \times \gamma^\mu \frac{\not{k}_{1\perp} - \not{p} + m}{2(q^+ + k_\gamma^+)p^- + M^2(\boldsymbol{k}_{1\perp} - \boldsymbol{p}_\perp)}\gamma^- \,, \\
R_5^\mu(\boldsymbol{k}_{1\perp}) &\equiv \gamma^+ \frac{\not{p}_\perp + \not{k}_{\gamma\perp} - \not{k}_{1\perp} - m}{2q^+(p^- + k_\gamma^-) + M^2(\boldsymbol{k}_{1\perp} - \boldsymbol{p}_\perp - \boldsymbol{k}_{\gamma\perp})} \\
&\quad \times \gamma^- \frac{\not{p} + \not{k}_\gamma - m}{(p+k_\gamma)^2 - m^2}\gamma^\mu \,,
\end{aligned}
\tag{A.6}
$$

for the scattering in the quark line, while

$$
\begin{aligned}
R_6^\mu(\boldsymbol{k}_{1\perp}) &\equiv \gamma^- \frac{\not{q}_\perp - \not{k}_{1\perp} + m}{2(p^+ + k_\gamma^+)q^- + M^2(\boldsymbol{k}_{1\perp} - \boldsymbol{q}_\perp)}\gamma^+ \frac{\not{p} + \not{k}_\gamma - m}{(p+k_\gamma)^2 - m^2}\gamma^\mu \,, \\
R_7^\mu(\boldsymbol{k}_{1\perp}) &\equiv -\gamma^- \frac{\not{q} - \not{k}_{1\perp} + m}{2(p^+ + k_\gamma^+)q^- + M^2(\boldsymbol{k}_{1\perp} - \boldsymbol{q}_\perp)} \\
&\quad \times \gamma^\mu \frac{\not{p} + \not{k}_{1\perp} - \not{P}_\perp - m}{2p^+(q^- + k_\gamma^-) + M^2(\boldsymbol{q}_\perp + \boldsymbol{k}_{\gamma\perp} - \boldsymbol{k}_{1\perp})}\gamma^+ \,, \\
R_8^\mu(\boldsymbol{k}_{1\perp}) &\equiv \gamma^\mu \frac{\not{q} + \not{k}_\gamma + m}{(q+k_\gamma)^2 - m^2}\gamma^- \\
&\quad \times \frac{\not{k}_{1\perp} - \not{q}_\perp - \not{k}_{\gamma\perp} - m}{2p^+(q^- + k_\gamma^-) + M^2(\boldsymbol{q}_\perp + \boldsymbol{k}_{\gamma\perp} - \boldsymbol{k}_{1\perp})}\gamma^+ \,,
\end{aligned}
\tag{A.7}
$$

are the structures from the antiquark line diagrams. The complex momentum dependence, here as for $T_{q\bar{q}}$, arises from the integration over k^- in the internal lines of the (anti) quark lines.

Additionally, Class C diagrams are constructed from the scattering of both the quark and antiquark lines into the target,

$$
T_{q\bar{q}}^\mu(\boldsymbol{k}_\perp, \boldsymbol{k}_{1\perp}) \equiv \sum_{\beta=9}^{12} R_\beta^\mu(\boldsymbol{k}_\perp, \boldsymbol{k}_{1\perp}) \,. \tag{A.8}
$$

The Dirac structures here are for $\beta = 9, \ldots, 12$, corresponding to

$$
\begin{aligned}
R_9^\mu(\boldsymbol{k}_\perp,\boldsymbol{k}_{1\perp}) \equiv & -\gamma^\mu \frac{\not{q}+\not{k}_\gamma+m}{(q+k_\gamma)^2-m^2}\gamma^+(\not{q}_\perp+\not{k}_\perp-\not{k}_{1\perp}+m) \\
& \times \frac{\gamma^-(\not{q}_\perp+\not{k}_{\gamma\perp}-\not{k}_\perp-\not{k}_{1\perp}+m)\gamma^+}{N_k(\boldsymbol{k}_\perp,\boldsymbol{k}_{1\perp})}\,, \\
R_{10}^\mu(\boldsymbol{k}_\perp,\boldsymbol{k}_{1\perp}) \equiv & \frac{\gamma^+(\not{q}_\perp-\not{k}_\perp+m)\gamma^-(\not{q}_\perp-\not{k}_\perp-\not{k}_{1\perp}+m)}{N_q(\boldsymbol{k}_\perp,\boldsymbol{k}_{1\perp})} \\
& \times \gamma^+\frac{\not{p}+\not{k}_\gamma-m}{(p+k_\gamma)^2-m^2}\gamma^\mu\,, \\
R_{11}^\mu(\boldsymbol{k}_\perp,\boldsymbol{k}_{1\perp}) \equiv & \frac{\gamma^+(\not{q}+m-\not{k}_\perp)\gamma^\mu}{S(\boldsymbol{k}_\perp,\boldsymbol{k}_{1\perp})N_k(\boldsymbol{k}_\perp,\boldsymbol{k}_{1\perp})} \\
& \times \Big[2p^+(\not{q}_\perp+\not{k}_{\gamma\perp}-\not{k}_\perp+m) \\
& \qquad -M^2(\boldsymbol{q}_\perp+\boldsymbol{k}_{\gamma\perp}-\boldsymbol{k}_\perp-\boldsymbol{k}_{1\perp})\gamma^+\Big] \\
& \times \gamma^-(\not{q}_\perp+\not{k}_{\gamma\perp}-\not{k}_\perp-\not{k}_{1\perp}+m)\gamma^+\,, \\
R_{12}^\mu(\boldsymbol{k}_\perp,\boldsymbol{k}_{1\perp}) \equiv & \frac{\gamma^+(\not{q}_\perp-\not{k}_\perp+m)\gamma^-}{S(\boldsymbol{k}_\perp,\boldsymbol{k}_{1\perp})N_q(\boldsymbol{k}_\perp,\boldsymbol{k}_{1\perp})} \\
& \times \Big[2q^+(\not{q}_\perp-\not{k}_{1\perp}-\not{k}_\perp+m)+M^2(\boldsymbol{q}_\perp-\boldsymbol{k}_\perp)\gamma^+\Big] \\
& \times \quad \gamma^\mu(\not{P}_\perp-\not{k}_{1\perp}-\not{k}_\perp-\not{p}+m)\gamma^+\,.
\end{aligned}
\tag{A.9}
$$

For clarity of presentation, the following functions in the denominators have been defined as

$$
\begin{aligned}
N_q(\boldsymbol{k}_\perp,\boldsymbol{k}_{1\perp}) \equiv & \; 2(p^+ + k_\gamma^+)M^2(\boldsymbol{q}_\perp-\boldsymbol{k}_\perp) \\
& + 2q^+M^2(\boldsymbol{q}_\perp-\boldsymbol{k}_\perp-\boldsymbol{k}_{1\perp})\,, \\
N_k(\boldsymbol{k}_\perp,\boldsymbol{k}_{1\perp}) \equiv & \; 2p^+M^2(\boldsymbol{q}_\perp+\boldsymbol{k}_{\gamma\perp}-\boldsymbol{k}_\perp) \\
& + 2(q^+ + k_\gamma^+)M^2(\boldsymbol{q}_\perp+\boldsymbol{k}_{\gamma\perp}-\boldsymbol{k}_\perp-\boldsymbol{k}_{1\perp})\,, \\
S(\boldsymbol{k}_\perp,\boldsymbol{k}_{1\perp}) \equiv & \; 4p^+q^+k_\gamma^- + 2q^+M^2(\boldsymbol{q}_\perp+\boldsymbol{k}_{\gamma\perp}-\boldsymbol{k}_\perp-\boldsymbol{k}_{1\perp}) \\
& + 2p^+M^2(\boldsymbol{q}_\perp-\boldsymbol{k}_\perp)\,.
\end{aligned}
\tag{A.10}
$$

As a general remark, we would like to add that these hard factors exhibit the following sum rules,

$$
\begin{aligned}
& T_g^\mu(\boldsymbol{P}_\perp)+T_q^\mu(\boldsymbol{P}_\perp)+T_{\bar q}^\mu(\boldsymbol{P}_\perp)-T_{q\bar q}^\mu(\boldsymbol{0},\boldsymbol{P}_\perp)=0\,, \\
& T_q^\mu(\boldsymbol{P}_\perp-\boldsymbol{k}_\perp)-T_{q\bar q}^\mu(\boldsymbol{k}_\perp,\boldsymbol{P}_\perp-\boldsymbol{k}_\perp)=0\,, \\
& T_{\bar q}^\mu(\boldsymbol{k}_{1\perp})-T_{q\bar q}^\mu(\boldsymbol{0},\boldsymbol{k}_{1\perp})=0\,,
\end{aligned}
\tag{A.11}
$$

which correspond to interference between the classes for a restricted kinematic window. These sum rules also aid to the cancellations in the amplitude in ref. [69], as well as the recovery of T_q and $T_{\bar q}$ in the $\boldsymbol{k}_\perp$-factorized amplitude.

Appendix B

Small angle approximation

In perturbation theory, the scattering amplitude for two-to-two processes diverges for vanishing momentum if the exchanged species is massless.Such is the case also for Compton, $gq \to q\gamma$, and annihilation, $q\bar{q} \to g\gamma$, processes in a colored medium. In this scenario, the amplitudes diverge when $\bar{t} = (p_1 - p)^2 \to 0$ and $u = (p_3 - p_1)^2 \to 0$, for a fixed $s = (p_1 + p_2)^2$ (see sec.2.2). The kinetic rate, will be dominated by this divergence, meaning that we can simplify it by expanding around the divergence [35, 138]. We will work explicitly with the annihilation rate [1], which is

$$E\frac{\mathrm{d}N_{anni}}{\mathrm{d}^4X\mathrm{d}^3p} = \frac{1}{2\,(2\,\pi)^{12}}\int \frac{\mathrm{d}^3\,p_3}{2E_3}\frac{\mathrm{d}^3\,p_2}{2E_2}\frac{\mathrm{d}^3\,p_1}{2E_1}\,|\mathcal{M}_{anni}|^2\,(2\,\pi)^4\,\delta^4(p_1+p_2-p_3-p) \times\; f_q(\boldsymbol{p}_1)\,f_q(\boldsymbol{p}_2)\,[1+f_g(\boldsymbol{p}_3)]\;\;, \tag{B.1}$$

The annihilation amplitude is given in . We will expand now in terms of the momentum exchange, which we define with respect to the change of the $\bar{t}$ channel $\boldsymbol{q} = \boldsymbol{p} - \boldsymbol{p}_1$. For this we expands the energy of the outgoing photon and gluon in terms of the energy of the exchange quark,

$$\begin{aligned} |\boldsymbol{p}| &= \boldsymbol{p}_1 + \boldsymbol{q}\cdot\boldsymbol{\beta}_1 + \mathcal{O}(|\boldsymbol{q}|^2) \\ |\boldsymbol{p}_3| &= \boldsymbol{p}_2 - \boldsymbol{q}\cdot\boldsymbol{\beta}_2 + \mathcal{O}(|\boldsymbol{q}|^2) \end{aligned} \tag{B.2}$$

where one can define the three-velocity $\boldsymbol{\beta}_i = \boldsymbol{p}_i/|\boldsymbol{p}_i|$. We will use this notation for every momentum variable, except for q. The Mandelstahm variables can be expanded around $\boldsymbol{q} = 0$, and are given by

$$\begin{aligned} s &= 2|\boldsymbol{p}_1||\boldsymbol{p}_2|(1-\boldsymbol{v}_1\cdot\boldsymbol{v}_2) \\ \bar{t} &= -\boldsymbol{q}^2 + (\boldsymbol{q}\cdot\boldsymbol{v}_1)^2 + \mathcal{O}(|\boldsymbol{q}|^3) \\ u &= -s + \mathcal{O}(|\boldsymbol{q}|^2) \end{aligned} \tag{B.3}$$

while energy conservation reads as

$$|\boldsymbol{p}_1| + |\boldsymbol{p}_2| - |\boldsymbol{p}_3| - |\boldsymbol{p}| = \boldsymbol{q}\cdot(\boldsymbol{v}_2 - \boldsymbol{v}_1) + \mathcal{O}(|\boldsymbol{q}|^2)\,. \tag{B.4}$$

Using these limits, the amplitude turns into

$$|\mathcal{M}_{anni}|^2 \approx \frac{160}{9}16\pi^2\alpha\alpha_s\frac{s}{|\boldsymbol{q}|^2\,(1-(\boldsymbol{v}\cdot\boldsymbol{v}_1)^2)} \tag{B.5}$$

[1] The u and t channels, will be expanded around the exchange vector q, for which the in the t channel the photon momentum will be $p_1 + q$, while in the u channel it will be $p_3 + q$. Both channels contribute in the same way, so they we will add a factor of 2 to account for this.

Integrating eq.(B.1) in terms of p_3 and plugging in eq. (B.5) we find the annihilation rate to be

$$E\frac{\mathrm{d}N_{anni}}{\mathrm{d}^4X\mathrm{d}^3p} = \frac{20}{9\pi^3}\alpha\alpha_s\int \mathrm{d}^3p_1\int\frac{\mathrm{d}^3p_2}{(2\pi)^3}\frac{1}{|\boldsymbol{p}_2||\boldsymbol{q}|^2}\frac{(1-\boldsymbol{v}_1\cdot\boldsymbol{v}_2)}{(1-(\boldsymbol{v}\cdot\boldsymbol{v}_1)^2)}\delta(\boldsymbol{q}\cdot(\boldsymbol{v}_2-\boldsymbol{v}_1)) \times f_q(\boldsymbol{p}_1)\,f_q(\boldsymbol{p}_2)\,[1+f_g(\boldsymbol{p}_2)] \tag{B.6}$$

We can now substitut $\boldsymbol{p}_1=\boldsymbol{p}-\boldsymbol{q}$, for which we will ignoring higher order terms in $|\boldsymbol{q}|$ arising from the substitution. From this we get

$$E\frac{\mathrm{d}N_{anni}}{\mathrm{d}^4X\mathrm{d}^3p} = \frac{20}{9\pi^3}\alpha\alpha_s\int \mathrm{d}^3q\int\frac{\mathrm{d}^3p_2}{(2\pi)^3}\frac{1}{|\boldsymbol{p}_2|}\frac{(1-\boldsymbol{\beta}\cdot\boldsymbol{\beta}_2)}{(|\boldsymbol{q}|^2-(\boldsymbol{q}\cdot\boldsymbol{\beta})^2)}\delta(\boldsymbol{q}\cdot(\boldsymbol{\beta}_2-\boldsymbol{\beta})) \times f_q(\boldsymbol{p})\,f_q(\boldsymbol{p}_2)\,[1+f_g(\boldsymbol{p}_2)] \tag{B.7}$$

Noticing that the distribution functions do not depend on the exhanged momentum, one can group all the q dependent terms, and define,

$$\int \mathrm{d}^3q\frac{(1-\boldsymbol{\beta}\cdot\boldsymbol{\beta}_2)}{(|\boldsymbol{q}|^2-(\boldsymbol{q}\cdot\boldsymbol{\beta})^2)}\delta(\boldsymbol{q}\cdot(\boldsymbol{\beta}_2-\boldsymbol{\beta}))\equiv 2\pi\mathcal{L} \tag{B.8}$$

where the logarithmic divergence can be regularized using the Coulomb logarithm,

$$\mathcal{L}=\int_{\Lambda_{IR}}^{\Lambda_{UV}}=\log\left[\frac{\Lambda_{IR}}{\Lambda_{UV}}\right] \tag{B.9}$$

As an interesting note, in thermal equilibrium the ration inside the logarithm is the ratio between the tempreature, T, and the Debye screening mass, $m_D\sim gT$. This makes the Coulomb logarithm roughly $\log(1/g)$. This dependence should be similar in the non-equilibrium context of Chapter 2. We will see that this dependence is observed in the leading log contribution, ref. [136].

We have finally simplified the rates down to the following expression

$$E\frac{\mathrm{d}N_{anni}}{\mathrm{d}^4X\mathrm{d}^3p} = \frac{40}{9\pi^2}\alpha\alpha_s\mathcal{L}f_q(\boldsymbol{p})\int\frac{\mathrm{d}^3p_2}{(2\pi)^3}\frac{1}{|\boldsymbol{p}_2|}\,f_q(\boldsymbol{p}_2)\,[1+f_g(\boldsymbol{p}_2)] \tag{B.10}$$

For the Compton scattering, the sameapproximation can be taken. The simplified version is then

$$E\frac{\mathrm{d}N_{Comp}}{\mathrm{d}^4X\mathrm{d}^3p} = \frac{40}{9\pi^2}\alpha\alpha_s\mathcal{L}f_q(\boldsymbol{p})\int\frac{\mathrm{d}^3p_2}{(2\pi)^3}\frac{1}{|\boldsymbol{p}_2|}\,f_g(\boldsymbol{p}_2)\,[1-f_q(\boldsymbol{p}_2)]\ . \tag{B.11}$$

Summing the two processes yields a cancellation that further simplifies the rate. This is how we get the final expression, used in sec. 2.2,

$$E\frac{\mathrm{d}N_{tot}}{\mathrm{d}^4X\mathrm{d}^3p} = \frac{40}{9\pi^2}\alpha\alpha_s\mathcal{L}f_q(\boldsymbol{p})\int\frac{\mathrm{d}^3p_2}{(2\pi)^3}\frac{1}{|\boldsymbol{p}_2|}\,[f_g(\boldsymbol{p}_2)+f_q(\boldsymbol{p}_2)] \tag{B.12}$$

A nice check of this approximation is that if thermal equilibrium distributions are plugged in, one gets the leading logarithm result up to a prefactor of 2. This can be absorbed by $\mathcal{L}$.

$$E\frac{\mathrm{d}N_{tot}}{\mathrm{d}^4X\mathrm{d}^3p}\approx\frac{10}{9}\frac{\alpha}{\alpha_s}2\pi T^2\mathcal{L}e^{p/T} \tag{B.13}$$

Appendix C

Thermal rates

After the thermalization of the colored medium, photons can be emitted from either a thermalized quark-gluon-plasma (QGP) or can be produced by hadronic processes in the hadron resonance gas phase (HRG). In the following we will summarize the rates used in Chapters 2 and 3 to compute the radiation from the thermal phases.

Thermal rate for Quark Gluon Plasma

To emit photons from the thermal QGP phase we will use the full LO rate of ref. [36], which was computed using weak-coupling expansion in a thermal QFT. This rate contains not only the two-to-two contributions which dominate at higher momenta, but also near-collinear bremsstrahlung and the inelastic pair annihilation, thereby fully including the Landau-Pomeranchiuk-Migdal effect, which can be understood as suppression of emission thanks to interference of multiple scatterings [224]. The rate used is, in the notation of Chapter 2,

$$E\frac{d\,N}{d^4\,X\,d^3\,p} = A(p)\,\nu_{LO}\left(\frac{p}{T}\right) \tag{C.1}$$

with the leading-log coefficient $\mathcal{A}(k)$, which is given by

$$A(p) = \frac{2\,\alpha}{(2\pi)^3} d_F \left[\sum_c q_c^2\right] m_D^2\, f_{q,eq}\left(\frac{E}{T}\right) \tag{C.2}$$

The remaining part of this rate is given by

$$\begin{aligned}\nu_{LO}\left(\frac{p}{T}\right) \equiv \frac{1}{2}\ln\left(\frac{2p}{T}\right) + C_{2\leftrightarrow 2}\left(\frac{p}{T}\right) \\ + C_{\text{brem}}\left(\frac{p}{T}\right) + C_{\text{annih}}\left(\frac{p}{T}\right)\end{aligned} \tag{C.3}$$

with the Fermi distribution function $n_f(k) = [\exp(k/T)+1]^{-1}$. The dimension of the quark representation is d_{F}, which is 3 in our case. Summing over the charges of quarks, q_s, one gets $d_{\mathrm{F}}\sum_s q_s^2 = 3\times(1\cdot(2/3)^2 + 2\cdot(1/3)^2) = 3\times 6/9$. The leading-order asymptotic thermal quark-mass m_∞ is given by [225] to be

$$m_\infty^2 = \frac{C_{\mathrm{F}} g_s^2 T^2}{4} \tag{C.4}$$

with the quadratic Casimir of the quark representation $C_{\rm F}$, which is $C_{\rm F} = 4/3$ for QCD, and the strong coupling $g_s = \sqrt{4\pi\,\alpha_s}$. Using the running coupling prescription,

$$\alpha_s(Q) = \frac{12\pi}{(11N_c - 2N_f)\log(Q^2/\Lambda^2_{QCD})} \tag{C.5}$$

where the cutoff scale, $\Lambda_{QCD} = 0.2$ GeV. For $SU(3)$, with $N_c = 3$ and three flavours, $N_f = 3$ we get that for ALICE energies, $\alpha_s \approx 0.3$. The functions that describe the two-to-two particle processes ($C_{2\leftrightarrow 2}$) and the in-medium bremsstrahlung ($C_{\rm brem}$) and annihilation ($C_{\rm annih}$) processes are,

$$\begin{aligned} C_{2\leftrightarrow 2} &= 0.041x^{-1} - 0.3615 + 1.01e^{-1.35x} \\ C_{\rm brem} + C_{\rm annih} &= \sqrt{1+\frac{1}{6}{\rm N_f}}\left[\frac{0.548\log(12.28+1/x)}{x^{2/3}} + \frac{0.133x}{\sqrt{1+x/16.27}}\right] \end{aligned} \tag{C.6}$$

with $x = p/T$ for three flavours, $N_f = 3$. These functions were obtained by approximating the full kinetic kernels. The full logarithm under the log will also be used to enhance the non-equilibrium rate, with the substitution $x = E/t \to x' = E/Q$.

Photon emission from the hadron resonance gas

For from the hadron resonance gas (HRG) phase, we use the the thermal photon emission rate the parametrization ref. [162]. These parametrizations have an underlying error of no more than 20% with the microscopic calculated values [226, 227]. We use htis parametrization since the inclusion of the full cross section into a phenomenological model is not practical, and very computationally expensive [162]. Two different contributions are included, one from the meson channel $\pi\pi \to \pi\pi\gamma$ and another one including the emission from in-medium ρ mesons. These paraemetrizations can be applied to photons with energies q_0 between 0.2 and 5 GeV, at temperatures between $T = 100 - 180$ MeV and baryon chemical potentials of $\mu_B = 0 - 400$ MeV. For these investigations we will set $\mu_B = 0$.

The contribution from in-medium ρ-mesons, including channels like $\pi N \to \pi N\gamma$ and $NN \to NN\gamma$, are universally given by [162],

$$q_0\frac{dR^\rho_\gamma}{d^3q}(q_0;0,T) = \exp\left[a(T)q_0 + b(T) + \frac{c(T)}{q_0+0.2}\right] \tag{C.7}$$

where we will use the fitted parameters given in ref. [162]

$$\begin{aligned} a(T) &= -31.21 + 353.61T - 1739.4T^2 + 3105T^3 \\ b(T) &= -5.513 - 42.2T + 333T^2 - 570T^3 \\ c(T) &= -6.153 + 57T - 134.61T^2 + 8.31T^3 \end{aligned} \tag{C.8}$$

Nevertheless, this contribution does not include meson-meson bremsstrahlung, strongly dominated by the $\pi\pi \to \pi\pi\gamma$ channel. The contribution from πK scattering is subleading, and will not be included, since it comprises at most an increase of 20%. The following fit function is used

$$q_0 \frac{dR_\gamma^{Brems}}{d^3q}(q_0;T) = \exp[\alpha_B(T)q_0 + \beta_B(T)q_0 + \gamma_B q_0^2 + \delta_B(T)(q_0+0.2)^{-1}] \tag{C.9}$$

with the following fitted parameters,

$$\begin{aligned}
\alpha_B(T) &= -16.28 + 62.45T - 93.4T^2 + 7.5T^3 \\
\beta_B(T) &= -35.54 + 414.8T - 2054T^2 + 3718.8T^3 \\
\gamma_B(T) &= 0.7364 - 10.72T + 56.32^2 - 103.5T^3 \\
\delta_B(T) &= -2.51 + 58.152T - 318.24T^2 + 610.7T^3
\end{aligned} \tag{C.10}$$

In the HRG, these two contributions are relevant for different kinematic windows of the photons. For a temperature of 150 MeV , soft photons ($q_0 < 0.4$ GeV) are strongly dominated by $\pi\pi$ scattering. On the other hand, the contribution form ρ-meson decays is an order of magnitude larger for $q_0 > 1$ GeV [227]. Therefore, in both contributions are included in Chapters 2 and 3.

Bibliography

[1] Andreas Trabesinger. "Complexity". In: *Nature Physics* 8 (Dec. 2011), 13 EP –. URL: https://doi.org/10.1038/nphys2198 (cit. on p. 1).

[2] Melanie Mitchell. *Complexity - A Guided Tour*. Jan. 2009. ISBN: 978-0-19-512441-5 (cit. on p. 1).

[3] Gordon Baym et al. "From hadrons to quarks in neutron stars: a review". In: *Rept. Prog. Phys.* 81.5 (2018), p. 056902. DOI: 10.1088/1361-6633/aaae14. arXiv: 1707.04966 [astro-ph.HE] (cit. on p. 1).

[4] D. Blaschke and N. Chamel. "Phases of dense matter in compact stars". In: *Astrophys. Space Sci. Libr.* 457 (2018), pp. 337–400. DOI: 10.1007/978-3-319-97616-7_7. arXiv: 1803.01836 [nucl-th] (cit. on p. 1).

[5] B. Schuetrumpf et al. "A Survey of Nuclear Pasta in the Intermediate Density Regime I: Shapes and Energies". In: (2019). arXiv: 1906.08155 [nucl-th] (cit. on p. 1).

[6] N. Cabibbo and G. Parisi. "Exponential Hadronic Spectrum and Quark Liberation". In: *Phys. Lett.* 59B (1975), pp. 67–69. DOI: 10.1016/0370-2693(75)90158-6 (cit. on p. 1).

[7] F. Becattini. "Thermal hadron production in high-energy collisions". In: *J. Phys.* G23 (1997), pp. 1933–1940. DOI: 10.1088/0954-3899/23/12/017. arXiv: hep-ph/9708248 [hep-ph] (cit. on p. 1).

[8] F. Becattini. "An Introduction to the Statistical Hadronization Model". In: *International School on Quark-Gluon Plasma and Heavy Ion Collisions: past, present, future Villa Gualino, Torino, Italy, December 8-14, 2008*. 2009. arXiv: 0901.3643 [hep-ph] (cit. on p. 1).

[9] Peter Brockway Arnold. "Quark-Gluon Plasmas and Thermalization". In: *Int. J. Mod. Phys.* E16 (2007), pp. 2555–2594. DOI: 10.1142/S021830130700832X. arXiv: 0708.0812 [hep-ph] (cit. on p. 1).

[10] David J. Gross. "The discovery of asymptotic freedom and the emergence of QCD". In: *Proceedings of the National Academy of Sciences* 102.26 (2005), pp. 9099–9108. ISSN: 0027-8424. DOI: 10.1073/pnas.0503831102. eprint: https://www.pnas.org/content/102/26/9099.full.pdf. URL: https://www.pnas.org/content/102/26/9099 (cit. on p. 2).

[11] *HERA Homepage*. http://www.desy.de/forschung/anlagen__projekte/hera/index_ger.html. Accessed: 25.7.2019 (cit. on p. 2).

[12] Henry W. Kendall. "Deep inelastic scattering: Experiments on the proton and the observation of scaling". In: *Rev. Mod. Phys.* 63 (3 1991), pp. 597–614. DOI: 10.1103/RevModPhys.63.597. URL: https://link.aps.org/doi/10.1103/RevModPhys.63.597 (cit. on p. 2).

[13] Francois Gelis et al. "The Color Glass Condensate". In: *Ann. Rev. Nucl. Part. Sci.* 60 (2010), pp. 463–489. DOI: 10.1146/annurev.nucl.010909.083629. arXiv: 1002.0333 [hep-ph] (cit. on pp. 2, 10, 12, 15, 29, 99).

[14] Sourav Sarkar, Helmut Satz, and Bikash Sinha. "The physics of the quark-gluon plasma". In: *Lect. Notes Phys.* 785 (2010), pp.1–369. DOI: 10.1007/978-3-642-02286-9 (cit. on p. 2).

[15] M. M. Aggarwal et al. "Observation of direct photons in central 158-A-GeV Pb-208 + Pb-208 collisions". In: *Phys. Rev. Lett.* 85 (2000), pp. 3595–3599. DOI: 10.1103/PhysRevLett.85.3595. arXiv: nucl-ex/0006008 [nucl-ex] (cit. on p. 2).

[16] Sanjin Benić et al. "Constraining unintegrated gluon distributions from inclusive photon production in proton–proton collisions at the LHC". In: *Phys. Lett.* B791 (2019), pp. 11–16. DOI: 10.1016/j.physletb.2019.02.007. arXiv: 1807.03806 [hep-ph] (cit. on pp. 2, 29).

[17] Raju Venugopalan. "From many body wee parton dynamics to perfect fluid: a standard model for heavy ion collisions". In: *PoS* ICHEP2010 (2010), p. 567. DOI: 10.22323/1.120.0567. arXiv: 1012.4699 [hep-ph] (cit. on p. 3).

[18] T. Lappi. "Theory overview of Heavy Ion collisions". In: *PoS* LHCP2016 (2016), p. 016. DOI: 10.22323/1.276.0016. arXiv: 1609.04917 [hep-ph] (cit. on p. 3).

[19] Heng-Tong Ding, Frithjof Karsch, and Swagato Mukherjee. "Thermodynamics of strong-interaction matter from Lattice QCD". In: *Int. J. Mod. Phys.* E24.10 (2015), p. 1530007. DOI: 10.1142/S0218301315300076. arXiv: 1504.05274 [hep-lat] (cit. on p. 3).

[20] Derek Teaney. "Chemical freezeout in heavy ion collisions". In: (2002). arXiv: nucl-th/0204023 [nucl-th] (cit. on p. 3).

[21] Ulrich W. Heinz and Gregory Kestin. "Jozso's Legacy: Chemical and Kinetic Freeze-out in Heavy-Ion Collisions". In: *Eur. Phys. J. ST* 155 (2008), pp. 75–87. DOI: 10.1140/epjst/e2008-00591-4. arXiv: 0709.3366 [nucl-th] (cit. on p. 3).

[22] Aleksi Kurkela et al. "Matching the non-equilibrium initial stage of heavy ion collisions to hydrodynamics with QCD kinetic theory". In: (2018). arXiv: 1805.01604 [hep-ph] (cit. on pp. 3, 50).

[23] Aleksi Kurkela et al. "Effective kinetic description of event-by-event pre-equilibrium dynamics in high-energy heavy-ion collisions". In: *Phys. Rev.* C99.3 (2019), p. 034910. DOI: 10.1103/PhysRevC.99.034910. arXiv: 1805.00961 [hep-ph] (cit. on p. 3).

[24] J. Berges et al. "Universality far from equilibrium: From superfluid Bose gases to heavy-ion collisions". In: *Phys. Rev. Lett.* 114.6 (2015), p. 061601. DOI: 10.1103/PhysRevLett.114.061601. arXiv: 1408.1670 [hep-ph] (cit. on p. 3).

[25] Jürgen Berges and Sören Schlichting. "The nonlinear glasma". In: *Phys. Rev.* D87.1 (2013), p. 014026. DOI: 10.1103/PhysRevD.87.014026. arXiv: 1209.0817 [hep-ph] (cit. on p. 3).

[26] Jürgen Berges et al. "Turbulent thermalization process in high-energy heavy-ion collisions". In: *Nucl. Phys.* A931 (2014), pp. 348–353. DOI: 10.1016/j.nuclphysa.2014.08.103. arXiv: 1409.1638 [hep-ph] (cit. on pp. 3, 4, 29).

[27] Jurgen Berges, Kirill Boguslavski, and Soren Schlichting. "Nonlinear amplification of instabilities with longitudinal expansion". In: *Phys. Rev.* D85 (2012), p. 076005. DOI: 10.1103/PhysRevD.85.076005. arXiv: 1201.3582 [hep-ph] (cit. on p. 3).

[28] R. Baier et al. "'Bottom up' thermalization in heavy ion collisions". In: *Phys. Lett.* B502 (2001), pp. 51–58. DOI: 10.1016/S0370-2693(01)00191-5. arXiv: hep-ph/0009237 [hep-ph] (cit. on pp. 3, 29, 35, 40, 69, 99).

[29] Ulrich W. Heinz. "The Little bang: Searching for quark gluon matter in relativistic heavy ion collisions". In: *Nucl. Phys.* A685 (2001), pp. 414–431. DOI: 10.1016/S0375-9474(01)00558-9. arXiv: hep-ph/0009170 [hep-ph] (cit. on p. 4).

[30] Edward V. Shuryak. "Are high-energy heavy ion collisions similar to a little bang, or just a very nice firework?" In: *6th International Workshop on Relativistic Aspects of Nuclear Physics (RANP2000) Caraguatatuba, Sao Paulo, Brazil, October 17-20, 2000*. 2000. DOI: 10.1142/9789812799814_0009. arXiv: hep-ph/0011208 [hep-ph] (cit. on p. 4).

[31] Raphael Micha and Igor I. Tkachev. "Turbulent thermalization". In: *Phys. Rev.* D70 (2004), p. 043538. DOI: 10.1103/PhysRevD.70.043538. arXiv: hep-ph/0403101 [hep-ph] (cit. on pp. 4, 78, 82, 90).

[32] Maximilian Prüfer et al. "Observation of universal dynamics in a spinor Bose gas far from equilibrium". In: *Nature* 563.7730 (2018), pp. 217–220. DOI: 10.1038/s41586-018-0659-0. arXiv: 1805.11881 [cond-mat.quant-gas] (cit. on pp. 5, 79).

[33] Jurgen Berges. "Nonequilibrium Quantum Fields: From Cold Atoms to Cosmology". In: (2015). arXiv: 1503.02907 [hep-ph] (cit. on pp. 5, 80, 82, 92, 93).

[34] F. Becattini, F. Piccinini, and J. Rizzo. "Angular momentum conservation in heavy ion collisions at very high energy". In: *Phys. Rev.* C77 (2008), p. 024906. DOI: 10.1103/PhysRevC.77.024906. arXiv: 0711.1253 [nucl-th] (cit. on pp. 5, 77, 101).

[35] Jurgen Berges et al. "What shines brighter, Glasma or Quark-Gluon Plasma: a parametric estimate of photon production at early times in heavy-ion collisions". In: (2017). arXiv: 1701.05064 [nucl-th] (cit. on pp. 6, 29, 30, 32, 33, 36, 37, 39, 41–45, 50, 69, 75, 99, 100, 109).

[36] Peter Brockway Arnold, Guy D. Moore, and Laurence G. Yaffe. "Photon emission from quark gluon plasma: Complete leading order results". In: *JHEP* 12 (2001), p. 009. DOI: 10.1088/1126-6708/2001/12/009. arXiv: hep-ph/0111107 [hep-ph] (cit. on pp. 6, 33, 34, 111).

[37] David J. Gross and Frank Wilczek. "Ultraviolet Behavior of Nonabelian Gauge Theories". In: *Phys. Rev. Lett.* 30 (1973). [,271(1973)], pp. 1343–1346. DOI: 10.1103/PhysRevLett.30.1343 (cit. on p. 9).

[38] H. David Politzer. "Reliable Perturbative Results for Strong Interactions?" In: *Phys. Rev. Lett.* 30 (1973). [,274(1973)], pp. 1346–1349. DOI: 10.1103/PhysRevLett.30.1346 (cit. on p. 9).

[39] L. V. Gribov, E. M. Levin, and M. G. Ryskin. "Semihard Processes in QCD". In: *Phys. Rept.* 100 (1983), pp. 1–150. DOI: 10.1016/0370-1573(83)90022-4 (cit. on pp. 10, 11).

[40] Johannes Blumlein. "The Theory of Deeply Inelastic Scattering". In: *Prog. Part. Nucl. Phys.* 69 (2013), pp. 28–84. DOI: 10.1016/j.ppnp.2012.09.006. arXiv: 1208.6087 [hep-ph] (cit. on p. 10).

[41] B. R. Webber. "Deep inelastic scattering: Theory and phenomenology". In: *Proceedings, 4th International Workshop on Deep inelastic scattering and related phenomena (DIS 96): Rome, Italy, April 15-19, 1996*. 1996, pp. 77–96. arXiv: hep-ph/9607441 [hep-ph] (cit. on p. 10).

[42] A. M. Cooper-Sarkar. "PDF Fits at HERA". In: *PoS* EPS-HEP2011 (2011), p. 320. DOI: 10.22323/1.134.0320. arXiv: 1112.2107 [hep-ph] (cit. on pp. 11, 99).

[43] Guido Altarelli and G. Parisi. "Asymptotic Freedom in Parton Language". In: *Nucl. Phys.* B126 (1977), pp. 298–318. DOI: 10.1016/0550-3213(77)90384-4 (cit. on p. 10).

[44] V. N. Gribov and L. N. Lipatov. "Deep inelastic e p scattering in perturbation theory". In: *Sov. J. Nucl. Phys.* 15 (1972). [Yad. Fiz.15,781(1972)], pp. 438–450 (cit. on p. 10).

[45] Yuri L. Dokshitzer. "Calculation of the Structure Functions for Deep Inelastic Scattering and e+ e- Annihilation by Perturbation Theory in Quantum Chromodynamics." In: *Sov. Phys. JETP* 46 (1977). [Zh. Eksp. Teor. Fiz.73,1216(1977)], pp. 641–653 (cit. on p. 10).

[46] Yuri V. Kovchegov and Eugene Levin. "Quantum chromodynamics at high energy". In: *Camb. Monogr. Part. Phys. Nucl. Phys. Cosmol.* 33 (2012), pp. 1–350. DOI: 10.1017/CBO9781139022187 (cit. on p. 10).

[47] L. N. Lipatov. "Reggeization of the Vector Meson and the Vacuum Singularity in Nonabelian Gauge Theories". In: *Sov. J. Nucl. Phys.* 23 (1976). [Yad. Fiz.23,642(1976)], pp. 338–345 (cit. on pp. 11, 17).

[48] E. A. Kuraev, L. N. Lipatov, and Victor S. Fadin. "The Pomeranchuk Singularity in Nonabelian Gauge Theories". In: *Sov. Phys. JETP* 45 (1977). [Zh. Eksp. Teor. Fiz.72,377(1977)], pp. 199–204 (cit. on p. 11).

[49] I. I. Balitsky and L. N. Lipatov. "The Pomeranchuk Singularity in Quantum Chromodynamics". In: *Sov. J. Nucl. Phys.* 28 (1978). [Yad. Fiz.28,1597(1978)], pp. 822–829 (cit. on p. 11).

[50] F. D. Aaron et al. "A Precision Measurement of the Inclusive ep Scattering Cross Section at HERA". In: *Eur. Phys. J.* C64 (2009), pp. 561–587. DOI: 10.1140/epjc/s10052-009-1169-x. arXiv: 0904.3513 [hep-ex] (cit. on p. 11).

[51] Marcel Froissart. "Asymptotic behavior and subtractions in the Mandelstam representation". In: *Phys. Rev.* 123 (1961), pp. 1053–1057. DOI: 10.1103/PhysRev.123.1053 (cit. on p. 11).

[52] Alfred H. Mueller and Jian-wei Qiu. "Gluon Recombination and Shadowing at Small Values of x". In: *Nucl. Phys.* B268 (1986), pp. 427–452. DOI: 10.1016/0550-3213(86)90164-1 (cit. on p. 11).

[53] Anna M. Stasto. "Nonlinear evolution equations in QCD". In: *Acta Phys. Polon.* B35 (2004), pp. 3069–3102. arXiv: hep-ph/0412084 [hep-ph] (cit. on pp. 12, 16).

[54] Boris Z. Kopeliovich, Alexander V. Tarasov, and Andreas Schafer. "Bremsstrahlung of a quark propagating through a nucleus". In: *Phys. Rev.* C59 (1999), pp. 1609–1619. DOI: 10.1103/PhysRevC.59.1609. arXiv: hep-ph/9808378 [hep-ph] (cit. on pp. 14, 19).

[55] Francois Gelis and Jamal Jalilian-Marian. "Photon production in high-energy proton nucleus collisions". In: *Phys. Rev.* D66 (2002), p. 014021. DOI: 10.1103/PhysRevD.66.014021. arXiv: hep-ph/0205037 [hep-ph] (cit. on pp. 14, 19).

[56] R. Baier, A. H. Mueller, and D. Schiff. "Saturation and shadowing in high-energy proton nucleus dilepton production". In: *Nucl. Phys.* A741 (2004), pp. 358–380. DOI: 10.1016/j.nuclphysa.2004.06.020. arXiv: hep-ph/0403201 [hep-ph] (cit. on pp. 14, 19).

[57] B. Z. Kopeliovich et al. "Azimuthal anisotropy of direct photons". In: *Phys. Rev.* D77 (2008), p. 034011. DOI: 10.1103/PhysRevD.77.034011. arXiv: 0711.3010 [hep-ph] (cit. on pp. 14, 19).

[58] B. Z. Kopeliovich et al. "Direct photons and dileptons via color dipoles". In: *Phys. Lett.* B653 (2007), pp. 210–215. DOI: 10.1016/j.physletb.2007.07.055. arXiv: 0704.0642 [hep-ph] (cit. on p. 14).

[59] B. Z. Kopeliovich et al. "Direct photons at forward rapidities in high-energy pp collisions". In: *Phys. Lett.* B675 (2009), pp. 190–195. DOI: 10.1016/j.physletb.2009.04.023. arXiv: 0902.4287 [hep-ph] (cit. on p. 14).

[60] Amir H. Rezaeian and Andreas Schafer. "Hadrons and direct photon in pp and pA collisions at LHC and saturation effects". In: *Phys. Rev.* D81 (2010), p. 114032. DOI: 10.1103/PhysRevD.81.114032. arXiv: 0908.3695 [hep-ph] (cit. on p. 14).

[61] Jamal Jalilian-Marian. "Photon + hadron production in high energy deuteron (proton)-nucleus collisions". In: *Nucl. Phys.* A770 (2006), pp. 210–220. DOI: 10.1016/j.nuclphysa.2006.02.013. arXiv: hep-ph/0509338 [hep-ph] (cit. on p. 14).

[62] Jamal Jalilian-Marian and Amir H. Rezaeian. "Prompt photon production and photon-hadron correlations at RHIC and the LHC from the Color Glass Condensate". In: *Phys. Rev.* D86 (2012), p. 034016. DOI: 10.1103/PhysRevD.86.034016. arXiv: 1204.1319 [hep-ph] (cit. on p. 14).

[63] Amir H. Rezaeian. "Semi-inclusive photon-hadron production in pp and pA collisions at RHIC and LHC". In: *Phys. Rev.* D86 (2012), p. 094016. DOI: 10.1103/PhysRevD.86.094016. arXiv: 1209.0478 [hep-ph] (cit. on p. 14).

[64] E. A. F. Basso, M. B. Gay Ducati, and E. G. de Oliveira. "Inclusive hadron and photon production at LHC in dipole momentum space". In: *Phys. Rev.* D87.7 (2013), p. 074023. DOI: 10.1103/PhysRevD.87.074023. arXiv: 1212.5549 [hep-ph] (cit. on p. 14).

[65] Amir H. Rezaeian. "Photon-jet ridge at RHIC and the LHC". In: *Phys. Rev.* D93.9 (2016), p. 094030. DOI: 10.1103/PhysRevD.93.094030. arXiv: 1603.07354 [hep-ph] (cit. on p. 14).

[66] B. Ducloué, T. Lappi, and H. Mäntysaari. "Isolated photon production in proton-nucleus collisions at forward rapidity". In: *Phys. Rev.* D97.5 (2018), p. 054023. DOI: 10.1103/PhysRevD.97.054023. arXiv: 1710.02206 [hep-ph] (cit. on p. 14).

[67] Tolga Altinoluk et al. "Soft photon and two hard jets forward production in proton-nucleus collisions". In: *JHEP* 04 (2018), p. 063. DOI: 10.1007/JHEP04(2018)063. arXiv: 1802.01398 [hep-ph] (cit. on pp. 14, 18).

[68] Sanjin Benic and Kenji Fukushima. "Photon from the annihilation process with CGC in the pA collision". In: *Nucl. Phys.* A958 (2017), pp. 1–24. DOI: 10.1016/j.nuclphysa.2016.11.003. arXiv: 1602.01989 [hep-ph] (cit. on pp. 14, 18, 99).

[69] Sanjin Benic et al. "Probing gluon saturation with next-to-leading order photon production at central rapidities in proton-nucleus collisions". In: *JHEP* 01 (2017), p. 115. DOI: 10.1007/JHEP01(2017)115. arXiv: 1609.09424 [hep-ph] (cit. on pp. 14, 17–19, 24, 28, 29, 99, 106, 108).

[70] Yan-Qing Ma and Raju Venugopalan. "Comprehensive Description of Production in Proton-Proton Collisions at Collider Energies". In: *Phys. Rev. Lett.* 113.19 (2014), p. 192301. DOI: 10.1103/PhysRevLett.113.192301. arXiv: 1408.4075 [hep-ph] (cit. on pp. 14, 23).

[71] Yan-Qing Ma, Raju Venugopalan, and Hong-Fei Zhang. "J/ψ production and suppression in high energy proton-nucleus collisions". In: *Phys. Rev.* D92 (2015), p. 071901. DOI: 10.1103/PhysRevD.92.071901. arXiv: 1503.07772 [hep-ph] (cit. on p. 14).

[72] Jian-Wei Qiu et al. "Universal Suppression of Heavy Quarkonium Production in pA Collisions at Low Transverse Momentum". In: *Phys. Rev.* D89.3 (2014), p. 034007. DOI: 10.1103/PhysRevD.89.034007. arXiv: 1310.2230 [hep-ph] (cit. on p. 14).

[73] Yan-Qing Ma et al. "$\psi(2S)$ versus J/ψ suppression in proton-nucleus collisions from factorization violating soft color exchanges". In: *Phys. Rev.* C97.1 (2018), p. 014909. DOI: 10.1103/PhysRevC.97.014909. arXiv: 1707.07266 [hep-ph] (cit. on p. 14).

[74] Yan-Qing Ma et al. "Event engineering heavy flavor production and hadronization in high multiplicity hadron-hadron collisions". In: (2018). arXiv: 1803.11093 [hep-ph] (cit. on pp. 14, 27).

[75] Adrian Dumitru et al. "Particle multiplicities in the central region of high-energy collisions from k_T-factorization with running coupling corrections". In: (2018). arXiv: 1805.02702 [hep-ph] (cit. on p. 14).

[76] Larry D. McLerran. "The Color glass condensate and small x physics: Four lectures". In: *Lect. Notes Phys.* 583 (2002), pp. 291–334. DOI: 10.1007/3-540-45792-5_8. arXiv: hep-ph/0104285 [hep-ph] (cit. on p. 15).

[77] F. Gelis. "Color Glass Condensate and Glasma". In: *Int. J. Mod. Phys.* A28 (2013), p. 1330001. DOI: 10.1142/S0217751X13300019. arXiv: 1211.3327 [hep-ph] (cit. on p. 15).

[78] Larry D. McLerran and Raju Venugopalan. "Computing quark and gluon distribution functions for very large nuclei". In: *Phys. Rev.* D49 (1994), pp. 2233–2241. DOI: 10.1103/PhysRevD.49.2233. arXiv: hep-ph/9309289 [hep-ph] (cit. on p. 15).

[79] Larry D. McLerran and Raju Venugopalan. "Gluon distribution functions for very large nuclei at small transverse momentum". In: *Phys. Rev.* D49 (1994), pp. 3352–3355. DOI: 10.1103/PhysRevD.49.3352. arXiv: hep-ph/9311205 [hep-ph] (cit. on p. 15).

[80] Larry D. McLerran and Raju Venugopalan. "Green's functions in the color field of a large nucleus". In: *Phys. Rev.* D50 (1994), pp. 2225–2233. DOI: 10.1103/PhysRevD.50.2225. arXiv: hep-ph/9402335 [hep-ph] (cit. on p. 15).

[81] Heribert Weigert. "Unitarity at small Bjorken x". In: *Nucl. Phys.* A703 (2002), pp. 823–860. DOI: 10.1016/S0375-9474(01)01668-2. arXiv: hep-ph/0004044 [hep-ph] (cit. on p. 16).

[82] Yuri V. Kovchegov. "Small x F(2) structure function of a nucleus including multiple pomeron exchanges". In: *Phys. Rev.* D60 (1999), p. 034008. DOI: 10.1103/PhysRevD.60.034008. arXiv: hep-ph/9901281 [hep-ph] (cit. on pp. 16, 23).

[83] Francois Gelis and Raju Venugopalan. "Large mass q anti-q production from the color glass condensate". In: *Phys. Rev.* D69 (2004), p. 014019. DOI: 10.1103/PhysRevD.69.014019. arXiv: hep-ph/0310090 [hep-ph] (cit. on p. 17).

[84] Jean Paul Blaizot, Francois Gelis, and Raju Venugopalan. "High-energy pA collisions in the color glass condensate approach. 1. Gluon production and the Cronin effect". In: *Nucl. Phys.* A743 (2004), pp. 13–56. DOI: 10.1016/j.nuclphysa.2004.07.005. arXiv: hep-ph/0402256 [hep-ph] (cit. on pp. 17, 18, 22).

[85] Francois Gelis and Yacine Mehtar-Tani. "Gluon propagation inside a high-energy nucleus". In: *Phys. Rev.* D73 (2006), p. 034019. DOI: 10.1103/PhysRevD.73.034019. arXiv: hep-ph/0512079 [hep-ph] (cit. on p. 17).

[86] Adrian Dumitru and Larry D. McLerran. "How protons shatter colored glass". In: *Nucl. Phys.* A700 (2002), pp. 492–508. DOI: 10.1016/S0375-9474(01)01301-X. arXiv: hep-ph/0105268 [hep-ph] (cit. on p. 17).

[87] Jean Paul Blaizot, Francois Gelis, and Raju Venugopalan. "High-energy pA collisions in the color glass condensate approach. 2. Quark production". In: *Nucl. Phys.* A743 (2004), pp. 57–91. DOI: 10.1016/j.nuclphysa.2004.07.006. arXiv: hep-ph/0402257 [hep-ph] (cit. on pp. 17, 18, 20–22).

[88] Tolga Altinoluk et al. "TMD factorization for dijets + photon production from the dilute-dense CGC framework". In: (2018). arXiv: 1810.11273 [hep-ph] (cit. on p. 18).

[89] Hirotsugu Fujii, Francois Gelis, and Raju Venugopalan. "Quantitative study of the violation of k-perpendicular-factorization in hadroproduction of quarks at collider energies". In: *Phys. Rev. Lett.* 95 (2005), p. 162002. DOI: 10.1103/PhysRevLett.95.162002. arXiv: hep-ph/0504047 [hep-ph] (cit. on pp. 20, 24).

[90] Hirotsugu Fujii, Francois Gelis, and Raju Venugopalan. "Quark pair production in high energy pA collisions: General features". In: *Nucl. Phys.* A780 (2006), pp. 146–174. DOI: 10.1016/j.nuclphysa.2006.09.012. arXiv: hep-ph/0603099 [hep-ph] (cit. on pp. 20, 24).

[91] R. J. Fries. "Higher twist effects in nuclei". In: *Ultrarelativistic heavy-ion collisions. Proceedings, 30th International Workshop on Gross Properties of Nuclei and Nuclear Excitations, Hirschegg, Austria, January 13-19, 2002*. 2002, pp. 348–357. arXiv: hep-ph/0201311 [hep-ph] (cit. on p. 20).

[92] Serguei Chatrchyan et al. "Measurement of isolated photon production in pp and PbPb collisions at $\sqrt{s_{NN}} = 2.76$ TeV". In: *Phys. Lett.* B710 (2012), pp. 256–277. DOI: 10.1016/j.physletb.2012.02.077. arXiv: 1201.3093 [nucl-ex] (cit. on pp. 22, 26).

[93] Vardan Khachatryan et al. "Measurement of the Isolated Prompt Photon Production Cross Section in pp Collisions at $\sqrt{s} = 7$ TeV". In: *Phys. Rev. Lett.* 106 (2011), p. 082001. DOI: 10.1103/PhysRevLett.106.082001. arXiv: 1012.0799 [hep-ex] (cit. on p. 22).

[94] Serguei Chatrchyan et al. "Measurement of the Differential Cross Section for Isolated Prompt Photon Production in pp Collisions at 7 TeV". In: *Phys. Rev.* D84 (2011), p. 052011. DOI: 10.1103/PhysRevD.84.052011. arXiv: 1108.2044 [hep-ex] (cit. on pp. 22, 26).

[95] G. Aad et al. "Measurement of the inclusive isolated prompt photon cross section in pp collisions at $\sqrt{s} = 7$ TeV with the ATLAS detector". In: *Phys. Rev.* D83 (2011), p. 052005. DOI: 10.1103/PhysRevD.83.052005. arXiv: 1012.4389 [hep-ex] (cit. on pp. 22, 27).

[96] O. Adriani et al. "Measurement of forward photon production cross-section in proton-proton collisions at $\sqrt{s}$ = 13 TeV with the LHCf detector". In: (2017). arXiv: 1703.07678 [hep-ex] (cit. on p. 22).

[97] K. Akiba et al. "LHC Forward Physics". In: *J. Phys.* G43 (2016), p. 110201. DOI: 10.1088/0954-3899/43/11/110201. arXiv: 1611.05079 [hep-ph] (cit. on p. 22).

[98] O. Adriani et al. "Technical design report of the LHCf experiment: Measurement of photons and neutral pions in the very forward region of LHC". In: (2006) (cit. on p. 22).

[99] Thomas Peitzmann. "Measurement of forward direct photon production in p-A at the LHC with ALICE - A probe for nuclear PDFs and saturation". In: *PoS* DIS2016 (2016), p. 273. arXiv: 1607.01673 [hep-ex] (cit. on p. 22).

[100] Stefano Frixione. "Isolated photons in perturbative QCD". In: *Phys. Lett.* B429 (1998), pp. 369–374. DOI: 10.1016/S0370-2693(98)00454-7. arXiv: hep-ph/9801442 [hep-ph] (cit. on p. 22).

[101] Raphaelle Ichou and David d'Enterria. "Sensitivity of isolated photon production at TeV hadron colliders to the gluon distribution in the proton". In: *Phys. Rev.* D82 (2010), p. 014015. DOI: 10.1103/PhysRevD.82.014015. arXiv: 1005.4529 [hep-ph] (cit. on p. 23).

[102] David d'Enterria and Juan Rojo. "Quantitative constraints on the gluon distribution function in the proton from collider isolated-photon data". In: *Nucl. Phys.* B860 (2012), pp. 311–338. DOI: 10.1016/j.nuclphysb.2012.03.003. arXiv: 1202.1762 [hep-ph] (cit. on pp. 23, 28).

[103] J. Pumplin et al. "New generation of parton distributions with uncertainties from global QCD analysis". In: *JHEP* 07 (2002), p. 012. DOI: 10.1088/1126-6708/2002/07/012. arXiv: hep-ph/0201195 [hep-ph] (cit. on p. 23).

[104] I. Balitsky. "Operator expansion for high-energy scattering". In: *Nucl. Phys.* B463 (1996), pp. 99–160. DOI: 10.1016/0550-3213(95)00638-9. arXiv: hep-ph/9509348 [hep-ph] (cit. on p. 23).

[105] Kevin Dusling, Wei Li, and Björn Schenke. "Novel collective phenomena in high-energy proton–proton and proton–nucleus collisions". In: *Int. J. Mod. Phys.* E25.01 (2016), p. 1630002. DOI: 10.1142/S0218301316300022. arXiv: 1509.07939 [nucl-ex] (cit. on p. 23).

[106] Jamal Jalilian-Marian et al. "The BFKL equation from the Wilson renormalization group". In: *Nucl. Phys.* B504 (1997), pp. 415–431. DOI: 10.1016/S0550-3213(97)00440-9. arXiv: hep-ph/9701284 [hep-ph] (cit. on p. 23).

[107] Jamal Jalilian-Marian, Alex Kovner, and Heribert Weigert. "The Wilson renormalization group for low x physics: Gluon evolution at finite parton density". In: *Phys. Rev.* D59 (1998), p. 014015. DOI: 10.1103/PhysRevD.59.014015. arXiv: hep-ph/9709432 [hep-ph] (cit. on p. 23).

[108] Edmond Iancu, Andrei Leonidov, and Larry D. McLerran. "Nonlinear gluon evolution in the color glass condensate. 1." In: *Nucl. Phys.* A692 (2001), pp. 583–645. DOI: 10.1016/S0375-9474(01)00642-X. arXiv: hep-ph/0011241 [hep-ph] (cit. on p. 23).

[109] Edmond Iancu, Andrei Leonidov, and Larry D. McLerran. "The Renormalization group equation for the color glass condensate". In: *Phys. Lett.* B510 (2001), pp. 133–144. DOI: 10.1016/S0370-2693(01)00524-X. arXiv: hep-ph/0102009 [hep-ph] (cit. on p. 23).

[110] Kevin Dusling et al. "Long range two-particle rapidity correlations in A+A collisions from high energy QCD evolution". In: *Nucl. Phys.* A836 (2010), pp. 159–182. DOI: 10.1016/j.nuclphysa.2009.12.044. arXiv: 0911.2720 [hep-ph] (cit. on p. 23).

[111] Amir H. Rezaeian et al. "Analysis of combined HERA data in the Impact-Parameter dependent Saturation model". In: *Phys. Rev.* D87.3 (2013), p. 034002. DOI: 10.1103/PhysRevD.87.034002. arXiv: 1212.2974 [hep-ph] (cit. on pp. 23, 43).

[112] Richard D. Ball et al. "Parton distributions with small-x resummation: evidence for BFKL dynamics in HERA data". In: *Eur. Phys. J.* C78.4 (2018), p. 321. DOI: 10.1140/epjc/s10052-018-5774-4. arXiv: 1710.05935 [hep-ph] (cit. on p. 24).

[113] S. Catani, M. Ciafaloni, and F. Hautmann. "High-energy factorization and small x heavy flavor production". In: *Nucl. Phys.* B366 (1991), pp. 135–188. DOI: 10.1016/0550-3213(91)90055-3 (cit. on p. 24).

[114] Javier L. Albacete et al. "AAMQS: A non-linear QCD analysis of new HERA data at small-x including heavy quarks". In: *Eur. Phys. J.* C71 (2011), p. 1705. DOI: 10.1140/epjc/s10052-011-1705-3. arXiv: 1012.4408 [hep-ph] (cit. on p. 28).

[115] John M. Campbell et al. "Direct photon production and PDF fits reloaded". In: *Eur. Phys. J.* C78.6 (2018), p. 470. DOI: 10.1140/epjc/s10052-018-5944-4. arXiv: 1802.03021 [hep-ph] (cit. on p. 28).

[116] S. P. Baranov, A. V. Lipatov. Reggeization, and N. P. Zotov. "Prompt photon hadroproduction at high energies in off-shell gluon-gluon fusion". In: *Phys. Rev.* D77 (2008), p. 074024. DOI: 10.1103/PhysRevD.77.074024. arXiv: 0708.3560 [hep-ph] (cit. on p. 29).

[117] Leszek Motyka, Mariusz Sadzikowski, and Tomasz Stebel. "Lam-Tung relation breaking in Z^0 hadroproduction as a probe of parton transverse momentum". In: *Phys. Rev.* D95.11 (2017), p. 114025. DOI: 10.1103/PhysRevD.95.114025. arXiv: 1609.04300 [hep-ph] (cit. on p. 29).

[118] L. E. Gordon and W. Vogelsang. "Polarized and unpolarized prompt photon production beyond the leading order". In: *Phys. Rev.* D48 (1993), pp. 3136–3159. DOI: 10.1103/PhysRevD.48.3136 (cit. on p. 29).

[119] Rupa Chatterjee et al. "Elliptic flow of thermal photons in relativistic nuclear collisions". In: *Phys. Rev. Lett.* 96 (2006), p. 202302. DOI: 10.1103/PhysRevLett.96.202302. arXiv: nucl-th/0511079 [nucl-th] (cit. on p. 29).

[120] L. Adamczyk et al. "Elliptic flow of electrons from heavy-flavor hadron decays in Au + Au collisions at $\sqrt{s_{\mathrm{NN}}} = 200$, 62.4, and 39 GeV". In: *Phys. Rev.* C95.3 (2017), p. 034907. DOI: 10.1103/PhysRevC.95.034907. arXiv: 1405.6348 [hep-ex] (cit. on p. 29).

[121] Shreyasi Acharya et al. "Direct photon elliptic flow in Pb-Pb collisions at $\sqrt{s_{\mathrm{NN}}} = 2.76$ TeV". In: (2018). arXiv: 1805.04403 [nucl-ex] (cit. on p. 29).

[122] Rupa Chatterjee et al. "Elliptic flow of thermal photons from event-by-event hydrodynamic model". In: *Phys. Rev.* C88 (2013), p. 034901. DOI: 10.1103/PhysRevC.88.034901. arXiv: 1305.6443 [hep-ph] (cit. on p. 29).

[123] Chun Shen et al. "Event-by-event direct photon anisotropic flow in relativistic heavy-ion collisions". In: *Nucl. Phys.* A931 (2014), pp. 675–680. DOI: 10.1016/j.nuclphysa.2014.08.030. arXiv: 1407.8533 [nucl-th] (cit. on p. 29).

[124] Hendrik van Hees, Min He, and Ralf Rapp. "Pseudo-critical enhancement of thermal photons in relativistic heavy-ion collisions?" In: *Nucl. Phys.* A933 (2015), pp. 256–271. DOI: 10.1016/j.nuclphysa.2014.09.009. arXiv: 1404.2846 [nucl-th] (cit. on pp. 29, 48).

[125] Chun Shen. "Recent developments in the theory of electromagnetic probes in relativistic heavy-ion collisions". In: *Proceedings, 7th International Conference on Hard and Electromagnetic Probes of High-Energy Nuclear Collisions (Hard Probes 2015): Montréal, Québec, Canada, June 29-July 3, 2015*. 2016. DOI: 10.1016/j.nuclphysbps.2016.05.014. arXiv: 1511.07708 [nucl-th] (cit. on p. 29).

[126] Larry McLerran and Bjoern Schenke. "The Glasma, Photons and the Implications of Anisotropy". In: *Nucl. Phys.* A929 (2014), pp. 71–82. DOI: 10.1016/j.nuclphysa.2014.06.004. arXiv: 1403.7462 [hep-ph] (cit. on pp. 29, 51).

[127] Larry McLerran. "A Phenomenological Model of the Glasma and Photon Production". In: *Acta Phys. Polon.* B45.12 (2014), p. 2307. DOI: 10.5506/APhysPolB.45.2307. arXiv: 1411.1548 [hep-ph] (cit. on p. 29).

[128] Vladimir Khachatryan et al. "Photons from thermalizing matter in heavy ion collisions". In: *Nucl. Phys.* A978 (2018), pp. 123–159. DOI: 10.1016/j.nuclphysa.2018.07.013. arXiv: 1804.09257 [nucl-th] (cit. on pp. 29, 51).

[129] Thomas Epelbaum and Francois Gelis. "Fluctuations of the initial color fields in high energy heavy ion collisions". In: *Phys. Rev.* D88 (2013), p. 085015. DOI: 10.1103/PhysRevD.88.085015. arXiv: 1307.1765 [hep-ph] (cit. on p. 29).

[130] J. Berges et al. "Turbulent thermalization process in heavy-ion collisions at ultrarelativistic energies". In: *Phys. Rev.* D89.7 (2014), p. 074011. DOI: 10.1103/PhysRevD.89.074011. arXiv: 1303.5650 [hep-ph] (cit. on pp. 29, 37, 69).

[131] A. Piñeiro Orioli, K. Boguslavski, and J. Berges. "Universal self-similar dynamics of relativistic and nonrelativistic field theories near nonthermal fixed points". In: *Phys. Rev.* D92.2 (2015), p. 025041. DOI: 10.1103/PhysRevD.92.025041. arXiv: 1503.02498 [hep-ph] (cit. on pp. 29, 78, 85, 90–93, 97).

[132] J. Berges et al. "Basin of attraction for turbulent thermalization and the range of validity of classical-statistical simulations". In: *JHEP* 05 (2014), p. 054. DOI: 10.1007/JHEP05(2014)054. arXiv: 1312.5216 [hep-ph] (cit. on pp. 30, 37, 100).

[133] Peter Brockway Arnold, Jonathan Lenaghan, and Guy D. Moore. "QCD plasma instabilities and bottom up thermalization". In: *JHEP* 08 (2003), p. 002. DOI: 10.1088/1126-6708/2003/08/002. arXiv: hep-ph/0307325 [hep-ph] (cit. on p. 30).

[134] Paul Romatschke and Raju Venugopalan. "Collective non-Abelian instabilities in a melting color glass condensate". In: *Phys. Rev. Lett.* 96 (2006), p. 062302. DOI: 10.1103/PhysRevLett.96.062302. arXiv: hep-ph/0510121 [hep-ph] (cit. on pp. 31, 82).

[135] Jean-Paul Blaizot et al. "Probabilistic picture for medium-induced jet evolution". In: *JHEP* 06 (2014), p. 075. DOI: 10.1007/JHEP06(2014)075. arXiv: 1311.5823 [hep-ph] (cit. on p. 32).

[136] Joseph I. Kapusta, P. Lichard, and D. Seibert. "High-energy photons from quark - gluon plasma versus hot hadronic gas". In: *Nucl. Phys.* A544 (1992), pp. 485C–492C. DOI: 10.1016/0375-9474(92)90603-H (cit. on pp. 32, 33, 110).

[137] R. Baier et al. "Production rate of hard thermal photons and screening of quark mass singularity". In: *Z. Phys.* C53 (1992), pp. 433–438. DOI: 10.1007/BF01625902 (cit. on p. 32).

[138] Jean-Paul Blaizot, Bin Wu, and Li Yan. "Quark production, Bose–Einstein condensates and thermalization of the quark–gluon plasma". In: *Nucl. Phys.* A930 (2014), pp. 139–162. DOI: 10.1016/j.nuclphysa.2014.07.041. arXiv: 1402.5049 [hep-ph] (cit. on pp. 33, 109).

[139] Naoto Tanji and Raju Venugopalan. "Effective kinetic description of the expanding overoccupied Glasma". In: *Phys. Rev.* D95.9 (2017), p. 094009. DOI: 10.1103/PhysRevD.95.094009. arXiv: 1703.01372 [hep-ph] (cit. on p. 33).

[140] Peter Brockway Arnold, Guy D. Moore, and Laurence G. Yaffe. "Photon emission from ultrarelativistic plasmas". In: *JHEP* 11 (2001), p. 057. DOI: 10.1088/1126-6708/2001/11/057. arXiv: hep-ph/0109064 [hep-ph] (cit. on pp. 33, 34, 70).

[141] H. Arthur Weldon. "Covariant Calculations at Finite Temperature: The Relativistic Plasma". In: *Phys. Rev.* D26 (1982), p. 1394. DOI: 10.1103/PhysRevD.26.1394 (cit. on p. 34).

[142] R. Baier et al. "Parton thermalization and energy loss". In: *Nucl. Phys.* A698 (2002), pp. 217–226. DOI: 10.1016/S0375-9474(01)01367-7 (cit. on pp. 35, 44, 45).

[143] Szabolcs Borsanyi et al. "The QCD equation of state with dynamical quarks". In: *JHEP* 11 (2010), p. 077. DOI: 10.1007/JHEP11(2010)077. arXiv: 1007.2580 [hep-lat] (cit. on p. 36).

[144] A. Bazavov et al. "The chiral and deconfinement aspects of the QCD transition". In: *Phys. Rev.* D85 (2012), p. 054503. DOI: 10.1103/PhysRevD.85.054503. arXiv: 1111.1710 [hep-lat] (cit. on p. 36).

[145] Juergen Berges et al. "Universal attractor in a highly occupied non-Abelian plasma". In: *Phys. Rev.* D89.11 (2014), p. 114007. DOI: 10.1103/PhysRevD.89.114007. arXiv: 1311.3005 [hep-ph] (cit. on pp. 37, 100).

[146] T. Lappi. "Wilson line correlator in the MV model: Relating the glasma to deep inelastic scattering". In: *Eur. Phys. J.* C55 (2008), pp. 285–292. DOI: 10.1140/epjc/s10052-008-0588-4. arXiv: 0711.3039 [hep-ph] (cit. on p. 37).

[147] I. S. Gradshteyn and I. M. Ryzhik. *Table of integrals, series, and products*. Seventh. Elsevier/Academic Press, Amsterdam, 2007, pp. xlviii+1171. ISBN: 978-0-12-373637-6; 0-12-373637-4 (cit. on p. 38).

[148] Bjoern Schenke, Prithwish Tribedy, and Raju Venugopalan. "Fluctuating Glasma initial conditions and flow in heavy ion collisions". In: *Phys. Rev. Lett.* 108 (2012), p. 252301. DOI: 10.1103/PhysRevLett.108.252301. arXiv: 1202.6646 [nucl-th] (cit. on p. 43).

[149] Bjoern Schenke, Prithwish Tribedy, and Raju Venugopalan. "Event-by-event gluon multiplicity, energy density, and eccentricities in ultrarelativistic heavy-ion collisions". In: *Phys. Rev.* C86 (2012), p. 034908. DOI: 10.1103/PhysRevC.86.034908. arXiv: 1206.6805 [hep-ph] (cit. on p. 43).

[150] Bjoern Schenke, Prithwish Tribedy, and Raju Venugopalan. "Multiplicity distributions in p+p, p+A and A+A collisions from Yang-Mills dynamics". In: *Phys. Rev.* C89.2 (2014), p. 024901. DOI: 10.1103/PhysRevC.89.024901. arXiv: 1311.3636 [hep-ph] (cit. on p. 43).

[151] P. Tribedy. Private communication (cit. on p. 43).

[152] Henri Kowalski and Derek Teaney. "An Impact parameter dipole saturation model". In: *Phys. Rev.* D68 (2003), p. 114005. DOI: 10.1103/PhysRevD.68.114005. arXiv: hep-ph/0304189 [hep-ph] (cit. on p. 43).

[153] Michael L. Miller et al. "Glauber modeling in high energy nuclear collisions". In: *Ann. Rev. Nucl. Part. Sci.* 57 (2007), pp. 205–243. DOI: 10.1146/annurev.nucl.57.090506.123020. arXiv: nucl-ex/0701025 [nucl-ex] (cit. on p. 43).

[154] Kenneth Aamodt et al. "Centrality dependence of the charged-particle multiplicity density at mid-rapidity in Pb-Pb collisions at $\sqrt{s_{NN}} = 2.76$ TeV". In: *Phys. Rev. Lett.* 106 (2011), p. 032301. DOI: 10.1103/PhysRevLett.106.032301. arXiv: 1012.1657 [nucl-ex] (cit. on p. 44).

[155] S. S. Adler et al. "Systematic studies of the centrality and s(NN)**(1/2) dependence of the d E(T) / d eta and d (N(ch) / d eta in heavy ion collisions at mid-rapidity". In: *Phys. Rev.* C71 (2005). [Erratum: Phys. Rev.C71,049901(2005)], p. 034908. DOI: 10.1103/PhysRevC.71.049901,10.1103/PhysRevC.71.034908. arXiv: nucl-ex/0409015 [nucl-ex] (cit. on p. 44).

[156] B. I. Abelev et al. "Systematic Measurements of Identified Particle Spectra in pp, d^+ Au and Au+Au Collisions from STAR". In: *Phys. Rev.* C79 (2009), p. 034909. DOI: 10.1103/PhysRevC.79.034909. arXiv: 0808.2041 [nucl-ex] (cit. on p. 44).

[157] Subrata Pal and Scott Pratt. "Entropy production at RHIC". In: *Phys. Lett.* B578 (2004), pp. 310–317. DOI: 10.1016/j.physletb.2003.10.054. arXiv: nucl-th/0308077 [nucl-th] (cit. on p. 44).

[158] Steven S. Gubser, Silviu S. Pufu, and Amos Yarom. "Entropy production in collisions of gravitational shock waves and of heavy ions". In: *Phys. Rev.* D78 (2008), p. 066014. DOI: 10.1103/PhysRevD.78.066014. arXiv: 0805.1551 [hep-th] (cit. on p. 44).

[159] W. Vogelsang. Private communication (cit. on p. 44).

[160] A. Adare et al. "Centrality dependence of low-momentum direct-photon production in Au+Au collisions at $\sqrt{s_{NN}} = 200$ GeV". In: *Phys. Rev.* C91.6 (2015), p. 064904. DOI: 10.1103/PhysRevC.91.064904. arXiv: 1405.3940 [nucl-ex] (cit. on pp. 45, 47–49).

[161] Simon Turbide, Ralf Rapp, and Charles Gale. "Hadronic production of thermal photons". In: *Phys. Rev.* C69 (2004), p. 014903. DOI: 10.1103/PhysRevC.69.014903. arXiv: hep-ph/0308085 [hep-ph] (cit. on p. 45).

[162] Matthew Heffernan, Paul Hohler, and Ralf Rapp. "Universal Parametrization of Thermal Photon Rates in Hadronic Matter". In: *Phys. Rev.* C91.2 (2015), p. 027902. DOI: 10.1103/PhysRevC.91.027902. arXiv: 1411.7012 [hep-ph] (cit. on pp. 45, 112).

[163] Nathan P. M. Holt, Paul M. Hohler, and Ralf Rapp. "Thermal photon emission from the $\pi\rho\omega$ system". In: *Nucl. Phys.* A945 (2016), pp. 1–20. DOI: 10.1016/j.nuclphysa.2015.09.008. arXiv: 1506.09205 [hep-ph] (cit. on p. 45).

[164] Jean-François Paquet. "Probing the space-time evolution of heavy ion collisions with photons and dileptons". In: *Nucl. Phys.* A967 (2017), pp. 184–191. DOI: 10.1016/j.nuclphysa.2017.06.003. arXiv: 1704.07842 [nucl-th] (cit. on pp. 46, 50).

[165] Jaroslav Adam et al. "Direct photon production in Pb-Pb collisions at $\sqrt{s_{NN}} =$ 2.76 TeV". In: *Phys. Lett.* B754 (2016), pp. 235–248. DOI: 10.1016/j.physletb.2016.01.020. arXiv: 1509.07324 [nucl-ex] (cit. on pp. 47, 48).

[166] Claus Slotta and Ulrich W. Heinz. "Photon spin and the shape of the two photon correlation function". In: *Phys. Lett.* B391 (1997), pp. 469–473. DOI: 10.1016/S0370-2693(96)01504-3. arXiv: nucl-th/9610016 [nucl-th] (cit. on pp. 48, 56).

[167] Scott Chapman and Ulrich W. Heinz. "HBT correlators: Current formalism versus Wigner function formulation". In: *Phys. Lett.* B340 (1994), pp. 250–253. DOI: 10.1016/0370-2693(94)01277-6. arXiv: hep-ph/9407405 [hep-ph] (cit. on pp. 48, 56).

[168] M. Gyulassy, S. K. Kauffmann, and L. W. Wilson. "Pion Interferometry of Nuclear Collisions. 1. Theory". In: *Phys. Rev.* C20 (1979), pp. 2267–2292. DOI: 10.1103/PhysRevC.20.2267 (cit. on pp. 48, 53, 56).

[169] Jean-François Paquet et al. "Production of photons in relativistic heavy-ion collisions". In: *Phys. Rev.* C93.4 (2016), p. 044906. DOI: 10.1103/PhysRevC.93.044906. arXiv: 1509.06738 [hep-ph] (cit. on p. 50).

[170] Aleksas Mazeliauskas and Jürgen Berges. "Prescaling and far-from-equilibrium hydrodynamics in the quark-gluon plasma". In: *Phys. Rev. Lett.* 122.12 (2019), p. 122301. DOI: 10.1103/PhysRevLett.122.122301. arXiv: 1810.10554 [hep-ph] (cit. on pp. 50, 92, 100).

[171] Naoto Tanji and Juergen Berges. "Nonequilibrium quark production in the expanding QCD plasma". In: *Phys. Rev.* D97.3 (2018), p. 034013. DOI: 10.1103/PhysRevD.97.034013. arXiv: 1711.03445 [hep-ph] (cit. on p. 50).

[172] Akihiko Monnai. "Possible non-prompt photons in pp collisions and their effects in AA analyses". In: *PoS* HardProbes2018 (2019), p. 173. DOI: 10.22323/1.345.0173. arXiv: 1812.08987 [nucl-th] (cit. on p. 51).

[173] Akihiko Monnai. "Prompt, pre-equilibrium, and thermal photons in relativistic nuclear collisions". In: (2019). arXiv: 1907.09266 [nucl-th] (cit. on p. 51).

[174] Simon Fölling et al. "Spatial quantum noise interferometry in expanding ultracold atom clouds". In: *Nature* 434.7032 (2005), pp. 481–484. DOI: 10.1038/nature03500. URL: https://doi.org/10.1038/nature03500 (cit. on p. 53).

[175] T. Rom et al. "Free fermion antibunching in a degenerate atomic Fermi gas released from an optical lattice". In: *Nature* 444.7120 (2006), pp. 733–736. DOI: 10.1038/nature05319. URL: https://doi.org/10.1038/nature05319 (cit. on p. 53).

[176] E. Calligarich et al. "Application of the Hanbury-Brown-Twiss Interferometry to the Production of Like Pions in pi- p Collisions at 11.2-GeV/c". In: *Lett. Nuovo Cim.* 16 (1976), pp. 129–136. DOI: 10.1007/BF02746938 (cit. on p. 53).

[177] S. Pratt. "Pion Interferometry for Exploding Sources". In: *Phys. Rev. Lett.* 53 (1984). [,160(1984)], pp. 1219–1221. DOI: 10.1103/PhysRevLett.53.1219 (cit. on p. 53).

[178] M. M. Aggarwal et al. "Interferometry of direct photons in central Pb-208+Pb-208 collisions at 158-A-GeV". In: *Phys. Rev. Lett.* 93 (2004), p. 022301. DOI: 10.1103/PhysRevLett.93.022301. arXiv: nucl-ex/0310022 [nucl-ex] (cit. on p. 53).

[179] K. Aamodt et al. "Two-pion Bose-Einstein correlations in central Pb-Pb collisions at $\sqrt{s_{NN}} = 2.76$ TeV". In: *Phys. Lett.* B696 (2011), pp. 328–337. DOI: 10.1016/j.physletb.2010.12.053. arXiv: 1012.4035 [nucl-ex] (cit. on p. 53).

[180] R. Hanbury Brown and R. Q. Twiss. "A New type of interferometer for use in radio astronomy". In: *Phil. Mag. Ser.7* 45 (1954), pp. 663–682. DOI: 10.1080/14786440708520475 (cit. on p. 54).

[181] R. Hanbury Brown and R. Q. Twiss. "A Test of a new type of stellar interferometer on Sirius". In: *Nature* 178 (1956), pp. 1046–1048. DOI: 10.1038/1781046a0 (cit. on p. 54).

[182] Ulrich W. Heinz. "Hanbury-Brown/Twiss interferometry for relativistic heavy ion collisions: Theoretical aspects". In: *Correlations and clustering phenomena in subatomic physics. Proceedings, NATO Advanced Study Institute, Dronten, Netherlands, August 5-16, 1996*. 1996, pp. 137–177. arXiv: nucl-th/9609029 [nucl-th] (cit. on pp. 54, 59, 60, 73).

[183] Fred Cooper and Graham Frye. "Comment on the Single Particle Distribution in the Hydrodynamic and Statistical Thermodynamic Models of Multiparticle Production". In: *Phys. Rev.* D10 (1974), p. 186. DOI: 10.1103/PhysRevD.10.186 (cit. on p. 57).

[184] Wojciech Florkowski. *Phenomenology of Ultra-Relativistic Heavy-Ion Collisions*. 2010. ISBN: 9789814280662 (cit. on p. 57).

[185] Evan Frodermann and Ulrich Heinz. "Photon HBT interferometry for non-central heavy-ion collisions". In: *Phys. Rev.* C80 (2009), p. 044903. DOI: 10.1103/PhysRevC.80.044903. arXiv: 0907.1292 [nucl-th] (cit. on pp. 58, 60, 62, 66, 72, 73).

[186] Scott Chapman, J. Rayford Nix, and Ulrich W. Heinz. "Extracting source parameters from Gaussian fits to two particle correlations". In: *Phys. Rev.* C52 (1995), pp. 2694–2703. DOI: 10.1103/PhysRevC.52.2694. arXiv: nucl-th/9505032 [nucl-th] (cit. on pp. 60, 62).

[187] Scott Chapman, Pierre Scotto, and Ulrich W. Heinz. "Model independent features of the two particle correlation function". In: *Acta Phys. Hung.* A1 (1995), pp. 1–31. arXiv: hep-ph/9409349 [hep-ph] (cit. on p. 60).

[188] Ulrich W. Heinz et al. "Lifetimes and sizes from two particle correlation functions". In: *Phys. Lett.* B382 (1996), pp. 181–188. DOI: 10.1016/0370-2693(96)00657-0. arXiv: nucl-th/9603011 [nucl-th] (cit. on p. 61).

[189] Scott Chapman, Pierre Scotto, and Ulrich W. Heinz. "A New cross term in the two particle HBT correlation function". In: *Phys. Rev. Lett.* 74 (1995), pp. 4400–4403. DOI: 10.1103/PhysRevLett.74.4400. arXiv: hep-ph/9408207 [hep-ph] (cit. on p. 61).

[190] Urs Achim Wiedemann, Pierre Scotto, and Ulrich W. Heinz. "Transverse momentum dependence of Hanbury-Brown-Twiss correlation radii". In: *Phys. Rev.* C53 (1996), pp. 918–931. DOI: 10.1103/PhysRevC.53.918. arXiv: nucl-th/9508040 [nucl-th] (cit. on p. 62).

[191] S. Chapman, P. Scotto, and Ulrich W. Heinz. "The 'Out longitudinal' cross term and other model independent features of the two particle HBT correlation function". In: *Nucl. Phys.* A590 (1995), pp. 449C–452C. DOI: 10.1016/0375-9474(95)00252-V. arXiv: hep-ph/9506470 [hep-ph] (cit. on p. 62).

[192] Urs Achim Wiedemann and Ulrich W. Heinz. "Particle interferometry for relativistic heavy ion collisions". In: *Phys. Rept.* 319 (1999), pp. 145–230. DOI: 10.1016/S0370-1573(99)00032-0. arXiv: nucl-th/9901094 [nucl-th] (cit. on p. 62).

[193] Björn Schenke, Chun Shen, and Prithwish Tribedy. "Features of the IP-Glasma". In: *Nucl. Phys.* A982 (2019), pp. 435–438. DOI: 10.1016/j.nuclphysa.2018.08.015. arXiv: 1807.05205 [nucl-th] (cit. on p. 68).

[194] Chun Shen et al. "The iEBE-VISHNU code package for relativistic heavy-ion collisions". In: *Comput. Phys. Commun.* 199 (2016), pp. 61–85. DOI: 10.1016/j.cpc.2015.08.039. arXiv: 1409.8164 [nucl-th] (cit. on p. 70).

[195] *VISHNU code package*. https://u.osu.edu/vishnu/downloads/. Accessed: 2018-03-14 (cit. on p. 70).

[196] Chun Shen. "The standard model for relativistic heavy-ion collisions and electromagnetic tomography". PhD thesis. Ohio State U., 2014-07-25. URL: http://rave.ohiolink.edu/etdc/view?acc_num=osu1405931790 (cit. on p. 70).

[197] Michael E. Peskin and Daniel V. Schroeder. *An Introduction to quantum field theory*. Reading, USA: Addison-Wesley, 1995. ISBN: 9780201503975, 0201503972. URL: http://www.slac.stanford.edu/~mpeskin/QFT.html (cit. on p. 77).

[198] D. E. Kharzeev et al. "Chiral magnetic and vortical effects in high-energy nuclear collisions—A status report". In: *Prog. Part. Nucl. Phys.* 88 (2016), pp. 1–28. DOI: 10.1016/j.ppnp.2016.01.001. arXiv: 1511.04050 [hep-ph] (cit. on p. 78).

[199] Kenji Fukushima. "Extreme matter in electromagnetic fields and rotation". In: (2018). arXiv: 1812.08886 [hep-ph] (cit. on pp. 78, 86).

[200] F. Becattini et al. "Local thermodynamical equilibrium and the beta frame for a quantum relativistic fluid". In: *Eur. Phys. J.* C75.5 (2015), p. 191. DOI: 10.1140/epjc/s10052-015-3384-y. arXiv: 1403.6265 [hep-th] (cit. on pp. 78, 84, 95, 101).

[201] Dmitri E. Kharzeev and Dam T. Son. "Testing the chiral magnetic and chiral vortical effects in heavy ion collisions". In: *Phys. Rev. Lett.* 106 (2011), p. 062301. DOI: 10.1103/PhysRevLett.106.062301. arXiv: 1010.0038 [hep-ph] (cit. on p. 78).

[202] Jaroslav Adam et al. "Polarization of Λ ($\bar{\Lambda}$) hyperons along the beam direction in Au+Au collisions at $\sqrt{s_{NN}}$ = 200 GeV". In: (2019). arXiv: 1905.11917 [nucl-ex] (cit. on p. 78).

[203] Sebastian Erne et al. "Universal dynamics in an isolated one-dimensional Bose gas far from equilibrium". In: *Nature* 563.7730 (2018), pp. 225–229. DOI: 10.1038/s41586-018-0667-0. arXiv: 1805.12310 [cond-mat.quant-gas] (cit. on p. 79).

[204] Julian S. Schwinger. "Brownian motion of a quantum oscillator". In: *J. Math. Phys.* 2 (1961), pp. 407–432. DOI: 10.1063/1.1703727 (cit. on p. 79).

[205] L. V. Keldysh. "Diagram technique for nonequilibrium processes". In: *Zh. Eksp. Teor. Fiz.* 47 (1964). [Sov. Phys. JETP20,1018(1965)], pp. 1515–1527 (cit. on p. 79).

[206] Asier Piñeiro Orioli. "Quantum dynamics and universality far from equilibrium". PhD thesis. U. Heidelberg, ITP, 2017. DOI: 10.11588/heidok.00023939 (cit. on p. 80).

[207] Paul A. M. Dirac. "Forms of Relativistic Dynamics". In: *Rev. Mod. Phys.* 21 (1949), pp. 392–399. DOI: 10.1103/RevModPhys.21.392 (cit. on p. 80).

[208] Raju Venugopalan. "Introduction to light cone field theory and high-energy scattering". In: *Lect. Notes Phys.* 516 (1999). [,89(1998)], p. 89. DOI: 10.1007/BFb0107312. arXiv: nucl-th/9808023 [nucl-th] (cit. on p. 80).

[209] T. Heinzl. "Light cone quantization: Foundations and applications". In: *Lect. Notes Phys.* 572 (2001), pp. 55–142. DOI: 10.1007/3-540-45114-5_2. arXiv: hep-th/0008096 [hep-th] (cit. on p. 80).

[210] Juergen Berges and Thomas Gasenzer. "Quantum versus classical statistical dynamics of an ultracold Bose gas". In: *Phys. Rev.* A76 (2007), p. 033604. DOI: 10.1103/PhysRevA.76.033604. arXiv: cond-mat/0703163 [cond-mat.other] (cit. on p. 81).

[211] Gert Aarts and Juergen Berges. "Classical aspects of quantum fields far from equilibrium". In: *Phys. Rev. Lett.* 88 (2002), p. 041603. DOI: 10.1103/PhysRevLett.88.041603. arXiv: hep-ph/0107129 [hep-ph] (cit. on p. 81).

[212] S. Yu. Khlebnikov and I. I. Tkachev. "Classical decay of inflaton". In: *Phys. Rev. Lett.* 77 (1996), pp. 219–222. DOI: 10.1103/PhysRevLett.77.219. arXiv: hep-ph/9603378 [hep-ph] (cit. on p. 82).

[213] D. T. Son. "Classical preheating and decoherence". In: (1996). arXiv: hep-ph/9601377 [hep-ph] (cit. on p. 82).

[214] Anatoli Polkovnikov. "Phase space representation of quantum dynamics". In: *Annals Phys.* 325 (2010), pp. 1790–1852. DOI: 10.1016/j.aop.2010.02.006. arXiv: 0905.3384 [cond-mat.stat-mech] (cit. on p. 82).

[215] Torsten V. Zache, Valentin Kasper, and Jürgen Berges. "Inflationary preheating dynamics with two-species condensates". In: *Phys. Rev.* A95.6 (2017), p. 063629. DOI: 10.1103/PhysRevA.95.063629. arXiv: 1704.02271 [cond-mat.quant-gas] (cit. on p. 82).

[216] Juergen Berges, Sebastian Scheffler, and Denes Sexty. "Bottom-up isotropization in classical-statistical lattice gauge theory". In: *Phys. Rev.* D77 (2008), p. 034504. DOI: 10.1103/PhysRevD.77.034504. arXiv: 0712.3514 [hep-ph] (cit. on pp. 82, 84).

[217] Juergen Berges et al. "Simulating plasma instabilities in SU(3) gauge theory". In: *Phys. Lett.* B677 (2009), pp. 210–213. DOI: 10.1016/j.physletb.2009.05.008. arXiv: 0812.3859 [hep-ph] (cit. on p. 82).

[218] Thorsten Zöller. "Nonequilibrium Formulation of Abelian Gauge Theories". PhD thesis. Darmstadt, Tech. U., 2013. URL: http://tuprints.ulb.tu-darmstadt.de/3373/ (cit. on p. 82).

[219] A. Schachner, A. Piñeiro Orioli, and J. Berges. "Universal scaling of unequal-time correlation functions in ultracold Bose gases far from equilibrium". In: *Phys. Rev.* A95.5 (2017), p. 053605. DOI: 10.1103/PhysRevA.95.053605. arXiv: 1612.03038 [cond-mat.quant-gas] (cit. on p. 85).

[220] Milton Abramowitz and Irene A. Stegun. *Handbook of Mathematical Functions with Formulas, Graphs, and Mathematical Tables*. ninth Dover printing, tenth GPO printing. New York: Dover, 1964 (cit. on p. 86).

[221] K. Atkinson. *An Introduction to Numerical Analysis*. Wiley, 1989. ISBN: 9780471624899. URL: https://books.google.de/books?id=cMLsbz0X6oIC (cit. on p. 89).

[222] Kenji Fukushima and Yoshimasa Hidaka. "Light projectile scattering off the color glass condensate". In: *JHEP* 06 (2007), p. 040. DOI: 10.1088/1126-6708/2007/06/040. arXiv: 0704.2806 [hep-ph] (cit. on p. 101).

[223] I. M. Georgescu, S. Ashhab, and Franco Nori. "Quantum Simulation". In: *Rev. Mod. Phys.* 86 (2014), p. 153. DOI: 10.1103/RevModPhys.86.153. arXiv: 1308.6253 [quant-ph] (cit. on p. 102).

[224] P. Aurenche, F. Gelis, and H. Zaraket. "Landau-Pomeranchuk-Migdal effect in thermal field theory". In: *Phys. Rev.* D62 (2000), p. 096012. DOI: 10.1103/PhysRevD.62.096012. arXiv: hep-ph/0003326 [hep-ph] (cit. on p. 111).

[225] H. Arthur Weldon. "Effective Fermion Masses of Order gT in High Temperature Gauge Theories with Exact Chiral Invariance". In: *Phys. Rev.* D26 (1982), p. 2789. DOI: 10.1103/PhysRevD.26.2789 (cit. on p. 111).

[226] Ralf Rapp and Jochen Wambach. "Low mass dileptons at the CERN SPS: Evidence for chiral restoration?" In: *Eur. Phys. J.* A6 (1999), pp. 415–420. DOI: 10.1007/s100500050364. arXiv: hep-ph/9907502 [hep-ph] (cit. on p. 112).

[227] W. Liu and R. Rapp. "Low-energy thermal photons from meson-meson bremsstrahlung". In: *Nucl. Phys.* A796 (2007), pp. 101–121. DOI: 10.1016/j.nuclphysa.2007.08.014. arXiv: nucl-th/0604031 [nucl-th] (cit. on pp. 112, 113).